UNIVERSITÄT BONN

A memory-based quantum network node with a trapped ion in an optical fibre cavity

Dissertation
zur
Erlangung des Doktorgrades (Dr. rer. nat.)
der
Mathematisch-Naturwissenschaftlichen Fakultät
der
Rheinischen Friedrich-Wilhelms-Universität Bonn

vorgelegt von
Pascal Kobel
aus
Fürth, Deutschland

Bonn 2021

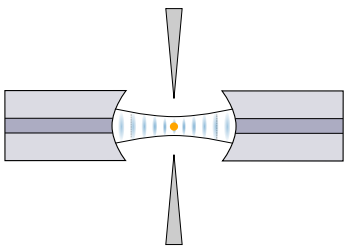

Angefertigt mit Genehmigung der Mathematisch-Naturwissenschaftlichen Fakultät der Rheinischen Friedrich-Wilhelms-Universität Bonn

1. Gutachter:	Prof. Dr. Michael Köhl
2. Gutachter:	Prof. Dr. Sebastian Hofferberth
Tag der Promotion:	06.10.2021
Erscheinungsjahr:	2022

Abstract

Exploiting quantum effects in the communication between different systems promise great capabilities as distributed quantum computing or provably secure communication. In this thesis we present the realisation of a memory-based quantum network node as a basic building block for quantum communication. The network node comprises of a single trapped ion as a stationary qubit, which is coupled to a light-matter interface linking the ion to a photonic communication channel. We present the application of an optical resonator, which consists of two opposing mirrors that we have realised at the end of two optical fibres. The small resonator volume (mode volume) increases the light-matter interaction rate, allowing a high bandwidth for the distribution of quantum information in a network via optical photons. In addition, the fibre-based resonator provides intrinsic coupling of the photons to optical fibres, which greatly simplifies their distribution in a network.

We demonstrate the first generation of quantum entanglement between a stationary qubit and a photon, with an optical fibre resonator as the interface between both qubits. Since a quantum state cannot be copied and transmitted classically, entanglement is essential for the purpose of quantum communication. We show that even at a distance (about 1.5 m) the ion and the photon share a common entangled quantum state with a high fidelity of $(90.1 \pm 1.7)\,\%$. The entangled state is generated on-demand by the deterministic excitation of the ion, where we achieve a detection rate of 62 Hz, enabled by the efficient interface between ion and photon.

The presented entanglement between an atom and a photon as two different types of qubits allows us to combine the advantages of information storage (atom) and long range distribution of quantum information (photon). In this context, we demonstrate the first implementation of a provably secure quantum key distribution (QKD) between two remote parties involving an entangled memory qubit. The presented method hereby addresses two principal challenges of quantum key distribution, namely key generation and long-range application. We show that the fundamental quantum mechanical properties of the entangled two-qubit state allow us to generate a key with certifiable randomness, which in this strong form is not possible classically. Furthermore, the presented methods of memory-based key distribution are particularly applicable in the context of quantum repeaters, in which quantum information is temporarily stored before further distribution. This enables long-range key distribution even beyond the point-to-point limit of optical quantum communication, which results from the absorption properties of optical photons as information carriers.

Parts of this thesis have been published or will be published in the following articles:

- [91] P. Kobel, R. Berner and M. Köhl. Secure distribution of a certified random quantum key using an entangled memory qubit, 2021 (submitted, preprint available on *arXiv:2111.14523*). https://doi.org/10.48550/arXiv.2111.14523

- [92] P. Kobel, M. Breyer and M. Köhl. Deterministic spin-photon entanglement from a trapped ion in a fiber Fabry–Perot cavity. *npj Quantum Information*, 7(1):6, Jan 2021. https://doi.org/10.1038/s41534-020-00338-2

- [93] P. Kobel, M. Link, and M. Köhl. Exponentially improved detection and correction of errors in experimental systems using neural networks, 2020 (submitted, preprint available on *arXiv:2005.09119*).

Contents

1 Introduction **1**

2 Theory of two-qubit entanglement **6**
2.1 Quantum bits . . . 6
2.1.1 State transformation . . . 7
2.2 Entanglement between two quantum bits . . . 9
2.3 Non-locality . . . 9
2.4 Bell's inequalities . . . 10
2.4.1 Loopholes . . . 11

3 Trapping of Yb^+ **12**
3.1 Experimental techniques . . . 13
3.1.1 Ion trapping and micromotion . . . 13
3.1.2 Isotope selective loading . . . 16
3.1.3 Cooling of $^{174}Yb^+$ and $^{171}Yb^+$ . . . 17
3.2 Experimental setup . . . 19
3.2.1 Laser system . . . 20
3.2.2 Optical access . . . 22
3.2.3 Free-space imaging . . . 25
3.2.4 Data acquisition and experimental control . . . 29

4 Optimising experimental calibration tasks with machine learning **32**
4.1 The task of stray field cancellation . . . 34
4.1.1 Micromotion detection and compensation along one spatial direction 35
4.1.2 Gradient descent optimisation . . . 38
4.1.3 Plane model . . . 38
4.2 Machine learning enhanced stray field compensation . . . 41
4.2.1 Unsupervised machine learning using principal component analysis . 41
4.2.2 Supervised machine learning using an artificial neural network . . . 45
4.3 Summary . . . 47

5 A fibre Fabry-Pérot cavity as a light-matter interface **49**
5.1 Fabry-Pérot resonator . . . 50
5.1.1 Longitudinal mode . . . 50
5.1.2 Transverse mode . . . 51
5.2 Development and assembly of the fibre Fabry-Pérot cavity . . . 53
5.3 Cavity lock and stability . . . 58
5.3.1 Locking scheme . . . 58
5.3.2 Reference laser calibration and measurement of the cavity length . . 59
5.3.3 Mechanical stability . . . 62
5.4 Light-matter interaction . . . 65
5.4.1 The electric dipole transition in a semi-classical description . . . 66
5.4.2 Rotating wave approximation . . . 67
5.4.3 Field quantisation . . . 68

5.4.4 A two-level system inside an optical resonator . . . 69
5.4.5 Ion position within the cavity mode . . . 72
5.5 Photons as travelling qubits . . . 75
5.5.1 Detection setup . . . 75
5.5.2 Time profile of the extracted photons and characterisation of the light-matter interface . . . 77
5.5.3 Discussion of the achieved cavity parameters . . . 79
5.5.4 Projective measurement of the photonic qubit state . . . 81
5.5.5 Birefringence of the fibre cavity . . . 85
5.6 Summary . . . 86

6 The ^{171}Yb ion as a memory qubit 88
6.1 State initialisation . . . 89
6.2 Fluorescence state detection . . . 90
6.2.1 Measurement of the expectation value . . . 92
6.2.2 Single shot readout . . . 93
6.2.3 Monte-Carlo simulation . . . 98
6.3 Pulsed excitation . . . 100
6.3.1 Optical Bloch equations . . . 100
6.3.2 Theory of pulse shapes . . . 103
6.3.3 Generation of pulses . . . 105
6.3.4 Spectral filtering of the pulses . . . 108
6.3.5 Calibration of pulse parameters . . . 109
6.3.6 Deterministic generation of single photons . . . 111
6.3.7 Impact of the pulsed laser calibration on the generation of an entangled spin-photon state . . . 113
6.3.8 Summary . . . 115
6.4 Hyperfine qubit manipulation . . . 116
6.4.1 Theory . . . 116
6.4.2 Basis selection of the atomic qubit readout . . . 121
6.4.3 Microwave setup . . . 126
6.4.4 Calibration of the microwave experimental parameters . . . 127
6.5 Coherence time . . . 128
6.6 Magnetic field control . . . 132
6.6.1 Orientation and magnitude of the magnetic field . . . 132
6.6.2 Stability of the magnetic field . . . 134
6.7 Summary . . . 139

7 Spin-photon entanglement 140
7.1 Generation of deterministic atom-photon entanglement . . . 140
7.1.1 Spontaneous decay in a two-level system . . . 141
7.1.2 Photon detection probability . . . 142
7.1.3 Spontaneous decay to multiple ground states . . . 143
7.1.4 Experimental implementation . . . 145

7.2 Experimental sequence . . . 146
7.2.1 Experimental rate . . . 147
7.3 Correlation measurements in the $\hat{\sigma}_z \otimes \hat{\sigma}_z$ basis . . . 149
7.3.1 Time dependence of the $\hat{\sigma}_z \otimes \hat{\sigma}_z$ basis . . . 151
7.3.2 Imperfections reducing the correlation contrast in $\hat{\sigma}_z \otimes \hat{\sigma}_z$ basis . . . 151
7.4 Correlation measurements in the rotated bases $\hat{\sigma}_{x/y}$ . . . 153
7.4.1 Time dependence of the rotated bases . . . 156
7.4.2 Imperfections reducing the correlation contrast in the rotated bases 158
7.5 Full quantum state tomography . . . 160
7.5.1 Density formalism . . . 161
7.5.2 Quantum state reconstruction . . . 162
7.5.3 Unitary transformations . . . 163
7.5.4 Ensure physical consistency using maximum likelihood estimation . 164
7.5.5 Entangled state fidelity . . . 164
7.6 Summary . . . 166

8 Quantum key distribution using an entangled memory qubit 167
8.1 Working principle of QKD . . . 169
8.2 Technical implementation and key distribution protocol . . . 170
8.3 Key rates, key reconciliation and privacy amplification . . . 172
8.3.1 Key rates . . . 172
8.3.2 Quantum bit error rate (QBER) . . . 173
8.3.3 Key reconciliation and privacy amplification . . . 175
8.4 Randomness certification using the violation of Bell's inequalities . . . 176
8.5 Security measures against side channel attacks . . . 180
8.6 Summary . . . 181

9 Summary and outlook 183
9.1 Summary . . . 183
9.2 Outlook . . . 185

10 Appendix 189
A Standard error on binned photon statistic . . . 189
B Clebsch-Gordan coefficients of $^{171}Yb^{+}$ . . . 189
C Spatial emission characteristics of a classical dipole . . . 191
D Magnetic field generation . . . 192
E Experimental setup . . . 193

List of Figures 195

List of Tables 198

Bibliography 199

1 Introduction

Exploring the potential of quantum effects is currently one of the main research areas in modern science and establishes a whole new category of technology [41]. Applications that employ quantum effects can be far superior to their classical counterparts in solving specific computational problems [3] or, in the domain of cryptography, offer alternative methods that can ensure provable security through the rules of quantum mechanics [182, 155, 89, 47]. The communication between different systems via a quantum channel plays a central role in this context because, on the one hand, a quantum channel enables a new type of information transmission between classical systems that employs the excellent cryptographic properties of distributed quantum keys [140]. On the other hand, it enables the connection of two distant quantum systems [121, 143], which in turn has the potential to create new applications in the field of quantum technology, such as distributed quantum computing [84, 39], remote quantum sensing [136] or true random number generation [138].

For the communication between individual quantum systems, the properties of quantum information must be taken into account. Unlike its classical counterpart, a quantum bit (qubit) can be in a superposition of its two basis states, which results in extraordinary properties for information processing. To extend this capability with the underlying properties of quantum information across multiple nodes of a network, it is necessary to distribute quantum states coherently across the network.

Since a quantum state cannot be cloned [182], quantum information can only be distributed by entangling the endpoint of a communication channel with that communication channel [23]. This makes entanglement a key resource for quantum technology, but also eliminates the possibility of transmitting quantum information as in classical networks by measuring a state, encoding it into a signal and transmitting it over the network. The architecture of a quantum network, therefore, has to differ substantially from that of a classical network and requires the distribution of entanglement between the nodes.

For the purpose of entanglement distribution, photons are excellent candidates. These fast information carriers can be guided through optical fibres which support their distribution in complex and long-distance networks. Furthermore, quantum information can be encoded, for example, in the time [50], frequency [56] or polarisation [23] degrees of freedom of a photon. However, in practical applications, photons usually travel through a medium, which implies a potential loss of an information carrier through absorption. This leads to an absolute distance limit for practicable point-to-point links in quantum communication [137]. The properties of a quantum network are thus strongly coupled to the respective communication channel, but are defined in particular by the capabilities of the network nodes.

To exploit the potential of quantum networks, information processing nodes are required which can send, receive and store quantum information [143]. The excellent properties of matter qubits for quantum information processing favour their use as stationary qubits at the nodes of a quantum network. There have been several approaches towards the experimental realisation of quantum network nodes with matter qubits, for example, using trapped ions [23, 164, 24, 163, 37], neutral atoms [180, 175], nitrogen-vacancy centres [167] or silicon-vacancy centres [124] in diamond, and semiconductor quantum dots [40, 56].

Each system has its advantages and especially with regard to large-scale quantum networks, the use of long-lived stationary qubits with the ability to store quantum information is desirable. In particular, to establish a practical network, the distribution of entanglement between the nodes has to be faster than its loss in the network. Therefore, the so-called memory qubits allow to overcome the limit of point-to-point quantum communication [21] by caching quantum information at the nodes of a network. This enables the realisation of long-distant quantum communication even despite the absorption properties of optical photons as information carriers. In particular, memory qubits could enable the realisation of a so-called quantum repeater, in which the quantum information is temporarily stored before further distribution [172].

For use as memory qubits, trapped ions have advantageous properties. Due to their decoupling from the environment, they offer long storage intervals of quantum information and individual addressing for example via laser beams for state manipulation and readout. Moreover, their long trapping times facilitate their use in quantum networks [121] and for quantum information processing [183].

In a quantum network node, linking the stationary qubit to the quantum communication channel is essential to combine the capabilities of the stationary information processing and storage qubit with the remote distribution of quantum information via a travelling qubit. For this purpose, efficient light-matter interfaces operating at the quantum limit are required that couple travelling qubits and stationary qubits in the network, see Figure 1.1.

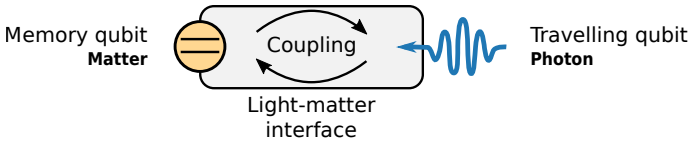

Figure 1.1: The joint use of light and matter in a quantum network requires interfaces for the exchange of quantum information.

Experimental approaches to light-matter interfaces have ranged from collecting light with high numerical aperture objectives [24, 161, 167, 2, 58, 175] to embedding emitters in macroscopic optical cavities in order to increase the light-matter coupling rate [180, 99, 164, 158, 143]. With optical cavities, the rate at which entanglement can be distributed across a quantum network can be greatly enhanced, for example by taking advantage of the improved photon collecting ability or the tunability of entanglement parameters [127].

The effective coupling of light and matter is an advanced property of optical cavities but requires, especially with respect to a single atom, the development of cavities that have small mode volumes. This generally entails small cavity lengths and positioning of the mirrors close to the atom, which becomes particularly difficult in combination with trapped ions, as the possible formation of stray electric charges on the dielectric surfaces of the mirrors affects trapping stability [65, 6].

A particularly elegant approach is the fabrication of mirror structures with small radii of curvature on the tips of optical fibres, which allows a miniaturised cavity to be realised that require only a small amount of dielectric material. This device consists of a pair of optical fibres whose micromachined end facets are coated with a highly reflective optical coating. Invented by Jakob Reichel's group in 2006 [160, 69], fibre-based cavities achieved a remarkable reduction of the mode volume due to mirror separations on

the order of 10–300 μm. They combine the best of two worlds: on the one hand, they are optical microresonators with small mode volume and on the other hand the cavity mode is directly fibre-coupled. Since they promise a large coupling strength between light and matter, coupling to fibre cavities has already been shown for neutral atoms [54, 36], nitrogen-vacancy centres [1] and semiconductor quantum dots [122]. In particular, the embedding of trapped ions in fibre cavities benefits from the miniaturised mirror surfaces. However, due to the numerous (mostly technical) challenges, only a few research groups have successfully combined fibre cavities with trapped ions [158, 165, 28].

In this thesis, we utilise a fibre cavity resonant to the principal ultraviolet (UV) transition of a trapped Ytterbium ion (Yb^+) as a light-matter interface to efficiently collect photons which are emitted by the ion together with a fast extraction of these information carriers. We demonstrate for the first time the generation and detection of an entangled light-matter state from a fibre cavity, which allows us to combine the advantageous properties of the trapped ion as a memory qubit with the fast distribution of quantum information offered by optical photons. This makes the presented system potentially applicable as a node in a large-scale quantum network or in a quantum repeater (see Figure 1.2).

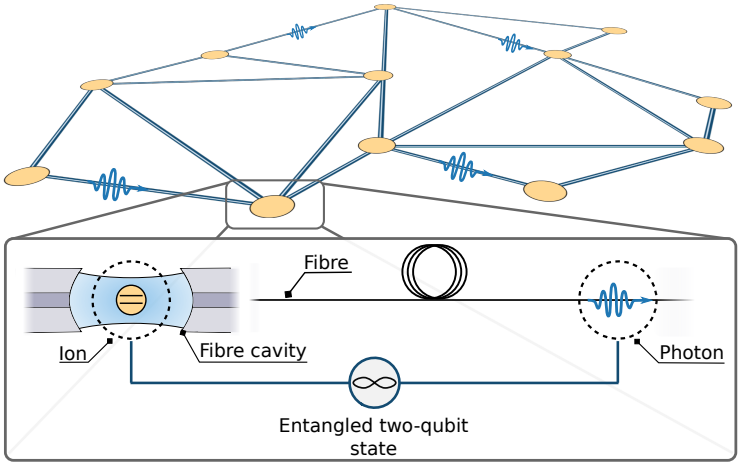

Figure 1.2: Sketch of a quantum network in which photons are guided as travelling qubits through optical fibres. The network node presented in this thesis is shown as a basic building block of the sketched network (box). For entanglement-based communication, phase coherence is distributed across the network nodes and must be maintained to sustain the entanglement. Efficient light-matter interfaces enable the scaling of the network in terms of nodes and distance.

In particular, the long-range application of quantum communication is of high interest in order to solve the so-called key distribution problem between two communication partners. Key distribution is most commonly realised using asymmetric cryptography in classical information theory, which is considered to become insecure in the post-quantum era [154]. The so-called quantum key distribution (QKD), offers a paradigm-changing solution to the key distribution problem [110], which is based on a quantum communication channel and for which several protocols and architectures have been proposed so far. Due to its simple prepare-and-measure architecture, the one-qubit BB84 protocol [14] was the first QKD protocol realised in an experimental setup. However, implementations of QKD protocols that require a direct link between the communication parties

(e.g. BB84) naturally encounter a physical limit when the loss of the communication channel over distance is considered [166]. As introduced by A. K. Ekert in 1991 [47], the concept of entanglement-based QKD is able to utilise fundamental quantum mechanical properties of entangled states that offer additional benefits, such as the application with memory-enhanced quantum communication capable of overcoming the rate-distance limit.

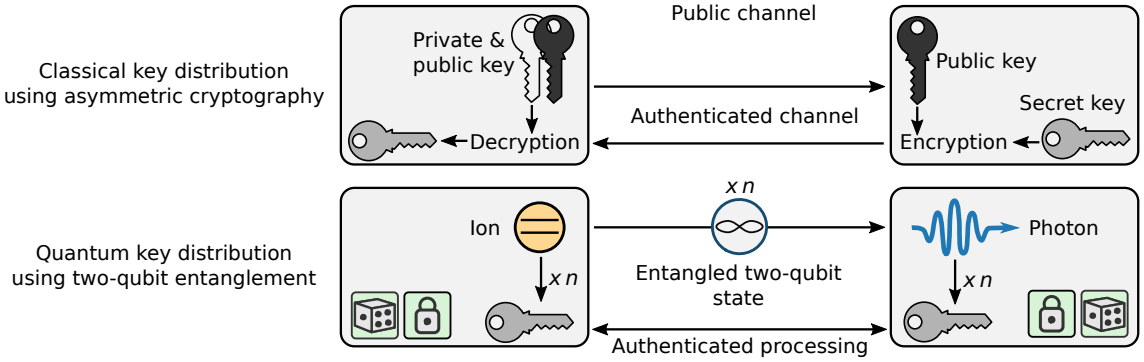

Figure 1.3: Classical and quantum approach for the distribution of a secret secret key between two remote communication parties. The classical approach most commonly utilises asymmetric cryptography based on computationally hard problems. Quantum key distribution as presented in this thesis utilises n measurements of an entangled two-qubit quantum state. The key can be distributed secure and generated certifiable random even when assuming an attacker with unlimited resources.

In this thesis, we present the first realisation of a true single-photon quantum key distribution protocol between two remote parties involving an entangled memory qubit (see Figure 1.3). The setup enables us to securely distribute a secret key between both endpoints of the quantum communication channel (see Figure 1.3). The derived key can be used for encryption with the andvanced encryption standard (AES), for example. This combination of QKD and AES is expected to provide secure remote communication even in the post-quantum era [26].

In addition to a potential long-range application of secure key distribution, the presented system has another outstanding feature from the perspective of information security. When it comes to the generation of secret keys, cryptographically secure random number generators are an essential building block of secure systems. However, true random numbers are hard to generate and even harder to verify. We demonstrate that we can certify the randomness of the distributed quantum key using the fundamental non-local properties of our entangled state, which in this strong form is not possible classically. Even when using quantum systems for the distribution of keys (e.g. in the context of BB84), true randomness of those quantum keys is only achieved for systems that exhibit a violation of the Bell inequalities [11, 138]. In total, we show that a secret key derived by both communication parties was distributed secure and generated with certified randomness, which combines the fundamental requirements on a shared secret quantity. The capability of the system to cache the required quantum information in a memory qubit potentially allows this key to be distributed over arbitrarily large distances in the framework of an ideal quantum repeater [172].

Thesis Structure

The following chapters of this thesis focus on different aspects of the presented quantum network node.

Chapter 2 briefly introduces the basic terminology used in this thesis, such as quantum bits, quantum states, entanglement and related specific quantum mechanical properties such as superposition and non-locality.

Chapter 3 introduces the main experimental techniques by which a single Ytterbium ion can be isolated and confined in a spatial region, allowing the addressing and manipulation of the atomic matter at the quantum mechanical level. The experimental setup used for this purpose is presented, together with the technical infrastructure for the measurements carried out in the context of this thesis.

Chapter 4 presents a novel approach to create an empirical model of an experimental apparatus employing machine learning. We apply this methodology to the trapping time optimisation of the ion by disturbance cancellation.

Chapter 5 introduces the fibre Fabry-Pérot cavity as an advanced light-matter interface in quantum network applications. In this context, we also introduce the photon as a travelling qubit.

Chapter 6 describes the usage of the trapped Yb^+ as a memory qubit with focus on the application in a quantum network. In this context, we present the requirements for the generation of entanglement between the trapped ion and an emitted photon.

Chapter 7 presents generation and detection of the ion-photon state. As a basic building block for entanglement-based quantum communication, we characterise the ion-photon state by performing a full state tomography and evaluating in detail the contributions of errors in generation and detection.

Chapter 8 describes the application of the generated ion-photon state for the purpose of provably secure quantum key distribution (QKD) exploiting the fundamental properties of quantum mechanics . We present the non-locality of our state as a highlight for the generation of a certifiable random key.

Chapter 9 concludes the work with a summary of the results and an overview of possible improvements. We put the presented setup in the context of a long-term perspective in quantum communication, where we point out the role of entanglement-based communication for large-scale networks, especially with regard to the realisation of a quantum repeater.

2 Theory of two-qubit entanglement

Contents

2.1 Quantum bits 6
2.2 Entanglement between two quantum bits 9
2.3 Non-locality 9
2.4 Bell's inequalities 10

2.1 Quantum bits

One can encode information in certain states of a system. This statement holds for classical information technology as well as for quantum technology. However, there is an important difference between a classical bit and a quantum bit (qubit). While the former occupies a single and defined state (e.g. charge (1) / no charge (0)) at a certain point in time, the latter can be in a superposition of states enabled through the quantum nature of the underlying system. For example, a quantum two-level system can be realised with two distinct energy levels in case of an atomic qubit or with different polarisations of light in case of a photonic qubit. We describe a quantum bit as a quantum mechanical two-level system where we can define an orthogonal basis of the corresponding state space known as Hilbert space. Analogously to a classical system where the states are named 0 and 1, we introduce for a quantum bit the states $|0\rangle$ and $|1\rangle$ as an orthogonal basis.

A quantum state $|\Psi\rangle$ of the system can be expressed through the probability $p_{0/1}$ to find the state $|\Psi\rangle$ in one of the states $|0\rangle$ / $|1\rangle$ as

$$|\Psi\rangle = c_0\,|0\rangle + c_1\,|1\rangle \quad \text{with} \quad p_{0/1} = |c_{0/1}|^2, \tag{2.1}$$

where the probabilities fulfil $p_0 + p_1 = 1$ for a pure state. In the experiment, we can obtain these probabilities from the expectation value $\left\langle \hat{O} \right\rangle$ of a measurement operator[1] $\hat{O}$. However, in general, a measurement $\hat{O}$ projects the quantum state $|\Psi\rangle$ to the eigenstates of the operator $\hat{O}$ ('von Neumann measurement').

For a quantum two-level system, a complete set of operators with orthogonal eigenstates are given by the Pauli operators (Pauli matrices):

$$\begin{aligned}
\hat{\sigma}_x &= \quad |1\rangle\langle 0| + |0\rangle\langle 1| = \begin{pmatrix} 0 & 1 \\ 1 & 0 \end{pmatrix} \quad \text{with eigenstates} \quad |\Psi_{\pm x}\rangle = \frac{1}{\sqrt{2}}\left(|1\rangle \pm |0\rangle\right), \\
\hat{\sigma}_y &= -i\,|1\rangle\langle 0| + i\,|0\rangle\langle 1| = \begin{pmatrix} 0 & -i \\ i & 0 \end{pmatrix} \quad \text{with eigenstates} \quad |\Psi_{\pm y}\rangle = \frac{1}{\sqrt{2}}\left(|1\rangle \pm i\,|0\rangle\right), \\
\hat{\sigma}_z &= \quad |1\rangle\langle 1| - |0\rangle\langle 0| = \begin{pmatrix} 1 & 0 \\ 0 & -1 \end{pmatrix} \quad \text{with eigenstates} \quad |\Psi_{+z}\rangle, |\Psi_{-z}\rangle = |1\rangle, |0\rangle
\end{aligned} \tag{2.2}$$

and

$$\hat{\sigma}_j\,|\Psi_{\lambda\cdot j}\rangle = \lambda \cdot |\Psi_{\lambda\cdot j}\rangle\,. \tag{2.3}$$

[1] In quantum mechanics, measurements on a state are described by Hermitian operators to account for the possibility of a measurement to change the quantum state

The matrix representation of the Pauli operators can be derived from a vector representation of the qubit state

$$|\Psi\rangle = \begin{pmatrix} c_1 \\ c_0 \end{pmatrix}. \tag{2.4}$$

The expectation value of the $\hat{\sigma}_z$ operator is given by the probabilities $p_{0/1}$ as

$$\langle \hat{\sigma}_z \rangle = \langle \Psi | \hat{\sigma}_z | \Psi \rangle = p_1 - p_0 \tag{2.5}$$

which gives $\langle \hat{\sigma}_z \rangle = -1$ for a state with $p_0 = 1$ and $\langle \hat{\sigma}_z \rangle = 1$ for $p_1 = 1$, where the basis states $|0\rangle$ / $|1\rangle$ are also the eigenstates of the operator $\hat{\sigma}_z$.

Using $p_0 + p_1 = 1$, we can rewrite a pure qubit quantum state $|\Psi\rangle$ as

$$|\Psi\rangle = \cos(\theta/2)\,|1\rangle + e^{i\phi} \sin(\theta/2)\,|0\rangle \;\text{ with } 0 \leq \theta \leq \pi \text{ and } 0 \leq \phi \leq 2\pi, \tag{2.6}$$

where we neglect any global phase of the quantum state, since it is not required to describe the state. The angular representation is reminiscent of spherical coordinates and indeed we can represent a two-level system state on a sphere (the so-called Bloch sphere) using the expectation values of the Pauli operators to form a basis for the representation as a vector (the so-called Bloch vector[2]):

$$x = \langle \hat{\sigma}_x \rangle\,,\; y = \langle \hat{\sigma}_y \rangle \;\text{ and }\; z = \langle \hat{\sigma}_z \rangle\,. \tag{2.7}$$

Figure 2.1 shows a representation of a pure state $|\Psi\rangle$ on the Bloch sphere[3] including the corresponding angles according to equation (2.6) and the eigenstates of the Pauli operators according to equations (2.2).

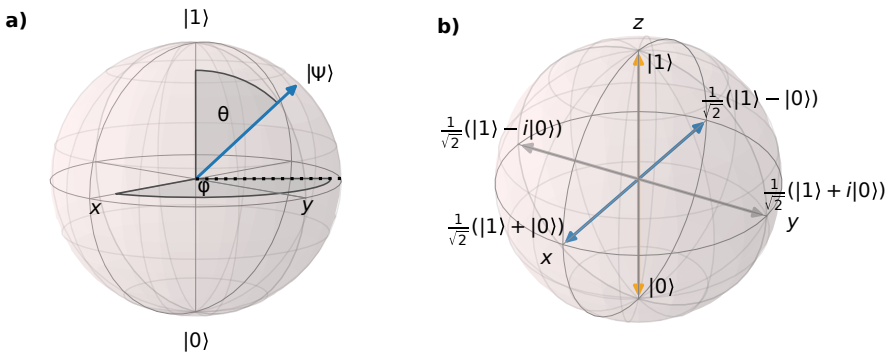

Figure 2.1: a) Example qubit state $|\Psi\rangle$ according to equation (2.6) with $\theta = 1/4 \cdot \pi$ and $\phi = 3/4 \cdot \pi$ visualised on the Bloch sphere. **b)** Bloch sphere representation of the eigenstates of the Pauli operators $\hat{\sigma}_{x/y/z}$ which are shown as arrows (blue/grey/yellow). The arrows are labelled with the corresponding state $|\Psi_{\pm x/y/z}\rangle$.

2.1.1 State transformation

A pure state $|\Psi\rangle$ can be transformed into any pure state $|\Psi'\rangle$ by rotating it with an angle α around a certain vector $\vec{r}$ on the Bloch sphere

$$|\Psi'\rangle = \hat{R}_{\vec{r}}\,|\Psi\rangle\,, \tag{2.8}$$

[2] Bloch vector and Bloch sphere named after Felix Bloch. Also known as Poincaré sphere in optics

[3] We use the package QUTIP in PYTHON for the Bloch-sphere plots

where the general rotation operator $\hat{R}$ is given by

$$\hat{R}^{\alpha}_{\vec{r}} = \exp\left(-\frac{i\alpha}{2} \cdot \vec{r} \cdot \begin{pmatrix} \hat{\sigma}_x \\ \hat{\sigma}_y \\ \hat{\sigma}_z \end{pmatrix}\right). \tag{2.9}$$

Here, $\hat{\sigma}_{x,y,z}$ are the Pauli-matrices and the rotation operator has to fulfil $\hat{R}^{\dagger}\hat{R} = \hat{R}\hat{R}^{\dagger} = \mathbb{I}$ and $||\vec{r}|| = 1$.

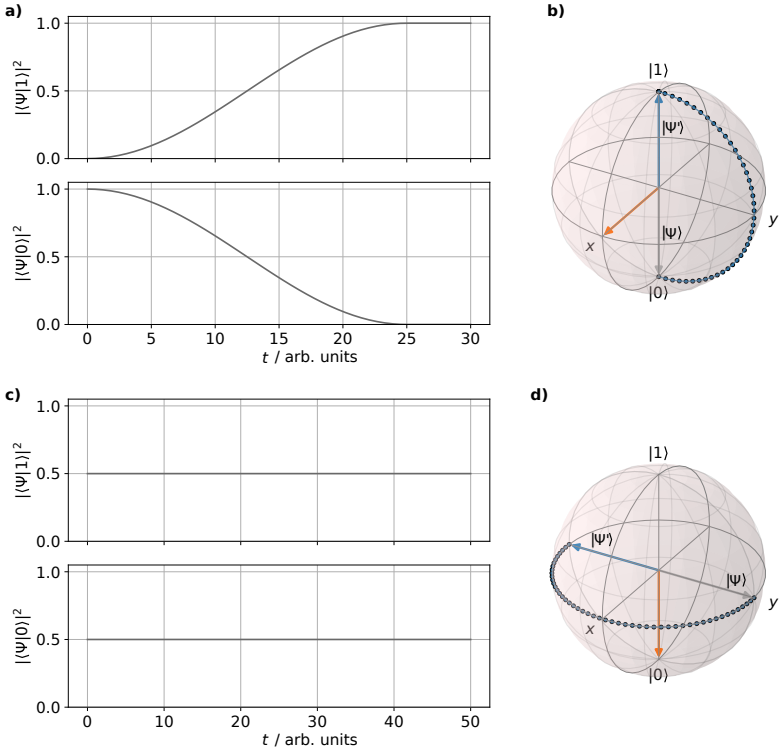

Figure 2.2: Rotation of a state $|\Psi\rangle$ to a state $|\Psi'\rangle$ according to equation (2.8). **a)** Evolution of the expectation values of the state projection to the basis states $|0\rangle$ and $|1\rangle$ for $\hat{R}^{\pi}_{\hat{e}_x}$. **b)** Evolution of the state on the Bloch-sphere. The initial state $|\Psi\rangle = |0\rangle$ is shown as grey arrow and the final state $|\Psi'\rangle = |1\rangle$ as blue arrow. The trace of the state on the Bloch-sphere is shown as blue points. The rotation axis $\vec{r} = \hat{e}_x$ is shown as orange arrow. **c)** Same as in a) but for $\hat{R}^{\pi}_{-\hat{e}_z}$ with $\vec{r} = \hat{e}_z$. Note that the expectation values of measuring the $|0\rangle$ or the $|1\rangle$ state do not change. Instead the phase ϕ changes from $\pi/2$ to $-\pi/2$. **d)** Same as in b) but for $\hat{R}^{\pi}_{-\hat{e}_z}$.

Figure 2.2 shows two fundamental qubit rotations: a)+b) a state flip, where the unit probability of measuring the $|0\rangle$ state is fully transferred to a unit probability of measuring the $|1\rangle$ state. c)+d) The relative phase ϕ of a superposition state flips sign without affecting the expectation values of measuring the $|0\rangle$ or $|1\rangle$ state. However, as is not evident from the shown expectation values of the latter example, there is still information encoded in the phase of the quantum state. The ability of the qubit to retain phase information is also called phase coherence and is a fundamental quantum mechanical property. It distinguishes a pure quantum state from a statistical mixed state.

2.2 Entanglement between two quantum bits

For a combined two-qubit system comprising of the qubits A and B, we have to consider a four-dimensional Hilbert space $\mathcal{H} = \mathcal{H}_a \otimes \mathcal{H}_b$ as a tensor product of the two two-dimensional Hilbert spaces $\mathcal{H}_a$ and $\mathcal{H}_b$ of the subsystems A and B. We name the state of the subsystem of qubit A $|\phi\rangle_a$ and $|\phi\rangle_b$ for qubit B, where we assume pure states. We name the two-qubit quantum state $|\phi\rangle_{a,b}$.

A particular interesting class of two-qubit states are entangled states which show non-classical correlations between the two qubits and are intrinsically linked to quantum phenomena. Nowadays, entanglement constitutes a key resource for quantum computing and quantum communication. In particular, the entanglement between light and matter is a key part of this thesis.

We can define entangled states by their opposite, non-entangled states. If the pure state $|\phi\rangle_{a,b}$ of the combined two-qubit system can be separated into a product state of the two individual subsystems A and B as

$$|\phi\rangle_{a,b} = |\phi\rangle_a \otimes |\phi\rangle_b \,, \tag{2.10}$$

the state $|\phi\rangle_{a,b}$ is not entangled, e.g. $|\phi\rangle_{a,b} = |1\rangle_a |1\rangle_b$ is a non-entangled two-qubit state. However, if we cannot find a state $|\phi\rangle_{a/b}$ that separately describes the system A/B, the state $|\phi\rangle_{a,b}$ is not a product state and is considered to be an entangled state [9]. The so-called Bell-states constitutes maximally entangled states and are given by:

$$\begin{aligned}
\left|\Phi^+\right\rangle_{a,b} &= \frac{1}{\sqrt{2}} \left(|0\rangle_a |0\rangle_b + |1\rangle_a |1\rangle_b\right) \\
\left|\Phi^-\right\rangle_{a,b} &= \frac{1}{\sqrt{2}} \left(|0\rangle_a |0\rangle_b - |1\rangle_a |1\rangle_b\right) \\
\left|\Psi^+\right\rangle_{a,b} &= \frac{1}{\sqrt{2}} \left(|0\rangle_a |1\rangle_b + |1\rangle_a |0\rangle_b\right) \\
\left|\Psi^-\right\rangle_{a,b} &= \frac{1}{\sqrt{2}} \left(|0\rangle_a |1\rangle_b - |1\rangle_a |0\rangle_b\right) .
\end{aligned} \tag{2.11}$$

The Bell-states are clearly not separable into a product state of qubit A and B.

Two-qubit entanglement can be realised, for example, between the polarisation states of photons [100] and also between the internal states of material qubits [170]. However, entanglement between light and matter, e.g. using trapped ions [23], allows to connect material qubits as quantum memories to a photonic communication channel, which is crucial for the realisation of quantum networks [84]. We discuss this in detail in chapter 7.

2.3 Non-locality

In 1935, Einstein, Podolsky and Rosen published what they considered to be a dilemma (EPR dilemma) [45] in which they describe the conflict between the ideas of a classical descriptive theory and quantum mechanical effects arising, for example, from entanglement. From their point of view, a physical theory should imply: completeness ('*every element of the physical reality must have a counterpart in the physical theory*'), realism (if one can predict with certainty the value of a physical quantity, there must exists an element as a counterpart in reality) and locality (physical systems can be spatially separated such that they are independent from each other, i.e. interactions can be neglected) .

However, if we consider two entangled quantum systems A and B that are far away from each other, a measurement on one system directly affects the other system, regardless of the distance between them: considering the maximally entangled state $\left|\Phi^+\right\rangle_{a,b}$ from equations (2.11), a measurement in basis $\hat{\sigma}_z$ on system A with result -1 (corresponding to state $\left|0\right\rangle_a$) directly changes the two-qubit state to $\left|0\right\rangle_a \otimes \left|0\right\rangle_b$ where the qubit on side B gets projected to the state $\left|0\right\rangle_b$ (similar for $\hat{\sigma}_{x/y}$ and ± 1 measurement outcome). This change occurs instantaneously and seems to conflict with the idea of special relativity that no signal can propagate faster than light. Hence, the property of non-locality has been given to entangled states to reflect the conflict with local realism (Qubit A and B exists regardless if they are measured and no signal can propagate faster than light) [9]. The EPR paradox is at least partially solved by the no-signalling theorem (Ghirardi, Rimini and Weber 1980), which states that the possible outcomes of measurements on side B are not influenced by a measurement on side A [9].

2.4 Bell's inequalities

The approach of describing quantum systems using so-called local hidden-variable models (LHVMs), which introduce deterministic correlation to the systems, leads to the Bell inequalities [11] which constitute a quantitative version of the EPR paradox.

In the following, we introduce a version of the Bell inequalities proposed by Clauser, Horne, Shimony and Holt (CHSH) [33], where the measurements outcomes are statistically determined by local hidden variables λ according to a local realistic theory. We define observables $A(\vec{a},\lambda) = \pm 1$ and $B(\vec{b},\lambda) = \pm 1$ as outcome of a state measurement on side A/B (locality) with the basis setting $\vec{a}/\vec{b}$ (reality). The expectation value of a joint measurement is given by

$$E(\vec{a},\vec{b}) = \int p(\lambda) A(\vec{a},\lambda) B(\vec{b},\lambda) d\lambda, \tag{2.12}$$

where p(λ) is the probability distribution with $\int p(\lambda) d\lambda = 1$. With the alternative bases $\vec{a}'$ and $\vec{b}'$ we can derive the CHSH version of Bell inequality by considering

$$\begin{aligned} E(\vec{a},\vec{b}) - E(\vec{a},\vec{b}') = & \int p(\lambda) \left[A(\vec{a},\lambda) B(\vec{b},\lambda) - A(\vec{a},\lambda) B(\vec{b}',\lambda) \right] d\lambda \\ = & \int p(\lambda) A(\vec{a},\lambda) B(\vec{b},\lambda) \left[1 \pm A(\vec{a}',\lambda) B(\vec{b}',\lambda) \right] d\lambda \\ & - \int p(\lambda) A(\vec{a},\lambda) B(\vec{b}',\lambda) \left[1 \pm A(\vec{a}',\lambda) B(\vec{b},\lambda) \right] d\lambda \end{aligned} \tag{2.13}$$

according to [9]. Finally, we find the following inequality:

$$|E(\vec{a},\vec{b}) - E(\vec{a},\vec{b}')| \leq 2 \pm \left[E(\vec{a}',\vec{b}') + E(\vec{a}',\vec{b}) \right]. \tag{2.14}$$

Quantum mechanically, the expectation value of a measurement performed on the entangled Bell state $|\Psi^-\rangle$ is given by [9]

$$E(\vec{a},\vec{b}) = \left\langle \Psi^- \right| \vec{a} \cdot \hat{\vec{\sigma}} \otimes \vec{b} \cdot \hat{\vec{\sigma}} \left| \Psi^- \right\rangle = -\vec{a} \cdot \vec{b}, \tag{2.15}$$

with $\hat{\vec{\sigma}} = (\hat{\sigma_x}, \hat{\sigma_y}, \hat{\sigma_z})$. For an appropriate choice of the measurement bases (Figure 2.3) one can derive

$$g_{qm} = |E(\vec{a},\vec{b}) - E(\vec{a},\vec{b}')| + |E(\vec{a}',\vec{b}') + E(\vec{a}',\vec{b})| = 2\sqrt{2}, \tag{2.16}$$

which violates the CHSH version of the Bell inequalities derived from LHVM in equation (2.14).

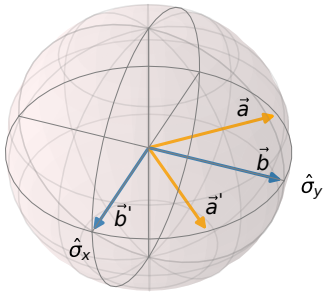

Figure 2.3: Choice of bases for a maximum violation of the CHSH inequality according to equation (2.14).

The first experiments showing a violation of the CHSH Bell-inequality were performed with photons [179, 4] and later, as in this thesis (section 8.4), also with entangled atom-photon states [120, 164]. However, all these experiments suffer from experimental shortcomings that open loopholes for a local realistic description.

2.4.1 Loopholes

The Bell inequalities can be utilised to proof systems for local causality. However, violating equation (2.14) in an experiment does not rule out every local realistic description. There could be still loopholes present (no matter if they are likely or not) which can enable a local realistic description.

- **Locality**
  Assuming that no signal can travel faster than the speed of light, the separation of the qubits has to be larger than the time it takes to perform the state measurement multiplied by the speed of light (Each qubit is outside the light cone of the other qubit).

- **Detection**
  In the optimal case, each realisation of the entangled state is measured. Otherwise, it could be that the subset of measured entanglement realisations violates the Bell inequality while the whole set does not. Usually, the experimental restrictions of limited detection or collection efficiencies are assumed to discard random events, leading to the assumption that the measured subset is representative of the entire set of entanglements generated (fair sampling assumption).

- **Random bases**
  To exclude any predetermined effects on the qubits, a random and independent choice of the measurement bases on side A and B is required.

A loophole-free test of the Bell inequalities requires closing all loopholes in a single experiment which was demonstrated in 2015 by B. Hensen et al. [66] using two entangled NV-centres.

3 Trapping of Yb^+

Contents

3.1 Experimental techniques 13
3.2 Experimental setup 19

The ability to confine a single charged particle in three spatial dimensions using oscillating electric fields was discovered by Wolfgang Paul in Bonn in the 1950s and the ion trap technique was awarded the Nobel Prize in 1989 [125]. The combination of a laser-cooled single ion in a Paul trap together with fluorescence-based detection was reported in 1980 by Neuhauser et al. in [123] and became a basic building block in many research fields, like precision spectroscopy [76] and quantum information [23, 8, 73]. In the presented experiment, we make use of a single Ytterbium ion (Yb^+) confined in a radiofrequency Paul trap as a memory qubit, which is embedded into a fibre Fabry-Pérot cavity acting as light-matter interface (see Figure 3.1).

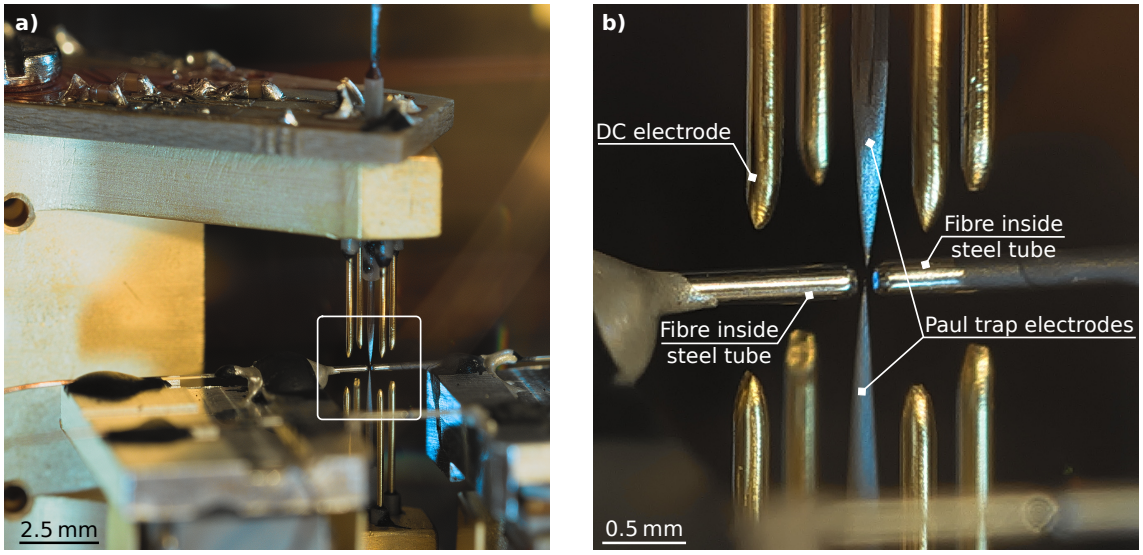

Figure 3.1: Realisation of a Paul trap with two needle-shaped electrodes. The trap is combined with a fibre cavity as ion-photon interface (see chapter 5). Trap and cavity were built in [6] and are shown here as an example because they are clearly visible from outside the vacuum chamber, in contrast to the setup used for the measurements presented in this thesis. However, both traps work according to the same principle and are similar in their construction. **a)** Full view. **b)** Enlarged section from a), marked with a white square. The needle-shaped electrodes are visible centrally in the upper and lower half of the photo. The blue reflected flash from the right-hand fibre tip mirror is visible centrally in the photo.

We choose Ytterbium as the element for trapping since it has one valence electron in the singly ionised state[4] and thus providing a comparably simple energy level structure. Furthermore, the level structure allows for Doppler cooling with a closed cooling cycle and optical state preparation, manipulation and readout. Due to a first-order magnetic field decoupled qubit, the isotope $^{171}Yb^+$ can be used to store quantum information with

[4] Yb^+ has the ground state configuration $[Xe]4f^{14}6s$

coherence times on the order of seconds to minutes [129, 178]. For this reasons, trapped ^{171}Yb ions have been used successfully in experiments for atomic clocks [76], quantum simulations [73], quantum computing [183] and quantum networks [121].

We introduce the experimental techniques for trapping and cooling Yb^+ in section 3.1 and present the experimental setup in section 3.2.

3.1 Experimental techniques

In this section, we present the general experimental techniques required to trap a single Yb ion. The working principle of a Paul trap is discussed in subsection 3.1.1. Ionisation and state selective loading of an Yb ion into the trap are presented in subsection 3.1.2. The relevant energy level scheme and transitions of Yb^+ are introduced in subsection 3.1.3.

3.1.1 Ion trapping and micromotion

For the observation and manipulation of individual particles, it is desirable to confine them to a spatial area. For charged particles, confinement via purely electrostatic fields is not possible due to Laplace's equation

$$\Delta\Phi = 0. \tag{3.1}$$

It states that a static electric potential Φ in three dimensions cannot have a local minimum (or maximum) in a charge-free spatial region. However, it was discovered by Wolfgang Paul that oscillating electric fields can be used for confining a charged particle in three spatial dimensions [132]. To this end, an oscillating radio frequency (RF) voltage is applied to a set of electrodes to form an electrical quadrupole field, which changes the direction of particle confinement for each half of an oscillation period.

One way of building a Paul trap is to use three electrodes to form a three-dimensional, cylindrically symmetric quadrupole field, with the electrodes shaped according to the equipotential lines of the field (see Figure 3.2 a)). The RF signal is applied to the top and bottom endcap electrodes while a ring electrode is set to zero potential (GND). In our setup we use a special case of this cylindrically symmetric trap by extending the ring electrode (formally) to the infinite while narrowing the top and bottom endcaps to needle-shaped electrodes (see Figure 3.2 b)). This provides improved optical access to the trapped particle.

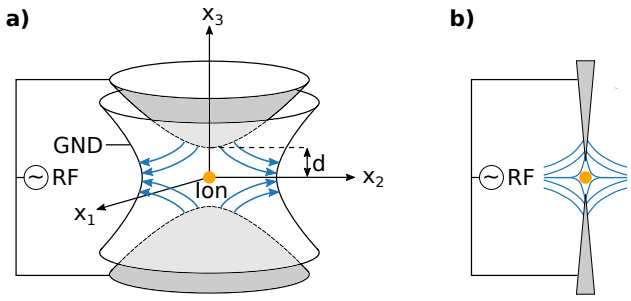

Figure 3.2: a) Cylindrically symmetric configuration of a Paul trap with a trapped ion (yellow dot). The electric field (blue arrows) between the endcaps (grey, top and bottom) and the grounded ring electrode is sketched for the positive half period of the applied radio frequency (RF) voltage (endcaps: +). **b)** A Paul trap in the needle configuration with the same colour coding as in a).

The ideal electrical quadrupole potential near the centre of a cylindrically symmetric Paul trap in needle configuration (Figure 3.2 b)) is given by [102]

$$\Phi(\vec{x},t) = (U_0 + U_\sim \cos(\Omega t)) \cdot \frac{x_1^2 + x_2^2 - 2x_3^2}{4d^2}, \tag{3.2}$$

assuming the boundary condition $\Phi(x_1 = x_2 = 0, x_3 = d, t = 0) = (U_0 + U_\sim)/2$ according to [115]. We define $U_0 + U_\sim \cos(\Omega t)$ as the driving field[5] applied to the top and bottom electrodes which have a distance of $2d$ along x_3. The classical equation of motion for an ion with mass m and charge $Z|e|$ is given by [102]

$$m\ddot{\vec{x}} = Z|e|\vec{E}(\vec{x},t) = -Z|e|\nabla\Phi. \tag{3.3}$$

Defining the parameters

$$a_1 = a_2 = -\frac{1}{2}a_3 = \frac{2Z|e|U_0}{md^2\Omega^2} \tag{3.4}$$

and

$$q_1 = q_2 = -\frac{1}{2}q_3 = \frac{Z|e|U_\sim}{md^2\Omega^2}, \tag{3.5}$$

brings the differential equation to the form

$$\ddot{x}_i + [a_i + 2q_i \cos(\Omega t)] \frac{\Omega^2}{4} x_i = 0, \tag{3.6}$$

which is known as Mathieu's equation. The parameters a and q are related to stability regions of the trapping potential. In presence of an external DC electric stray field $\vec{E}_{\text{stray}}$ equation (3.6) changes to [19, 60]

$$\ddot{x}_i + [a_i + 2q_i \cos(\Omega t)] \frac{\Omega^2}{4} x_i = \frac{Q \cdot E_{\text{stray},i}}{m}, \tag{3.7}$$

where $E_{\text{stray},i}$ is the ith spatial component of the stray field vector $\vec{E}_{\text{stray}}$ which is assumed to be static and gradient-free[6]. Equation (3.7) can be solved in adiabatic approximation ($|a_i|, q_i^2 \ll 1$) [19, 60] as

$$x_i \approx [x_{0,i} \cos(\omega_i t + \phi_i)] \left(1 + \frac{q_i}{2} \cos(\Omega t)\right) + x_{\text{stray},i} + \frac{q_i \cdot x_{\text{stray},i}}{2} \cos(\Omega t), \tag{3.8}$$

where $\vec{x}_{\text{stray}}$ is the average spatial displacement of the ion originating from the stray field $\vec{E}_{\text{stray}}$.

From equation (3.8) we can infer that the ion undergoes a superposition of different periodic oscillations (see Figure 3.3). The slower oscillation with period $\omega_i = \Omega/2\sqrt{a_i + q_i^2/2}$ is called the secular motion and is related to an approximation of the trap potential as an harmonic pseudo potential (see equation (3.9)). The faster oscillation exhibits the period of the driving RF field Ω and is called (intrinsic) micromotion of the ion. It exhibits a much smaller amplitude than the secular motion.

[5] With DC part U_0 and RF part $U_\sim \cos(\Omega t)$

[6] One can make these assumptions since the region of interest is small compared to the trap setup and the drift of a stray field in the experiment occurs on a time scale of several hours

The pseudo potential of the trap can be obtained by time averaging over one period of the secular motion. Using equation (3.8) with no external stray field, i.e. $\vec{x}_{\text{stray}} = 0$, we obtain for the kinetic energy in one spatial direction [19]

$$< E_{\text{kin}} >_i = \frac{1}{2} m < \dot{x}_i^2 > \approx \frac{1}{4} m \omega_i^2 x_{0,i}^2 \left(1 + \frac{q_i^2}{q_i^2 + 2a_i}\right). \tag{3.9}$$

For the needle trap used in this thesis, the ion is confined with trap frequencies of $\omega_1 \sim 2\pi \cdot 3\,\text{MHz}$, $\omega_2 \sim 2\pi \cdot 5\,\text{MHz}$ (cavity axis) and $\omega_3 \sim 2\pi \cdot 7\,\text{MHz}$ (trap axis) by applying a driving RF field of $\Omega \approx 2\pi \cdot 21\,\text{MHz}$. We measured the trap frequencies using parametric excitation of the ion's motion by modulating a weak sideband on the driving RF field and observing the heating of the ion via fluorescence detection [70].

From equation (3.8) it becomes clear that the micromotion is the reason for the spatial confinement, since the energy of the ion increases with increasing $|\vec{x}|$ along all spatial directions. Since the amplitude of the micromotion is determined by the amplitude of the secular motion, both can be reduced by lowering the potential energy (temperature) of the ion, e.g. by laser cooling in the case of $\vec{x}_{\text{stray}} = 0$. A cooling of the ion corresponds to a damping of the oscillation in the pseudo-potential picture of the Paul trap as a harmonic oscillator.

Figure 3.3 shows trajectories of an ion in the Paul trap, which we simulated numerically[7] according to equation (3.7). In the undisturbed case, i.e. without a stray field $\vec{E}_{\text{stray}}$, the trap centre is the midpoint of the ion's trajectory. For an external stray electric field $\vec{E}_{\text{stray}} \neq 0$, the centre position of the trajectory gets shifted from the trap centre by [60]

$$\vec{x}_{\text{stray}} \approx \frac{Q}{m} \sum_{i=1}^{3} \frac{E_{\text{stray},i}}{\omega_i^2} \mathbf{e}_{x_i}, \tag{3.10}$$

with the unit vector $\mathbf{e}_{x_i}$ along the ith spatial component.

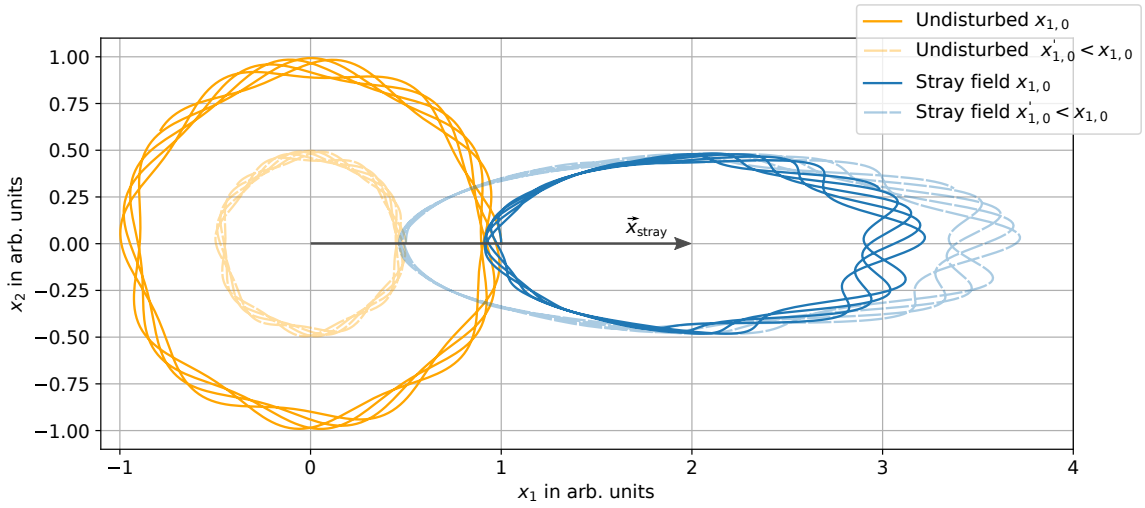

Figure 3.3: Ion trajectories in the x_1-x_2 plane as numerical solution to equation (3.7) without a stray field (orange curves) and with a stray field along the x_1 axis (blue curves). The shift due to a stray electric field $\vec{x}_{\text{stray}}$ is indicated as arrow. The starting point of the simulation is $x_1(t = 0) \equiv x_{1,0}$. The dashed lines with lighter colour constitutes simulations with a starting condition $x'_{1,0}$ of the ion closer to the origin, i.e. $x'_{1,0} < x_{1,0}$.

[7] We use the PYTHON package SCIPY.INTEGRATE for this purpose

Due to the shifted position, the ion experiences a stronger amplitude in the oscillating electric field which induces additional motion to the ion. The additional motion is called excess micromotion and is a driven oscillation as can be seen from equation (3.8). For this reason, it is difficult to reduce the excess micromotion by laser cooling. For an efficient reduction of the ion's energy, a compensation of the electric field reducing $\vec{x}_{\text{stray}}$ is crucial. In chapter 4, we present strategies for the detection and compensation of (excess) micromotion.

3.1.2 Isotope selective loading

Different isotopes of Ytterbium have different capabilities for specific experimental tasks. Therefore, it is important to load only the desired isotope into the trap. For quantum communication tasks, we use $^{171}Yb^+$ because its hyperfine splitting of energy levels due to a nuclear spin of $I = 1/2$ offers a number of interesting properties, as described in chapter 6. However, for certain tasks not related to the specific level structure of $^{171}Yb^+$, it may be advantageous to trap $^{174}Yb^+$ instead, as it has a simpler level structure. For this isotope, trapping and cooling is less challenging and more fault-tolerant than for $^{171}Yb^+$. This makes $^{174}Yb^+$ ideal for calibration tasks, which are not related to a specific isotope. In each case, the deterministic selection of the isotope to be loaded into the Paul trap is important.

For isotope selective loading of an ion into the trap, we use resonance-enhanced two-photon ionisation [87]. To this end, we drive the optical $^1S_0 \leftrightarrow {}^1P_1$ transition of neutral Ytterbium at 398.9 nm. The ionisation of the excited neutral atom from the $^1P_1$ state is done via a second laser[8] at 370 nm, which at the same time is resonant to the cooling transition of Yb^+ and directly acts as a cooling laser for an ionised Yb atom.

The neutral Yb atoms thermal evaporate from a foil located in a heated steel tube (Yb oven), which produces a diverging atom beam leaving the heated tube at its open end. Since the beam axis of the 398.9 nm laser and the tube axis are aligned perpendicular to each other, we probe the neutral atoms almost Doppler-free with this laser. In Figure 3.4 the spectrum of neutral Yb is shown, which was recorded by tuning the frequency of the 398.9 nm laser while monitoring the rate of photons scattered by the atoms on the $^1S_0 \leftrightarrow {}^1P_1$ transition. By selecting the resonant frequency of a certain isotope for the first ionisation laser, we perform the isotope selective loading. For ^{171}Yb, we choose the $|{}^1S_0, F = 1/2\rangle \leftrightarrow |{}^1P_1, F' = 3/2\rangle$ transition for the first ionisation step.

For loading an ion into the trap, we continuously turn on atomic beam, 370 nm and 399 nm laser for up to 50 s. It takes some time for the atomic beam to reach a sufficient density of atoms, so we turn on the heating of the steel tube ~ 40 s before the lasers.

[8] The wavelength of the second ionisation laser has to be $\lesssim 394$ nm [130]

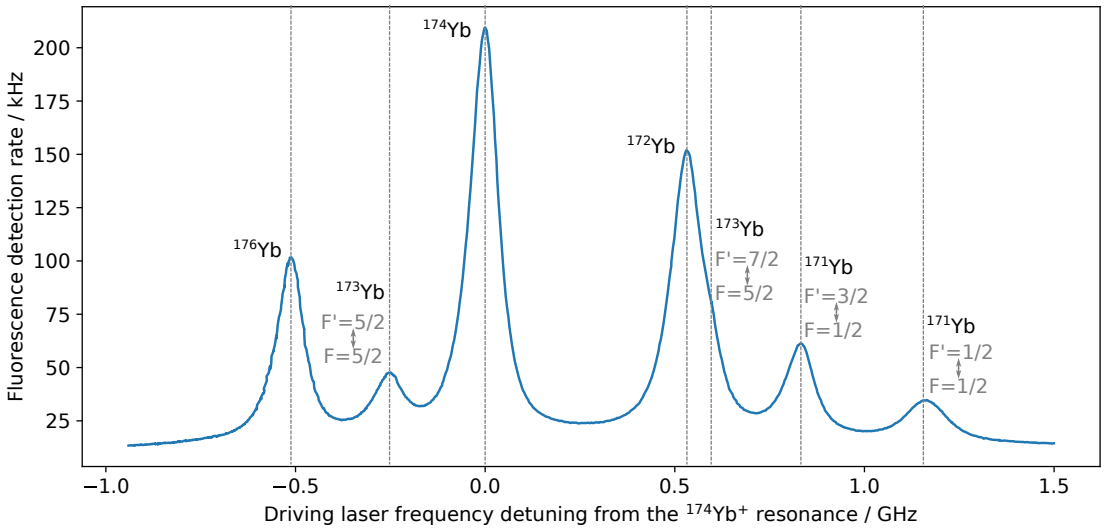

Figure 3.4: Resonances of the $^1S_0 \leftrightarrow {}^1P_1$ transition for multiple isotopes of neutral Ytterbium (Yb) measured on a separate spectroscopy cell [20]. For isotopes exhibiting a non-zero nuclear spin the F/F' quantum numbers are given for the ground/excited state. The isotopes were assigned to the resonances using [6].

The absolute measurement of our frequencies[9] in the laboratory varies over $\sim 100\,\mathrm{MHz}$ on a daily basis, which is a multiple of the natural linewidth of $2\pi \cdot 28.9\,\mathrm{MHz}$ [135] of neutral Yb. Therefore, we have to perform a daily calibration of the $^1S_0 \leftrightarrow {}^1P_1$ transition frequencies in order to maintain a high ionisation efficiency. For this purpose, we use a separate spectroscopy cell that automates the spectroscopy. This allows us to leave the main setup untouched, which is beneficial due to the high optimisation of this setup for the detection of 370 nm fluorescence.

3.1.3 Cooling of $^{174}Yb^+$ and $^{171}Yb^+$

Doppler-cooling was initially proposed in [181] and makes use of photons having slightly less energy than the atomic resonance. In terms of energy, the absorbance of photons having less energy than the on average emitted photons cools down the ion. In terms of momentum, the absorbance of photons coming from one direction and the isotropic emission of photons into 4π solid angle slows down the atom with a propagation direction opposite to that of the photons.

This subsection gives an introduction to the Doppler cooling of $^{174}Yb^+$ and $^{171}Yb^+$, which is used to counteract the heating rate of the ion inside the trap but also enables the probing of the ion in the trap using the amount of scattered photons as a response. Throughout this thesis, we use the rate of photons scattered on the cooling transition as feedback from the ion, making this quantity one of the most important experimental observables.

Laser cooling requires a closed cycle of the atomic population to ensure a stable steady state population of the energy levels of the cooling transition. For Yb^+ we investigate the level structure in the following. The valence electron of Yb^+ can be excited from the

[9] Wavemeter WS7 from HighFinesse

6s orbital to the 6p orbital with a transition resonant radiation wavelength of 369.54 nm [114]. The total angular momentum given by the LS-coupling results in the fine structure states $^2S_{1/2}$, $^2P_{1/2}$ and $^2P_{3/2}$ for these orbitals. We use the $^2S_{1/2} \leftrightarrow {}^2P_{1/2}$ transition for Doppler-cooling. Due to a finite branching ratio of the $^2P_{1/2}$ excited state manifold to the $^2D_{3/2}$ manifold, we close the cooling cycle by using a 935.2 nm laser to repump the population from the $^2D_{3/2}$ levels [114] (see Figure 3.5 a)).

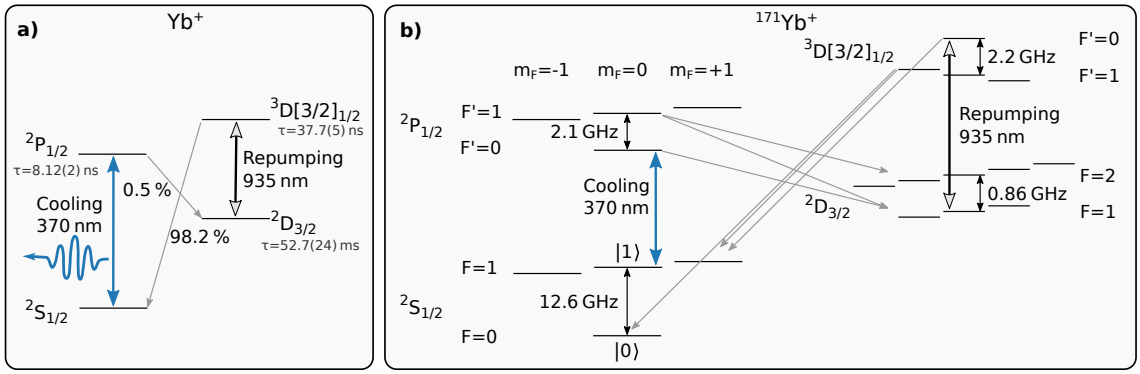

Figure 3.5: Relevant energy levels of **a)** Yb^+ and **b)** more specific for $^{171}Yb^+$. The light grey arrows indicate the allowed transitions between the hyperfine levels but do not consider m_F quantum numbers of the states. The branching ratios are taken from [129, 159]. Transition frequencies, allowed transitions and wavelength are taken from [114, 129]. Lifetimes from [17, 185, 128].

Due to a nuclear spin of $I = 1/2$ and the resulting hyperfine structure of energy levels, cooling of $^{171}Yb^+$ requires additional effort (see Figure 3.5 b)). Here, the $^2P_{1/2}$ manifold splits up into a $F' = 0$ and a $F' = 1$ manifold. We use the $\left|{}^2S_{1/2}, F = 1\right\rangle \leftrightarrow \left|{}^2P_{1/2}, F' = 0, m_F = 0\right\rangle$ transition as the cooling transition for $^{171}Yb^+$. From the excited state of the cooling transition the decay into the $\left|{}^2S_{1/2}, F = 0, m_F = 0\right\rangle \equiv |0\rangle$ state is forbidden due to dipole selection rules. But trapping of population in the $|0\rangle$ dark state is possible through off-resonant scattering on the $\left|{}^2P_{1/2}, F' = 1\right\rangle$ levels. To avoid population trapping in the $|0\rangle$ state, we modulate a 14.7 GHz sideband to the cooling laser using an electro-optic-modulator (EOM) acting as a hyperfine repump of population back to the cooling cycle from that state. A detailed discussion of the allowed $^2S_{1/2} \leftrightarrow {}^2P_{1/2}$ transitions for $^{171}Yb^+$ including the Clebsch-Gordan coefficients can be found in Appendix B.

Also the repumping of population from the $^2D_{3/2}$ manifold at 935 nm requires additional effort for $^{171}Yb^+$. The repumping is necessary due to the finite probability of the excited state of the cooling transition $\left|{}^2P_{1/2}, F' = 1, m_F = 0\right\rangle$ to decay into the $\left|{}^2D_{3/2}, F = 1\right\rangle$ state. From the $\left|{}^3D[3/2]_{1/2}, F' = 0\right\rangle$ state, a transition to the dark $|0\rangle$ state is forbidden, which makes the repumping of the trapped $\left|{}^2D_{3/2}, F = 1\right\rangle$ population to the cooling transition via this level desirable by using the 935 nm laser. In order to clear out accidental population of the $\left|{}^2D_{3/2}, F = 2\right\rangle$ level, a ~ 3 GHz sideband is modulated to the 935 nm repumping laser.

Coherent population trapping
For the cooling transition of $^{171}Yb^{+}$, a higher degeneracy of the ground state than that of the excited state leads to the formation of coherent dark states in the $(^2S_{1/2}, F = 1)$ manifold [18]. This coherent population trapping effect reduces the fluorescence of the ion and becomes stronger especially for lower magnetic fields and a decreasing Zeeman splitting of the m_F hyperfine states. We observe a drastic decrease of the ion fluorescence to $\sim 25\,\%$ of the full value for magnetic fields lower than 1 G ($\sim 2\pi \cdot 3\,\mathrm{MHz}$ splitting between the $m_F = \pm 1$ levels). There are a few experimental techniques, which we found to at least partly destroy the dark states. Due to a formation mainly at low magnetic fields, it is possible to destroy the dark states by increasing the magnetic field. However, due to the inductance of the magnetic field coils, which are designed to generate a constant and stable offset magnetic field, a minimum ramping time of the magnetic field of 10 ms was achieved. This switching time between two magnetic field values potentially reduces the repetition rate of sequences that require, for example, a low magnetic field in the main time and a high magnetic field towards the end, e.g. for readout purposes of the atomic state. Using a second cooling laser through a different beam port with different polarisation compared to the main cooling beam turns out to be a better option. This 'bright pump' laser is able to partly destroy the dark states and recovers the fluorescence of the ion to $\sim 50\%$. However, also a fast modulation of the polarisation of a single cooling laser can be used to destroy the dark states [18].

The reduced fluorescence of the ion is important for the detection of spin-photon entanglement in chapter 7. There, it requires a trade-off between the phase evolution of the superposition spin states due to Larmor precession (less timing precision required for low magnetic fields) and the state detection fidelity of the ion based on fluorescence (better for high magnetic fields).

3.2 Experimental setup

Since 2009 the experimental system is under construction and continuously progress. The coupling of a trapped ion to a single mode of a fibre cavity was demonstrated in the infrared spectral regime in [158, 159]. Subsequently, a fibre resonator working in the UV spectral regime was integrated into a newly built second ion-trap setup in [6] and the coupling of this resonator to the principal UV transition of Yb^{+} was demonstrated.

At this point, the research phase of this PhD project started with the goal of realising a quantum network node that employs the fibre resonator as a light-matter interface for the distribution of quantum information in the form of ion-photon entanglement. However, the previously existing fibre cavities had some known shortcomings, and to address these, we have developed a new fibre cavity in the context of this thesis, in which we have implemented the previous findings, especially on stability and mirror degradation (for details, see section 5.2). The new cavity was then assembled as part of a master's thesis in [29].

In parallel, we successfully performed first correlation measurements between the photonic and atomic qubit state in the $\hat{\sigma}_z$-basis on the existing ion-cavity setup built in [6], where we bypassed a cavity-microwave incompatibility using a two-photon Raman-transition for the manipulation of the atomic qubit. On this setup, we reworked the hard

and software of the data acquisition and data analysis to implement, among other things, conditional real-time branching of fast experimental sequences (see subsection 3.2.4).

After assembly, we combined the new UV cavity with an existing Paul trap originally built in [115, 157] and installed the infrastructure of this new trap-cavity setup, where we implemented what we have learned so far. In particular, this includes: i) an improved imaging system of the ion using a high NA objective, ii) a stable beam pointing for all lasers due to the implementation of stable beam paths and a continuous monitoring, iii) a low noise magnetic field generation (see Appendix D) and iv) a setup generating phase stable microwave pulses (see subsection 6.4.3). Fortunately, the final assembled new fibre cavity has a much better microwave compatibility than the one used so far and we switched from qubit manipulation with two-photon Raman transitions to the use of microwave pulses, since we achieved higher rotation fidelities with the latter. Furthermore, we added passive and active magnetic field shielding to the setup (see subsection 6.6.2) and built a setup for polarisation-resolved detection of photons leaving the fibre cavity (see subsection 5.5.1). We also had to implement the hardware and software for data collection and analysis at the same level we had achieved with the second setup.

We present most of these points in the following subsections in detail. The remaining parts are discussed in the stated subsections of other chapters.

3.2.1 Laser system

The control of matter using coherent light is a fundamental part of the experiment. Most interactions with the trapped ion are taking part via optical transitions and (near) resonant light. As a source of coherent radiation, lasers enable trapping, cooling, state control and readout of the atomic qubit. But they can also serve as a frequency reference for cavities and other lasers.

The laser system was built up step by step and parts were added in [115, 6, 157] and during this work. However, with a few exceptions[10], the entire laser system of both traps was gradually reworked or rebuilt in the context of this thesis. Figure 3.6 shows a sketch of the laser system, which is distributed over two optical floating tables to dampen vibrations (photo see Figure 10.4). All tables, lasers and cavities are temperature stabilised.

[10] transfer lock and continuous wave frequency doubling (ring cavity)

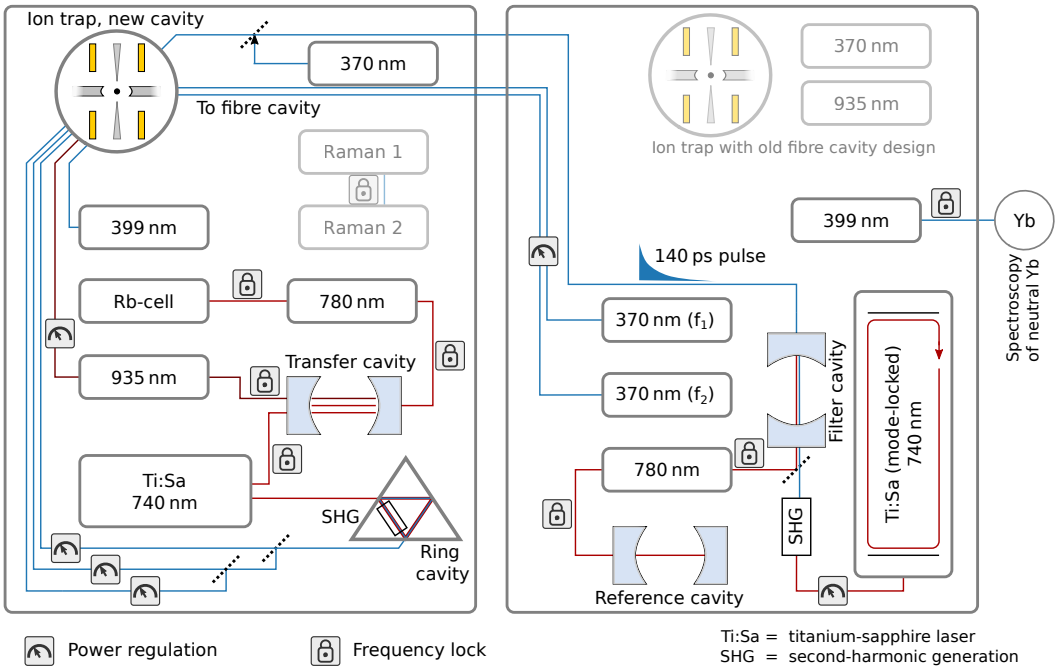

Figure 3.6: Simplified sketch of the laser setup, which is extended over two optical tables (indicated as two big rectangles). The radiation wavelengths of the lasers are given. The frequency and power stabilisation of the lasers are indicated, if available. For the sake of clarity, we omit almost all optical elements in the sketch. For completeness, the position of the second trap setup with the corresponding cooling and repumping laser is indicated as part of the second table and the Raman laser pair as part of the first table (less opaque). Details of the pulsed laser setup are given in subsection 6.3.3. Details of the fibre cavity reference lasers f_1 and f_2 are given in subsection 5.3.2.

For Doppler-cooling, micromotion detection, state readout and state initialisation of the ion, we can generate up to 80 mW laser light at 369.54 nm from a frequency doubled Ti:sapphire laser[11] running at 740 nm. The 740 nm Ti:sapphire and the 935.2 nm repumper diode laser are locked via a transfer cavity to a Rubidium cell providing an atomic frequency reference at 780 nm according to the locking scheme presented in [115, 157].

We use two 399 nm lasers resonant with neutral Ytterbium (one for the spectroscopy cell, one for ionisation in the experiment) and three 370 nm reference lasers, two of which are used for calibration and locking of the fibre cavity (see section 5.3). The third one is used for calibration and coupling purposes of a picosecond pulsed laser. The setup of this mode-locked Ti:sapphire laser requires a separate discussion, which is given in subsection 6.3.3. The 399 nm and 370 nm lasers are free running diode lasers and frequency stabilised at a low bandwidth (~ 1 s) to the wavemeter[12], which provides us with a frequency measurement of our lasers. A second 780 nm laser is locked to an ultra-stable reference cavity and serves as a frequency reference for the pulsed laser setup.

The power regulation of the lasers is realised using acousto-optic modulators (AOMs) which also allows to turn the continuous wave lasers on and off within $\sim 1\,\mu$s.

[11] SolsTiS from M Squared lasers, frequency doubling from [115]
[12] Wavemeter WS7 from HighFinesse

3.2.2 Optical access

The used experimental techniques for controlling the trapped ion with coherent light benefit from well-aligned laser beams to achieve the desired experimental precision. In particular, a high fluorescence signal and a low noise floor is important while driving the cooling transition $^2S_{1/2} \leftrightarrow {}^2P_{1/2}$ at 370 nm, since we use this signal as a main feedback from the ion. A high signal-to-noise ratio can be achieved with small beam waists at the position of the trapped ion in order to enhance light-matter coupling and to suppress accidental illumination of the trap components which could cause stray light.

Position and focus

Due to a potential charging of trap elements, the UV lasers require a high degree of beam alignment. The best sensor for beam alignment is the trapped ion and for the 370 nm laser, we can find the optimal beam position by having the ion at the trap centre and optimising the rate of scattered photons from the (weakly[13]) driven ion. However, we do not have such feedback available for the 399 nm ionisation laser. We send the 399 nm beam together with the main cooling beam (beam 1) to the ion, but due to the dispersion of the optical elements, we have to optimise its position and performance separately by monitoring the time needed to load an ion into the trap on the one hand and the charging of the trap elements on the other hand.

We can measure the charging effect of the 399 nm beam by using the so-called Doppler correlation method. To this end, the ion is continuously driven by the main cooling laser at 370 nm and the 399 nm laser is turned on for a defined time interval. A possible formation of a stray electric field due to the charging of trap elements would subsequently displace the ion from the trap centre, which in turn would manifest itself as an increased amplitude of the ion's motion. An increased micromotion amplitude can be detected using the correlations between the trap RF and the scattering rate of photons by the ion according to subsection 4.1.1. Figure 3.7 shows charging and discharging of trap elements for two different positions of the 399 nm beam focus. We observed that a discharge of trap elements can take a comparatively long time, but also that the charging can be minimised by beam alignment.

The loading efficiency of an ion into the trap is mainly determined by the overlap of the 370 nm and 399 nm lasers and the relative position of the resulting ionisation region to the trap centre [130]. In the experiment, we find the optimal overlap iteratively. The overlap of the 399 nm laser and the thermal atomic beam, however, can be taken as given due to the large diameter of the atomic beam.

[13] A higher driving power due to a better beam alignment could also result in a reduced scattering rate of photons for $^{171}Yb^+$ if the power of the probing laser is initially set too high, as described in [46]

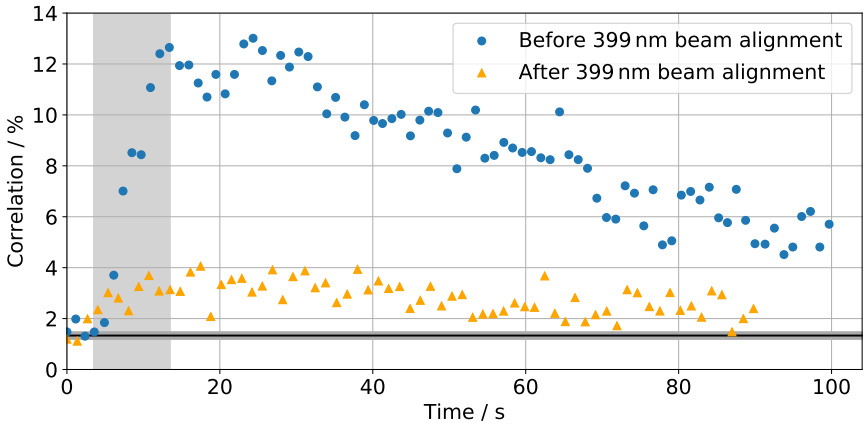

Figure 3.7: Estimation of the charging of trap elements during a 10 s pulse of the 399 nm laser at 40 uW. The time interval of the 399 nm pulse is shown as a grey shaded area. The offset correlation for a minimised motion of the ion is shown as a black line with the standard error as shaded area.

We usually operate the lasers at low power ($\sim 0.5\,\mu$W–$40\,\mu$W) in continuous wave mode. As an exception, the 935 nm repumping laser allows for a higher beam power ($\sim 300\,\mu$W) and at least one magnitude lower positional an focal alignment precision. This is due to the experimental setup being insensitive to infrared radiation in terms of static charging and stray light.

The experimental setup exhibits three non-collinear 370 nm laser beam paths used for interaction with the $^2S_{1/2} \leftrightarrow {}^2P_{1/2}$ transition of the Yb ion (referred to as beam 1/2/3, see Figure 3.8). In particular, the minimisation of the ion's motion benefits from this setup (see subsection 4.1.1). However, trapping and cooling of an ion works also with only one beam (beam 1 in our case). We monitor radial profile, position and focus of each beam using so-called 'beam microscopes'. We image each of the beams on a CCD camera focused to the trap plane and showing the needles as a sharp image[14] (see Figure 3.8). We align the optical axis of each microscope to the corresponding beam axis using a set of apertures, since we found this to be crucial for correct estimation of the beam profile. For a focal alignment of the laser beams, we can find the correct position of the focusing lens up to a few millimetres by minimising the beam diameter on the CCD image. However, small readjustments using the fluorescence signal of the trapped ion are usually necessary. Beam 1 and beam 2 are focused with a $f = 150$ mm lens to the ion allowing for a minimal beam waist ($1/e^2$ radius) of

$$\omega_0 \approx \frac{2\lambda}{\pi}\frac{f}{D} \sim 7\,\mu\text{m}, \tag{3.11}$$

which we verify approximately using the CCD camera (see inset in Figure 3.8). We calculate ω_0 by matching the total angular spread of a diverging Gaussian beam in vacuum $\theta = \frac{2\lambda}{\pi\omega_0}$ to the angle of aperture of the lens $\theta/2 \approx \tan(\theta/2) = \frac{D/2}{f}$. We hereby assume a collimated input beam with diameter of $D \sim 5$ mm.

Beam 1 and beam 3 incident perpendicular to the quantisation axis (cavity axis) with $\alpha = 90°$ (see Figure 3.8). The angle between beam 2 and the quantisation axis is $\alpha = 75°$.

[14] We use collimated laser light or incoherent LED light for focusing the beam microscopes to the trap plane

Since beam 2 has a component along the cavity axis, static charging of the cavity mirrors due to incident UV light is the strongest for this beam.

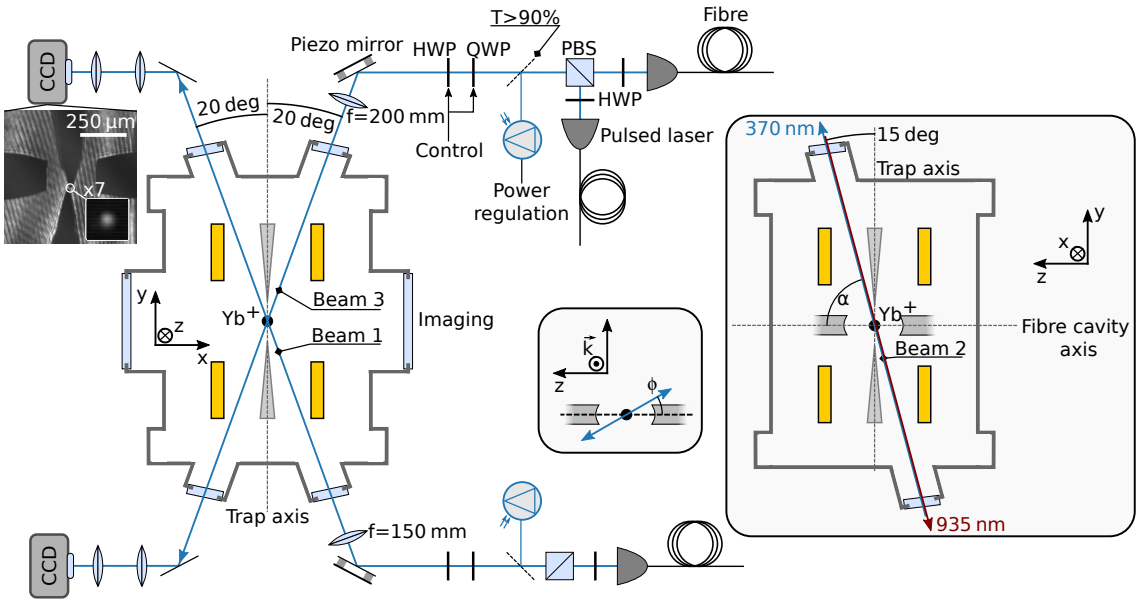

Figure 3.8: The vacuum chamber with beam ports and imaging access is sketched. The Paul trap is sketched as grey needles with DC electrodes in yellow. Using an external magnetic field, we set the quantisation axis along the cavity axis (z-axis). The windows of the viewports are angled by 7 degree in order to mitigate back reflections may causing stray light at the trap [157]. Note that the positioning of the lenses behind the final adjustment mirror is non-optimal for the radial beam profile. We accept slightly imperfect beam profiles for gaining smaller beam waists by being able of using smaller focal lengths of the focusing lenses. On the top left corner, a recorded image of the main cooling beam on the corresponding CCD camera is shown. The image also shows the shadows of the trap needles (bottom/top shadows) and cavity steel-tubes (left/right shadows). Due to the viewing angle, the distance of the needles appears to be reduced with respect to the cavity mirror distance.

Polarisation

Each beam is coupled through a single-mode fibre before being directed towards the trap to ensure a high initial spatial mode quality. After out coupling, each beam is polarisation cleaned using a polarising beam splitter (PBS). For all beams, we adjust the polarisation right before the trap using a $\lambda/2$ and a $\lambda/4$ wave plate.

The optimal polarisation of each beam depends on the specific isotope of Yb. A maximal scattering rate of photons and hence optimal Doppler cooling for a ^{171}Yb ion can be achieved when driving all three polarisation components $(\pi, \sigma^{\pm})$ approximately equal in their amplitude [46]. Here, equal coupling[15] to all ground states of the $(^2S_{1/2}, F = 1)$ manifold is achieved. In order to compute the required polarisation orientation of each beam, we assume linearly polarised light with the electric field vector having an angle ϕ with respect to the quantisation axis (see Figure 3.8). The incident angle of the beam α is considered with respect to the quantisation axis of the ion as well. We compute the relative strengths of the polarisation components π, σ^+ and σ^- (with unit vectors $\hat{e}_\pi, \hat{e}_{\sigma^+}, \hat{e}_{\sigma^-}$) of

[15] The Clebsch-Gordan coefficient of the involved couplings are equal

a certain polarisation state $\mathbf{S}$ using the Jones matrix formalism as

$$D_x(\mathbf{S}) = r(\mathbf{S}, \hat{e}_x) \text{ with } x \in \left\{\pi, \sigma^+, \sigma^-\right\} \tag{3.12}$$

using the polarisation state overlap

$$r(\mathbf{u}, \mathbf{v}) = \left|\mathbf{u}_e^\dagger \mathbf{v}_e\right|^2 \text{ with the unit vectors } \mathbf{u}_e = \frac{\mathbf{u}}{|\mathbf{u}|} \text{ and } \mathbf{v}_e = \frac{\mathbf{v}}{|\mathbf{v}|}. \tag{3.13}$$

We define the combined contrast of all polarisation components as

$$\chi = |D_\pi - D_{\sigma^+}| + |D_{\sigma^-} - D_\pi| + |D_{\sigma^+} - D_{\sigma^-}|. \tag{3.14}$$

If all components have equal strengths, the combined polarisation contrast is $\chi = 0$. In Figure 3.9 the angular dependence of χ is shown.

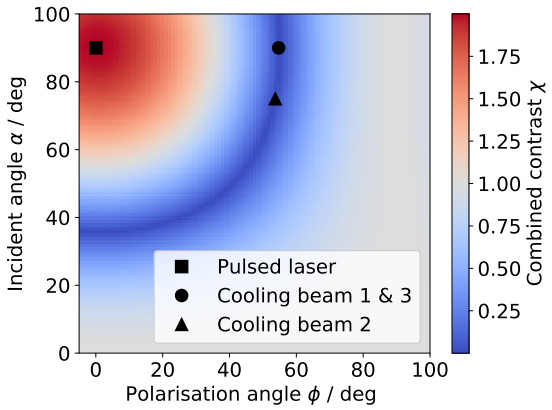

Figure 3.9: The combined polarisation contrast χ is shown as a function of the beam incident angle α and the angle ϕ of the linearly polarised electric field, both with respect to the quantisation axis (see Figure 3.8). A contrast of $\chi = 2$ indicates a pure π, σ^+ or σ^- polarisation, whereas at $\chi = 0$ all polarisation components have equal strengths.

We can derive an expression in terms of ϕ and α for which the polarisation components are equal in their relative strengths:

$$(\cos\phi \cdot \sin\alpha) \approx \cos(54.7°). \tag{3.15}$$

For the pulsed excitation of the ion (see section 6.3), we aim to drive only the $\Delta m_F = 0$ transition by using linearly polarised light parallel to the quantisation axis. Since the pulsed laser and cooling beam 3 share a common beam path, we use motorised waveplate mounts to adjust the beam polarisation according to the intended use (see Figure 3.8).

3.2.3 Free-space imaging

The ability to detect photons scattered by the ion into free space is a basic requirement for running the experiment. The access to several information depends on the photon statistic received from the ion, such as its optimal position within the trap (subsection 4.1.1), frequency and position calibration of the lasers and readout of the ion state (section 6.2). In this subsection, we introduce and characterise the imaging system used for collection and detection of parts of the light scattered by the ion at 369.5 nm into 4π solid angle.

Since the ion can be seen as an ideal point source isotropically emitting light into 4π solid angle, the point spread function (PSF) of an optical system can be used straight forward to evaluate the imaging system. The PSF describes the spatial optical transfer characteristics of an ideal point source as an input of an imaging system to its output [146]. From the PSF it can be deduced whether an imaging system is limited by diffraction[16] or whether, even with a perfectly aligned lens system, the imperfections of the optical path reduce the imaging quality.

From the evaluation[17] of the PSFs for different imaging setups, we know that varying optical path lengths for different beam incidence angles on a vacuum chamber window lead to a limitation of the usable numerical aperture (see Figure 3.10 c)). For a vacuum chamber window of $\sim 6\,\mathrm{mm}$ thickness, a maximum NA of 0.32 was calculated in [6], at which the imaging system becomes diffraction limited. For the presented experiment, we aimed for an even higher usable NA of 0.48. We need a high collection efficiency of scattered photons for a high fidelity detection of the atomic qubit state (see subsection 6.2.2), which directly is determined by the usable NA. Therefore, we had to think about alternatives to the previous used imaging setups.

To avoid the effect of varying optical path lengths for the setup presented in this thesis, we placed the light collecting objective[18] inside the vacuum chamber to achieve parallel rays for light collected from the ion as a point source (see Figure 3.10 a),b) & d)). In this case, the numerical aperture is solely limited by the geometry of the objective lens and the image quality is even insensitive to a tilted chamber window as long as the point source is in focus of the light collecting objective. Otherwise, we can observe strong astigmatism for a focused beam travelling non-perpendicular through a window.

[16] Light entering the objective from a point source is focused to a radius of the central airy disc of $1.22\lambda/(D/f)$ in the imaging plane with the objective aperture diameter D and focal length f (Rayleigh criterion)

[17] Using OSLO from Lambda Research Corporation

[18] AFL25-25-S-U from Asphericon

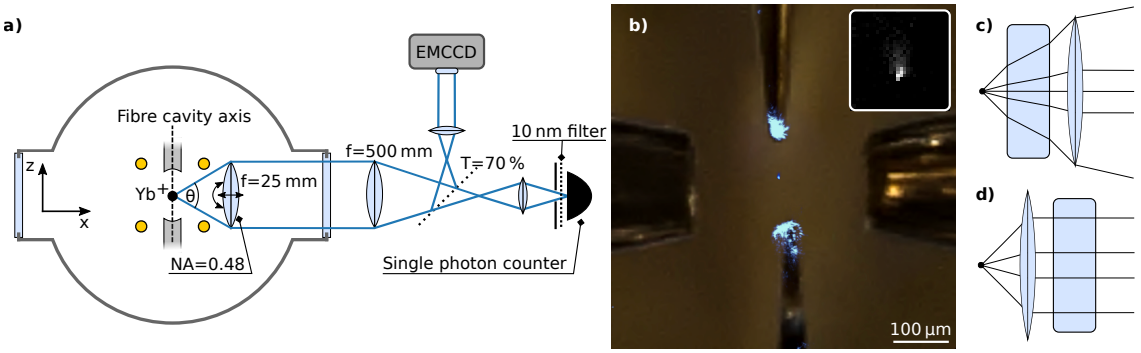

Figure 3.10: a) Sketch of the free-space imaging of the ion fluorescence. The objective is placed inside the vacuum chamber (grey circle). **b)** Greyscale data recorded with the EMCCD (blue coloured) at full achievable NA ($\sim$ 0.47) superimposed with an image recorded on an APS-C sensor using a 150 mm macro objective. A single Yb ion is trapped centrally between the needles (top and bottom) and scatters light at 370 nm. The needles scatter the laser light as well. The tubes containing the cavity fibres are visible on the left and right hand side respectively. Inset: original sensor data of the EMCCD cropped to the position of the ion (30×30 pixel). The pixel size of the EMCCD is $4\,\mu\text{m} \times 4\,\mu\text{m}$. **c)** Optical beam path for light emitted by a point source (black dot). A glass window is placed between source and the light collecting objective. While for small NA the rays are approximately parallel behind the objective, the imaging error for the outermost rays (high NA) increases. **d)** Same as in c) but with the objective being placed in front of the glass window. All rays passing the window in parallel in the ideal case.

We optimise the alignment of the objective lens within the chamber by using the ion as a true point source. To this end, the lens is mounted[19] tiltable around the z-axis and y-axis and is movable along the x-axis.

We split the collected ion fluorescence using 30 % of the light for imaging on an electron multiplying CCD sensor[20] (EMCCD) and detect the remaining light on a single photon counter[21] (SPC) (see Figure 3.10 a)). We use a variable and movable aperture ($\varnothing \sim 100\,\mu$m) to crop the part visible to the SPC to the ion fluorescence in order to suppress stray light (e.g. from the needles, see Figure 3.10 b)). Furthermore, we apply a 10 nm spectral filtering[22] with $\sim$ 92 % transmittance in advance to the SPC. We end up in total with a dark count rate of $\sim 120\,\frac{\text{counts}}{\text{s}}$ on the SPC.

Measurement of the collection efficiency

In order to quantify the performance of the imaging system, we measure the detection efficiency of the whole setup by pumping a trapped ^{174}Yb ion into the $^2\text{D}_{3/2}$ manifold. From the decay constant of the population in the bright state and the branching ratios of the transitions, we can calculate the rate of scattered photons by the driven ion (see Figure 3.11 a)). To this end, we drive the ion on the $^2\text{S}_{1/2} \leftrightarrow {}^2\text{P}_{1/2}$ transition and disable the 935 nm repump laser at a certain point in time (see Figure 3.11 b)).

Since the branching ratio of the excited state manifold $^2\text{P}_{1/2}$ into the $^2\text{D}_{3/2}$ manifold is 0.501(15) % [129], the probability $P_{\text{bright}}(t)$ to find the ion after $N = R_{4\pi} \cdot t$ photon

[19] PA35-H Port-Aligner from UHV-Design
[20] Luca EMCCD from Andor
[21] H7360-01 from Hamamatsu. Dark counts per second typ. 15, max. 80 according to the manufacturer
[22] FF01-370/10-25 from Semrock

scattering events still within the $^2S_{1/2}$ manifold is

$$P_{\text{bright}}(t) = 0.995^{R_{4\pi} \cdot t}. \tag{3.16}$$

Here, $R_{4\pi}$ is the rate of scattered photons on the driven atomic transition into free space. With η_D being the detection efficiency of the whole free space imaging setup, we detect a fractional rate of photons $\cdot\, s^{-1}$ of

$$D_0 = \eta_D \cdot R_{4\pi} \tag{3.17}$$

on the single photon counter.

For a single experimental run, the ion is either in the $^2S_{1/2}$ manifold and still coupled to the 370 nm driving laser field or in the $^2D_{3/2}$ manifold, where it remains dark and does not scatter photons any more. Averaging the detected free space photons over 50,000 repetitions of the sequence shown in Figure 3.11 b), we obtain an average detection rate of photons $D(t) = D_0 \cdot P_{\text{bright}}(t)$ which decays exponentially according to equation (3.16). The decay constant τ is then given by

$$\tau = \frac{1}{R_{4\pi} \cdot \ln(0.995)}. \tag{3.18}$$

The detection efficiency is calculated from the decay of the detection rate $D(t)$ as shown in Figure 3.11 b) using equations (3.17) and (3.18) as follows:

$$\eta_D = \frac{D_0}{R_{4\pi}} = D_0 \cdot \tau \cdot \ln(0.995) = 0.46(1)\,\% \quad \text{with} \quad \tau = 10.13(9)\,\mu s. \tag{3.19}$$

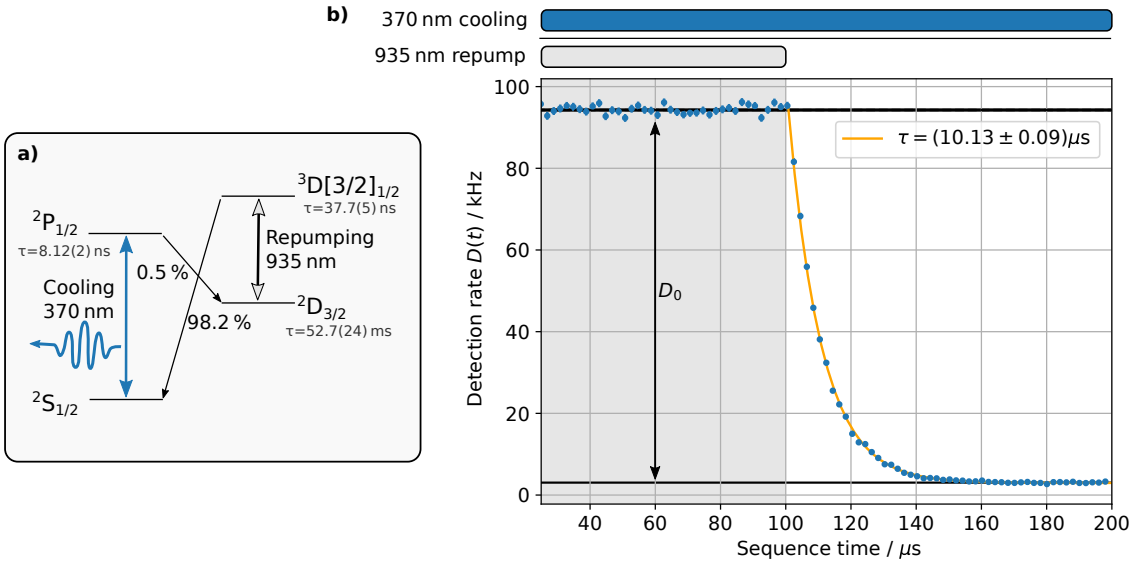

Figure 3.11: a) Relevant energy levels of $^{174}Yb^+$ according to Figure 3.5 a). **b)** Binned photon detection times (blue dots) for 50,000 repetitions of the shown sequence (top). The standard error is given as error bar for each data point (mostly not visible on this scale). The solid black horizontal lines constitute the averaged measured detection rates for a bright ion (top line), where the 935 nm laser is enabled (grey shaded area) and for a dark ion pumped to the state $^2D_{3/2}$ (bottom line), where the 935 nm laser is turned off. The thickness of the lines reflects the standard deviation of the rates. From the difference of the rates, we extract the detected scattering rate of photons D_0 for a bright ion. A least-square fit of an exponential decay function is shown as orange solid line with decay constant τ.

If the light is emitted by a point source isotropically into 4π solid angle and the imaging system is adjusted such that it is only limited by diffraction, then the following equation applies for the collection efficiency η_C of the light [6]:

$$\theta = 2 \arccos\left(-2 \cdot \eta_C + 1\right). \tag{3.20}$$

Here, θ is the maximum angle of a light cone coming from the point source that can enter the imaging lens according to Figure 3.10 a). The numerical aperture NA of the lens is given by

$$\mathrm{NA} = \sin\left(\theta/2\right). \tag{3.21}$$

From equations (3.20) and (3.21) we can compute an effective numerical aperture of the setup by using the estimated collection efficiency of the objective $\eta_C = \eta_D/(\eta_{\mathrm{path}} \cdot \eta_{\mathrm{spc}}) = 5.9(2)\,\%$, where we determined the optical path efficiency to be $\eta_{\mathrm{path}} = (54 \pm 1.5)\,\%$ from evaluating the transmission coefficients[23] of each optical element shown in Figure 3.10 a). The single photon counter (SPC) quantum efficiency is $\eta_{\mathrm{spc}} = 0.145$ according to the manufacturer. We obtain for the effective numerical aperture

$$\mathrm{NA}_{\mathrm{eff}} = 0.471(7). \tag{3.22}$$

The value is close to the nominal[24] numerical aperture of the objective lens of $\mathrm{NA}_{\mathrm{nom}} = 0.48$, which states that we have aligned the whole imaging system close to the optimal diffraction-limited situation.

3.2.4 Data acquisition and experimental control

The acquisition of experimental data and the execution of preparatory tasks require the use of automated experimental control sequences. We distinguish between fast control sequences of the experiment and slow sequences (e.g. loading an ion into the trap). For the former, TTL pulses ($\geq 10\,\mathrm{ns}$) are distributed over high-frequency point-to-point links for experimental control with an accuracy of $\lesssim 1\,\mu\mathrm{s}$, while for the latter we use TCP Ethernet communication, which has higher latency but is easier to scale. Figure 3.12 shows a block diagram of the experimental control setup, which has a modular structure. Groups of hardware devices are controlled via micro severs running on microcontrollers or small computers. This allows for distributing the hardware load and increases the failure safety of the whole experiment, since single modules can be replaced and added with low impact for the whole experiment. Furthermore, for future applications including two or more ion traps, hardware could be shared between the setups and experimental control could be distributed among multiple control computers.

[23] Asphericon AFL25-25-S-U 8 mm fused Silica: $T = 0.95$, Thorlabs vacuum chamber window 5 mm NBK7: $T = 0.954$, Thorlabs Lens LA4782-UV 4.4 mm UV fused Silica: $T = 0.97$, Edmund optics 30/70 BS: $T = 0.95 \cdot 0.7$, Thorlabs lens 9 mm NBK7: $T = 0.92$. An error of $\Delta T = 0.01$ is assumed.

[24] According to Asphericon

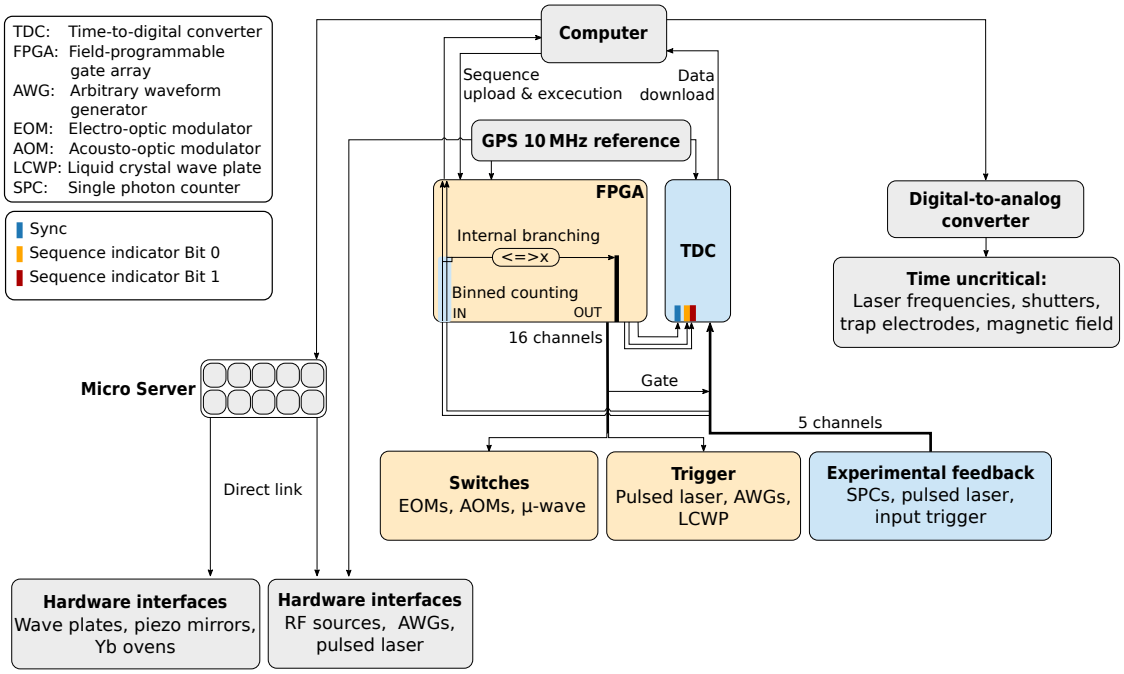

Figure 3.12: Block diagram of the experimental control. Elements of the fast experimental control system (FECS) with a precision of $\lesssim 1\,\mu$s are coloured according to their role (yellow: experimental control, blue: data acquisition).

We use a field-programmable gate array[25] (FPGA) for application of fast control sequences, where we upload and execute the sequences from the control computer. The FPGA exhibits number of 20 TTL compatible output channels and two input channels, which we access as binning counters from the control computer. The inputs can be further used as real-time decision branching during the execution of a sequence, where the condition is formed by the number of events impinging within a certain time window to the inputs.

A time-to-digital converter[26] (TDC) assigns continuous 48-bit time stamps to incoming pulses originating for example from the single photon counters with a time resolution of $< 35\,$ps. As a result, the string of time stamps has to be chunked in post-processing according to the corresponding sequences executed by the FPGA (see Figure 3.13). To this end, three of the eight input channels of the TDC are used for synchronisation with the FPGA.

[25] XEM6001 from Opal Kelly
[26] TDC8HP from RoentDek

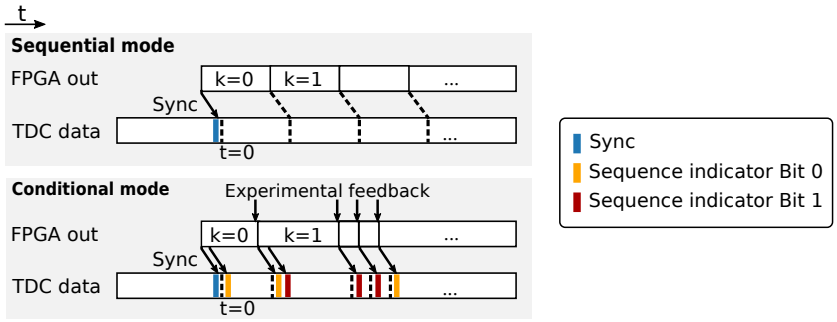

Figure 3.13: Post-processing of recorded TDC data. The data gets divided into chunks according to the control sequences executed by the FPGA which are numbered consecutively with $k \geq 0$. The sync pulse indicates the point in time when the FPGA started executing the control sequences. In conditional mode, the FPGA outputs a 2-bit sequence fingerprint in addition.

We distinguish between two modes of FPGA operation: i) In the sequential mode, the FPGA runs a fixed number n of repetitions of one control sequence with a fixed length l. In the post-processing of the data, a sync pulse sent out from the FPGA at the beginning of the sequences is used to determine the point in time for the definition of $t = 0$ within the measured data of the TDC. From here, the data is split into n chunks of length l, which are numbered with an integer $k < n$. ii) Using the conditional mode, multiple branches of a sequence are programmed into the FPGA and their executions are based on real-time input conditions. In particular, this speeds up the experimental repetition rate if one longer sequence is based on the success of a shorter sequence. This mode is used for the presented spin-photon entanglement measurement and the quantum key distribution (see chapters 7 and 8). In the conditional mode, the post-processing is applied according to a 2-bit value recorded on the TDC allowing for a fingerprinting of three different sequences. The 2-bit value comprises of two TTL pulses which were sent out simultaneously at two different channels of the FPGA[27]. Based on the occurrences of these fingerprints and a subsequent sanity check, the TDC data is split into the corresponding sequences.

[27] The fingerprint bit size can be extended at the cost of available output channels on the FPGA and available input channels on the TDC

4 Optimising experimental calibration tasks with machine learning

Successful acquisition of data requires careful calibration and correction of environmental influences, as can be seen from the previous chapter. However, this also applies to many other experimental setups. Across the fields of atomic and condensed matter physics, the continuously increasing requirements regarding the precision of experiments entail the need for ever better cancellation of disturbances. Detecting and reacting to an external noise source, which drives an experimental system out of its optimal state is a frequent challenge for many experimental platforms. This can be particularly cumbersome when the timescale required for readjustment of the setup is comparable to the timescale of the temporal deviation of the noise source. Therefore, efficient and fast methods for the detection and compensation of external perturbations are of high importance.

In this chapter, we present the use of two machine learning algorithms to create an empirical model of an experimental apparatus capable of predicting an experimental parameter set for the compensation of an external perturbation from a minimised number of measurements of the perturbation. Due to the large number of different experimental setups and the large number of calibration tasks, we first describe these tasks in general.

We consider an experimental system driven out of its optimal operation condition by noise sources $\mathbf{N}_i$ which add up to $\mathbf{N} = \sum_j^m \mathbf{N}_j$ (Figure 4.1 a)). The noise is considered as vector in the parameter space of the compensation control parameters. Furthermore, there are no cross-correlations assumed between the noise sources. In particular, the goal of any compensation task is the cancellation of the noise $\mathbf{N}$ by applying a compensation $\mathbf{C}$ which itself consists out of a k-dimensional set of control parameters C_i (see Figure 4.1 b)). Examples would be magnetisation of parts of the experimental setup, heating from a defined source or, as relevant in our case, electrical charging of elements in a setup. Since the external noise sources disturbing the experimental system have a predictable physical origin, we assume that the resulting disturbance is not inherently random. We explicitly exclude the cancellation of any random noise from the applicability of the presented methods (e.g. white noise).

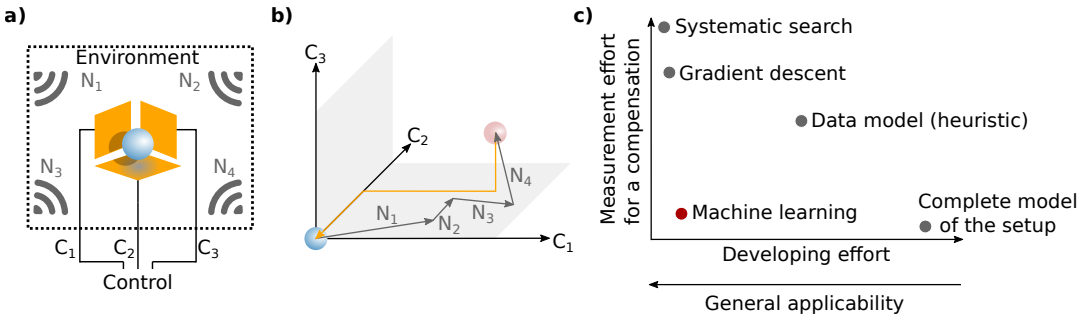

Figure 4.1: a) The experimental system (blue ball) is disturbed by a set of noise sources N_j (grey). **b)** The noise sources drive the system out of the equilibrium position (red ball). The external disturbance can be cancelled using in total k control parameters C_i, $i \in \{1, ..., k\}$ (orange trace). **c)** Classification of various methods which can be used for a compensation. We classify measurement and developing effort of a method. Figures a) and b) have been published in a similar manner in [93].

Systematic search

In the most general case, the desired set of compensations $\{C_i\}$ can be found by scanning a k-dimensional hypercubic grid with n steps along each axis $i \in \{1, ..., k\}$. The value of n is determined by the required precision. This systematic search scales with n^k required data points exponentially in the dimension of control parameters. As soon as the perturbation changes, the same search has to be performed again because no knowledge about the system itself was gained. While this method is able to compensate even random perturbations, it is inefficient for experiments which are facing (partly) predictable noise. It is not necessary to apply the whole systematic search procedure for a compensation by having knowledge of how to predict the noise manifestation.

Complete model of the setup

In principle, a changing compensation could be predicted with minimal measurement effort from a model including the origin of perturbation and all unique features of the experimental system. Such a model constitutes the opposite to the systematic search approach, as it requires minimal measurement effort but maximal development work (see Figure 4.1 c)). However, such a simulation is usually impossible since it would require deep knowledge of all special characteristics of the setup and the noise sources. When weighting up effort and gain of a universal applicable simulation to a systematic search for optimal compensation, the latter wins in most cases regardless the fact that it can only cover the current temporal deviation.

Data describing models

A compromise between these two approaches are data models that use certain underlying physical aspects of the noise and control parameters to introduce dependencies between them. As an example, extrapolating the remaining experimental disturbance as a function of the control parameters C_i allows to find a parameter setting where $\mathbf{N}$ is compensated with reduced effort. These data describing models can be found heuristically or on the basis of physical effects. Data describing (heuristic) models can greatly reduce the amount of measurements needed for a compensation since they do not require a lengthy exploration through parameter space. Usually the measurement effort then reduces to a linear dependence and can be described as

$$Y = a_{\text{model}} \cdot n \cdot k, \tag{4.1}$$

where Y is the total number of measuring points and n represents the number of data points of a one-dimensional line segment in a k-dimensional hypercube in the control parameter space. The factor a_{model} measures the specific scaling of a model.

Combining the best features

In the following, we introduce a method capable of combining the generality of the systematic search with the reduced measurement effort of a complete model having precise knowledge about the system. To this end, we utilise methods to reveal information hidden in a large dataset originating from machine learning research, which in recent years has found its way into the domain of physics [32]. For example, reinforcement learning techniques have been utilized to systematically scan large potential parameter spaces in search for optimal values [169] and supervised learning techniques yielded improved measurements and optimised critical parameters [112].

In the following, we present a new approach based on machine learning that creates an accurate empirical model of the underlying experimental system that allows us to access the correlations between parameters induced, for example, by the geometry of the setup. The presented methodology yields improvements for two distinct cases:

(1) Approaching a general compensation problem when no data model of the system exists. Prominent examples of such tools are systematic search and gradient descent optimisation. We add a supervised learning approach to this toolkit making use of a feed forward artificial neural network (ANN) and benchmark its performance with respect to the systematic search and gradient descent optimisation.

(2) If a data model is known, we demonstrate that we can even outperform the state-of-the art models in terms of required number of measurements and hence time needed to perform a compensation. Using unsupervised learning, namely Principal Component Analysis (PCA), we are able to reveal hidden correlation between the compensation parameters in order to cover the origin of disturbance and not only its compensation.

In section 4.1, we introduce the task of excess micromotion minimisation in a Paul trap by external stray field cancellation and discuss the common strategies to find a compensating electric field. In order to test the accuracy of the prediction of the various optimisation procedures, we define a measure σ as the standard deviation of predicted compensation points for a common manifestation of a stray electric field. The standard deviation is calculated in terms of the Euclidean distance of the predicted points in the parameter space of applied compensation electric fields. We have verified that the actual compensation point is located in at least 68% of the cases within one standard deviation from the predicted one. For reference, the typical range of compensation drift averages to $\sim 600\,\mathrm{V/m}$ over a few months[28].

In section 4.2 we create an empirical model of the setup using the presented machine learning approach. We show that the ANN performs on par with a PCA-enhanced heuristic model and we see that by taking accuracy measures into account, the amount of input data can be reduced to a minimum in the case of the ANN, which is even below the principle minimum of k data points of the PCA.

4.1 The task of stray field cancellation

An experimental task frequently arising in the presented setup of a radio frequency Paul trap is the compensation of electric stray fields building up at the ion's position. Stray electric fields push the ion away from the symmetry point of the quadrupole field and increase the temperature of the ion in terms of micromotion. This limits the trapping time and thus also, on a practical level, the time available for data acquisition. But it also reduces the general usability of the ion as a stationary qubit in a quantum network. Furthermore, cold ions are not only required in quantum information processing [22] but also in precision spectroscopy like for atomic clocks [81].

In this section we present the detection and minimisation of micromotion along one spatial direction leading to the complex problem of minimising the micromotion along all

[28] We determine the drift by using an arithmetic mean of the measured compensation points in the parameter space of applied electric fields and computing the standard deviation of their Euclidean distance to that point.

three spatial directions. In this context we benchmark two approaches to find the point of minimal motion in three dimensions, namely gradient descent optimisation and a heuristic model making use of hyperplanes in the parameter space of applied compensation voltages.

4.1.1 Micromotion detection and compensation along one spatial direction

The working principle of a Paul trap and the influence of a stray electric field to the micromotion of a trapped ion is discussed in subsection 3.1.1. In this subsection, we introduce the experimental techniques available for the compensation of a stray electric field. In general, we intent to apply an electric field $\vec{E}_{\text{comp}}$ which cancels the stray field $\vec{E}_{\text{stray}}$. We are able to apply an electric field $\vec{E}_{\text{dc}}$ along any spatial direction using three sets of grouped DC electrodes (see Figure 4.2 a)+b)). The resulting electric field is determined by the geometry of the electrodes as a linear combination of the electrode groups and was measured in [157]. It can be computed in units of V/m as

$$\vec{E}_{\text{dc}}(V_{x_1}, V_{x_2}, V_{x_3}) = (-250 \pm 30) \cdot V_{x_3} + (389 \pm 11) \cdot (V_{x_1} + V_{x_2}), \tag{4.2}$$

where $(V_{x_1}, V_{x_2}, V_{x_3})$ denotes the DC voltage applied to the respective electrode group representing the three spatial directions. Hence, the compensation field can be written as

$$\vec{E}_{\text{dc}}(V_{x_1 c}, V_{x_2 c}, V_{x_3 c}) = -\vec{E}_{\text{stray}} \equiv \vec{E}_{\text{comp}}. \tag{4.3}$$

We refer to the voltage set $\vec{V}_c = (V_{x_1 c}, V_{x_2 c}, V_{x_3 c})$ as compensation point in the following.

Various methods have been developed to determine the compensation point. These methods are based on measuring the equilibrium position of the ion [60], parametric excitation of the ion [70] or correlation measurements between the photon scattering rate of the ion and the trap RF frequency [151]. The latter is known as the Doppler correlation method and was first demonstrated in [19].

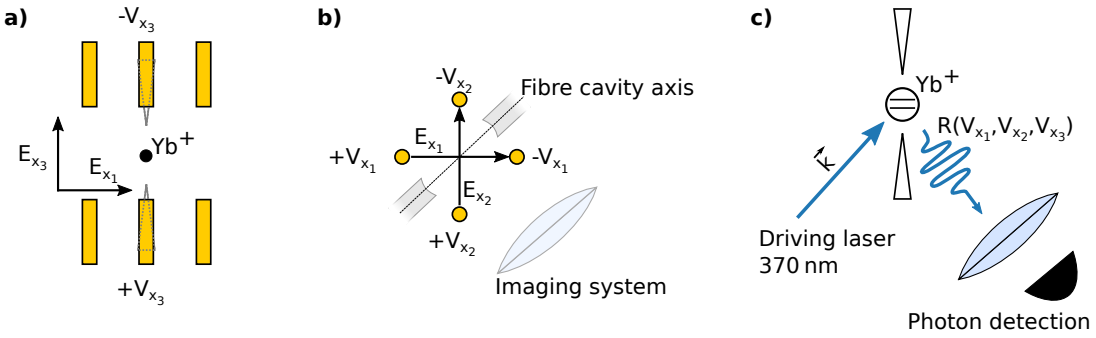

Figure 4.2: a) Sketched side view of the trap including the DC electrodes (yellow). Applying DC voltages to a group of electrodes results in an electric field at the ion's position. For an electric field along the trap axis (E_{x_3}) top and bottom electrode groups are set to a negative and positive potential respectively. **b)** Top view of the trap (x_1-x_2 plane). The axes of the imaging and the fibre cavity are shown for the sake of completeness. **c)** The Yb ion is driven by a laser beam with wave vector $\vec{k}$. The rate of scattered photons into free space R depends on the velocity of the ion according to equation (4.5) and hence on the applied DC voltage.

We utilise the Doppler correlation method as a starting point for our optimisation. To this end, we illuminate the ion with a laser beam and measure the rate of photons R

scattered by the ion into free space (see Figure 4.2 c)). The Doppler effect connects the motion of the ion along the driving laser beam axis to a modulation of the scattering rate R of photons. This is due to a variation of the detuning between the driving laser frequency f_l and the resonance frequency of the atomic transition f_{res} given by $\Delta = f_l - f_{\text{res}}$. In the motional frame of the ion, the laser frequency

$$f_{l,\text{ion}} = f_{l,\text{lab}} \left(1 - \frac{\vec{v} \cdot \vec{k}}{c \cdot |\vec{k}|}\right) \tag{4.4}$$

varies according to the current velocity of the ion $\vec{v} = \dot{\vec{x}}$. Using the steady state solution of the scattering rate of a driven two-level system from equation (6.28) together with equation (4.4), we obtain

$$R(\vec{v}, \vec{k}) = \frac{\Gamma}{2} \cdot \frac{I/I_0}{1 + I/I_0 + 4\left(\frac{2\pi \cdot \Delta_{\text{lab}} - \vec{v} \cdot \vec{k}}{\Gamma}\right)^2}. \tag{4.5}$$

According to above equation, the scattering rate of photons depends on direction and velocity of the ion's motion. From equation (3.8) we know that the oscillation frequency of the (excess) micromotion is equal to the frequency Ω of the driving trap RF field. Therefore, the amplitude of the cross-correlation between the arrival times of scattered photons on the detector and the trap radio frequency Ω directly measures the excess motion of the ion along the wave vector $\vec{k}$ of the driving laser field according to equation (4.5) [29].

The presented method requires the saturation parameter I/I_0 to be approximately constant over the region of interest, which limits the range of applicable DC voltages. Moreover, it requires a well aligned cooling beam centred to the ion's position.

We measure the cross-correlations for a duration of 1 s by using the time-to-digital converter and a FPGA according to [189] and [157]. Upon scanning the electric field components, one can find a minimum of correlations (see Figure 4.3 a)). This reveals a set of $\vec{V}_m = (V_{x_1 m}, V_{x_2 m}, V_{x_3 m})$ for which the motion of the ion is minimal along the driving beam axis $\vec{k}$. We determine the electric field $\vec{E}_{\text{dc}}(\vec{V}_m)$ with a measurement accuracy of $(54 \pm 3)\,\text{V/m}$, which we infer from the measurement uncertainty in terms of applied DC voltages and equation (4.2). It is important to understand that this methodology so far only provides information about the component of the ion's motion that is parallel to the wave vector of the laser beam, while the motion along orthogonal axes cannot be detected. Therefore, by minimising the motion along this axis, likely additional motion is induced along directions orthogonal to the beam axis (Figure 4.3 b)).

[29] Note that equation (4.5) is more an approximation in this case since $\Omega \ll \Gamma$ is not true in our experiment. Furthermore, the scattering rate of photons follows a more complicated dependence for the isotope $^{171}\text{Yb}^+$ which is described in [46].

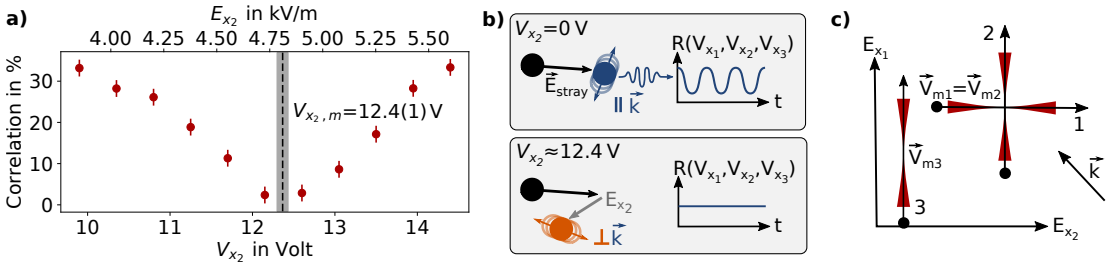

Figure 4.3: a) Correlation measurement between the trap frequency Ω and the scattering rate of photons $R(V_{x_1}, V_{x_2}, V_{x_3})$ while varying V_{x_2} (trajectory 1 in c)) and assuming an external stray field $\vec{E}_{\text{stray}} \neq 0$. The dashed line denotes the voltage setting of minimal motion of the ion $V_{x2,m}$ along the driving beam axis $\vec{k}$ (the grey area depicts the measurement uncertainty). **b)** A simplified sketch of the ion's motion displaced by the stray field from the trap centre is shown for no applied compensation field ($V_{x_2} = 0$) and minimised correlation ($V_{x_2} = 12.4(1)\,\text{V} \equiv V_{x_2,m}$). For the latter, likely additional motion is induced along directions orthogonal to the beam axis ($\vec{v} \perp \vec{k}$, orange arrows). **c)** The ion is driven with a laser beam with wave vector $\vec{k}$ which exhibits a waist larger than the region of interest. A set of three ion trajectories is sketched in the x_1-x_2 plane upon variation of the corresponding electric field. The corresponding measurable correlations as shown in a) for trajectory 1 are indicated as red area. The three dimensional voltage settings of minimum correlation are denoted with $\vec{V}_{m1/2/3}$.

Figure 4.3 c) shows three simplified trajectories of the ion in the radial plane of the trap (x_1-x_2) upon variation of the DC electrode voltages V_{x_1} and V_{x_2}. A scan of E_{x_2} ends up with trajectory 1 leading to $\vec{V}_{m1}$ as a point of minimised motion. However, we gain no further information by just switching the direction of the scan for example to E_{x_1} (trajectory 2: $\vec{V}_{m1} = \vec{V}_{m2}$). New information about the system is obtained by changing an electric field component which is not currently scanned. Changing E_{x_2} with respect to trajectory 2 and scanning E_{x_1} gives a new set of voltages $\vec{V}_{m3}$ where the motion of the ion is minimal along the probing beam axis (trajectory 3). We present in subsection 4.1.3 that all points for which we detected minimal motion along one probe laser beam axis, form a hyperplane in parameter space for the investigated region. But this still only covers one component of the ion's motion.

A full three-dimensional minimisation of the micromotion is equal to a full compensation of all three stray electric field components and requires three non-collinear laser beams to detect the three spatial components of the ion's motion. However, the complex relation between the direction of the stray field and the direction of the ion's motion, the relative orientation of the laser beams, trap geometry and direction of applied electric DC fields complicate an intuitive approach to the problem.

To solve this rather complex optimisation problem, a very general approach is the systematic search of the correct voltage set $\vec{V}_c$ to minimise the ion motion along all three spatial directions by just scanning all three components of the compensation field over a cubic grid. However, the systematic search is inefficient due to an exponential scaling in the dimensions k of the parameter-space (here $k = 3$). We present more efficient methods in the following sections.

4.1.2 Gradient descent optimisation

The performance of gradient descent optimisation (GDO) strongly depends on the specific problem. Benchmarking the performance of GDO for the presented compensation problem using the real experimental setup would take several weeks due to the large amount of measurements required. Therefore, we fully simulated the three-dimensional stray field compensation problem starting from a Paul trap and adding the ion trajectory, DC electrodes, Doppler correlation measurement and beam vectors according to the real experimental setup using equations (3.7), (4.2) and (4.5) and the beam orientations from Figure 3.8. We tested the simulation for consistency with real experimental data.

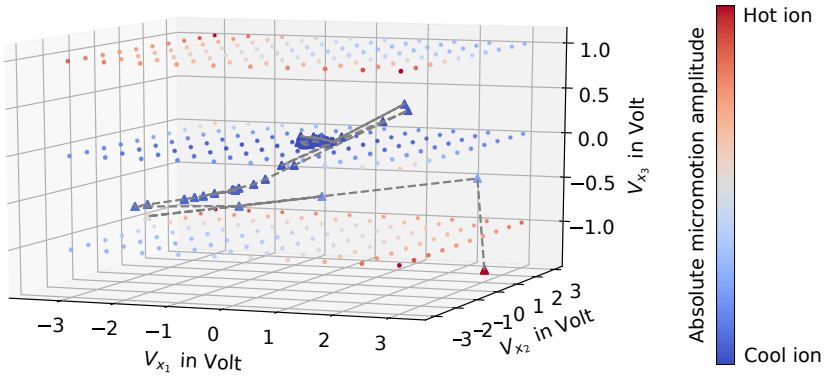

Figure 4.4: Trace of a single gradient descent optimisation (GDO) of the electric stray field compensation using the BFGS algorithm. We take the correct compensation point as an offset to the shown parameter space of applied compensation voltages such that the ion exhibits minimal motion at the origin. Steps of the GDO are shown as triangular coloured points. The starting point of the compensation is shown at the lower right (single red triangle) and converges to the optimal compensation point located at the origin. A linear interpolation between the algorithm steps is shown as grey dashed line. Small coloured points indicate the total micromotion amplitude of the ion at this point in parameter space according to the simulation and are given as additional information. For a better visibility we provide 3 simulation layers containing a 10x10 grid respectively.

We use the algorithm of non-linear conjugate gradient by Polak and Ribiere (CG) and the quasi-Newton method of Broyden, Fletcher, Goldfarb, and Shanno (BFGS) as described in [126] on top of our simulation for minimisation[30] of the three-dimensional correlations (see Figure 4.4). We observe that both algorithms failed in $\sim 1/3$ of all attempts to converge to the compensation point. For the remaining attempts, the performance averaged over 27 successful compensations[31] is shown in Figure 4.11. We choosed the BFGS algorithm as a benchmark for GDO, since it showed a slightly better performance than the CG algorithm for our optimisation problem.

4.1.3 Plane model

In subsection 4.1.2 we have seen an optimisation strategy (GDO) for the compensation problem which works without any data describing (heuristic) model. However, data describing models can drastically reduce the amount of measurements needed for a compen-

[30] We use the function SCIPY.OPTIMIZE.MINIMIZE in PYTHON. See documentation for details.
[31] We use the same stray electric field manifestation as for the PCA and ANN benchmarks

sation. In the following, we introduce a heuristic model for our compensation problem, which makes use of the observation that all points for which we detect minimal motion along one probe laser beam axis, form a hyperplane in the parameter space of $(V_{x_1}, V_{x_2}, V_{x_3})$ for the investigated region (see Figure 4.5 a)). The intersection point of three planes in $k = 3$ dimensions constitutes the optimal setting $\vec{V}_c$ for the compensation electrodes. Using this model, we are able to predict the compensation point with a measurement accuracy of $\sim 54\,\mathrm{V/m}$ with $8 \cdot k = 24$ measurements.

The plane model is based on the assumption that the stray field at the position of the ion is gradient free and linear in direction, which is true for an investigated spatial region that is small compared to the trap geometry. The point of minimal ion motion along the investigated transversal direction of the beam can therefore be expressed as a linear equation of three non-collinear spacial directions. Consequently, the points of minimal correlation $\vec{V}_m$ along one the probe beam axis form a hyperplane in parameter space with

$$\vec{n} \cdot \vec{V}_m - c = 0, \tag{4.6}$$

where $\vec{n}$ is the normal vector of the plane and c is the offset of the plane. We confirm the validity of this model by evaluating the distances of the measured points to the fitted plane. They distribute around zero Euclidean distance with a maximal standard deviation of $(173 \pm 20)\,\mathrm{V/m}$ in the case of beam 2 (see Figure 4.5 b)).

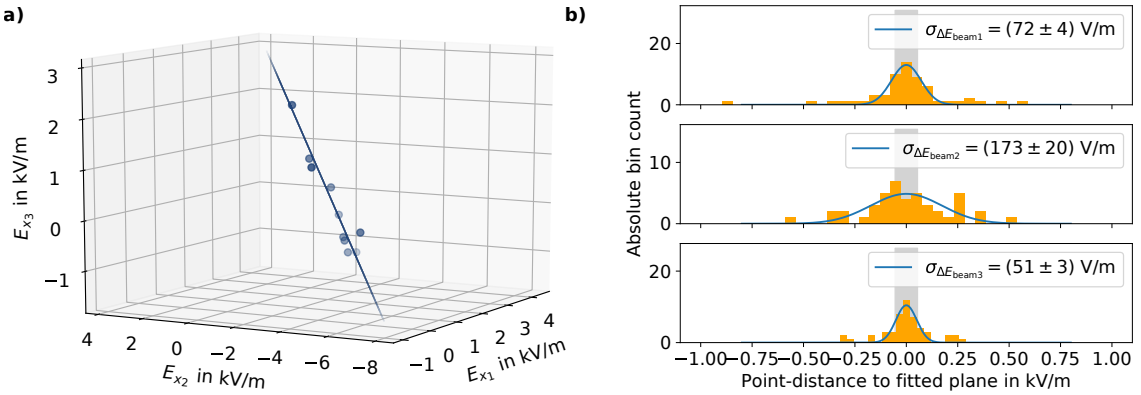

Figure 4.5: a) Side view of a hyperplane in the parameter space of applied compensation electric fields (visible as line). We fitted the plane to the points of minimal correlation (dots), which were measured using the first probe beam (Beam 1 in Figure 4.6). **b)** Fit of a Gaussian distribution (solid line) to the binned Euclidean distances of the measured points to the corresponding hyperplane for each of the three probe beams respectively. The standard deviation σ is extracted from the fits.

The orientation of a plane depends on the coupling between the experimental parameters and needs not to be orthogonal to the corresponding beam axis. Figure 4.6 shows the three planes of the three separate laser beams, whose k-vectors are non-collinear. The planes do intersect in one point in the three-dimensional parameter space of applied DC voltages, which constitutes the optimal setting for the compensation electrodes. This method enables us to detect and compensate for an arbitrary electric field in three dimensions.

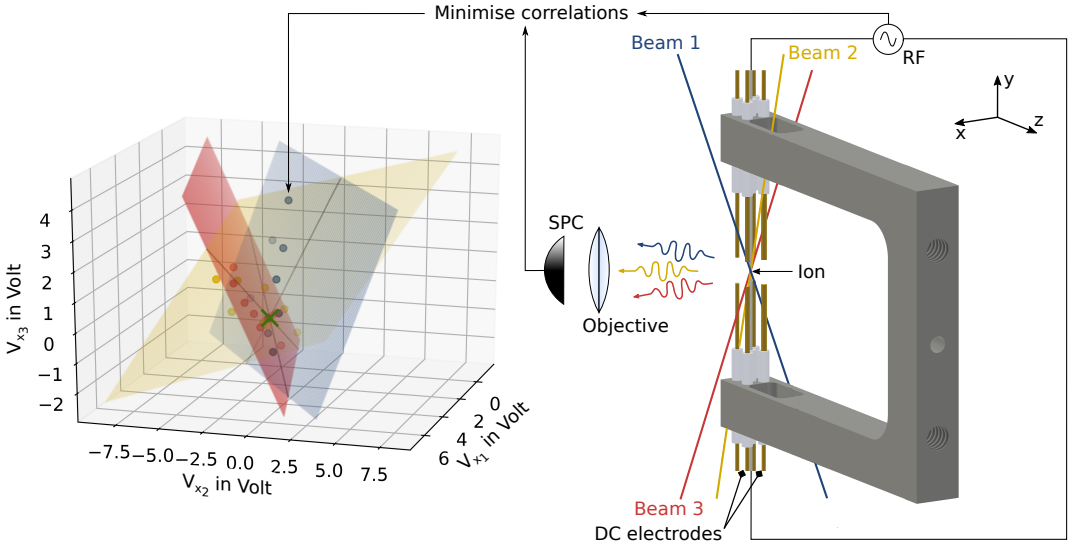

Figure 4.6: Schematic of the Paul trap and the compensation of one stray field manifestation using the plane model approach. The three cooling laser beams illuminate the trapped ion and the fluorescence counts are detected on a single-photon counter. The correlation between photon counts and supplied radio frequency measures the ion movement along the illuminating laser beam axis. Points of minimal detected correlations lie on a plane for each beam. The intersection point of the three planes is the optimal stray field compensation (denoted by a green X). Paul trap, cooling beams, DC electric fields and the planes of minimal motion are shown consistent according to their real orientation in the experiment. Distances are not to scale.

From a purely geometric point of view, the calculation of the plane parameters requires a minimum of three correlation measurements per plane, so that a total of at least nine measurements are required to determine the compensation point in three dimensions. The minimal approach of nine measurements provides us with $\sigma = 734\,\mathrm{V/m}$ and therefore the accuracy is worse than the typical range of compensation drift, which averages to $\sim 600\,\mathrm{V/m}$ over a few months. The reason for this short-fall is that the quality of the fitted plane parameters and hence the determination of their crossing depends critically on the number of data points per plane. In practice, we have found that we require a minimum of eight points per plane (i.e. 24 in total) to calculate the point of intersection with a precision down to measurement accuracy (see Figure 4.7 and Figure 4.11). In this case we obtain $a_{\mathrm{plane}} \cdot n = 8$.

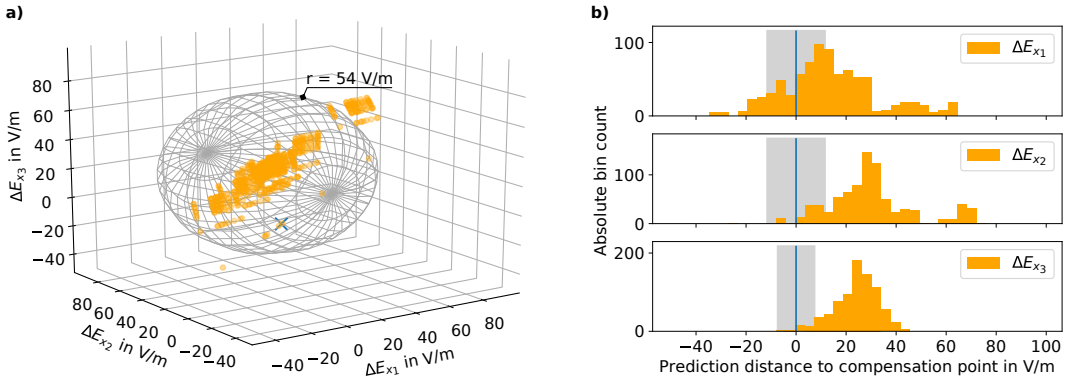

Figure 4.7: Distance spread of the predicted compensation points with respect to the actual measured compensation point using $n = 8$ points per plane for prediction. **a)** The spread is shown in terms of electric field components. The standard deviation of the spread in terms of Euclidean distance is $\sigma = 54\,\mathrm{V/m}$ and includes the measured compensation point (blue cross). **b)** Breakdown of the prediction point spread to the three spatial axes. The actual measured compensation point is shown as vertical blue line with the measurement error as grey area.

4.2 Machine learning enhanced stray field compensation

As discussed in the previous section on the example of a trapped ion, determination of the compensation point for an external perturbation could be non-trivial. Like most data describing models, the plane model introduced in subsection 4.1.3 outperforms the systematic search and gradient descent optimisation approach (subsection 4.1.2) in finding the optimal compensation point $\vec{V}_c$ for a specific external stray electric field. The accuracy of the compensation prediction is limited by the measurement precision only for this model. But as with most (heuristic) models, the applicability is limited to a specific problem.

We show in subsection 4.2.1 that using principal component analysis (PCA) as an unsupervised machine learning approach, we can enhance the plane model by exploiting previous unused hidden correlations in the model. In subsection 4.2.2, we present the ability of building a model directly from the compensation datasets using an artificial neural network (ANN), which does not require any predefined model such as the plane model. Therefore, in terms of methodology, this approach is applicable to a general set of problems.

4.2.1 Unsupervised machine learning using principal component analysis

The Principal Component Analysis (PCA) [133, 67] is an unsupervised learning algorithm which can identify the direction of maximum variance within a dataset in parameter space. In the best case, all deviations from the optimally compensated experiment can be explained by one principal component $\hat{e}_{\lambda_1}$. In this case, the multiplicative factor a_{PCA} of equation (4.1) approaches $a_{\mathrm{PCA}} = 1/k$, which is equivalent to a search of the optimal compensation point in one dimension. We can expect this, for example, for an electric or magnetic field perturbing a very small object such that field gradients can be neglected. Having access to an experimental observable directly related to the field components along a full set of axes, it is possible to determine the field axis from a PCA. In this case, the task

of experimental optimisation can be reduced to the determination of a single value λ_1 in a transformed parameter space along the axis of the first principal component $\hat{e}_{\lambda_1}$. However, the PCA method works even for more general and more complicated noise manifestations and in the presented case, one cannot directly infer a field component from the amplitude of the micromotion.

We apply the PCA to a training dataset containing the information about the plane orientations from seven full compensation measurements, each representing a different charge distribution in our setup and consisting in total out of 137 three-dimensional measured data points $\vec{V}_m$. For all sets of the training data we ensure the same environmental conditions, i.e. beam angles, measurement method and trap geometry. We expect all these conditions to have influence on the correlations between the compensation parameters.

We describe the planes obtained from the training dataset each with a normal vector $\vec{n}$ and the offset c according to equation (4.6). For each plane, we have three independent variables since the length of the normal vector $|\vec{n}| = |(n_1, n_2, n_3)|$ is not important. We therefore set $n_3 = 1$ without loss of generality. We train the PCA with the parameter sets $d_i = (n_1, n_2, c)_i$ and stack the training datasets d_i to a vector

$$\mathbf{D} = \begin{pmatrix} d_1 \\ ... \\ d_7 \end{pmatrix} = \begin{pmatrix} (n_1, n_2, c)_1 \\ ... \\ (n_1, n_2, c)_7 \end{pmatrix} \tag{4.7}$$

for each beam. We centre the data around the origin by subtracting the main value of each data column $\overline{\mathbf{D}} = (\overline{n_1}, \overline{n_2}, \overline{c})$ from each row of the original data vector as

$$\mathbf{D_N} = \mathbf{D} - \overline{\mathbf{D}}. \tag{4.8}$$

Using eigendecomposition of the covariance matrix $\Sigma = \mathrm{Cov}\left((\mathbf{D}_N)^T\right)$, we get for each beam a decomposition into the eigenbasis $(\hat{e}_{\lambda_1}, \hat{e}_{\lambda_2}, \hat{e}_{\lambda_3})$ ordered by the magnitude of their eigenvalues $(v_{\lambda_1}, v_{\lambda_2}, v_{\lambda_3})$ with $v_{\lambda_1} \geq v_{\lambda_2} \geq v_{\lambda_3}$. Note that for unsupervised training, no 'correct' compensation point needs to be provided to the learning algorithm.

From a parameter set (n_1, n_2, c), we can calculate the corresponding point $(\lambda_1, \lambda_2, \lambda_3)$ in the eigendecomposition space of the covariance matrix $(\hat{e}_{\lambda_1}, \hat{e}_{\lambda_2}, \hat{e}_{\lambda_3})$ by applying following transformation:

$$\begin{pmatrix} \lambda_1 \\ \lambda_2 \\ \lambda_3 \end{pmatrix} = \begin{pmatrix} \hat{e}_{\lambda_1} \\ \hat{e}_{\lambda_2} \\ \hat{e}_{\lambda_3} \end{pmatrix}^T \cdot \left(\begin{pmatrix} n_1 \\ n_2 \\ c \end{pmatrix} - \overline{\mathbf{D}} \right)^T . \tag{4.9}$$

Conversely, we can transform any point $(\lambda_1, \lambda_2, \lambda_3)$ in the PCA eigenspace into parameter space (n_1, n_2, c) by computing

$$\begin{pmatrix} n_1 \\ n_2 \\ c \end{pmatrix} = \left(\begin{pmatrix} \lambda_1 \\ \lambda_2 \\ \lambda_3 \end{pmatrix} \begin{pmatrix} \hat{e}_{\lambda_1} \\ \hat{e}_{\lambda_2} \\ \hat{e}_{\lambda_3} \end{pmatrix} \right)^T + \overline{\mathbf{D}}, \tag{4.10}$$

which defines a plane in the compensation voltage space.

For prediction of the compensation point, we need to compute the intersection point of the three planes. We construct each plane from equation (4.10) by using only the first principal component $\hat{e}_{\lambda_1}$ in PCA eigenspace. Along the remaining axes we set $\lambda_{2/3,\text{plane-}i} = 0$.

This reduces the task of finding the correct plane parameters to a single degree of freedom for each beam. The value of $\lambda_{1,\text{plane-}i}$ determines the plane orientation and we can deduce it from one measured point of minimum correlation for each beam $\vec{V}_{m,\text{beam-}i}$ with $i = 1, 2, 3$ (see Figure 4.8 a)). We choose the specific value of $\lambda_{1,\text{plane-}i}$ for which the back-transformed plane in compensation voltage space comes closest to the respective point of measured minimum correlation. The three planes subsequently intersect in one point which is the optimal compensation point for the external disturbance. In the following, we refer to the three planes as plane 1/2/3 for beam 1/2/3 respectively.

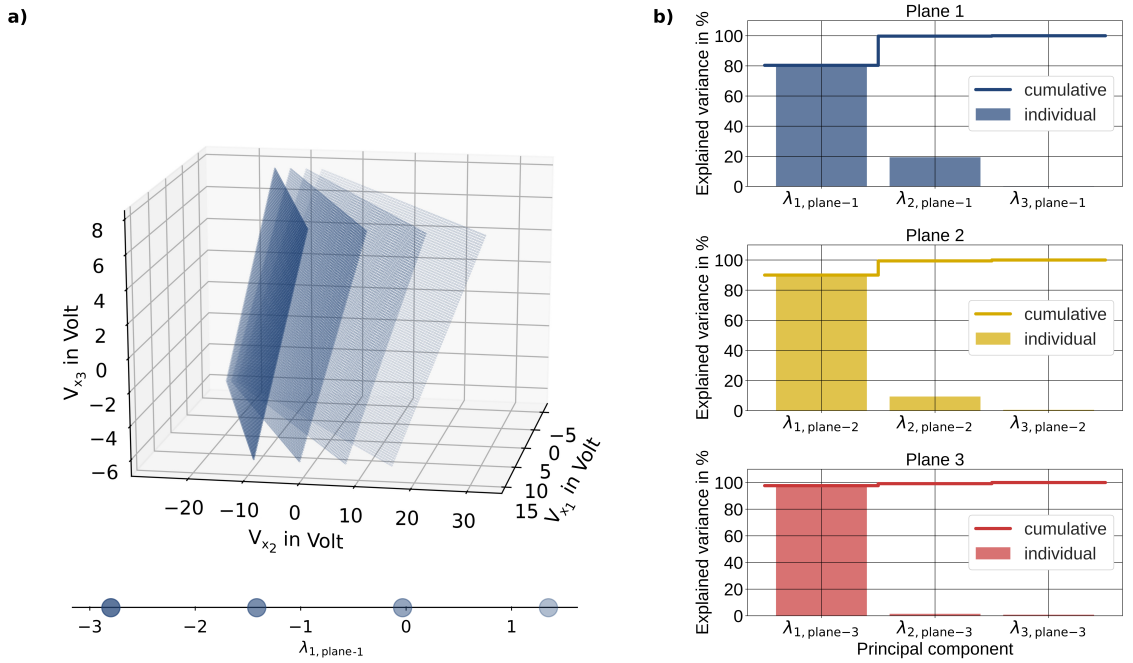

Figure 4.8: a) Variation of the plane orientation for beam 1 (also referred to as plane 1) in compensation voltage space for different values of the first principal component $\lambda_{1,\text{plane-1}}$ of this plane in PCA eigenvalue space. **b)** Cumulative and individual explained variance of the training dataset by the principal components of each plane respectively. Using just the first principal component $\lambda_{1,\text{plane-}i}$ of each plane $i = 1, 2, 3$ explains 89 % of the variance and reduces the plane model dimensionality by a factor of 3.

This method allows for a prediction of a full compensation using one data point per beam (i.e. $a_{\text{PCA}} \cdot n = 1$). Remarkably, this is below the minimal requirement of measurements for the mathematical definition of a plane. With the self-learned correlations, which previously were not covered by our data model, we are able to predict the correct compensation point with an accuracy of $\sigma = 42\,\text{V/m}$. The PCA-enhanced plane model reduces the number of measurements required by one order of magnitude, from 24 to 3, with even improved values of σ. This advantage originates in the PCA method's capability of revealing possible correlations between the plane parameters without knowing the final optimal compensation point. Using the first principal component $\lambda_{1,\text{plane-}i}$ of each plane $i = 1, 2, 3$ explains 89 % of the total data variance which shows that recurrent charge distribution originating from any specific element being charged induces correlations between a subset of parameters (see Figure 4.8 b)).

Interestingly, for this kind of machine learning algorithm, we are able to visualise what has been learned by the algorithm. For this purpose, we feed a cubic grid of equal spaced points in the combined PCA eigenspace of the first principal components for each plane $(\hat{e}_{\lambda_{1,\text{plane-1}}}, \hat{e}_{\lambda_{1,\text{plane-2}}}, \hat{e}_{\lambda_{1,\text{plane-3}}})$ into equation (4.10) and visualise the resulting intersection points of the three planes in compensation voltage space (see Figure 4.9 a)). Using this technique, we can visualise that the PCA-enhanced plane model identified the axis of the fibre cavity as the main charging direction, which we also would expect from the large amount of dielectric material being close to the trap. This finding is in agreement with previous observations confirming the sensibility of trapped ions to dielectric surfaces [65]. The PCA-enhanced model has learned these hidden information about the direction of charging from the bare plane model and we can use it to reduce the amount of needed measurements for a compensation of the resulting stray electric field.

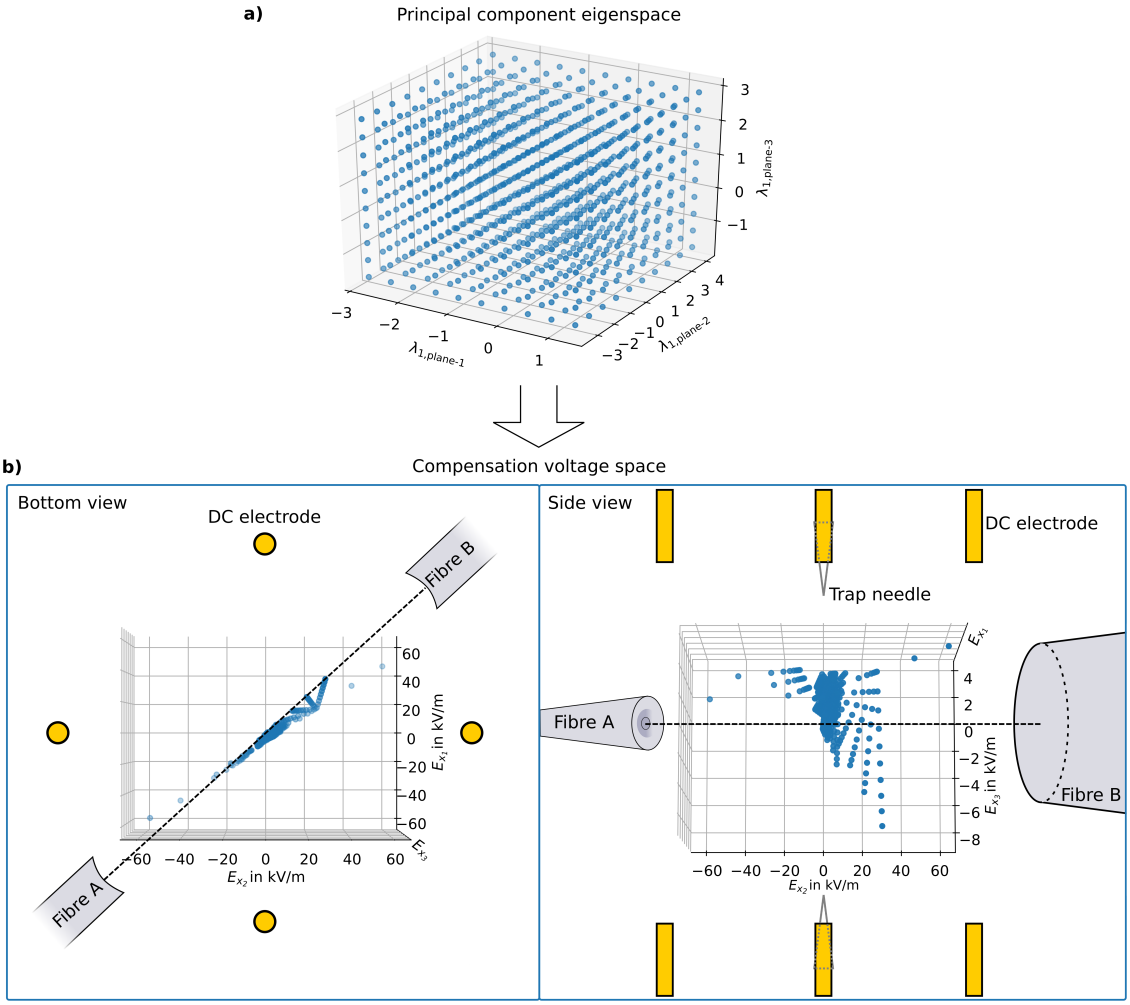

Figure 4.9: a) Cubic grid of equal spaced points within the eigenspace spanned by the three first principal components $\hat{e}_{\lambda_{1,\text{plane-}i}}$ of each plane $i \in \{1, 2, 3\}$ respectively. The size of the cube in terms of values $\lambda_{1,\text{plane-}i}$ is chosen precisely to contain all variances of plane orientation included in the training dataset. **b)** The cubic grid in a) transforms to a set of predictions for stray field cancellation in the compensation voltage space (blue dots) as described by equation (4.10). Using the geometry of electrodes, we visualise the direction of the resulting compensating electric field in real space. The dashed black line depicts the axis of the fibre cavity.

Since the sources of disturbing noise are hard to locate and/or to simulate in general, we expect that most (heuristic) models used for state-of-the-art compensation do not cover the origin of disturbance but only its compensation which leaves important information unused. We have demonstrated that unsupervised machine learning can reveal information about the physical origin of these external disturbances. In the following subsection, we present another method providing access to the hidden information, but this time even without having any (heuristic) model by the hand: a supervised learning neural network.

4.2.2 Supervised machine learning using an artificial neural network

Inspired by the human brain, the simulation of neural events using an electronic circuit was first realised in 1943 by W.S. McCulloch and W. Pitts [113]. With increasing computational power, the idea of machine learning through brain inspired networks got a boost in recent years for various fields including physics and also quantum information.

The term 'learning' means to adjust weights w of the connections between the neurons of an input layer and the neurons of an output layer in order to produce a desired output on the neurons of the output layer. Networks in which each neuron i of one layer is connected to each neuron j of the following layer are called fully connected neural networks with weights w_{ij} (see Figure 4.10 a)). As the information proceeds from the input layer to the output layer, the network is called feed forward. We choose this kind of network because it has a comparably simple architecture that supports rapid implementation and adaption to a particular data representation.

The training effort depends on the size of the neural network (NN) and the number of parameters to be optimised. The network used here includes a hidden layer with a size of 16 neurons and an output layer with a size of 3 neurons representing the 3 spatial components of the compensation point (see Figure 4.10 a)). For the input layer, we compare two different sizes, namely 9 neurons representing three points $\vec{V}_{m,i}$ in parameter space (one point per beam) and 4 neurons representing one point in parameter space and the identification of the beam X along which the ions's motion was minimised $X \in \{1, 2, 3\}$. We make use of the rectifier linear unit (ReLU) as activation function for each neuron, since it was shown in [61] that purely supervised training of a deep neural network using this activation function is efficient in terms of computational power and learning success.

In contrast to the self-learning PCA algorithm presented in subsection 4.2.1, we have to provide 'correct' labels for the training of the NN. We use the same training dataset as for the unsupervised learning and label the data with the corresponding experimentally measured compensation point as the 'correct' output of the NN. For each training epoch, we randomise the data and split it into batches containing 12(64) data points for the 9(4) neuron input network.

For the purpose of training, the batches are fed to the input layer of the NN and subsequently the Euclidean distance between the prediction on the output layer and the provided 'correct' compensation point is computed. This error is then fed backwards through the network which is called back-propagation [147] (see Figure 4.10 b)). The weights w_{ij} are adjusted for each data batch using gradient descent parameter update through adaptive moment estimation (ADAM) [86]. Over-fitting of the NN occurs as soon as the network starts to learn specific features of the training dataset to assign a correct

result. At this point, the prediction error on an unknown dataset starts to increase, as the network prediction loses generality (see Figure 4.10 c)). The optimal stopping point for training of the NN is reached when the prediction accuracies on the unknown dataset and the training dataset become equal.

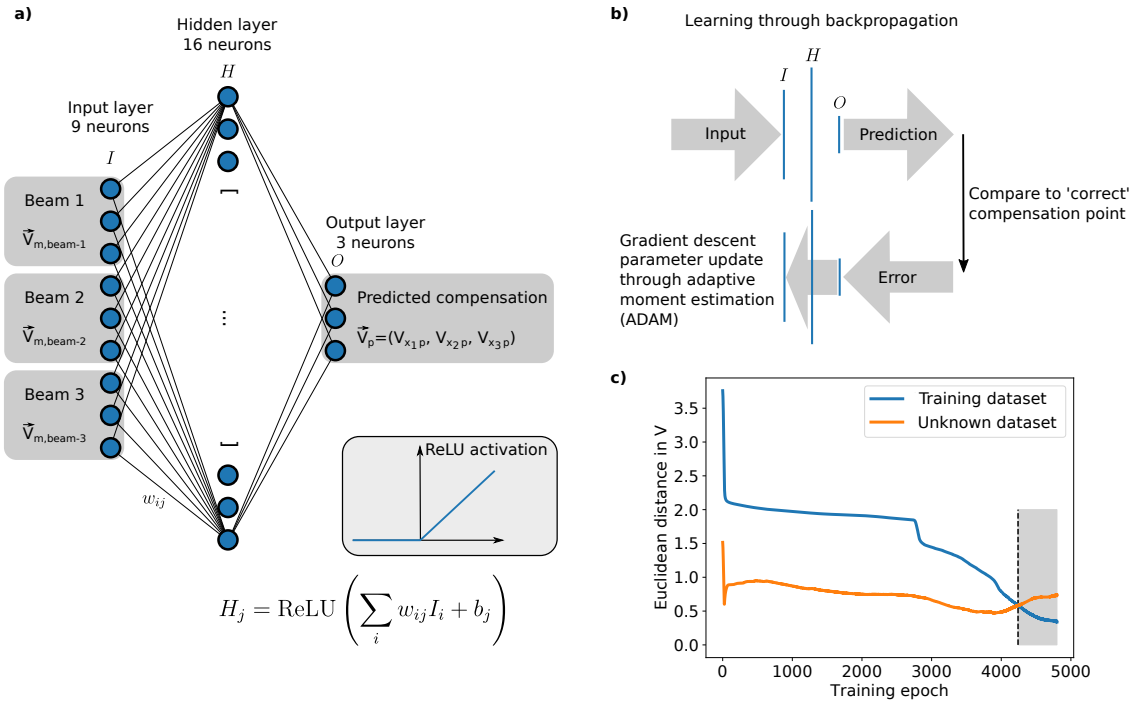

Figure 4.10: a) Sketch of a neural network architecture having 9 input neurons. The network takes three points of minimal ion motion measured along each of the three beam axes as an input (I). The layers are fully connected and neurons are activated using the rectifier linear unit (ReLU) function (inset). As an output (O), the neural networks predicts a three-dimensional set of voltages for the DC electrodes to fully compensate the external stray electric field. **b)** Supervised training scheme of the neural network. The deviation from the 'correct' point is feed back through the network and the internal parameters are updated using adaptive moment estimation based gradient descent optimisation (ADAM GD). **c)** The Euclidean distance of the predicted compensation point to the 'correct' point is shown for a full training on the training dataset (blue curve) and an unknown dataset (orange curve). At $\sim$ 4200 epochs the training reaches its optimum, since afterwards an over-fitting of the network can be observed (grey shaded area).

Due to its architecture, already the comparably small amount of data is sufficient to train the network, such that the compensation point can be predicted on an unknown dataset with $\sigma_{\mathrm{ANN},9} = 34\,\mathrm{V/m}$ for an input layer of 9 neurons. The unknown dataset is the same one we used for benchmarking gradient descent optimisation (subsection 4.1.2) and PCA (subsection 4.2.1).

As long as the environmental conditions do not change, we can react on a real-time scale to a varying stray electric field, since the NN has learned the diversity of charging distributions on a certain setup geometry. Upon a change of beam angles, measurements method or trap geometry, we have to invest again in acquiring a training dataset, which then is not real-time. We expect the same behaviour on other experiments dealing for example with magnetisation, heating, charging or similar disturbances.

In the case of a 4-neuron input network, the accuracy drops by about 30 % and shows that the provided information of one data point is not sufficient to create a model as precise as for a 9-neuron input. However, in cases where lower accuracy is acceptable an additional factor of 3 can be gained in the number of measurements required. The use of two hidden layers (each 16 neurons) for the neural networks brought no further improvement.

4.3 Summary

In Figure 4.11 we compare the presented algorithms for determining a three-dimensional compensation for an external stray electric field via measurements of the motion of an ion in a Paul trap. The unbiased systematic sampling of applied compensation voltages shows the slowest convergence as a function of the number of measurements, reaching a compensation uncertainty of 60 V/m only after 1,000 measurements. For comparison, the model using the intersecting planes reaches a comparable accuracy already after 24 measurements. Even though this gain is quite impressive, the machine learning algorithms achieved a further reduction in measurements of one order of magnitude.

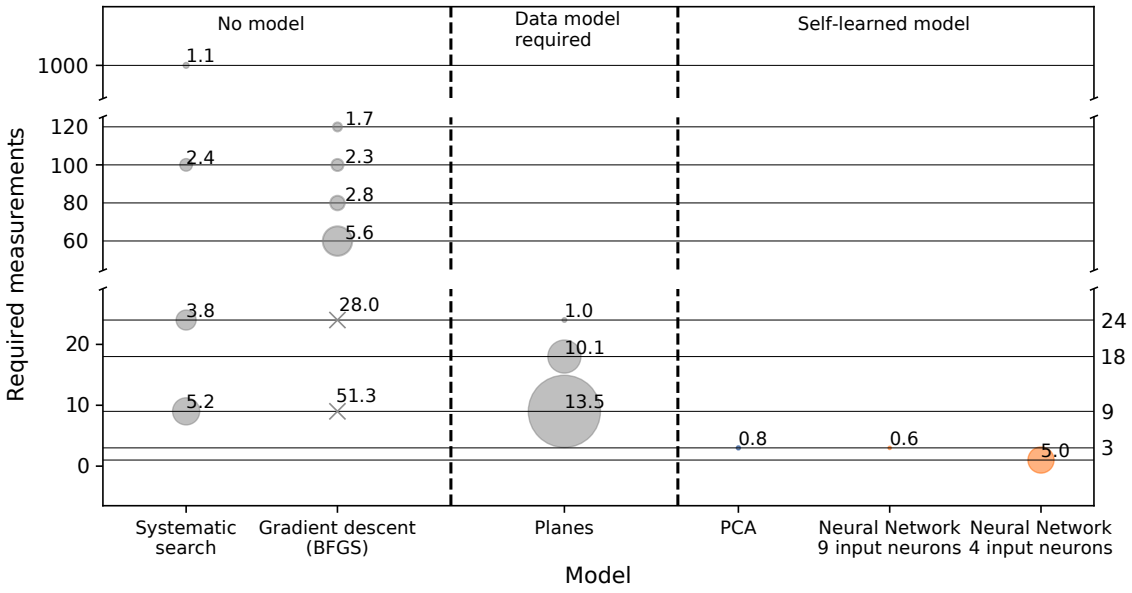

Figure 4.11: Comparison of the performance of the different compensation methods. The vertical axis depicts the number of required measuring points. The diameter of the circles denotes the standard deviation of the spread σ of the method's predicted compensation electric fields normalised to the measurement accuracy of $\sigma_{\text{meas}} = (54 \pm 3)\,\text{V/m}$. The normalised standard deviation $\sigma/\sigma_{\text{meas}}$ is annotated to the corresponding circle. For points where the size of the circle is too large for the diagram, the circle is replaced by a grey 'X'. For reference, over three months of operation the spread of measured compensation points amounts to 600 V/m ($\sigma/\sigma_{\text{meas}} \approx 11$) which reflects the changing environmental conditions in the apparatus. The data has been partially published also in [93].

The neural network (9-neuron input) compares to the PCA-enhanced plane model in accuracy and amount of needed data (training data and data points needed for a prediction). However, the big advantage of the neural network is that it does not take any model such as the plane model into account and is therefore applicable even in cases where no specific (heuristic) model is known. This makes the network comparable in terms of usability with general approaches such as GDO and systematic search. In terms of required measurements, however, the NN performs superior (see Figure 4.11).

Furthermore, the reduction to only one data point in case of the 4-neuron NN leads to a significant simplification of the measurement process. In this case, we achieve a remarkable reduction of $a_{\mathrm{ANN},4} \cdot n \cdot k = 1$ which means that our system requires a smaller number of data points than the dimension k of the problem. This is comparable to a perfect k-dimensional mathematical model where just one unique point is enough to complete the whole model and derive the compensation point from, except for the fact that with the ANN we only have access to this single compensation point instead of the whole point-space.

We have demonstrated the presented machine learning approach on a generic optimisation problem and expect that the methodology is widely applicable to a broad range of experimental settings. We found that the accuracy is solely limited by the quality of the data provided to the machine learning algorithms.

Using the presented methodology to optimise the position of the ion in the Paul trap makes it possible to increase the stability of trapping with a greatly reduced amount of required data. This allows the ion trapping time to be extended to up to 60 minutes, compared to 1–10 minutes for a non–ideal localisation of the ion. On the one hand, this achievement supports data collection on this particular setup, as more time is available for measurements. On the other hand, the availability of the ion enables the implementation of scalable applications such as multipartite entanglement or long-range communication.

5 A fibre Fabry-Pérot cavity as a light-matter interface

Contents

5.1 Fabry-Pérot resonator 50
5.2 Development and assembly of the fibre Fabry-Pérot cavity . . 53
5.3 Cavity lock and stability 58
5.4 Light-matter interaction 65
5.5 Photons as travelling qubits 75
5.6 Summary 86

The communication between different quantum nodes is central to many branches of quantum technology, such as quantum computation [84] and secure communication [182, 155]. Quantum network nodes consist of an interface between a stationary qubit (usually matter) and a travelling qubit (usually light). The development of effective light-matter interfaces operating at the quantum limit and providing control of the quantum states of both the travelling qubit and the stationary qubit is of great importance. For the use of cavities as interfaces, the light-matter coupling strength g is an essential property and requires the development of cavities that have small mode volumes. So far, for the usage of entangled ions as quantum network nodes together with cavities as light-matter interfaces [164, 99], the coupling strength g was increased by near-concentric optical resonator configurations that minimised the mode waist of the resonators [142] but maintained a sufficient distance between the mirrors and the ion in order to mitigate charging effects and to stabilise the trapping. As a compromise between trap stability and light-matter coupling strength, these experiments used cavities with a minimum length of $\approx 19\,\mathrm{mm}$ [162, 99] reaching mode waists of $\omega_0 > 12\,\mu\mathrm{m}$. In contrast, micromachined fibre-based cavities require only a small amount of dielectric material and offer a way to place the mirrors extremely close to the ion ($\sim 150\,\mu\mathrm{m}$), with mode waists of $\omega_0 \approx 3\,\mu\mathrm{m}$ [6].

In the context of this thesis, we demonstrated the usage of a fibre cavity as a light–matter interface for the realisation of a quantum network node. The fibre cavity is a key element and allows us to collect the light emitted by the trapped ion with a high efficiency and with a fast extraction of the collected photons, both of which are prerequisites for the realisation of quantum networks with high bandwidth in terms of data transmission rate. In addition, photons leaving or entering the fibre cavity exhibit a defined spatial mode due to the optical single-mode fibre. For application in quantum networks, the inherent fibre coupling of the photons enables efficient distribution to other elements of the network. For this reason and due to their small mode volumes, fibre cavities are considered to be a promising route for quantum communication [127].

This chapter provides a detailed discussion of the fibre cavity as a light-matter interface. We constructed the cavity from two concave, highly reflective mirrors realised on the end facets of two optical fibres. The fibres are facing each other and together form a Fabry-Pérot resonator with a length of $l \approx 260\,\mu\mathrm{m}$ (see Figure 5.1 and section 5.1). We choose a symmetric confocal resonator design because this type of resonator has the lowest loss by diffraction at the resonator mirrors and the highest robustness to alignment errors [142]. Further details of the fibre resonator design are discussed in sections 5.2 and 5.3.

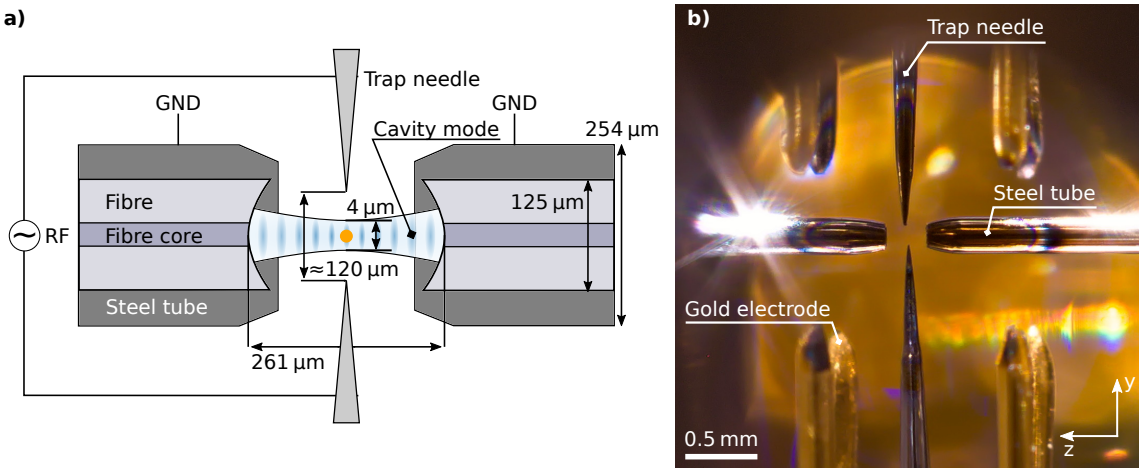

Figure 5.1: a) Sketch of the light-matter interface. The trapped ion (yellow dot) is embedded into the fibre Fabry-Pérot cavity. The fibres are located within steel tubes which are electrically grounded. Distances are not to scale. **b)** Fibre cavity and Paul trap combined within the vacuum chamber.

We use the fibre cavity resonant to the principal UV transition of Yb^+ to efficiently collect photons emitted from the ion. The coupling of the ion to the cavity mode takes place via the atomic dipole moment at 370 nm. For a similar configuration, we have recently achieved the highest reported coupling strength to date of $g \approx 2\pi \cdot 67(1)$ MHz between a single ion and a single mode of a radiation field by more than one order of magnitude [7]. Based on the theoretical description of the light-matter interaction in section 5.4, we quantify the performance of the presented fibre cavity in the experiment in section 5.5. In this last section of the chapter, we also introduce the photon as a travelling qubit.

5.1 Fabry-Pérot resonator

5.1.1 Longitudinal mode

An optical resonator is formed by two opposing and partially reflecting mirrors at a distance l. In a simplified picture, due to the boundary conditions of the mirrors on the electric field, the formation of a standing light wave inside the resonator can only occur if the length of the resonator is an integer multiple of half the wavelength $\lambda/2$ of the standing light wave. This leads to the relation

$$l = n \cdot \frac{\lambda}{2} = \frac{nc}{2\nu}, \; n \in \mathbb{N}. \tag{5.1}$$

As a consequence, light with frequency ν can be coupled into the resonator for different lengths l which differ by $\lambda/2$. For a given l, the distance between two neighbouring longitudinal modes $(n, n \pm 1)$ in terms of frequency is defined as the free spectral range (FSR) of the cavity

$$\Delta\nu_{\text{fsr}} = c/2l. \tag{5.2}$$

An intuitive picture for the free spectral range is the round trip time for a photon in the resonator which is given by $\tau_{\text{round}} = 2l/c = 1/\Delta\nu_{\text{fsr}}$. Considering coherence properties

of the electric field results in interference for multiple round-trips of the light within the resonator. The power transmission of a cavity is then given as [149]

$$\mathcal{T}(\nu) = \mathcal{T}_{\max} \cdot \frac{1}{1 + 4\mathcal{F}^2/\pi^2 \cdot \sin^2\left(\pi\nu/\Delta\nu_{\text{fsr}}\right)}, \tag{5.3}$$

where the Finesse of the resonator

$$\mathcal{F} = \frac{\pi \sqrt[4]{\mathcal{R}_1\mathcal{R}_2}}{1 - \sqrt{\mathcal{R}_1\mathcal{R}_2}} \tag{5.4}$$

is determined by the reflectivity of the two mirrors $\mathcal{R}_{1,2}$. From the frequency response according to equation (5.3) the full width at half maximum (FWHM) of the transmission peaks can be given as

$$\Delta\nu_{\text{fwhm}} = \Delta\nu_{\text{fsr}}/\mathcal{F} \tag{5.5}$$

for $\mathcal{F} \gg 1$.

For a high reflective mirror, we expect a low transmission of light T for reasons of energy conservation

$$1 = T + \mathcal{R} + L, \tag{5.6}$$

where L is the loss of photons accounting for imperfections of the mirror. Two high reflective mirrors $\mathcal{F} \gg 1$ forming a resonator enhance the power of light between them as long as the power coupled into the resonator is equal to the transmitted power $\mathcal{T}(\nu)$. This is referred to as a pumped cavity. As soon as we switch off the pumping of the cavity (instantaneously), the light field within the resonator decays due to the leakage of photons through the mirrors. We can express this decay in terms of the light intensity $I(t)$ stored in the resonator as

$$\dot{I(t)} = -(T_1 + T_2) \cdot \frac{c}{2l} I(t), \tag{5.7}$$

where the transmission of each mirror is multiplied by the rate at which the photons impinging on the mirror. The solution of the differential equation (5.7) is given by

$$I(t) = I_0 \cdot e^{-t/\tau_{\text{cavity}}} \qquad \text{with} \qquad \tau_{\text{cavity}} = \frac{1}{(T_1 + T_2) \cdot \frac{c}{2l}}. \tag{5.8}$$

Using the electric field decay rate κ, the decay constant τ_{cavity} can be further expressed as

$$\tau_{\text{cavity}} = \frac{1}{2\pi \cdot \Delta\nu_{\text{fwhm}}} = \frac{1}{2\kappa}, \tag{5.9}$$

which is more practicable if the linewidth of the cavity is known. The decay rate of the electric field in the cavity κ sets the timescale for the resonator dynamics. Processes that happen much faster with $\Delta t \ll \tau_{\text{cavity}}$ can be seen as 'instantaneous'.

5.1.2 Transverse mode

Due to the high number of photon round trips in the cavity, the shape of the mirrors is important in order to find a region of stability where the photons are confined within the cavity. For this purpose, it is feasible to have concave and spherical mirror structures on

the fibre tips. The stability condition for the formation of a standing wave within the resonator is given by [94]

$$0 < \left(1 - \frac{l}{R_1}\right)\left(1 - \frac{l}{R_2}\right) < 1, \tag{5.10}$$

with the radii of curvature of the mirrors denoted with R_i for the two mirrors $i = 1, 2$. The radius of curvature of the mode wavefront inside the cavity must match the curvature R_i of the mirror i at its position. The lowest transverse electromagnetic (TEM) mode of the cavity (TEM_{00}) follows a Gaussian radial intensity profile. From the matching condition of wavefront and mirror curvature, the $1/e^2$-intensity radius of the TEM_{00} mode at its smallest size can be calculated as [94]

$$\omega_0^2 = \frac{\lambda}{\pi} \cdot \sqrt{\frac{l \cdot (R_1 - l)(R_2 - l)(R_1 + R_2 - l)}{(R_1 + R_2 - 2l)^2}} \tag{5.11}$$

For a symmetric cavity ($R_1 = R_2 = R$), the smallest mode waist $\omega_0^2 = \lambda/(2\pi) \cdot \sqrt{l(2R - l)}$ is located at half the distance between the mirrors (see Figure 5.2 a)). We define this point as $z = 0$ and find the mirrors at positions $z = \pm\, l/2$. The mode waist at the point of the mirrors can be calculated as

$$\omega_c = \omega(z = \pm\, l/2) = \omega_0 \cdot \sqrt{1 + \left(\frac{l/2}{z_R}\right)^2}, \tag{5.12}$$

using $\omega(z) = \omega_0 \cdot \sqrt{1 + \left(\frac{z}{z_R}\right)^2}$ with the Rayleigh range of the cavity mode $z_R = \pi\omega_0^2/\lambda$. If the radius of curvature R is large compared to w_c, the overlap ϵ_m between the resonator mode and the mode of the fibre ω_f can be approximated by [69]

$$\epsilon_m \approx \left(\frac{2\omega_f \omega_c}{\omega_f^2 + \omega_c^2}\right)^2, \tag{5.13}$$

which is also known as mode matching of the cavity (see Figure 5.2 b)).

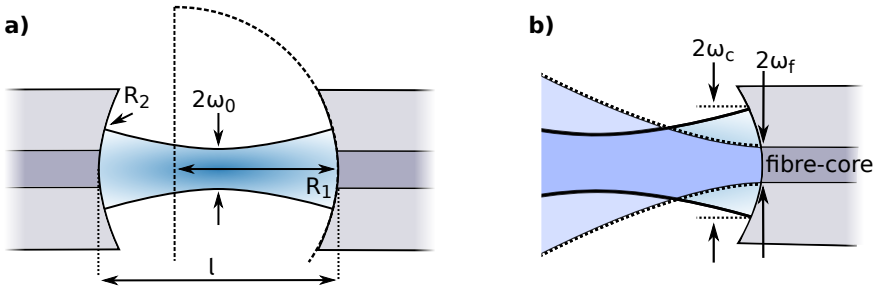

Figure 5.2: a) The concave mirrors are located on top of a fibre tip and form a resonator with length l. For symmetric radii of curvature $R_1 = R_2$ the smallest TEM_{00} mode waist ω_0 is located at the mid point between the mirrors. **b)** Due to different mode waists ω_c and ω_f the in-/out-coupling of light is reduced by a mode matching factor ϵ_m (eq. (5.13)).

The mode volume V_m of a resonator becomes particularly important for the coupling between the light mode and a two-level system located in the resonator (see section 5.4).

The mode volume can be calculated as [98]

$$V_m = \frac{\int_{\mathcal{V}} \epsilon(\vec{r})\vec{E}^2(\vec{r})\, d\vec{r}}{\max\left[\epsilon(\vec{r})\vec{E}^2(\vec{r})\right]}, \tag{5.14}$$

where the integration is performed over the quantisation volume $\mathcal{V}$ and we have assumed optimal coupling of the two-level system to the resonator mode. Assuming a constant permittivity of the resonator, i.e. $\epsilon(\vec{r}) = \text{const}$, the mode volume V_m of the TEM_{00} mode in a symmetric resonator (mirrors at $z = \pm l/2$) can be obtained by integrating

$$f(\rho, z) = \left(\frac{\omega_0}{\omega(z)}\right)^2 \exp\left(-\frac{2\rho^2}{\omega^2(z)}\right) \tag{5.15}$$

along the cavity axis z and the radial direction ρ using a volume integral in cylindrical coordinates as

$$V_m = \int_{-l/2}^{l/2} \int_0^{2\pi} \int_0^{\infty} f(\rho, z) \cdot \rho \cdot \, d\rho \, d\phi \, dz = \frac{\pi}{2} \cdot l \cdot \omega_0^2. \tag{5.16}$$

5.2 Development and assembly of the fibre Fabry-Pérot cavity

In this section we present the details of the fibre resonator assembly. We chose the parameters of the cavity (e.g. mirror coatings) to fit our application of the cavity as a light-matter interface and to provide a high collection efficiency of photons together with a fast extraction from the cavity (see subsection 5.4.4). The final cavity was assembled in context of a master's thesis [29].

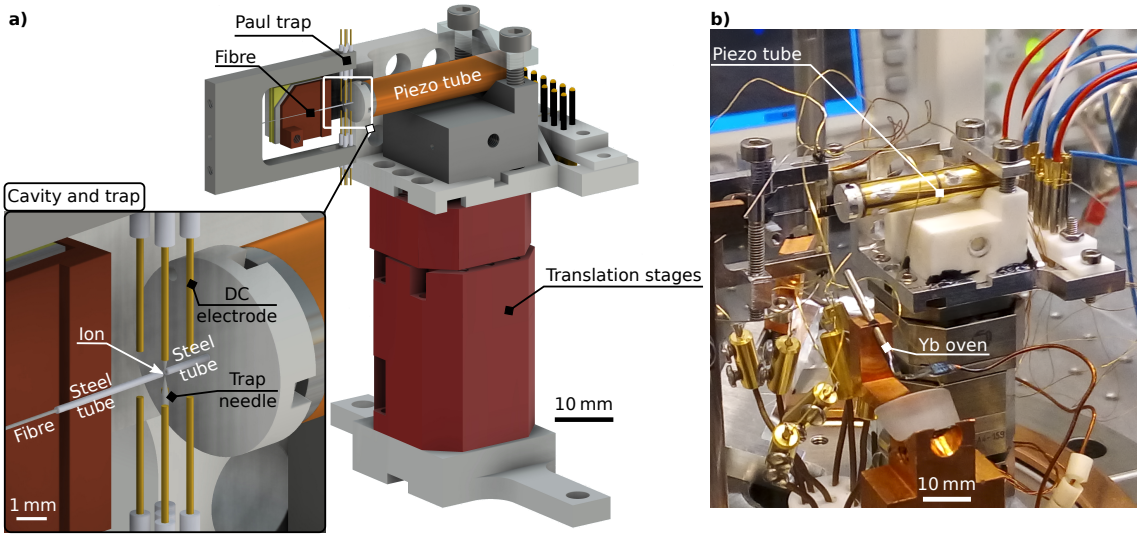

Figure 5.3: a) 3D CAD model of the cavity-trap setup including contributions from M. Steiner, H.M. Meyer, M. Link and M. Breyer. For the purpose of electric field shielding or application of custom voltages, the fibres are inserted into electrically connected steel tubes for the last millimetres. **b)** The final assembled cavity-trap setup prior to insertion into the vacuum chamber. Photo by H.M. Meyer.

In general, due to the small structures involved, building a stable fibre cavity is a challenging task which requires positional alignment and stability of the components in the range of a few micrometres. Therefore, the design of the presented fibre cavity was developed in several iterations steps [104, 90, 29]. A 3D CAD model[32] and a picture of the full assembly are shown in Figure 5.3.

The fibre Fabry-Pérot cavity itself composes of two optical single-mode fibres, each having a concave mirror structure on its front facet. The usage of single-mode fibres guarantees the coupling of photons into and out of the cavity in a single spatial mode. We select the fibre tips from a pool of fibres on which we machined concave structures using a pulsed CO_2 laser [90] and applied a custom reflective coating[33]. The selected fibres have approximately the same radii of curvature with an average of $R = (280 \pm 36)\,\mu$m to form a symmetric confocal cavity[34]. We chose this type of cavity because it has the highest robustness to mirror misalignment, which is particularly advantageous for fibre cavities. For stability reasons, the distance between the mirrors should be slightly smaller than the radius of curvature of the mirrors [142]. We built the cavity at a mirror separation of $l \sim 260\,\mu$m. The fibres were inserted into steel tubes[35], each of which allows an electrical potential to be applied. Therefore, we can use the tubes as additional DC electrodes that support the compensation of a potential stray electric field along the cavity axis (see Figure 4.9) or enable a deeper trapping potential by applying DC offset voltages [6]. For reasons of stray electric field shielding, however, we keep them electrically grounded for the measurements presented.

During the fabrication of the fibres, we found that concave structures that are of good quality over large areas can be achieved on the tips of photonic crystal fibres[36] (PCF). The usable area of the structure is important for building long fibre cavities in order to avoid mode clipping or similar losses on the edges of the fibre mirror. In addition, due to the larger mode diameter of the light within the PCF, we would expect a mode matching efficiency with the cavity mode of $\epsilon_m \sim 0.74$ according to equation (5.13). Therefore, we built the cavity using a PCF and a conventional single-mode fibre[37] (see Figure 5.4). Unfortunately, the PCF broke during the final assembly of the cavity, preventing us from exploring the possibilities of PCFs in a fibre-based light-matter interface.

[32] We use Inventor from Autodesk for the 3D model
[33] Coated by Laseroptik
[34] $R_1 = (255 \pm 17)\,\mu$m and $R_2 = (304 \pm 34)\,\mu$m according to the analysis in Figure 5.4
[35] 5 mm × 254 μm × 127 μm (length × outer Ø × inner Ø) from VitaNeedles
[36] LMA-8 from NKT-Photonics
[37] S405-XP from Thorlabs

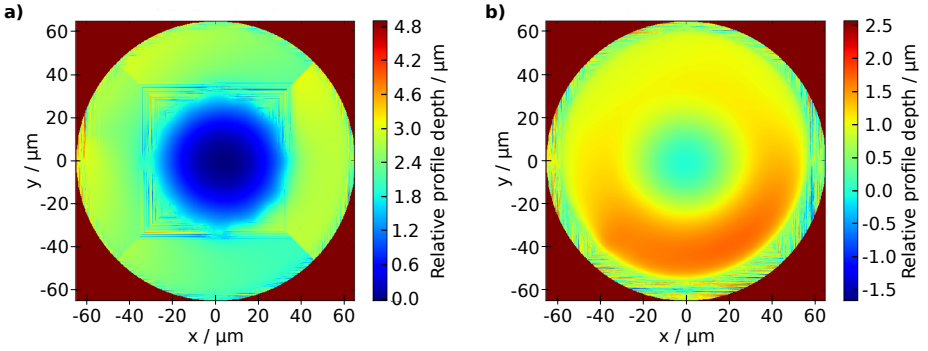

Figure 5.4: Surface profile of the structure machined on the tips of the individual fibres using a CO_2 laser pulse. The profile is obtained from a phase-shifting interferometry. **a)** PCF LMA-8. **b)** Conventional single-mode fibre S405-XP. The analysis has been performed with the tools presented in [131].

The cavity exhibits an asymmetric mirror coating with transmissions of $T_1 = 500\,\text{ppm}$ and $T_2 = 100\,\text{ppm}$, respectively. From the measured finesse of $\mathcal{F} = 4700 \pm 700$ [29] we estimate the losses of the mirror coatings to be $L = (350 \pm 100)\,\text{ppm}$ (see equation (5.4)), in agreement with the manufacturer's expectation. The round trip losses of the cavity correspond to a cavity linewidth of $\kappa = 2\pi \cdot (58 \pm 9)\,\text{MHz}$ (see Figure 5.5). This leads to a decay time of the mode intensity of

$$\tau_{\text{cavity}} = \frac{1}{2\kappa} = 1.4(1)\,\text{ns}. \tag{5.17}$$

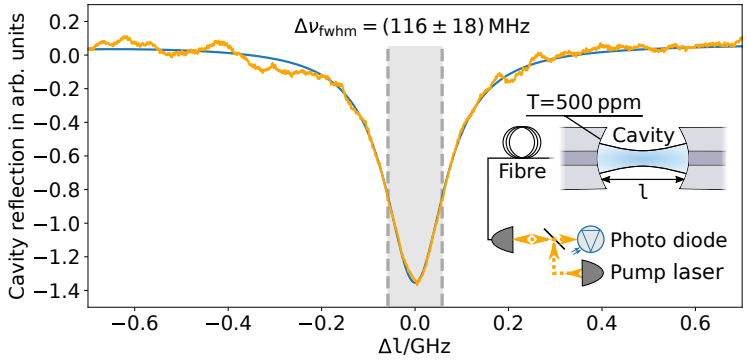

Figure 5.5: Reflection signal from the pumped fibre cavity while scanning the cavity length l (yellow curve). The pump light has a narrow bandwidth $\ll \kappa$. We fit a Lorentzian profile to the data (blue curve).

The asymmetric reflection coating of the fibre mirrors results in a directional extraction probability of photons through the conventional single-mode fibre. The probability of a photon to be extracted through the desired low-reflectivity cavity mirror is

$$\eta_{\text{ext}} = \frac{T_2}{T_1 + T_2 + L_{1+2}} = 0.53(6). \tag{5.18}$$

The mode matching efficiency between the conventional single-mode optical fibre and the TEM_{00} mode of the cavity can be computed according to equation (5.13) as [29]

$$\epsilon_m = 0.44(3). \tag{5.19}$$

The setup has been developed to solve a number of known problems with previous fibre cavities, which occurred particularly in the UV range: i) strong charging of the dielectric surfaces, ii) increasing cavity losses due to degrading mirror coatings, iii) the need for relative positional alignment of the two fibre tips after the final assembly, iv) heating of the fibre cavity assembly when exposed to microwave radiation and v) general stability and lock-ability of the cavity (see section 5.3.3). We discuss the points i)-v) in the following.

i) Charging of the dielectric surfaces

From previous experiments with fibre cavities in the UV spectral regime [7] we know that charging of the dielectric mirror surfaces can lead to serious problems with regard to trap stability. There, we explored the regime of small mode-volumes in the UV regime with a cavity length of 150 μm and decided to aim for a larger cavity length in the future. For this reason, the fibre cavity used in this work is slightly longer with $l \sim 260\,\mu$m. In order to minimise the amount of dielectric material next to the trap, we electrically ground the steel tubes in which the fibres were inserted.

ii) Mirror degrading

Due to the small size of the structures machined on the fibre tips, their sensitivity in terms of relative alignment is a few micrometres. Up to know, we found the best way of building fibre cavities is gluing of at least one fibre using long curing glue with a low deformation. Any mechanical approach of fixing the fibres has so far caused a greater misalignment of the fibres than an alignment device with sufficient stability could compensate for (e.g. solid piezo actuators). The drawback of the gluing method is the evaporation of hydrocarbons or other organic compounds next to the cavity, which was found to be the reason for a degrading cavity finesse over time [150]. Degradation of the mirrors has been reported in several cavity based experiments [28, 55, 7] even despite a protective SiO_2 layer on the mirrors [7]. In [150], a fully mechanical macroscopic cavity design solved the degrading issue even in the UV spectral range. For the fibre cavity used in this thesis, a minimal glue approach was successful concerning the stability of the cavity finesse. During $\sim$ 6 months of investigation, we did not observe a degradation of the mirror coatings (see Figure 5.6).

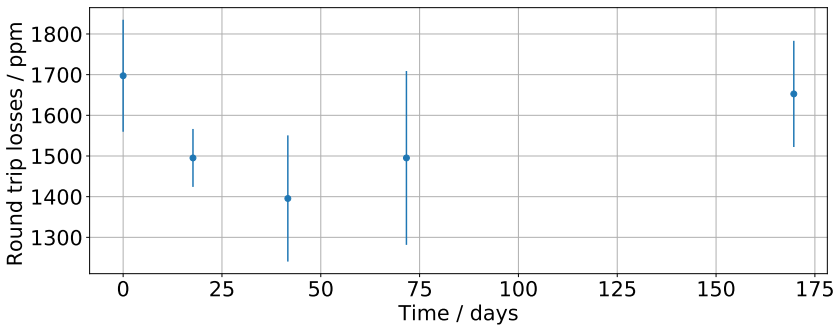

Figure 5.6: a) Investigation of the fibre cavity finesse for $\sim$ 6 months of operation. The measured round trip losses $T + L = 1 - \mathcal{R}$ according to equation (5.4) are shown. Measurements were performed by M. Breyer. The standard deviations are given as error bars.

iii) Positional alignment

The ability to move the fibres relative to each other is particularly important for length adjustment of the resonator along its axis (see section 5.3). Also in radial direction, the relative alignment of the fibres becomes important when considering processes which might misplace the fibres from optimal relative alignment like water evaporation of drying glue or heating processes during the vacuum chamber bake out. For this purpose, a piezo tube[38] with a maximal radial displacement of $\pm 16\,\mu$m (at $\pm 250\,$V on opposite electrodes) carries one of the two fibres. Axial displacement is provided by a stack of two shear piezo actuators (CSAP03 from Noliac), each of which allows a maximum travel range of $1.5\,\mu$m (between $\pm 320\,$V, according to the manufacturer). An overview of the relative alignment capabilities of the fibres is shown in Figure 5.7 a). We place electrically grounded metal shields between the piezo actuators and the ion in order to shield the ion from the electric fields.

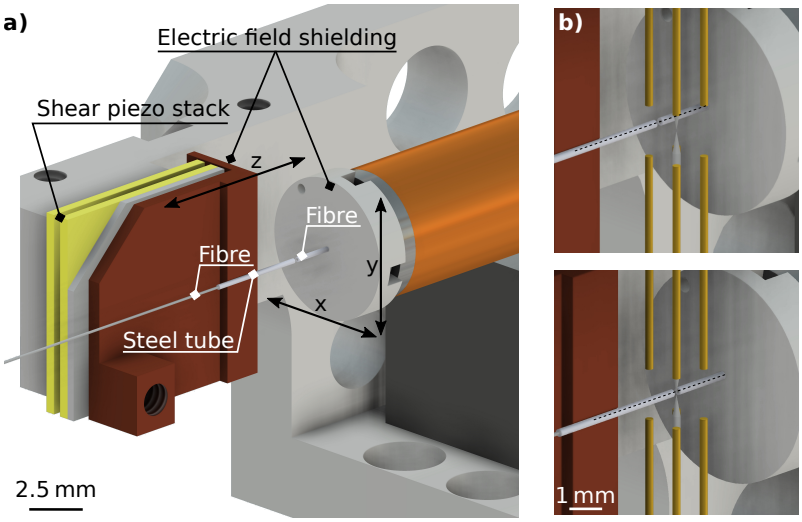

Figure 5.7: a) Relative alignment of the two fibres. The distance between the fibres is controlled by a stack of shear piezo actuators (z-axis). The piezo tube controls the orthogonal axes. **b)** We are able to move the cavity to optimise the ion position within the resonator mode.

The whole cavity can be moved along each spatial axis by using a set of positioning stages[39] (see Figure 5.3 a)). We use the stages to optimise the ion position within the resonator mode (Figure 5.7 b)), but we are also able to move the cavity away from the trap centre and even behind the DC gold electrodes. With the latter, the charge sensitivity of the trap setup is drastically reduced and this increases the stability of trapping. This is particular useful for bringing the setup into an operational mode for the first time or doing a coarse optimisation of the setup.

iv) Cavity-microwave compatibility

In earlier cavity setups containing large stacks of piezo actuators, we observed a strong heating of the setup even at small microwave radiation powers[40]. This made the

[38] PT230.14 from PI Ceramic GmbH
[39] Two ANPx101 and one ANPz101 from Attocube Systems AG
[40] microwaves are used for the ion qubit state manipulation

simultaneous use of fibre cavities and microwave radiation impossible. In the newer design, we have replaced the piezo stacks with the piezo tube for mechanical stability reasons with regard to the cavity length. However, we found that this also dramatically increased the tolerance of the assembly to microwave radiation.

5.3 Cavity lock and stability

In order to achieve a strong light-matter coupling and thus a high emission probability of photons by the ion into the resonator mode, the resonance frequency of the cavity ω_c must be stabilised via the length of the cavity to the atomic transition ω_a (see equations (5.51), (5.53) and (5.60)). For this purpose, the distance l between the mirrors has to be hold stable with a precision in the sub-wavelength regime ($\sim$ nm).

Using a Pound-Drever-Hall (PDH) lock [43], the cavity length can be stabilised to a reference laser which itself is stabilised to the atomic transition. For previous fibre cavity designs, strong mechanical resonances at $\sim 2\,\mathrm{kHz}$ [6] prevent any of such stabilisation attempts from being successful. Several iterations [90, 29] of the cavity design were necessary to eliminate strong mechanical resonances for the purpose of length stabilisation. Even for the presented setup, the mechanical stability is not optimal and reduces the effective coupling to the Yb ion (see subsection 5.3.3).

5.3.1 Locking scheme

For length stabilisation of the cavity, we derive the error signal from a reference laser coupled to the fibre cavity. We have to use the laser light reflected from the cavity, since we broke one fibre while assembling the setup. On the first attempt, we realise a PDH locking scheme using a current modulated reference laser at $8\,\mu\mathrm{W}$ power coupled to the fibre cavity. We were able to stabilise the length of the resonator using a PID-feedback based on a PDH error signal.

Unfortunately, in combination with a trapped ion we were facing problems with charging of the dielectric cavity mirror surfaces when light gets coupled into the resonator. This is always the case as soon as the cavity is (near) resonant to the reference laser. A charging of dielectric surfaces which are exposed to ultraviolet light has already been reported in [65] for 375 nm by M. Harlander et al. For 422 nm, however, they observed a drop in the charging beyond a measurable threshold. We observed charging of the cavity mirrors for reference laser light at 370 nm, 393 nm, 401 nm and 405 nm. Based on these findings, we decided to develop a different lock technique that works on a single photon level in order to reduce charging. To this end, we superimpose the TTL output pulses of two single photon counters[41] (SPCs) and perform a time integration of the pulses on a low-pass filter (integrator). The cut-off frequency of the low-pass filter is $f_{\mathrm{LP}} \approx 16\,\mathrm{kHz}$ and it outputs a continuous voltage signal which is proportional to the actual total count rate of both SPCs (see Figure 5.8). We chose the cut-off frequency to allow sufficiently fast feedback under changing resonance conditions. We use both SPCs for the derivation of the signal to be independent from the changing detection rates on the individual SPCs for changing polarisation properties of the optical path (see subsection 5.5.1).

[41] Of course, detecting the light using one SPC would work as well, but the polarisation-resolved detection of single photons requires two SPCs (subsection 5.5.1)

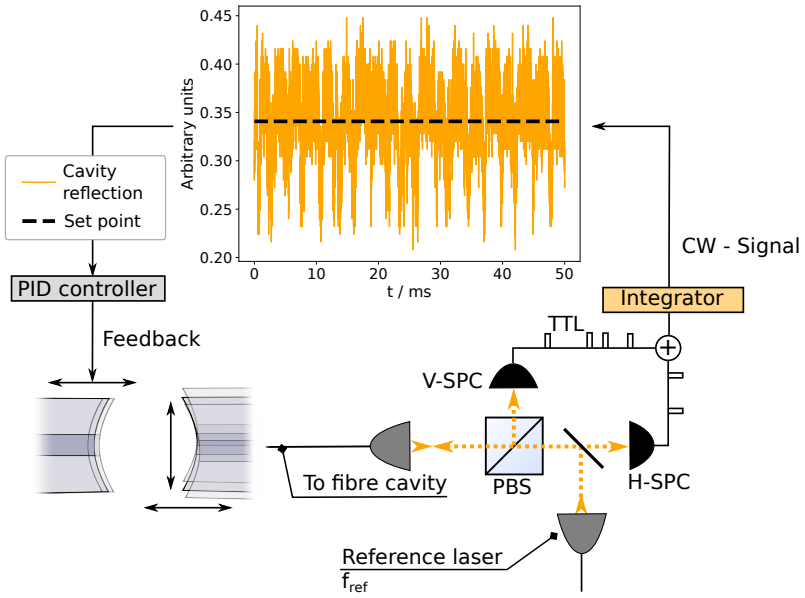

Figure 5.8: Important elements of the cavity length stabilisation setup. A low-pass filter acts as an integrator (cut-off $f_{\mathrm{LP}} \approx 16\,\mathrm{kHz}$). It converts a rate of TTL pulses (single photon detection events) to a continuous voltage signal. The variable cavity length causes the intensity of the reflected laser light to change due to the changing resonance condition. The continuous voltage signal serves as an input to the PID-controller which provides the feedback signal for the stack of shear piezo actuators. They control the position of one fibre along the cavity axis. For the second fibre, mechanical oscillations orthogonal and parallel to the cavity axis are sketched. A time snipped of the voltage signal obtained from the cavity reflection during length stabilisation is shown as orange line.

Scanning the cavity length at 80 Hz allows the resonance condition to be observed as a dip in the integrator signal when reference laser light is coupled into the resonator. We use a side-of-fringe locking to stabilise the cavity length to the side fringe of the cavity resonance dip using a PID controller with a regulation bandwidth of $\sim 20\,\mathrm{kHz}$. We conduct the lock at ultra-low light levels of less than 50 pW going to the fibre cavity, which mitigates the charging problem of the dielectric mirror surfaces exposed to ultraviolet light. Using this method, we do not observe the formation of additional stray fields originating from the cavity lock within the accuracy of our stray field measurement (see section 4.1).

For the detection of photons emitted by the ion into the cavity mode during an experimental sequence, we switch off the cavity pump for a maximum of $2\,\mu\mathrm{s}$ using an acousto-optic modulator (AOM) (see Figure 5.10 a)). This is much faster than the bandwidth of the PID-controller, but long enough to extract an emitted photon from the cavity and detect it on one of the SPCs (see subsection 5.5.2). A high suppression of the reference laser light of 10,000 : 1 is achieved for the 'on' to 'off' state of the AOM after 2.5 m optical path.

5.3.2 Reference laser calibration and measurement of the cavity length

For length stabilisation of the fibre cavity, we derive the error signal from a reference laser coupled to the resonator (see Figure 5.8). The reference laser with frequency $\omega_{\mathrm{ref}} = 2\pi \cdot f_{\mathrm{ref}}$ can be either resonant to the atomic transition ω_{decay} or detuned in terms of integer

multiple k of the free spectral range $\Delta\nu_{\mathrm{fsr}}$ of the fibre cavity (see equation (5.2)), which leads to the expression

$$\omega_{\mathrm{decay}} = \omega_{\mathrm{ref}} + k \cdot 2\pi \cdot \Delta\nu_{\mathrm{fsr}},\ k \in \mathbb{N}. \tag{5.20}$$

In particular, we aim for the cavity being resonant to the $\left|{}^2P_{1/2}, F' = 1\right\rangle \leftrightarrow \left|{}^2S_{1/2}, F = 1\right\rangle$ transition of the ion (see Figure 5.9 a)). If we choose $k = 0$, i.e. the reference laser being resonant to the atomic transition ($\omega_{\mathrm{decay}} = \omega_{\mathrm{ref}}$), the pumped cavity induces a coupling between the $\left|{}^2S_{1/2}, F = 1\right\rangle$ and $\left|{}^2P_{1/2}, F' = 1\right\rangle$ manifolds. This coupling is desired when pumping the ion into the dark state $|0\rangle$ for initialisation (see section 6.1). However, we want the coupling being present solely on this stage of the experimental sequence. To avoid unnecessary dark pumping of the ion, we far detune the cavity reference laser from the atomic transition by at least one free spectral range of the cavity $\Delta\nu_{\mathrm{fsr}} \sim 500\,\mathrm{GHz}$ (i.e. $k > 0$ in eq. (5.20)). To determine a frequency of the cavity reference laser $f_{\mathrm{ref}} = \omega_{\mathrm{ref}}/(2\pi)$ satisfying equation (5.20) with an integer k, we use a second laser resonant to ω_{decay} as an atomic reference laser (see Figure 5.9 b)).

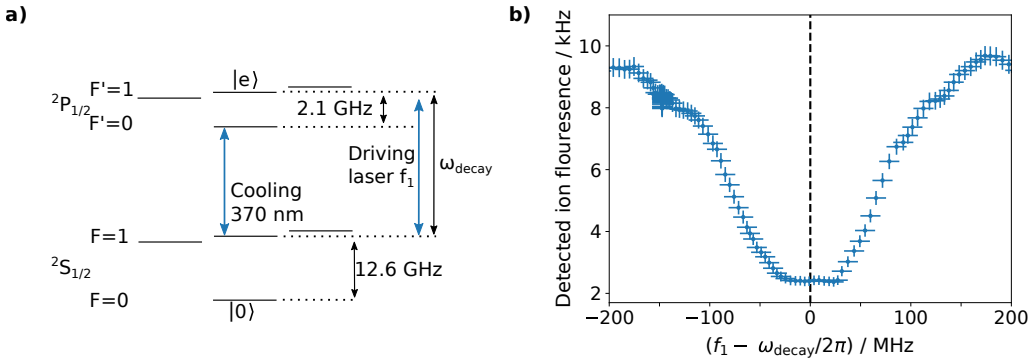

Figure 5.9: Calibration of a laser with frequency f_1 to the atomic decay transition $\left|{}^2\mathrm{P}_{1/2}, F' = 1\right\rangle \leftrightarrow \left|{}^2\mathrm{S}_{1/2}, F = 1\right\rangle$. **a)** Relevant energy levels of $^{171}\mathrm{Yb}^+$. **b)** Measured rate of photons scattered by the ion in steady state into free space while scanning the laser frequency of the atomic reference laser f_1. The frequency f_1 is adjusted to be resonant to the atomic decay transition $f_{\mathrm{decay}} = \omega_{\mathrm{decay}}/(2\pi)$ by pumping the ion into the dark state $|0\rangle$ (dashed line). Error bars are given for the data, indicating the standard errors for the detection rate and the standard deviation of the frequency measurement.

To calibrate the atomic reference laser, we employ a pumping of the ion to the dark state $|0\rangle$ using this laser. In order to find the atomic resonance frequency, it is practical to measure the pumping in a steady state configuration. Therefore, we drive the ion simultaneously with the cooling laser. The resulting detected fluorescence of the ion in steady state depends on several experimental parameters such as power, detuning and polarisation of the reference laser pumping the ion to the dark state. Furthermore it depends on 370 nm cooling and 935 nm repumping laser and the applied 14.7 GHz sideband. Therefore, the resulting fluorescence as a function of the dark pumping laser frequency is non-trivial[42], but we verified that it is symmetric around the resonance ω_{decay} . To obtain this result, we solved the Hamiltonian combined with a list of collapse operators

[42] The fluorescence signal does not necessarily has a minimum at resonance

of the system numerically[43] in the steady state and checked this result in the experiment. Finally, we overlap the resonances of the atomic reference laser and the cavity-lock laser in the reflection signal of the cavity (see Figure 5.10).

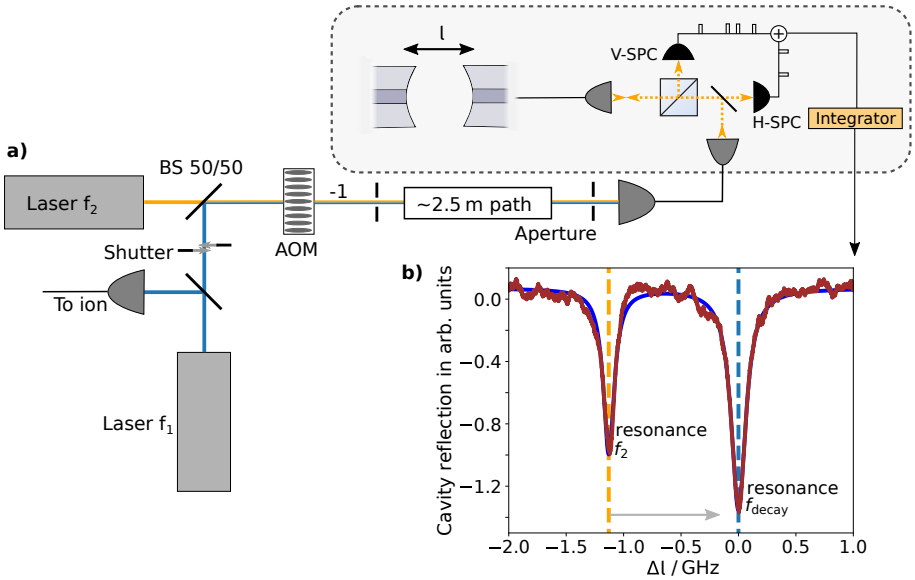

Figure 5.10: Calibration of the cavity-reference laser with frequency f_2 to the laser resonant to the atomic decay transition (f_{decay}). Both lasers have to be resonant to the fibre cavity for the same length l. **a)** Sketch of the laser setup containing the atomic and the cavity reference laser (f_1 and f_2). The detection setup of the cavity reflection is shown as inset. **b)** The solid line (dark blue) is a double Lorentzian fit to the measured cavity reflection data (red) from which we extract the distance of the dips while scanning l.

For a daily calibration of the reference laser we usually stop at this point, however, a deeper analysis of the overlap process allows for a precise measurement of the cavity length l. Since the fibre cavity has a symmetric near confocal resonator design, we have to consider an absolute frequency shift induced by the Gouy phase for a computation of the resonator length as [142]

$$l = \frac{nc}{2f} + \eta \cdot \frac{c}{2f}, \; n \in \mathbb{N}. \tag{5.21}$$

The shift due to the Gouy phase can be computed as

$$\eta \cdot \frac{c}{2f} \qquad \text{with} \qquad \eta = \frac{1}{\pi} \arccos(\sqrt{g_1 g_2}) = 0.478 \pm 0.226, \tag{5.22}$$

where $g_{1,2} = 1 - l/R_{1,2} > 0$ with the radii of curvature of the mirrors $R_{1,2}$. For a perfectly symmetric confocal resonator, we expect $\eta = 0.5$. Since we do not have accurate knowledge about the cavity length at this point, we deduce a cavity length of $l = (260 \pm 20)\,\mu$m from previous measurements [29] for the calculation of η.

For a single laser coupled to the cavity, it is hard to determine the exact n in equation (5.21) because switching to the neighbour free spectral range, i.e $n \pm 1$, requires a length change of only half the wavelength. However, an approximate bound to the value

[43] We use the PYTHON package QUTIP.STEADYSTATE

of n can be given. For two lasers with n_1, f_1 and n_2, f_2 fulfilling the resonant condition of equation (5.21) at the same time, it follows

$$\frac{n_1 c}{2f_1} = \frac{n_2 c}{2f_2}. \tag{5.23}$$

From the laser frequencies $f_1 = f_{\text{decay}}$ and $f_2 = f_{\text{ref}}$ both being resonant to the cavity according to Figure 5.10, we obtain

$$\frac{n_2}{n_1} = \frac{f_{\text{ref}}}{f_{\text{decay}}} = 0.939137(1). \tag{5.24}$$

The frequencies are measured to a relative precision of $\sim 2 \times 10^{-7}$ (absolute 150 MHz), which allows a precise computation of the ratio of the number of standing wave nodes. Within the bounds of the previously estimated cavity length of $l = (260 \pm 20)\,\mu$m, we find only one pair of $n_{1,2}$ which fulfils equations (5.23) and (5.21):

$$n_1 = 1327 \text{ and } n_2 = 1413. \tag{5.25}$$

Using the exact integers n_1 and n_2, we get a precise cavity length from equation (5.21) for this particular measurement of

$$l = 261.16(4)\,\mu\text{m},$$

when both lasers are resonant to the cavity. The accuracy of the length determination is limited by the error on the Gouy phase estimation.

5.3.3 Mechanical stability

In this subsection, we investigate the mechanical stability of the fibre cavity setup. A stabilisation of the cavity mode frequency to the atomic transition requires the cancellation of resonator length changes, which can originate, for example, from mechanical excitations of the cavity structure. External noise or electronic noise of the control signal itself can excite mechanical resonances. To mitigate electronic noise, we use three battery boxes for the control of the piezo actuators (see Figure 5.11). The boxes consists of stacked 9 V block-batteries and their output can be tuned from -198 V to 198 V. For the piezo tube, which controls the relative orientation of the fibres, one box each is used for horizontal and vertical axis. The third box serves as voltage offset for the PID-controller of the cavity length stabilisation, which can only output between -10 V and 10 V and thus has a limited range of applicable feedback. This voltage offset turned out to be a good compromise between electronic noise and locking bandwidth, as filtering a feedback signal always reduces the bandwidth of the lock.

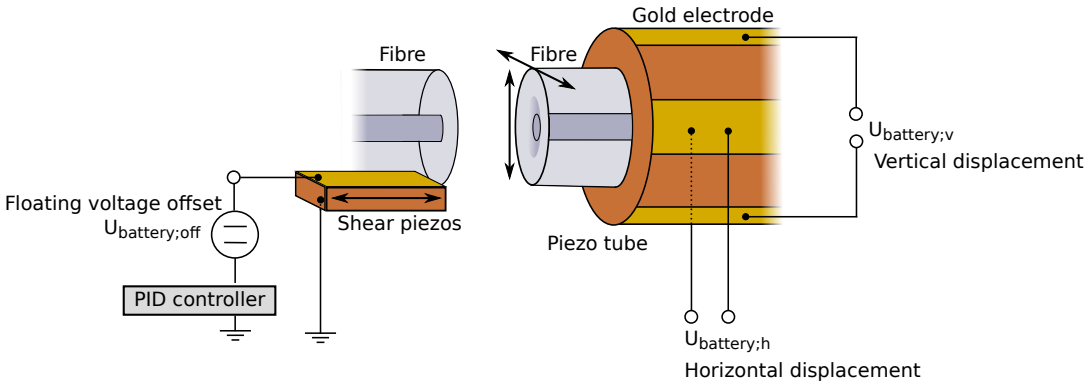

Figure 5.11: Wiring of the piezo actuators. The piezo tube controlling horizontal and vertical alignment of one fibre is powered by two battery-stacks. The position of the second fibre along the cavity axis is determined by a stack of two shear piezo actuators, which are fine-tuned on a low voltage level ($\pm\,10\,\mathrm{V}$) using a PID controller. A coarse voltage offset is supplied by a third floating battery-stack. Sketched elements are not to scale.

For cavity length stabilisation, we use a stack of two shear piezo actuators that move one of the fibres along the cavity axis (see section 5.2). However, mechanical oscillations orthogonal to the cavity axis may also result in effective length changes of the cavity. Counteracting these vibrations along the cavity axis, which is not the vibration axis, is not optimal and can induce additional vibrations. Overall, it becomes clear that it is important to minimise the influence of mechanical resonances already in the design phase of the cavity setup.

This requires an accurate characterisation of the mechanical resonances. We did this for the piezo tube using a lock-in amplifier [90]. This applies an alternating voltage signal with variable frequency to the piezo while monitoring the voltage drop across the piezo tube (Figure 5.12 a)). The capacitance of the piezo C together with a resistor forms a low-pass filter, whose characteristic signal we obtain as the overall signal (Figure 5.12 b)). In the frequency range close to a mechanical resonance of the piezo, the system can additionally be described as a driven harmonic oscillator. In response to a force F resulting from the driven mechanical oscillations, we can measure the induced charge Q_i on the piezo electrodes

$$Q_i = d \cdot F = U_i \cdot C \tag{5.26}$$

as a small induced voltage U_i, where d is a material-specific constant. The induced voltage is observable as a small deviation from the expected low-pass signal. Using the differential equation of a driven harmonic oscillator, we can infer the Q-factor of each resonance from the data.

One approach to stabilise the assembly is to shift the mechanical resonances to higher frequencies, which can reduce the probability of excitation if the spectrum of the excitation noise follows a $1/f$ dependence (pink noise). Another approach is the damping of high Q resonances because they have most influence on the vibration amplitude [6]. Figure 5.12 c) shows the result of the design considerations, where we tried avoid high Q resonances of the assembly at low frequencies in an early stage of the design process.

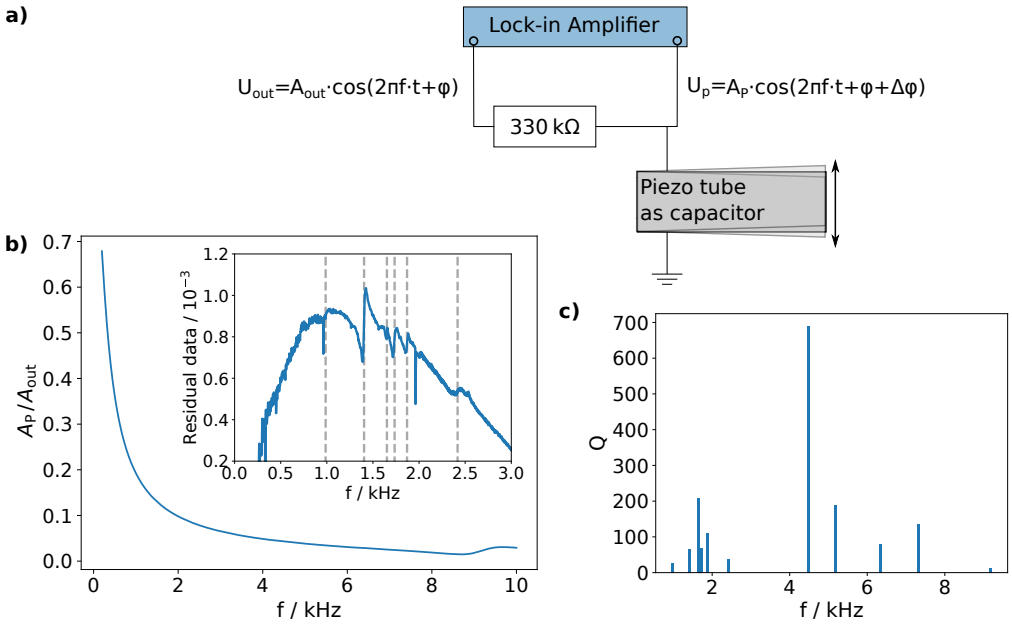

Figure 5.12: Mechanical resonances of the assembly measured in an early stage of the design process [90]. **a)** Wiring diagram of the test setup. Once the applied RF-signal hits a mechanical resonance, the piezo actuator starts to oscillate which changes its impedance. **b)** Spectral response of the setup sketched in a). Mechanical oscillations results in small deviations from an ideal low-pass signal which can be analysed quantitatively. A cut out of the deviation from an ideal low-pass signal is shown as inset where the investigated resonances are denoted with dashed vertical lines. **c)** Quality factor of the investigated resonances based on the residual data shown in b).

In order to determine which resonances contribute to the mechanical instability of the final assembled cavity setup, we investigate the signal obtained during side-of-fringe locking (Figure 5.8). We obtain the vibrational frequencies using a fast Fourier transformation (FFT) on the measured reflection signal of the cavity (see Figure 5.13). Since the reference laser runs at fixed frequency f_{ref}, the changing resonant conditions originate from a varying cavity length.

From the FFT analysis, we determine the dominant resonance to be at $\sim 400\,\mathrm{Hz}$ and observe further excitations mainly at lower frequencies. This is the expected behaviour for a noise spectral density dependency of $1/f$ which mainly excites the mechanical resonances at low frequencies of the excitation spectrum, which we expect for the final assembly to be similar to that of Figure 5.12 c).

From the lower frequency excitation spectrum of the piezo tube, mechanical oscillations orthogonal to the cavity axis as sketched in Figure 5.8 can be expected. We know that these oscillations cause a change in the effective cavity length, which is then compensated by the shear piezo stack along the cavity axis. We suppose that the mismatch between oscillation and regulation axes makes a stable lock difficult to realise and that this could likely be the reason for the remaining vibrations on the length stabilisation. These are important results when considering the coupling between cavity and ion and can explain the deviation from the measured to the expected coupling between light and matter investigated in the next section.

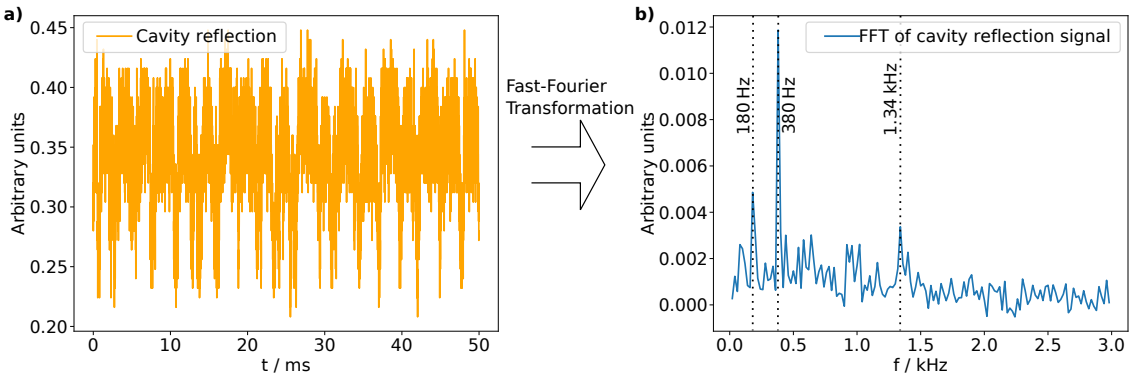

Figure 5.13: Resonance investigation of the final fibre cavity assembly. **a)** Reflected light intensity during length stabilisation. **b)** Fast Fourier transformation (FFT) of the reflection signal. We performed the analysis of resonances up to 10 kHz, but were not able to identify resonances above 3 kHz. We have indicated the corresponding frequencies of the identified resonances in each case. In addition to the shown mechanical oscillations of the cavity setup, the measured signal in a) exhibits noise originating from the measurement electronics. For the FFT analysis we remove the noise contributions by subtracting an FFT spectrum of an idle signal.

5.4 Light-matter interaction

We present the application of the fibre resonator as a light-matter interface in this section. To this end, we introduce a quantum mechanical formalism to describe the interaction between a radiation field and an atomic system. We reduce the atomic system to a two-level system $|g\rangle$ / $|e\rangle$, where ground and excited state gets near resonant coupled by the radiation field. We start with a semi-classical approach, where we describe the radiation field as a single-mode electric field interacting with the atomic two-level system in dipole approximation (see subsection 5.4.1). In subsection 5.4.3, we consider the quantisation of the radiation field over the resonator mode volume, which subsequently can be used to describe the atom-cavity coupling in subsection 5.4.4. The resulting concept of coupling a two-level system to a continuum of modes also allows the description of the spontaneous decay of an excited level as introduced in subsection 7.1.1.

As a basis of the Hilbert space of the two-level system, we define the states $|g\rangle = |n, l, m\rangle$ and $|e\rangle = |n', l', m'\rangle$ of the atom with the corresponding quantum numbers and $|e\rangle\langle e| + |g\rangle\langle g| = \mathbb{I}$. The Hamiltonian for the unperturbed system is given by $\hat{H}_{\text{atom}}$ which can be expressed in composition of its eigenstates $|i\rangle \in \{|g\rangle, |e\rangle\}$ as

$$\hat{H}_{\text{atom}} = \hbar \sum_i \omega_i |i\rangle\langle i| . \tag{5.27}$$

By setting the point of zero energy half between the ground state and the excited state, we derive $\omega_g = -\omega_a/2$ and $\omega_e = \omega_a/2$ with $\omega_a = \omega_e - \omega_g$ and obtain $\hat{H}_{\text{atom}} = \frac{\hbar\omega_a}{2}\hat{\sigma}_z$ with $\hat{\sigma}_{x,y,z}$ being the Pauli matrices.

The interaction between the two-level system and the radiation field is described by a Hamiltonian $\hat{H}_{\text{I}}$. Figure 5.14 shows a sketch of the different approaches used to describe the atom-field interaction with the corresponding definitions.

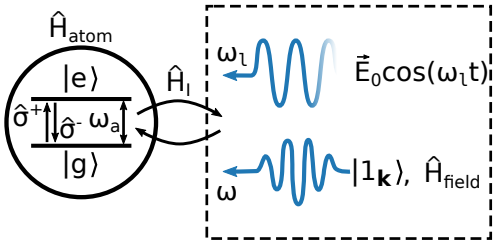

Figure 5.14: Overview of the different approaches used to describe atom-field interaction with corresponding definitions. An atomic two-level system (circle) with Hamiltonian $\hat{H}_{\text{atom}}$ is coupled to a radiation field (dashed box) via the interaction Hamiltonian $\hat{H}_I$. The operators $\hat{\sigma}^{+/-}$ denotes the atomic raising/lowering operators. The field can be described either in a semi-classical approach using an oscillating electric field (box, top) or in the field quantisation approach, where we consider a single photon $|1_{\mathbf{k}}\rangle$ as an excitation of a radiation mode $\omega = c|\mathbf{k}|$ with wave vector $\mathbf{k}$ (box, bottom). For the field quantisation approach, the energy of the field is considered in $\hat{H}_{\text{field}}$.

5.4.1 The electric dipole transition in a semi-classical description

In dipole approximation, the spatial variation of the electric field on the length scale of the atom is neglected, since the length of the atomic dipole moment is assumed to be much smaller than the wavelength of the electric field λ. In particular, $|\mathbf{r}| \sim a_0$ (Bohr radius) and $\exp(i\mathbf{k}\cdot\mathbf{r}) = \exp(i \cdot 2\pi/\lambda \cdot |\mathbf{r}|) \approx 1$. Therefore, we can drop the spatial dependence in the expression of the electric field and write a single mode of a linearly polarised electric field as

$$\mathbf{E} = E_0 \cos(\omega_l t)\, \mathbf{e}_E, \tag{5.28}$$

where the field is oscillating along an axis with unit vector $\mathbf{e}_E$. The electron density of an atom in state $|g\rangle$ gets displaced by the electric field and a superposition state of $|g\rangle$ and $|e\rangle$ may be induced, which exhibits a dipole moment $\hat{\mathbf{d}} = -e \cdot \hat{\mathbf{r}}$ with elementary charge e and the electron position $\hat{\mathbf{r}}$. The interaction Hamiltonian between radiation field and the electric dipole is given by[44]

$$\hat{H}_{I,s} = \hat{\mathbf{d}} \cdot \mathbf{E} = -eE_0 \cos(\omega_l t)\, \hat{\mathbf{r}} \cdot \mathbf{e}_E. \tag{5.29}$$

In order to better understand the physics behind this Hamiltonian, we express $\hat{H}_{I,s}$ in terms of the basis states of the Hilbert space $|i\rangle, |j\rangle \in \{|g\rangle, |e\rangle\}$ as

$$\begin{aligned} \hat{H}_{I,s} &= \sum_{i,j} |i\rangle \langle i| \hat{H}_{I,s} |j\rangle \langle j| \\ &= -eE_0 \cos(\omega_l t) \cdot \sum_{i,j} |i\rangle \langle i| \hat{\mathbf{r}} \cdot \mathbf{e}_E |j\rangle \langle j| \end{aligned} \tag{5.30}$$

using $|e\rangle\langle e| + |g\rangle\langle g| = \mathbb{I}$ and $\hat{A} = \mathbb{I}\hat{A}\mathbb{I}$ for any operator $\hat{A}$. The value of $\langle i|\hat{\mathbf{r}}\cdot\mathbf{e}_E|j\rangle$ depends on the atomic wave function of $|i\rangle$ and $|j\rangle$ respectively. The expression $\langle i|\hat{\mathbf{r}}\cdot\mathbf{e}_E|j\rangle$ is only non-zero for $i \neq j$ and transitions $|g\rangle \leftrightarrow |e\rangle$ complying with the electric dipole selection rules.

In general, for computing $\langle i|\hat{\mathbf{r}}\cdot\mathbf{e}_E|j\rangle$, the overlap of the angular part of the wave functions of $|i\rangle$ and $|j\rangle$ with the driving field has to be considered (see Clebsch-Gordan

[44] The subscript 's' indicates the context of the semi-classical approach

coefficients in Appendix B for details). In general, the driving electric field $\mathbf{E}$ could be also a superposition of linear and circular polarisation components with a more complex time dependence. However, for simplicity, we consider the linear field of equation (5.28) in the following and define the polarisation axis $\mathbf{e_E}$ as parallel to the atomic quantisation axis, which has maximal overlap with an electric dipole transition of $\Delta m = m' - m = 0$. From here on we take this condition as given for the investigated two-level system $|g\rangle/|e\rangle$.

We define $\mathbf{d}_{ij} = \mathbf{d}^*_{ji} = e \langle i| \hat{\mathbf{r}} |j\rangle$ and define following expression of the Rabi frequency:

$$\Omega_R = \frac{|\mathbf{d}_{ij}| \cdot E_0}{\hbar}. \tag{5.31}$$

Using this definition of the Rabi frequency and $|\mathbf{d}_{ii}| = |\mathbf{d}_{jj}| = 0$, the interaction Hamiltonian of equation (5.30) reads

$$\begin{aligned} \hat{H}_{I,s} &= \hbar\Omega_R \cos(\omega_l t) \left[|e\rangle\langle g| + |g\rangle\langle e| \right] \\ &= \hbar\Omega_R \cos(\omega_l t)\, \hat{\sigma}_x. \end{aligned} \tag{5.32}$$

Finally, we write the full Hamiltonian of the semi-classical description as

$$\hat{H} = \underbrace{\frac{\hbar\omega_a}{2}\hat{\sigma}_z}_{\hat{H}_{\text{atom}}} + \underbrace{\hbar\Omega_R \cos(\omega_l t)\, \hat{\sigma}_x}_{\hat{H}_{\text{I,s}}} = \hbar \begin{pmatrix} \omega_a/2 & \Omega_R \cos(\omega_l t) \\ \Omega_R \cos(\omega_l t) & -\omega_a/2 \end{pmatrix}. \tag{5.33}$$

5.4.2 Rotating wave approximation

According to equation (2.8), a two-level system state $|\Psi\rangle_2$ can be transformed into a state $|\Psi'\rangle_2(t)$ rotating with frequency ω around any axis $\mathbf{r}_r$ by applying a unitary transformation T_2 as

$$|\Psi'\rangle_2(t) = T_2 |\Psi\rangle_2 \tag{5.34}$$

with

$$T_2 = \cos(\omega t/2)\, \mathbb{I} + i \sin(\omega t/2) \cdot \mathbf{r}_r \cdot \begin{pmatrix} \hat{\sigma}_x \\ \hat{\sigma}_y \\ \hat{\sigma}_z \end{pmatrix} = \exp\left(\frac{i\omega t}{2} \cdot \mathbf{r}_r \cdot \begin{pmatrix} \hat{\sigma}_x \\ \hat{\sigma}_y \\ \hat{\sigma}_z \end{pmatrix} \right). \tag{5.35}$$

However, this is also true for a general state $|\Psi\rangle$ with the corresponding unitary transformation T. The time evolution of $|\Psi\rangle$ is given by the time-dependent Schrödinger equation as

$$i\hbar \frac{d}{dt} |\Psi(t)\rangle = \hat{H}' |\Psi(t)\rangle. \tag{5.36}$$

Using the Schrödinger equation, one can show that if a state $|\Psi\rangle$ in the Schrödinger picture transforms according to equation (5.34), the Hamiltonian transforms as

$$\hat{H}' = T\hat{H}T^\dagger - i\hbar T \frac{\partial T^\dagger}{\partial t}. \tag{5.37}$$

For the driven two-level system described in this subsection, we apply the transformation

$$T = \exp\left(i\frac{\omega_l}{2} t\, |e\rangle\langle e| - i\frac{\omega_l}{2} t\, |g\rangle\langle g| \right) = \exp\left(\frac{i\omega_l t}{2} \cdot \hat{\sigma}_z \right), \tag{5.38}$$

which is, according to equation (2.9), a rotation around the z-axis with frequency ω_l. Applying the transformation of equation (5.37) to the Hamiltonian derived in equation (5.33), we obtain

$$\hat{H}' = \frac{\hbar}{2}\left(-\Delta\hat{\sigma}_z + \Omega_R\hat{\sigma}_x\right) \equiv \hat{H}_{\mathrm{rwa}}. \tag{5.39}$$

We hereby neglect fast oscillating terms of $O(2\omega_l)$, which is known as the rotating wave approximation (RWA). Furthermore, we introduce the detuning $\Delta = \omega_l - \omega_a$ of the driving field to the atomic transition.

From the driven two-level Hamiltonian of equation (5.39) with the ansatz $|\Psi\rangle = c_e(t)\,|e\rangle + c_g(t)\,|g\rangle$ and using equation (5.36), we obtain a set of coupled differential equations for a driven two-level system, whose analytical solution is well known [53]. The probability to find the system in the excited state $|e\rangle$ is given as

$$\eta_{\mathrm{exc}}(t) = |\langle e|\Psi(t)\rangle|^2 = |c_e(t)|^2 = \frac{\Omega_R^2}{(\Omega_R')^2}\cdot\left(\frac{1}{2} - \frac{1}{2}\cos\left(\Omega_R' t\right)\right), \tag{5.40}$$

with $\Omega_R' = \sqrt{\Omega_R^2 + \Delta_R^2}$ being the generalised Rabi frequency. Equation (5.40) describes an oscillation of the excited state population with $\Omega_R' \cdot t$, which is known as Rabi oscillation.

5.4.3 Field quantisation

In this subsection, we introduce the concept of field quantisation and the interaction with a two-level system in the dipole picture and the rotating wave approximation, similar as for the semi-classical approach in subsections 5.4.1 and 5.4.2. The concept of field quantisation is essential for the description of two main aspects of this work. First, it leads to a quantum mechanical description of spontaneous decay (see subsection 7.1.1) via coupling to the electro magnetic vacuum. Second, the coupling of a two-level system to a single mode of a radiation field quantised over the mode volume of an optical resonator leads to the Purcell effect, which is important for understanding the working principle of optical resonators acting as light-matter interfaces (see subsection 5.4.4).

We start with the Hamiltonian of the driven two-level system [152]

$$\hat{H} = \hat{H}_{\mathrm{atom}} + \hat{H}_{I,q} + \underbrace{\sum_{\mathbf{k}} \hbar\omega_{\mathbf{k}}\left(\hat{a}_{\mathbf{k}}^\dagger\hat{a}_{\mathbf{k}} + \frac{1}{2}\right)}_{\hat{H}_{\mathrm{field}}}, \tag{5.41}$$

that now includes a term describing the energy of the quantised field $\hat{H}_{\mathrm{field}}$ according to Figure 5.14. We name[45] the interaction Hamiltonian of the quantised field approach $\hat{H}_{I,q}$. The operators $a_{\mathbf{k}}^\dagger$ and $a_{\mathbf{k}}$ each create and annihilate a photon with wave vector $\mathbf{k}$ in the corresponding mode of the radiation field.

A linearly polarised electric field in dipole approximation at the position of the atom is given by [152]

$$\mathbf{E} = \sum_{\mathbf{k}} \mathbf{e}_{\mathbf{k}}\epsilon_{\mathbf{k}}\left(\hat{a}_{\mathbf{k}} + \hat{a}_{\mathbf{k}}^\dagger\right), \tag{5.42}$$

with $\epsilon_{\mathbf{k}} = \sqrt{\hbar\omega_{\mathbf{k}}/2\epsilon_0 V}$ and V being the quantisation volume. In the case of a resonator, the quantisation volume is equivalent to the mode volume V_m introduced in equation (5.16).

[45] The subscript 'q' indicates the context of the quantised field approach

The interaction Hamiltonian then reads

$$\hat{H}_{I,q} = \hat{\mathbf{d}} \cdot \mathbf{E} = \hbar \sum_{ij} \sum_{\mathbf{k}} g_{\mathbf{k}}^{ij} \left(\hat{a}_{\mathbf{k}} + \hat{a}_{\mathbf{k}}^{\dagger} \right) |i\rangle \langle j| , \tag{5.43}$$

with the light-matter coupling coefficient

$$g_{\mathbf{k}}^{ij} = |\mathbf{d}_{ij} \cdot \mathbf{e}_{\mathbf{k}}| \epsilon_k / \hbar. \tag{5.44}$$

We can see from equation (5.44) that a smaller cavity mode volume V_m enhances the light-matter coupling strength. For a single mode of the field we can write

$$g \propto 1/\sqrt{V_m}. \tag{5.45}$$

Applying the rotating wave approximation to the Hamiltonian of equation (5.41) we obtain [152]

$$\hat{H} = \frac{\hbar \omega_a}{2} \hat{\sigma}_z + \hbar \sum_{\mathbf{k}} g_{\mathbf{k}} \left(\hat{\sigma}^{+} \hat{a}_{\mathbf{k}} + \hat{a}_{\mathbf{k}}^{\dagger} \hat{\sigma}^{-} \right) + \sum_{\mathbf{k}} \hbar \omega_{\mathbf{k}} \hat{a}_{\mathbf{k}}^{\dagger} \hat{a}_{\mathbf{k}}, \tag{5.46}$$

where we omitted the constant energy offset of $\hat{H}_{\text{field}}$ and assumed $g_{\mathbf{k}}^{ij} = g_{\mathbf{k}}^{ji} = g_{\mathbf{k}}$. We define $\hat{\sigma}^{+/-}$ to be the atomic raising/lowering operator with $\hat{\sigma}^{+} = |e\rangle \langle g|$ and $\hat{\sigma}^{-} = |g\rangle \langle e|$.

The Hamiltonian of equation (5.46) describes the interaction between a two-level system and multiple modes of a radiation field. Considering only a single mode of the radiation field in equation (5.46) yields the so-called Jaynes-Cummings Hamiltonian.

5.4.4 A two-level system inside an optical resonator

In a simple classical picture, an optical resonator is able to increase the probability of a photon to interact with an atom that is within the resonator mode by reflecting the photon back and forth several times. The chance of the photon to 'hit' the atom in the resonator with mode area $A = \pi \omega_0^2$ can be expressed as

$$P_{\text{hit}} = \frac{\sigma_{\text{abs}}}{A} \cdot \frac{\mathcal{F}}{\pi}, \tag{5.47}$$

where the atomic cross section is given by $\sigma_{\text{abs}} = \frac{3\lambda^2}{2\pi}$. The number of photon reflections is twice the number of round trips $2 \cdot N = 2 \cdot \tau_{\text{cavity}} / \tau_{\text{round}} = 2 \cdot \frac{\mathcal{F}}{2\pi}$, which is determined by the finesse of the resonator $\mathcal{F}$. Even in this simple picture, the advantage of the enhanced light-matter interaction in a resonator becomes clear due to the increased number of round trips compared to a free-space approach.

Also from a quantum mechanical point of view, the combination of optical resonators with single emitters is well suited as a light-matter interface but requires a more sophisticated description. To this end, we consider the coupling of an atomic two-level system to a single mode of the cavity, which means in particular that we assume only one mode ω_c of the resonator to be near resonant to the two-level transition frequency ω_a. Depending on the properties of the resonator and the atom, there are several regimes in which the combined atom-cavity system can be operated. For a description of these regimes, the fundamental rates of the atom-cavity system are frequently used, see Figure 5.15. We introduce these rates in the following.

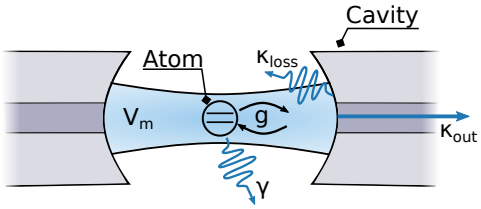

Figure 5.15: Sketch of a two-level system coupled to a resonator with mode volume V_m. The fundamental rates describing the combined atom-cavity system are given as light-matter coupling rate g, scattering rate of photons into free space $\Gamma_{4\pi} = 2\gamma$ and photon loss rate from the cavity mode $\kappa = \kappa_{\text{out}} + \kappa_{\text{loss}}$.

In subsection 5.4.3, we derive the full Hamiltonian of the system, which we here constrain to a single mode of the radiation field. The light-matter coupling rate of equation (5.44) then reads

$$g = \sqrt{\frac{|d_{eg}|^2 \omega_c}{2\epsilon_0 \hbar V_m}}, \tag{5.48}$$

where ω_c is the centre frequency of the resonator mode. The field decay rate γ of the system to the free-space vacuum states is given by the linewidth of the atomic transition as

$$\Gamma_{4\pi} = 2\gamma. \tag{5.49}$$

which is related to a scattering rate of photons $R_{4\pi} = \Gamma_{4\pi} \cdot \rho_{ee}^{ss}$ into free space without a cavity being present (see equation (6.28)). We have to explicitly differentiate between a (near) resonant cavity being present or not, since we showed in [7] that we can enhance or suppress the scattering rate of photons through coherent back action of the cavity field on the position of the ion, i.e. $R_{4\pi} \neq R_{4\pi,c}$ with $R_{4\pi,c}$ being the free space detected scattering rate of photon with a (near) resonant cavity in place. The scattering of photons into free space can be seen as a loss of energy, since photons are scattered out of the atom-cavity system. Further losses are given by photon absorption or scattering on the cavity mirrors, which is taken into account with κ_{loss} and together with the field decay rate κ_{out} of the resonator mode through the mirrors gives the total loss rate of the cavity

$$\kappa = \kappa_{\text{loss}} + \kappa_{\text{out}}. \tag{5.50}$$

In the context of this work, a fast extraction of photons from the resonator mode determined by κ_{out} is a desired property and can be seen as a loss only in terms of the energy of the combined atom-cavity system. We chose the reflective coating of the fibre mirrors accordingly to achieve a high κ_{out} so that the quantum information transmission rate in a network is not limited by the photon storage time within the cavity.

Regarding the field rates of the system, we can distinguish between strong coupling $g \gg \kappa, \gamma$ and weak coupling $g \ll \kappa, \gamma$. In the strong coupling regime, the system can be described by the Jaynes-Cummings Hamiltonian introduced in subsection 5.4.3 which leads to interesting quantum electro dynamic (QED) phenomena like atom-photon quantum gates [141] or reversible mapping of quantum states between light and matter [27]. In the weak coupling regime, the system is dominated by its loss rates. This regime is particularly interesting for the implementation of quantum networks. Fast cavities, where the dominant rate is the field decay rate of the resonator ($\kappa > \gamma, g$), provide fast

access to the photons emitted by the stationary qubit into the resonator mode. In this regime, we can describe the atom-cavity interaction via perturbation theory [53] as done in the following.

Purcell effect

The coupling of a two-level system to a continuum of modes of an electro magnetic field leads to a spontaneous decay of the excited state with time constant $1/\Gamma$ (see subsection 7.1.1). The rate Γ can be obtained via Fermi's golden rule using the density of modes of the radiation field $\rho(\omega)$ (also called density of states) as

$$\Gamma = \frac{2\pi}{\hbar^2}|M_{eg}|^2\rho(\omega), \tag{5.51}$$

with $|M_{eg}|^2 = |\langle \mathbf{d}\cdot\mathbf{E}\rangle|^2 = \frac{1}{3}|d_{eg}|^2\epsilon_{\mathbf{k}}^2$ being the transition matrix element[46] [53] and using the definition of $\epsilon_{\mathbf{k}}$ from subsection 5.4.3 for a single field mode. In free space (4π solid angle) the density of states is given by $\rho_{4\pi}(\omega) = \frac{\omega^2 V_0}{\pi^2 c^3}$ [53] where V_0 is the quantisation volume, which leads to the same expression of $\Gamma_{4\pi}$ as derived in equation (7.6) for the quantum mechanical treatment of spontaneous decay into free space

$$\Gamma_{4\pi} = \frac{1}{4\pi\epsilon_0}\frac{4\omega^3|d_{eg}|^2}{3\hbar c^3}. \tag{5.52}$$

Considering the decay into a cavity mode, the density of states can be approximated by a Lorentzian function with a FWHM of $\Delta\omega_c$ and the resonance frequency ω_c as [53]

$$\rho_c(\omega) = \frac{2}{\pi\Delta\omega_c}\frac{\Delta\omega_c^2}{4(\omega-\omega_c)^2+\Delta\omega_c^2}. \tag{5.53}$$

For an atomic transition with ω_a, we have to evaluate $\rho(\omega_a)$, which becomes at resonance

$$\rho_c(\omega_a=\omega_c) = \frac{2Q}{\pi\omega_a}, \tag{5.54}$$

where $Q = \omega_c/\Delta\omega_c = \omega_c/(2\kappa)$ is the quality factor of the cavity. Using again Fermi's golden rule, we obtain for the time constant of photon emission into the cavity on resonance ($\omega_c = \omega_a$)

$$\Gamma_c = \frac{2\pi}{\hbar^2}\underbrace{|M_{eg}|^2}_{|d_{eg}|^2\epsilon_{\mathbf{k}}^2} = \frac{2Q|d_{eg}|^2}{\epsilon_0 V_m \hbar}, \tag{5.55}$$

where we assume the dipole to be oriented along the field direction [53].

The Purcell factor f_p describes the ratio of the two decay rates

$$f_p = \frac{\Gamma_c}{\Gamma_{4\pi}} = \frac{3Q\lambda^3}{4\pi^2 V_m}, \tag{5.56}$$

with $\omega/c = (2\pi)/\lambda$. The total decay rate Γ' of the atom-cavity system can be given as the sum of the individual rates

$$\Gamma' = \Gamma_{4\pi} + \Gamma_c = \Gamma_{4\pi}\left(1+f_p\right), \tag{5.57}$$

[46] The factor of 1/3 comes from averaging all possible orientations of the atomic dipole with respect to the field direction [53]

since the cavity provides additional field modes along its axis and we assume that the density of free space modes is mainly unaffected [53]. Using equations (5.48), (5.49) and (5.52), one can further find the relation

$$f_p = 2 \cdot \frac{g^2}{2\kappa\gamma} \equiv 2C_0, \tag{5.58}$$

with which we have derived a common expression of the so-called cooperativity C_0 of the cavity. The cooperativity is expressed through the fundamental rates of the atom-cavity system. We can interpret the cooperativity in terms of the simple picture introduced at the beginning of this subsection by using the probability P_{hit} from equation (5.47). For the TEM_{00} mode of a symmetric resonator configuration[47] both expression are equivalent, i.e.

$$C_0 = P_{\text{hit}}. \tag{5.59}$$

Using the decay rates $\Gamma_{4\pi}$ and Γ_c, we can compute the important quantity of the probability of a photon to be emitted into the cavity mode

$$P_c = \frac{\Gamma_c}{\Gamma'} = \frac{2C_0}{2C_0 + 1}, \tag{5.60}$$

which is also called the collection efficiency of the cavity. From equation (5.60) it is clear why the use of resonant cavities is advantageous for the collection of photons emitted by an atom. Already in the medium coupling regime with $C_0 \approx 1$, the collection efficiency of emitted photons becomes $P_{c,\text{cavity}} \approx 66\,\%$. In contrast, state of the art high resolution objective lenses can reach numerical apertures of about NA ~ 0.92 [145], which gives a collection efficiency of $P_{c,\text{high NA}} \approx 30\,\%$ according to equations (3.20) and (3.21).

Application in quantum networks

For an application of cavities as light-matter interfaces in a quantum network, a high collection efficiency P_c along with a fast extraction of collected photons is desirable. A single photon emitted into a mode of the cavity will remain within the cavity for a finite time, which sets a lower limit on the time it takes for the photon to reach further elements of the network. This sets the limit of the bandwidth of a quantum network node in terms of data transmission rate to $\sim \kappa/2$. After a time of $\Delta t = 1/(\kappa/2)$, about 2 % of the photon intensity still remains in the resonator. From a quantum mechanical point of view, this is the probability of finding the photon still within the resonator.

The cooperativity C_0 of a resonator is therefore an important design factor as it determines P_c and includes the cavity decay rate κ as $C_0 \propto 1/(\kappa \cdot V_m)$. By building a small resonator with a small mode volume V_m, we can realise fast light-matter interfaces where κ is the dominant rate of the system and at the same time achieve efficient collection of photons due to a cooperativity of $C_0 \approx 1$.

5.4.5 Ion position within the cavity mode

For the light-matter coupling, the position of the ion within the cavity mode is important. Optimal coupling is achieved at high electric field amplitudes of the radiation mode, which

[47] For which the mode volume V_m was calculated in eq. (5.16)

is especially the case at the mode waist of the TEM_{00} mode. But also transversely, the standing wave pattern of the cavity mode has to be considered.

Once we moved the cavity to the trap position, we are able to keep it in this position and to load the ion into the trap with the cavity in place. This enables a durable fine tuning of the ion's position within the cavity mode by slightly moving the cavity with respect to the ion. In order to enable a full optimisation, the whole cavity structure is mounted on a three axes positioning stage. But there are also alternative approaches. In other experiments dealing with trapped ions in fibre cavities, attempts were made to move the ion with respect to the cavity by shifting the trap centre with additional RF electrodes [78]. However, the additional electrodes worsen the optical access to the trapped ion and the phase mismatch of the additional RF signals induce excess micromotion of the ion which has to be compensated.

In our case, we have to perform several iterative steps of the optimisation strategy described below, since the electric stray field situation in the trap changes due to the movement of the cavity. After each step, we need to compensate the stray fields in order to realign the position of the ion to the RF-null of the trap (see subsection 4.1.1). Otherwise, a cavity optimisation to a non-optimal ion position could be the result.

Coarse alignment

Before we start with a precise cavity alignment using direct feedback from the ion, we can estimate a good starting point for the iterative optimisation even without a trapped ion. Previous experiments [116] have shown that placing objects within the cavity mode introduce additional losses to the cavity system, which reduce the coupling efficiency of light to the cavity mode. We use this method to determine the coordinates of the triaxial positioning stage at which the coupling efficiency of the pump light into the cavity decreases as a trap needle approaches the cavity mode. For a symmetric trap, the ion is expected to be confined central between the two needles and we move the cavity to the midpoint of the above determined needle positions. This method provides a sufficient starting point for the following optimisation.

Transverse optimisation

We optimise the ion coupling to the TEM_{00} mode of the cavity by pumping this mode with an external laser. The theoretical waist of the mode is $\omega_0 = 4.1(2)\,\mu$m at its smallest size (equation (5.11)). To optimise the position of the ion inside the cavity, we drive the ion with the cavity field and monitor the rate of photons $R_{4\pi}$ scattered by the ion into free space. To this end, we tune the cavity-pump laser on resonance with the atomic cooling transition $^2S_{1/2} \leftrightarrow {}^2P_{1/2}$ of $^{174}Yb^+$ and hold the cavity resonant to this laser. According to equation (5.44), the coupling rate g between the cavity mode and the ion is proportional to the cavity electric field amplitude $E(r)$ at the position of the ion

$$g(r) \propto E(r) \propto e^{-\frac{r^2}{{w_0}^2}}, \tag{5.61}$$

where r denotes the radial position of the ion within the cavity mode (see Figure 5.16 a)). The light-matter coupling strength allows for probing of the electric field at the ion's position and was first demonstrated in [64] for an optical cavity and a single ion.

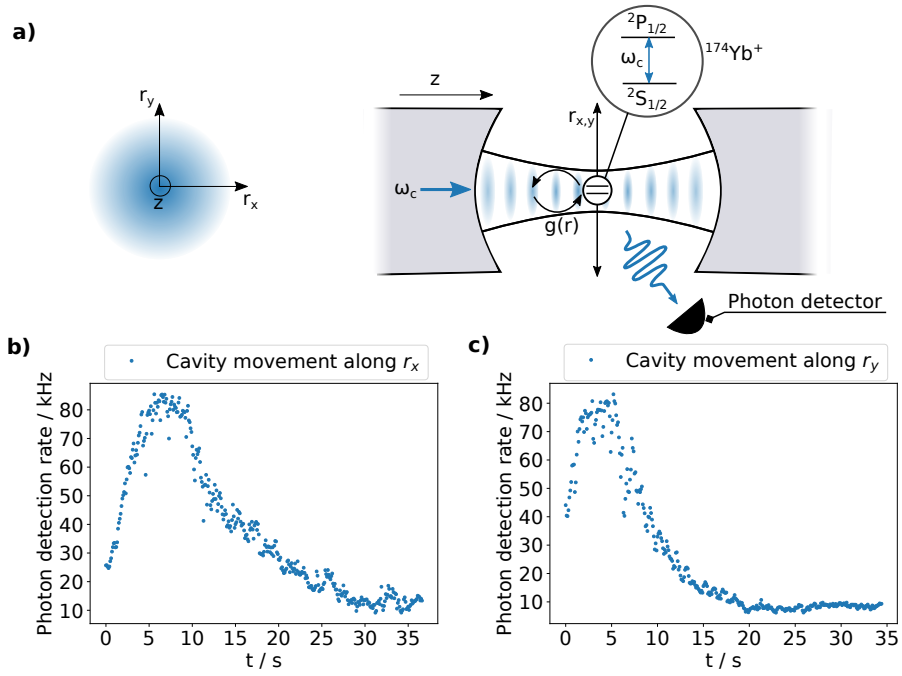

Figure 5.16: Optimisation of the light-matter coupling rate $g(r)$ by adjusting the transversal cavity mode to the ion's position. **a)** Sketch of the TEM_{00} cavity mode with radial axes definition. The cavity is pumped by a weak laser resonant to the $^2\mathrm{S}_{1/2} \leftrightarrow {}^2\mathrm{P}_{1/2}$ transition of $^{174}\mathrm{Yb}^+$. The z-axis is defined as the cavity axis. **b)** We continuously move the cavity along the x-axis while monitoring the scattering rate of photons $R_{4\pi}$ into free space. **c)** Same as in b) but for the cavity moving along the y-axis. **b)+c)** The error on the detection rate of photons can be estimated as the standard deviation of the points which is determined by cavity oscillations and heating of the ion.

We scan the position of the cavity with respect to the ion (see Figure 5.16 b)+c)) and observe a maximum scattering rate if the light-matter coupling rate is maximal as well. This is due to the dependence

$$R_{4\pi} \propto \rho_{ee} \propto g^2(r) \propto e^{-\frac{2r^2}{w_0{}^2}}, \tag{5.62}$$

where the steady state population of the $^2\mathrm{P}_{1/2}$ level ρ_{ee} is proportional to $g^2(r)$ for a weakly driven ion in a pumped cavity [6].

While continuously scanning the cavity position along the x-axis or the y-axis, we found a clear maximum of the light-matter coupling rate g in both cases (see Figure 5.16 b)+c)). Nevertheless, we cannot prove the expected Gaussian shape of the TEM_{00} mode for the following reason. The movement of the cavity changes the conditions for trapping, i.e. the magnitude and direction of the stray electric field at the position of the ion. Without a recalibration of the compensation field, this leads to a heating of the ion and to a strong Doppler broadening of the atomic resonance. Since we drive the ion slightly red detuned from the resonance, this then increases the scattering rate $R_{4\pi}$, which we can observe especially in Figure 5.16 b) as a more flat falling slope on the right-hand side of the curve.

Longitudinal optimisation
The effects we observe for the transverse displacement are even stronger for the longitudinal displacement of the cavity (z-axis), as the cavity mirror moves directly towards or away from the ion. Calibration of the ion's position along this direction requires a more stepwise approach with small adjustment steps and compensations in between. This approach is limited by the hysteresis of the cavity positioning stage and we suspect that the longitudinal alignment is not optimal.

In summary, with the positioning of the cavity, we achieved the maximal overlap of transversal cavity mode and ion. However, the uncertainty in the longitudinal positioning of the ion could lead to a reduced light-matter coupling. We investigate the light-matter coupling in detail in the next section.

5.5 Photons as travelling qubits

Photons have advantageous properties for the distribution of quantum information between the nodes of a quantum network. These are, for example, the speed of light, coupling to stationary qubits via the optical dipole moment and guiding through optical fibres. In this thesis, we use the enhanced light-matter interaction in the fibre cavity to effectively collect photons emitted from the trapped ion. Photons leaving the resonator mode are intrinsically fibre coupled.

As a light-matter interface, the cavity must provide control over the quantum state of the emitted photon. In this thesis, this requires that the photon is collected along a specific axis (see subsection 7.1.3), since the entangled state between ion and photon depends on the observation angle of the photon. This is due to the quantum information being encoded in the polarisation degree of freedom of the photon. Due to its small solid angle, the fibre cavity has the conceptual advantage of overcoming difficulties of orthogonality of polarisations in light collection with high numerical aperture objectives [23, 161]. The photons are collected and extracted in a defined spatial mode.

We present a polarisation state sensitive detection of these photons in subsection 5.5.1. In addition, we show in subsection 5.5.2 that the extracted photons also have a defined time profile. Based on this profile, we perform a detailed analysis of the achieved cavity parameters including collection and detection efficiencies in subsections 5.5.2 and 5.5.3. In subsection 5.5.4 we present how a projective measurement of the polarisation state of the photon in an arbitrary basis can be realised.

5.5.1 Detection setup

We apply a magnetic field along the cavity axis in order to define the quantisation axis and suppress emission into the cavity mode with a change of magnetic quantum number of $\Delta m_F = 0$. Hence, only circular polarised photons are emitted by the ion into the cavity mode. After $\sim 1.5\,\mathrm{m}$ of fibre, we perform a detection of light leaving the cavity mode at a single photon level. In order to perform a projective measurement of the photon polarisation state, we use a polarising beam splitter (PBS) and two single photon counters[48] (SPCs), one on each exit path of the PBS, detecting horizontal (H) or vertical

[48] H12775 from Hamamatsu

(V) polarised photons (see Figure 5.17). To suppress stray light, we apply a 10 nm spectral filtering[49] in front of the SPCs. The basis to which we project the photon state is defined by a quarter-wave plate (QWP) and a half-wave plate (HWP), which are able to rotate the polarisation qubit state to any state on the Bloch-sphere (subsection 5.5.4).

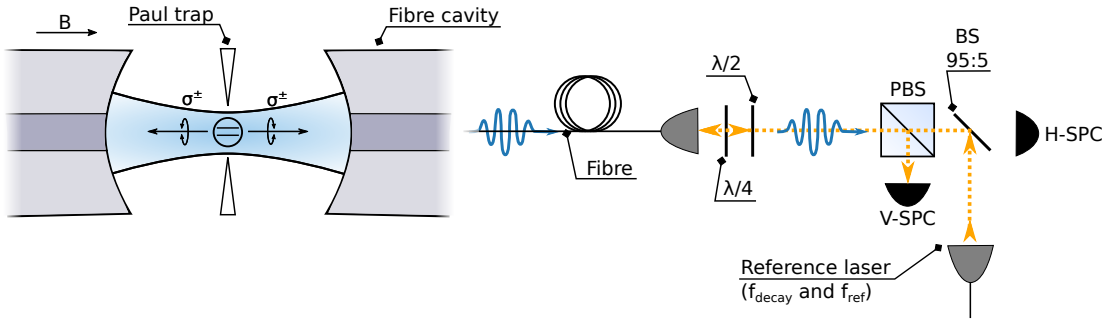

Figure 5.17: Sketch of the setup used for the detection of photons leaving the cavity mode. We collect the single emitted photons along the quantisation axis using the resonant cavity. Photons leaving the cavity through the single-mode fibre are projected to horizontal (H) and vertical (V) polarisation on each arm of the polarising beam splitter (PBS) respectively. We use a reference laser for stabilisation of the cavity length and calibration of the setup (yellow dashed line) (see section 5.3 and subsection 5.5.4).

Electronic processing of SPC signals

The key role of the cavity photons for the experiment entails a number of requirements for the detection setup. First, the length stabilisation of the fibre cavity requires a continuous feedback generated from the reflected photons of a probe laser at a medium regulation bandwidth (< 20 kHz). Second, the real-time feedback of single-photon detection events is required for a conditional branching of experimental sequences, which is highly time-critical ($< 1\,\mu$s). Furthermore, the suppression of false-positive events is crucial for high fidelity detection of the entangled state (subsection 7.4.2). We achieve above requirements with a real time electronic processing of the single photon counter TTL pulses (10 ns width), see Figure 5.18.

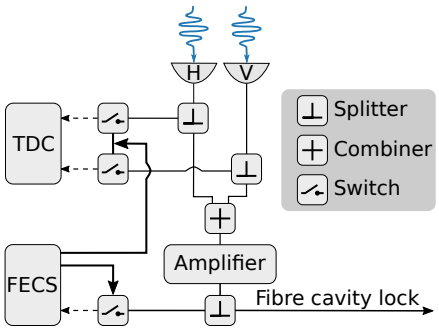

Figure 5.18: Sketch of the electronic circuit which processes the TTL pulses from the cavity SPCs. Photon counts are passed to the conditional sequence branching (FECS) and the TDC only during a 1 μs time window where photons from the trapped ion are expected.

The polarisation-resolved detection of the photons is performed by the SPCs in combi-

[49] FF01-370/10-25 from Semrock

nation with the TDC, where timestamps with a time resolution of $< 35\,\mathrm{ps}$ are assigned to the photon counts. The fast experimental control system (FECS) (see subsection 3.2.4) gates in-sequence decision branching and data acquisition on the TDC, while a separated signal is generated for the fibre cavity lock from the TTL pulses of the SPCs. For this purpose and for the purpose of conditional sequence branching at the stage of the FECS no differentiation of photon detection events by polarisation is necessary.

5.5.2 Time profile of the extracted photons and characterisation of the light-matter interface

In this subsection, the time profile of the photons extracted from the ion-cavity system is investigated. The photons are emitted by the excited ion through spontaneous decay of the $\left|{}^2\mathrm{P}_{1/2}, F' = 1, m_F = 0\right\rangle \equiv |e\rangle$ excited state into a single mode of the resonator and subsequently extracted through one of the fibre cavity mirrors (see Figure 5.17). The natural lifetime of the $|e\rangle$ state is $8.12(2)\,\mathrm{ns}$ [128]. We derive in subsection 7.1.2 that the time profile of a photon emitted spontaneously during the decay process of an excited state into free space has a characteristic exponentially decaying time shape whose time constant is determined by the lifetime of the excited state. However, for the presented measurement, the atom-cavity system as a whole determines the time profile of the extracted photons, which includes Purcell effect, cavity decay time and light-matter coupling regime as discussed in the following.

We can measure the photon time profile as a statistic of arrival times on the SPCs over multiple repetitions of atomic excitation and decay. In Figure 5.19 a) the binned arrival times of the detected photons extracted from the cavity are shown for H- and V-detector respectively. Due to an excitation pulse length of $\sim 130\,\mathrm{ps}$, the population transfer to the ion's excited state can be seen as instantaneous ($1/(130\,\mathrm{ps}) \gg \kappa, \Gamma$). We would expect a sharp rising edge of the photon time profile from this condition, however, the time profile is rounded by the cavity decay time (see equation (5.63)). Since the excitation pulse of the ion is detuned by $12.6\,\mathrm{GHz}$ from the resonance frequency of the cavity mode, we can neglect stray-light originating from the pulse appearing in the photon statistic (see section 6.3). The detection time stamp of each photon is synchronised to the arrival time of the excitation pulse in order to reach a sufficient time measurement accuracy. Otherwise, the $18.5\,\mathrm{ns}$ timing jitter of the excitation pulse would blur the time statistic of photon detection events (see subsection 6.3.3).

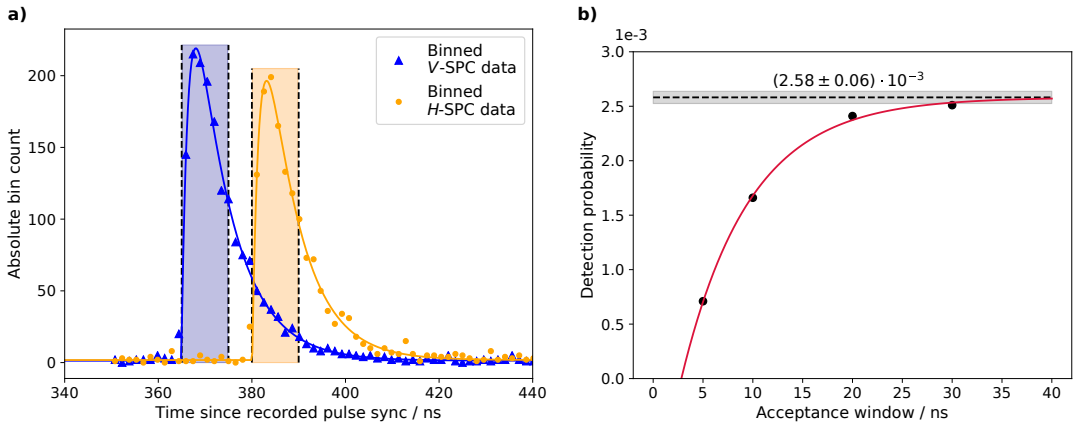

Figure 5.19: a) Binned detection times of the photons extracted through the fibre cavity on the V/H-detector (blue triangles/orange dots). The detection times are synchronised to the arrival time of the excitation pulse of the ion ('pulse sync'). The solid lines are fits according to two convolved exponential decay functions (equation (5.63)). The blue/orange shaded area represents a post-selection acceptance window of 10 ns. **b)** Measured detection probabilities of a photon per ion excitation attempt for different acceptance windows as shown in a). The values include the excitation probability $\eta_{\text{exc}} = 0.99(1)$ of the ion (see equation (6.42)). The solid line represents a fit to the measured data from which the the detection efficiency $P_{\text{d,measured}}$ is extracted (dashed line). The standard deviation error on $P_{\text{d,measured}}$ is given as grey shaded area. The data in a) have also been published in [92].

The time offset between H- and V-photon counts originate from a different wiring between the photon detectors and the time-to-digital converter (TDC). The optical path lengths for H and V are equal on the investigated timescale. The differing heights of the photon statistics for H and V originate from the path efficiencies which differ due to a beam splitter inserted for the reference laser into the H-path (see Figure 5.17).

We measure a full-width-at-half-maximum (FWHM) of the photon's temporal profile of 9.3(9) ns, which could be beneficial for impedance matching to further elements of a quantum network, especially when considering a hybrid network with different kind of nodes [117].

We can extract the Purcell-enhanced linewidth Γ' of the exited state manifold $^2\text{P}_{1/2}$ using the time profiles shown in Figure 5.19 a). The fast cavity regime ($\kappa \gg \gamma, g$) allows us to describe the photon time profile by convolving two exponential decays $f(t) = A \cdot e^{-t/\tau}$ for the cavity and $h(t) = e^{-t\cdot\Gamma'}$ for the spontaneous emission of the ion with $\tau = 1/(2\kappa)$ and $\Gamma = 2\gamma$ as

$$S(t>0) = \int_0^t f(x)h(t-x)\cdot dx = -\tau \cdot A \cdot \frac{e^{-t/\tau} - e^{-t\cdot\Gamma'}}{1-\tau\cdot\Gamma'} \qquad (5.63)$$
$$\text{and } S(t\leq 0) = 0.$$

The boundaries of the integral avoid causality issues for $t < 0$ and $t - x < 0$ for an ion excitation at $t = 0$. The amplitude A has to be introduced as a global scaling for $S(t)$ only for one of the decay functions f or h. We extract the Purcell-enhanced linewidth Γ' of the ion for the H- and V-detector signals respectively and average the two values to

$$\Gamma' = \Gamma\,(1 + 2C_{0,\text{eff}}) = 2\pi \cdot 21.39(51)\,\text{MHz}. \qquad (5.64)$$

We calculate the effective cooperativity to be $C_{0,\mathrm{eff}} = 0.046(13)$ according to equation (5.57) and deduce the effective light-matter coupling rate from this value as

$$g_{\mathrm{eff}} = \sqrt{C_{0,\mathrm{eff}} \cdot 2 \cdot \kappa \cdot \gamma} = 2\pi \cdot (7.2 \pm 1.2)\ \mathrm{MHz}\ , \tag{5.65}$$

with the atomic linewidth $\Gamma = 2\gamma = 2\pi \cdot 19.6\,\mathrm{MHz}$ [128]. The effective values include the effects of imperfect light-matter coupling, which could be caused, for example, by shortcomings in locking the cavity to the atomic resonance (see subsection 5.3) or overlapping the ion's position with the cavity mode (see subsection 5.4.5).

Knowing $C_{0,\mathrm{eff}}$, we can calculate the probability of a photon to get emitted into the cavity mode according to equation (5.60) as

$$P_{\mathrm{c,eff}} = \frac{2C_{0,\mathrm{eff}}}{2C_{0,\mathrm{eff}} + 1} = (8.4 \pm 2.2)\,\%. \tag{5.66}$$

From the characterisation of the cavity photon detection path, we determine the probability of detecting a photon on the single-photon counting modules per generation trial as

$$P_{\mathrm{d,eff}} = \eta_{\mathrm{exc}} \cdot P_{\mathrm{c,eff}} \cdot \eta_{\mathrm{ext}} \cdot \epsilon_m \cdot \eta_{\mathrm{path}} \cdot \eta_{\mathrm{Detector}} = 2.5(8) \times 10^{-3}\ \frac{\text{photons}}{\text{generation attempt}}, \tag{5.67}$$

where we used the excitation efficiency of the ion $\eta_{\mathrm{exc}} = 0.99(1)$ from equation (6.42), the mode matching between fibre and cavity $\epsilon_m = 0.44(3)$ (eq. (5.19)), the extraction probability through the desired cavity mirror $\eta_{\mathrm{ext}} = 0.53(6)$ (eq. (5.18)) and the quantum efficiency of the single-photon counters of $\eta_{\mathrm{Detector}} = 0.215$ according to the manufacture's specifications. We estimate the path efficiency η_{path} considering the transmission of the focussing lens in front of the SPCs 0.93(3), spectral filter 0.92(2), the fibre coupler 0.92(4) and the fibre 0.83(10) (per metre) [29] and calculate

$$\eta_{\mathrm{path}} = 0.60(11). \tag{5.68}$$

The transmission loss on the wave plates is negligible.

The estimated value of the detection efficiency $P_{\mathrm{d,eff}}$ from equation (5.67) agrees with the value of

$$P_{\mathrm{d,measured}} = 2.58(6) \times 10^{-3}\ \frac{\text{photons}}{\text{generation attempt}} \tag{5.69}$$

obtained from the measured probabilities for different acceptance windows as shown in Figure 5.19 b).

5.5.3 Discussion of the achieved cavity parameters

In order to better understand the measurement results of the previous subsection, we calculate in the following which results we expect based on the design parameters of the cavity. We start with a calculation of the achievable cooperativity based on the cavity waist ω_0. According to equation (5.11), we obtain for the TEM_{00} mode with $R = (280 \pm 36)\,\mu\mathrm{m}$ a waist of

$$\omega_0 = 4.1(2)\,\mu\mathrm{m}. \tag{5.70}$$

Using equations (5.47) and (5.59) for the cooperativity, we derive

$$C_{0,g0,\text{theo}} = \frac{\sigma}{A} \cdot \frac{F}{\pi} = 1.9(4), \tag{5.71}$$

with $\sigma = \frac{3\lambda^2}{2\pi}$ being the cross section of the ion, $A = \pi {\omega_0}^2$ the area of the cavity mode at its smallest waist and the finesse of the cavity $\mathcal{F} = 4700 \pm 700$ [29]. The cooperativity obtained from equation (5.71) assumes a light-matter coupling of g_0, whereas for the $\sigma^{\pm}$ decay we have to consider a factor of $\left(\sqrt{\frac{2}{3}}\right)^2$ coming from the Clebsch-Gordan coefficients $c_{\sigma^{\pm}}$ of the $\Delta m_F = \pm 1$ transitions (see Appendix B). This reduces the light-matter coupling rate to

$${g^2} = {g_0}^2 \cdot \sum_{k=\sigma^+,\sigma^-} c_i \quad \Rightarrow \quad g = \sqrt{\frac{2}{3}} \cdot g_0. \tag{5.72}$$

We calculate the cooperativity corrected for the observation of photons along the cavity axis as

$$C_{0,\text{theo}} = \frac{2}{3} \cdot C_{0,g0,\text{theo}} = 1.3(3). \tag{5.73}$$

From here, we perform the same calculation as for the effective values in the previous subsection by computing the collection and detection efficiencies $P_{\text{c,theo}}$ and $P_{\text{d,theo}}$. The effective values calculated from the measurement of the Purcell-enhanced linewidth (subsection 5.5.2) and the theoretical values calculated from cavity parameters can be found in Table 1 for a better comparison.

Experimental parameter	Effective value	Theoretical value
C_0	0.046(13)	1.3(3)
P_c / %	8.4 ± 2.2	72 ± 5
P_d / 10^{-3}	2.5 ± 0.8	21 ± 5
$\frac{g}{2\pi}$ / MHz	7.2 ± 1.2	38 ± 5

Table 1: Effective experimental parameters calculated from the measurement of the Purcell-enhanced linewidth and the theoretical values calculated from cavity parameters.

We measured significantly less coupling between the atom and the cavity than expected from the cavity design parameters of the cavity. We suppose that the experimental shortcomings in the fibre cavity stabilisation and the ion localisation within the cavity mode are the main reasons for this (see subsections 5.3.3 and 5.4.5).

A comparison of the presented fibre cavity system with previous realisations of cavities as light matter interfaces for atom-photon entanglement generation can be found in Table 2. It is apparent that the advantages of the fibre cavity are primarily the basis rates of the system and that a stable light-matter coupling can provide a collection efficiency on par with previous implementations.

Ref.	Atom	$\frac{g}{2\pi}$ / MHz	$\frac{\kappa}{2\pi}$ / MHz	$\frac{\gamma}{2\pi}$ / MHz	P_c	η_{ext}	ϵ_m
[143]	^{87}Rb	≤ 5	3	3	$\leq 0.6^{\dagger}$	0.9	$\leq 0.9^{**}$
[99]	$^{40}Ca^{+}$	1.53(1)	0.070(2)	11.45	$\leq 0.75^{*}$	0.83(3)	$0.5(1)^{**}$
[164, 162]	$^{40}Ca^{+}$	1.4	0.05	11.2	$\approx 1^{\dagger}$	0.2	no fibre
This work	$^{171}Yb^{+}$	7.2 ± 1.2 $\{38 \pm 5\}$	58 ± 9	9.8	0.08(2) $\{0.72(5)\}$	0.53(6)	0.44(3)

Table 2: Characteristic parameters achieved with previous cavity-based atom-photon entanglements. Theoretically achievable values for the presented experiment are written in curly brackets. * Parameter calculated from g, κ, Γ. ** Equivalent fibre coupling efficiency is given for a macroscopic cavity. † Equivalent photon generation efficiency. Due to a different photon generation scheme, there is no collection efficiency P_c in the sense of this thesis.

5.5.4 Projective measurement of the photonic qubit state

Due to the polarising beam splitter (PBS), the projective measurement of a photon's polarisation state always happens to the horizontal (H) and vertical (V) polarisation basis states. In order to project the photon state to an arbitrary basis, we have to rotate the polarisation state along the optical path accordingly. This then determines the mapping of the polarisation eigenstates of a given basis onto the linear H- and V- detection basis. The mapping can be defined in general as a rotation on the Bloch-sphere, where HWP and QWP implement distinct rotation operations. Since other elements of the optical path can also rotate the polarisation state, we need to fully characterise the polarisation properties of each optical element along the photonic path to enable the state detection of the photon in a defined basis.

To describe the photonic path, we use the Jones matrix formalism and start with a polarisation state of the photon $\mathbf{S}_{\text{in}}$ in the cavity mode and calculate the polarisation rotation of the state along the optical path (Figure 5.17). The polarisation state after its rotation and right before the PBS can be calculated as

$$\mathbf{S}_{\text{out}} = \text{HWP}\left(\theta_{\text{hwp}}\right) \cdot \text{QWP}\left(\theta_{\text{qwp}}\right) \cdot M_{\text{fibre}}\left(\theta_{\text{fibre}}, \phi\right) \cdot \mathbf{S}_{\text{in}}. \tag{5.74}$$

The influence of HWP and QWP on the polarisation state are well known, but additional elements in the setup may rotate the polarisation state as well. Starting from a photon state in the cavity, we summarise the state manipulation up to the position of the wave plates as a single arbitrary phase retarder M_{fibre} [50]. The rotation matrices of the path are given as:

$$M_{\text{fibre}}\left(\theta_{\text{fibre}}, \phi\right) = R_z(\theta_{\text{fibre}}) \cdot \begin{pmatrix} 1 & 0 & 0 \\ 0 & e^{i\phi} & 0 \\ 0 & 0 & 1 \end{pmatrix} \cdot R_z(-\theta_{\text{fibre}}), \tag{5.75}$$

$$\text{HWP}\left(\theta_{\text{hwp}}\right) = R_z\left(\theta_{\text{hwp}}\right) \cdot \begin{pmatrix} 1 & 0 & 0 \\ 0 & -1 & 0 \\ 0 & 0 & 1 \end{pmatrix} \cdot R_z\left(-\theta_{\text{hwp}}\right), \tag{5.76}$$

[50] We assume that the fibre has the main influence there

$$\mathrm{QWP}\left(\theta_{\mathrm{qwp}}\right) = R_z\left(\theta_{\mathrm{qwp}}\right) \cdot \begin{pmatrix} 1 & 0 & 0 \\ 0 & i & 0 \\ 0 & 0 & 1 \end{pmatrix} \cdot R_z\left(-\theta_{\mathrm{qwp}}\right). \tag{5.77}$$

The given Jones matrices allow a transformation of the polarisation state with respect to the orientation of the amplitude vector of the electric field of a photon. However, they must not be used for interference calculations of electric fields. We define the z-axis as propagation direction of the photon. Furthermore, we define $R_z\left(\theta\right)$ as the rotation matrix around the z-axis by an angle θ, which is used for rotation of the fast axis of a polarisation element with respect to the x- and y-axis defining vertical and horizontal polarisation respectively.

The PBS always projects the polarisation state $\mathbf{S}_{\mathrm{out}}$ to the linear polarisation basis H and V. By assigning a Jones vector $\mathbf{S}_X$ to each detection arm of the PBS with $X \in \{H, V\}$, we infer the detection probability of an incoming photon on one of the detection arms from the state overlap as

$$D_X(\mathbf{S}_{\mathrm{out}}) = r(\mathbf{S}_{\mathrm{out}}, \mathbf{S}_X) \quad \text{with} \quad \mathbf{S}_H \equiv \begin{pmatrix} 0 \\ 1 \\ 0 \end{pmatrix}, \mathbf{S}_V \equiv \begin{pmatrix} 1 \\ 0 \\ 0 \end{pmatrix}. \tag{5.78}$$

We calculate the state overlap of two Jones vectors u and v as

$$r(\mathbf{u}, \mathbf{v}) = \left|\mathbf{u}_e^\dagger \mathbf{v}_e\right|^2 \quad \text{with} \quad \mathbf{u}_e = \frac{\mathbf{u}}{|\mathbf{u}|} \text{ and } \mathbf{v}_e = \frac{\mathbf{v}}{|\mathbf{v}|}. \tag{5.79}$$

In order to determine the free parameters in equation (5.74), we probe the photon path using a weak laser ($\sim 50\,\mathrm{pW}$) coupled through the PBS into the fibre (see Figure 5.17). Since the laser frequency is off-resonant by a few GHz with respect to the cavity mode, it gets reflected on the first fibre mirror. Monitoring the count rate of reflected photons on the V-SPC for different wave plate rotation angles leads to a heat map as shown in Figure 5.20 a).

To reproduce this data with our model, we propagate an initial H-polarised photon backwards through the path described in equation (5.74). Subsequently, we simulate the reflection on a mirror and propagate again though the original path. We end up with a polarisation state $\mathbf{S}_{\mathrm{out}}$ of the photon for which we calculate the probability $D_V(\mathbf{S}_{\mathrm{out}})$ to trigger a count on the V-SPC using equation (5.78). Doing this for all measured wave plate angles while performing a least square fit[51] to the two-dimensional scalar data set, we are able to determine the polarisation retardation of the fibre as well as the rotation offset of the fast axes of our wave plates.

[51] using the Python package scipy.optimize.curve_fit with standard parameters

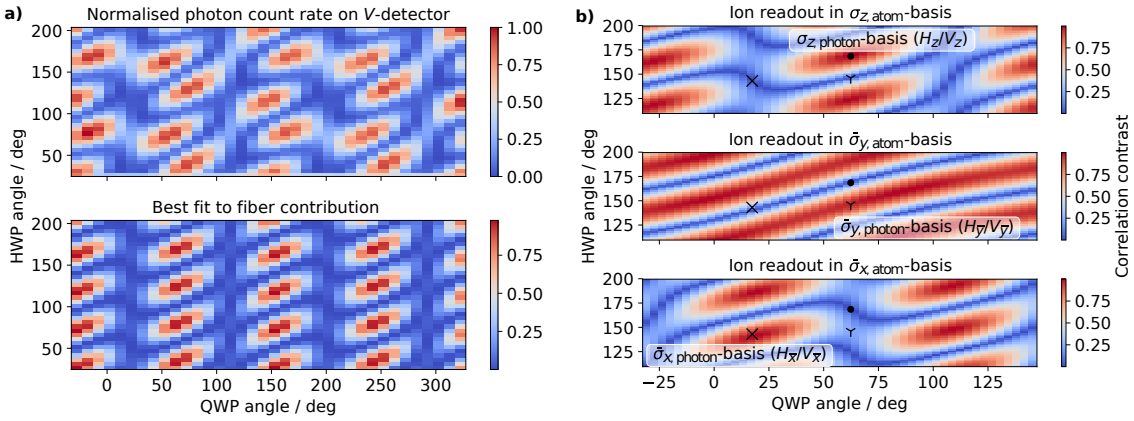

Figure 5.20: a) Characterisation of the polarisation rotation of the photon detection setup using a reference laser as shown in Figure 5.17. The normalised count rate of reflected photons on the V-detector for different wave plate angles is shown (top). Fit of the data assuming the fibre to be an arbitrary polarisation element (bottom). **b)** Calculated correlation heat-map estimated from the separability defined in equation (5.84) and optical path parameters determined from the fit in a). We repeat the calculation for different starting polarisations $\mathbf{S}_{\text{in}}$ corresponding to different atomic qubit readout bases. The corresponding wave plate settings for a photon readout in the same basis are labelled accordingly with lower indices H_i/V_i with $i \in (\bar{x}, \bar{y}, z)$. For definition of $\bar{\hat{\sigma}}_{x,y}$, see equation (5.87). The data have also been published in [92].

Once we have characterised the photon path, we use the obtained values to simulate the propagation of a photon along this path using equation (5.74). In order to project the photon state onto a certain basis $\hat{\sigma}_j$, the eigenstates of this basis given according to equation (2.3) as

$$\hat{\sigma}_j \left|\Psi_{\lambda\cdot j}\right\rangle = \lambda \cdot \left|\Psi_{\lambda\cdot j}\right\rangle \tag{5.80}$$

must be mapped to the eigenstates of the projective measurement $|H\rangle$ and $|V\rangle$. The following calculations were made for the entangled atom-photon state

$$\left|\Psi_{\text{atom-photon}}\right\rangle = \frac{1}{\sqrt{2}}\left(\left|\sigma^+\right\rangle\left|g^+\right\rangle - \left|\sigma^-\right\rangle\left|g^-\right\rangle\right), \tag{5.81}$$

which is generated in the presented experiment according to chapter 7. However, the methodology is applicable to any definition of the basis states $|\Psi_{\lambda\cdot j}\rangle$.

For the wave plate setting corresponding to a photon state detection in the $\hat{\sigma}_z$ basis, the eigenstates $|\sigma^{\pm}\rangle$ are mapped to horizontal and vertical polarisation in a single pass of the optical path as follows:

$$\begin{aligned} \left|\sigma^+\right\rangle &\equiv \left|\Psi_z\right\rangle &&\rightarrow \left|V\right\rangle, \\ \left|\sigma^-\right\rangle &\equiv \left|\Psi_{-z}\right\rangle &&\rightarrow \left|H\right\rangle. \end{aligned} \tag{5.82}$$

Which circular polarisation state is mapped to which linear polarisation state is not important at this point at the beginning of the considerations. However, the mapping of the remaining photonic bases and the mapping of the atomic state in chapter 6 must take this definition into account.

The mapping described in equations (5.82) requires the optical path of the photon to act in total as a quarter-wave plate. For the reflection of the initial H-polarised reference light,

this results in maximal counts on the V-SPC[52] (local maximum in Figure 5.20 a)). For this wave plate settings, a maximal correlation contrast between the detected photon state and the detected ion state both measured in $\hat{\sigma}_z$ basis can be expected for entanglement between atom and photon (see Figure 5.20 b)).

We can use a purely classical description of the polarisation states, since each individual particle of an entangled pair is not in a phase-coherent quantum state by itself, but in a statistical mixed state [174]. Therefore, a quantum mechanical description including the full ion-photon state is not necessary when focusing on the polarisation manipulation of the photonic path.

To compute the expected correlation contrast, we propagate the two polarisation eigenstates $\mathbf{S}_{\Psi_{\pm j}}$ for a given basis $\hat{\sigma}_j$ along the optical path using equation (5.74) and compute how well the two output states $\mathbf{S}_{\text{out},\pm j}$ separate at the two detection arms H and V of the PBS for different angles of HWP and QWP (see Figure 5.20 b)). We calculate the separation w as

$$\begin{aligned} w_{V\text{-detector}} &= \left\| \frac{(D_V(\mathbf{S}_{\text{out},+j}) - D_V(\mathbf{S}_{\text{out},-j})}{(D_V(\mathbf{S}_{\text{out},+j}) + D_V(\mathbf{S}_{\text{out},-j})} \right\| \text{ and} \\ w_{H\text{-detector}} &= \left\| \frac{(D_H(\mathbf{S}_{\text{out},+j}) - D_H(\mathbf{S}_{\text{out},-j})}{(D_H(\mathbf{S}_{\text{out},+j}) + D_H(\mathbf{S}_{\text{out},-j})} \right\| \end{aligned} \tag{5.83}$$

from which we obtained the average separability as

$$w_{\text{tot}} = (w_{V\text{-detector}} + w_{H\text{-detector}})/2. \tag{5.84}$$

The separability directly states the expected correlation contrast between atomic and photonic state for a detection of the entangled state in the $\hat{\sigma}_{\text{atom}} \otimes \hat{\sigma}_{\text{photon}}$ basis. The state projection on the atomic side $\hat{\sigma}_{\text{atom}}$ is reflected by the eigenstates $\mathbf{S}_{\Psi_{\pm j}}$, which were used as a starting polarisation state $\mathbf{S}_{\text{in}}$. The state projection on the photonic side $\hat{\sigma}_{\text{photon}}$ is defined by the remaining free parameters of equation (5.74).

The eigenstates of the $\hat{\sigma}_z$ basis $|\Psi_{\pm z}\rangle = |\sigma^{\pm}\rangle$ are represented by the polarisation state vectors $\mathbf{S}_{\Psi_{\pm z}} = \mathbf{S}_{\sigma^{\pm}}$ in the Jones-formalism as

$$\mathbf{S}_{\sigma^+} = 0.5 \cdot \begin{pmatrix} 1-i \\ 1+i \\ 0 \end{pmatrix} \quad \text{and} \quad \mathbf{S}_{\sigma^-} = 0.5 \cdot \begin{pmatrix} -1+i \\ 1+i \\ 0 \end{pmatrix} \tag{5.85}$$

For the rotated bases ($\hat{\sigma}_{x,y}$), a superposition of the polarisation basis states $|\sigma^{\pm}\rangle$ has to be mapped to horizontal and vertical polarisation as

$$\begin{aligned} |\Psi_{x,y}\rangle &= \frac{1}{\sqrt{2}} \left(\left|\sigma^+\right\rangle + e^{i\beta_{x/y}} \cdot \left|\sigma^-\right\rangle \right) \rightarrow |V\rangle \text{ and} \\ |\Psi_{-x,-y}\rangle &= \frac{1}{\sqrt{2}} \left(\left|\sigma^+\right\rangle - e^{i\beta_{x/y}} \cdot \left|\sigma^-\right\rangle \right) \rightarrow |H\rangle\,, \end{aligned} \tag{5.86}$$

with $\beta_x = 0$ and $\beta_y = \pi/2$, where β is controllable by the wave plates. This mapping of the eigenstates preserves the corresponding eigenvalue ($\lambda = \pm 1$) for all bases $\hat{\sigma}_{x/y/z}$ according to equation (5.80).

[52] A path of QWP→mirror→QWP maps H to V polarisation for a fast axis rotated by 45 degree with respect to the polarisation axis.

However, we found that defining the rotated bases as $\bar{\hat{\sigma}}_k$, $k \in (x, y)$ with the eigenstates

$$\left\{ \left|\Psi_{\bar{k}}\right\rangle, \left|\Psi_{-\bar{k}}\right\rangle \right\} = \left\{ \frac{1}{\sqrt{2}} \left(\left|\sigma^+\right\rangle + e^{i\beta_{\bar{k}}} \left|\sigma^-\right\rangle \right), \frac{1}{\sqrt{2}} \left(\left|\sigma^+\right\rangle + e^{i\beta_{\bar{k}}+\pi} \left|\sigma^-\right\rangle \right) \right\}, \tag{5.87}$$

where $\beta_{\bar{x}} = \pi/4$ and $\beta_{\bar{y}} = 3\pi/4$ results in easily accessible angles of the wave plates as shown in Figure 5.20 b).

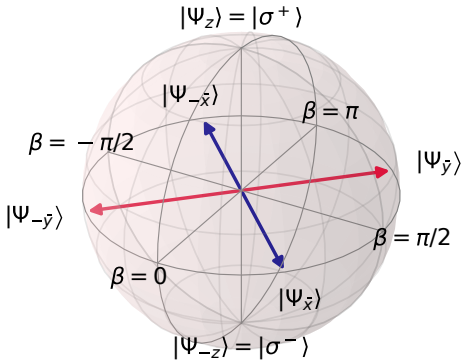

Figure 5.21: Basis definition of polarisation states on the Bloch-sphere. The eigenstates of $\bar{\hat{\sigma}}_{x/y}$ from equation (5.87) are sketched as blue/red arrows.

The set of bases $\{\bar{\hat{\sigma}}_x, \bar{\hat{\sigma}}_y, \hat{\sigma}_z\}$ for which we present the measured correlations in sections 7.3 and 7.4 are shown in Figure 5.21. The same basis definition holds for the ion, since detection of a photon projects the ion to the corresponding state. We verified from the simulation of the photon path that we project the eigenstate $\left|\Psi_{\pm\bar{k}}\right\rangle$ of the basis $\bar{\hat{\sigma}}_k$ according to

$$\begin{aligned} \left|\Psi_{+\bar{k}}\right\rangle &\rightarrow |V\rangle \text{ and} \\ \left|\Psi_{-\bar{k}}\right\rangle &\rightarrow |H\rangle . \end{aligned} \tag{5.88}$$

This ensures that also for this definition of the bases the mapping of the eigenstates preserves the corresponding eigenvalue ($\lambda = \pm 1$) for all bases $\hat{\sigma}_{\bar{x}/\bar{y}/z}$.

5.5.5 Birefringence of the fibre cavity

Due to a potential elliptic shape, our fibre mirrors usually exhibit birefringence which manifests itself in a frequency splitting $\nu_{\Delta\mathrm{HV}}$ of the linear polarisation modes H/V within a fibre resonator. The frequency splitting due to a birefringent dephasing on the elliptic paraboloidal mirrors can be calculated as [57]

$$\nu_{\Delta\mathrm{HV}} = \kappa \cdot \frac{\lambda\mathcal{F}}{2\pi^2} \cdot \sqrt{\delta_1^2 + \delta_2^2 + 2\delta_1\delta_2\cos(2\theta)} \quad \text{with} \quad \delta_i = \frac{1}{R_{a,i}} - \frac{1}{R_{b,i}}, \tag{5.89}$$

where $R_{a,i}$ is the long and $R_{b,i}$ the short radius of curvature (ROC) along the eigenaxes of the mirror $i \in \{1, 2\}$ and $\delta_i \cdot \frac{\lambda}{2\pi} \ll 1$. The angle θ states the relative orientation of the fast axes of the two mirrors. The fast axes of the first mirror is assumed to be parallel to the vertical direction.

Since for our pool of fibres the ROCs were determined from the phase-shifting interferometry of the fibre tips with an accuracy of $\sim 30\,\mu$m, we can chose a set of fibres which radii

of curvature result in $\nu_{\Delta\mathrm{HV}}$ being smaller than the cavity linewidth $\kappa = 2\pi \cdot (58 \pm 9)\,\mathrm{MHz}$. However, the splitting of the H/V modes could be in fact still much higher than the energy splitting $\omega_L \sim 2\pi \cdot 1.6\,\mathrm{MHz}$ of the stationary qubit levels $|g^{\pm}\rangle$ (see Figures 5.22 and 6.1).

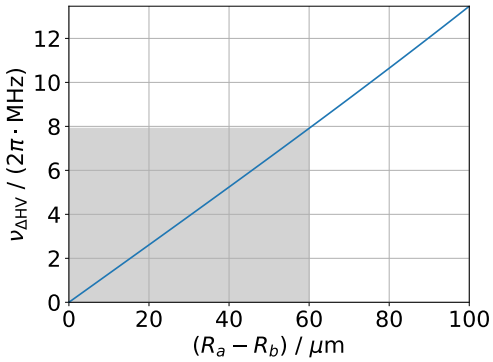

Figure 5.22: Estimated frequency splitting of the polarisation modes H/V in the cavity with Finesse $\mathcal{F} \sim 4700$, linewidth $\kappa \sim 2\pi \cdot 58\,\mathrm{MHz}$, $(R_{a,i} + R_{b,i})/2 \sim 280\,\mu\mathrm{m}$ and $\theta = 0$. The grey shaded area denotes the uncertainty region resulting from $\max\left[R_{a,i} - R_{b,i}\right] \approx 60\,\mu\mathrm{m}$ for $i = 1, 2$. For the calculation we assumed $R_{a,1} = R_{a,2} = R_a$ and $R_{b,1} = R_{b,2} = R_b$.

An energy splitting of the photonic modes of the entangled ion-photon state can cause the phase of the the entangled state to rotate at the corresponding frequency. However, for the emission of circularly polarised photons into the cavity mode, we do not observe a significantly increased phase evolution of the ion-photon state. The measured results are consistent to a phase evolution with a timescale being of the order of the atomic level splitting (see subsection 7.4.2). We suppose that the equal superposition of linear polarisation modes in a circular polarisation state cancel out a potential frequency splitting $\nu_{\Delta\mathrm{HV}}$ in phase evolution. Nevertheless, the emission probability of circularly polarised photons into the cavity mode could depend on the spectral overlap of the H- and V-polarised resonator modes, which could reduce the rate of entanglement generation.

5.6 Summary

We have introduced a fibre Fabry-Pérot resonator as a light-matter interface, which constitutes a key element of the quantum network node presented in this thesis. The fibre cavity not only enables the efficient collection and extraction of photons in a defined spatial mode, it also provides control over the polarisation state and time profile which are prerequisites for an application of the collected photons as travelling qubits in quantum communication.

We measure an effective light-matter coupling rate of $g_{\mathrm{eff}} = 2\pi \cdot (7.2 \pm 1.2)\,\mathrm{MHz}$ and a collection efficiency of photons of $P_{c,\mathrm{eff}} = (8.4 \pm 2.2)\,\%$ while maintaining a fast extraction of photons out of the cavity of 1.4(1) ns. These properties are enabled by the small resonator mode volume. Compared to previous cavity-based realisations of entangled atom-photon states, we achieved to our knowledge the yet shortest temporal shape of photons of 9.3(9) ns extracted through the cavity by more than one order of magnitude [143, 99, 164] (see chapter 7 for the verification of entanglement). This is not only advantageous for impedance matching to further nodes, but also allows the cavity to be used in

networks with a high data throughput.

In the context of quantum communication, we presented the projective polarisation state detection a photon extracted from the fibre cavity, where we achieved full insight into the polarisation rotation of the detection setup are are able to project the state to an arbitrary basis. Furthermore, we have shown that with the cavity assembly presented in this thesis we have overcome some of the limiting shortcomings of previous fibre cavity realisations, such as mirror degradation, lock-ability, microwave incompatibility and destabilisation of the ion trapping. We identified mechanical low-frequency resonances of the piezo tube, probably excited by $1/f$ noise, as the main problem for the length stabilisation of the resonator. To this end, we investigated the excitation resonances of the cavity design up to 10 kHz. For the length stabilisation, we realised a side-of-fringe locking scheme working at ultra-low light powers of ~ 50 pW, which mitigates the charging problem of the dielectric mirror in combination with UV light.

6 The ^{171}Yb ion as a memory qubit

Contents

6.1 State initialisation 89
6.2 Fluorescence state detection 90
6.3 Pulsed excitation 100
6.4 Hyperfine qubit manipulation 116
6.5 Coherence time 128
6.6 Magnetic field control 132
6.7 Summary 139

Memory qubits are a crucial part of quantum information processing. Besides the implementation of universal quantum computers [183], the ability to coherently store quantum information allows overcoming the rate-distance limit of point-to-point quantum communication [137, 21] that arises from the absorption of information carriers in a medium. Therefore, memory qubits enable the realisation of large-scale quantum networks.

In practice, there are important points to consider in order to successfully store quantum information in a memory qubit: first, the qubit should be accessible to high-fidelity initialisation, manipulation and readout. Second, the time span in which the coherent information can be retrieved from the qubit with sufficiently low error (coherence time) must scale with the characteristic timescale of the targeted application. In a quantum network, this timescale is usually determined by the characteristic distance and the number of nodes of the network. Third, in a quantum network, the efficient mapping of information between the travelling qubit states and the long-lived memory qubit states is essential. We introduced an effective light-matter interface for this purpose in the previous chapter.

In this chapter, we discuss the capabilities of the ^{171}Yb ion with respect to an application as a stationary memory qubit in quantum communication. The level scheme of $^{171}Yb^{+}$ exhibits a hyperfine splitting of the $^2S_{1/2}$ manifold of 12.6 GHz which is well suited for coherently storing and manipulating quantum information. From Figure 6.1, we identify a total of three microwave-accessible two-level hyperfine transitions that enable encoding of quantum information: $|0\rangle \leftrightarrow |g^-\rangle$, $|0\rangle \leftrightarrow |g^+\rangle$ and $|0\rangle \leftrightarrow |g^0\rangle$, where we defined

$$\begin{aligned}
\left|^2S_{1/2}, F=1, m_F=-1\right\rangle &\equiv \left|g^+\right\rangle, \\
\left|^2S_{1/2}, F=1, m_F=+1\right\rangle &\equiv |g^-\rangle, \\
\left|^2S_{1/2}, F=1, m_F=0\right\rangle &\equiv \left|g^0\right\rangle \text{ and} \\
\left|^2S_{1/2}, F=0, m_F=0\right\rangle &\equiv |0\rangle .
\end{aligned} \tag{6.1}$$

The first-order magnetic field insensitive transition between the $|0\rangle$ state and the $|g^0\rangle$ state constitutes a so-called 'clock transition' and is often used as a memory qubit, due to achievable coherence times in the order of seconds to minutes [129, 178].

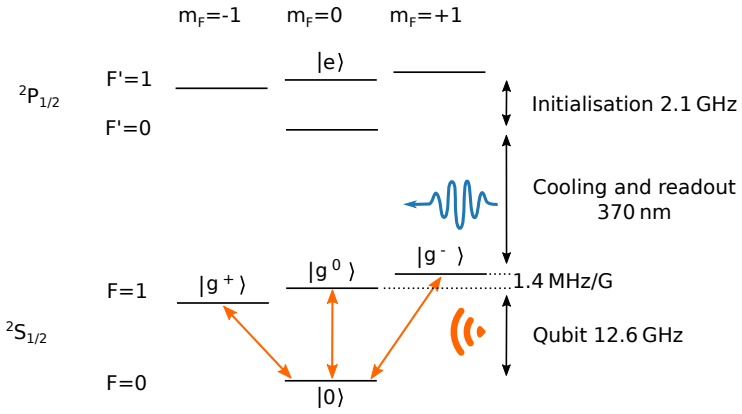

Figure 6.1: Relevant energy levels of $^{171}\mathrm{Yb}^+$. The microwave transitions are shown as orange arrows. Energy splitting not to scale.

We present in section 6.1 how we initialise a qubit state with high fidelity and in section 6.2 how we read out a qubit state. In section 6.3, we present the deterministic excitation of the ion using an ultra-fast laser pulse to an excited state $|e\rangle$. The precise state manipulation together with the spontaneous decay of the excited level makes the trapped Yb ion well suited as a deterministic single photon emitter. In addition, the long-lived internal memory qubit states favour the creation of an entangled two-qubit state between the ion and the emitted photon.

We present the manipulation of the atomic spin state using phase-coherent microwave pulses in section 6.4 and introduce a theoretical model capable of describing the coherent state manipulation and the mapping of information between the hyperfine qubits. This enables quantum information processing with the atomic qubit and allows the projection of the atomic state to an arbitrary basis. We measure the coherence time of the hyperfine qubits $|0\rangle \leftrightarrow |g^{\pm}\rangle$ and $|0\rangle \leftrightarrow |g^0\rangle$ and the Zeeman qubit $|g^-\rangle \leftrightarrow |g^+\rangle$ in section 6.5. Finally, we use the magnetic field dependence of the two-level transitions as a sensor in section 6.6 to characterise the magnetic field to an accuracy of $\sim 100\,\mu$G, which we utilise to improve the coherence time of the qubit transitions by noise reduction.

6.1 State initialisation

The majority of experimental sequences and techniques presented in this chapter requires a defined state of the atomic qubit as a starting point for further operation. For state initialisation, we optically pump the ^{171}Yb ion to the $|0\rangle$ state. This state is far detuned with $\sim 12.6\,$GHz from the Doppler cooling light, which is near resonant to the $\left|^2\mathrm{S}_{1/2}, F=1\right\rangle \leftrightarrow \left|^2\mathrm{P}_{1/2}, F'=0\right\rangle$ transition with a natural linewidth of $\Gamma = 2\pi \cdot 19.6\,$MHz.

Since electric dipole transitions with $\Delta F = 0 \wedge \Delta m_F = 0$ are forbidden by selection rules, coupling to the $|0\rangle$ state of $^{171}\mathrm{Yb}^+$ happens via scattering on the $\left|^2\mathrm{P}_{1/2}, F'=1\right\rangle$ levels. For this purpose, we modulate a 2.1 GHz sideband to the Doppler cooling light which facilitates scattering on the $\left|^2\mathrm{P}_{1/2}, F'=1\right\rangle$ levels (see Figure 6.2 a)). At the same time, we switch off the 14.7 GHz modulated sideband of the cooling laser, which transfers population back from the $|0\rangle$ state to the cooling cycle (see subsection 3.1.3). Therefore, population remains in the $|0\rangle$ state, which enables fast initialisation into this dark state with fidelities exceeding 99 % (see Figure 6.2 b)).

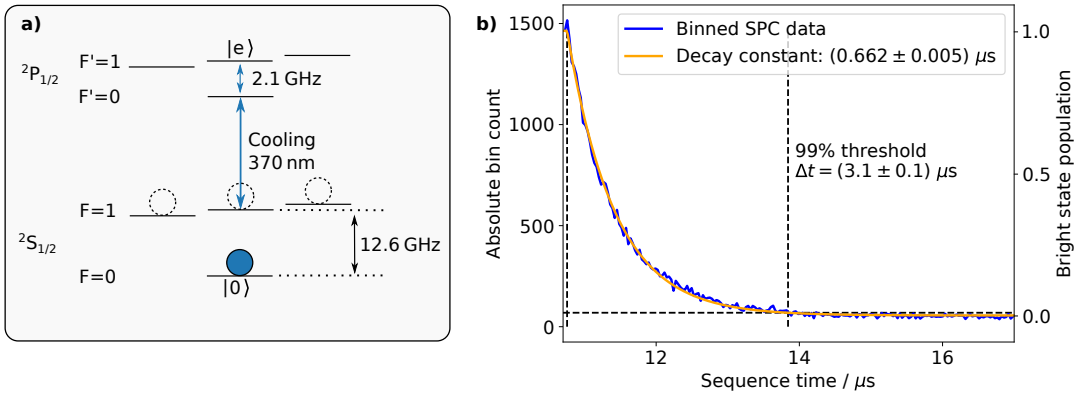

Figure 6.2: State initialisation of the atomic qubit. **a)** Relevant hyperfine energy level scheme of $^{171}Yb^+$. The ion is optically pumped to the $|0\rangle$ dark state (blue circle) using a 2.1 GHz sideband modulated to the Doppler cooling laser. The dashed circles denotes the populated energy levels during the cooling process, which gets emptied during initialisation. **b)** The free-space detection rate of scattered photons by the driven ion (blue line) decreases over time while the population gets transferred from the bright states $\left|^2S_{1/2}, F = 1\right\rangle$ to the $|0\rangle$ state. We fit an exponential decay (orange line) with a decay constant of 0.662(5) μs to the binned photon detection events obtained from 8.4×10^6 initialisation runs. The initialisation starts at a time offset of 10.8 μs.

We use the $|0\rangle$ state as a starting point for coherent manipulation of the hyperfine qubits or for ultra-fast excitation of the ion. For any experimental sequence which includes a state initialisation, the initialisation time constitutes a fundamental limit on the repetition rate of the specific sequence. For the presented implementation of a quantum network node, the data throughput is limited to ~ 300 kHz as we can not generate entangled atom-photon states faster than the minimal initialisation time of the atomic qubit of $\Delta t = 3.1(1)\,\mu$s. However, the initialisation time depends on the specific implementation. State preparation times of a few hundreds of nano-seconds are possible with trapped ions [161]. In our case, we could shorten the initialisation time by using, for example, a separate laser for pumping the ion into the $|0\rangle$ state instead of a weak sideband on the cooling laser.

6.2 Fluorescence state detection

In addition to initialising the qubit, it is of course also important to access information stored in the qubit with a high fidelity. To this end, we present in this section the readout of the atomic state based on fluorescence detection.

A projective measurement of a state, also called 'von Neumann measurement', describes an observable quantity A represented by a Hermitian operator $\hat{A}$ [9]. The eigenvalues λ_n of the operator $\hat{A}$ are possible results of the observable A and are related to the eigenstates $|\lambda_n\rangle$ of the operator as

$$\hat{A}\,|\lambda_n\rangle = \lambda_n\,|\lambda_n\rangle\,. \tag{6.2}$$

In the case of a bright $|B\rangle$ and a dark $|D\rangle$ state of an atom with respect to a driving laser field, the observable A is given by the observation of a bright atom (scattered photons) or a dark atom (no photons) (see Figure 6.3 a)). We define $\lambda_B = +1$ for the observation of a bright ion and $\lambda_D = -1$ for the observation of a dark ion. If the eigenstates form a basis

of the investigated Hilbert space, we can write

$$\hat{A} = \sum_n \lambda_n |\lambda_n\rangle \langle\lambda_n| = |B\rangle \langle B| - |D\rangle \langle D|, \tag{6.3}$$

where the probability of a measurement to give the result λ_n is given by [9]

$$P(\lambda_n) = \langle\lambda_n| \hat{\rho} |\lambda_n\rangle = \mathrm{Tr}(\hat{\rho} |\lambda_n\rangle \langle\lambda_n|). \tag{6.4}$$

The density matrix $\hat{\rho}$ represents the state ot the atom prior to the measurement. If the measurement is repeated several times with the same realisations of the state $\hat{\rho}$, then the expected value of the measurement result is

$$\left\langle \hat{A} \right\rangle = \sum_n P(\lambda_n) \cdot \lambda_n. \tag{6.5}$$

The average population of the bright state $|B\rangle$ is then given as $\rho_{\mathrm{bright}} = P(\lambda_B)$, which for our definition of $\lambda_{\substack{B \\ D}} = \pm 1$ can be written as

$$\rho_{\mathrm{bright}} = \frac{1 + \left\langle \hat{A} \right\rangle}{2}. \tag{6.6}$$

As an example, the mixed state $\hat{\rho}_{\mathrm{mixed}} = \frac{1}{2}(|B\rangle \langle B| + |D\rangle \langle D|)$ gives $\left\langle \hat{A} \right\rangle = 0$ and $\rho_{\mathrm{bright}} = 0.5$ on average. For a single measurement of the state, however, we measure either a dark atom $\lambda_D = -1$ with a probability of $P(\lambda_D)$ or a bright atom with probability $P(\lambda_B)$ and $\lambda_B = +1$. In the subsections 6.2.1 and 6.2.2 we discuss the respective experimental implementation of $\left\langle \hat{A} \right\rangle$ and $\hat{A}$ in more detail, but we start with a presentation of the overall experimental framework in the following.

We use a 370 nm laser to perform a projective measurement of the atomic state by driving the ion near resonant on the $\left|{}^2S_{1/2}, F = 1\right\rangle \leftrightarrow \left|{}^2P_{1/2}, F' = 0\right\rangle$ transition in order to distinguish between the $\left|{}^2\mathrm{S}_{1/2}, F = 1\right\rangle$ states and the $|0\rangle$ dark state. In the experiment, we switch of the hyperfine repumping sideband at 14.7 GHz, but keep the 935 nm repump laser enabled to achieve that the $\left|{}^2\mathrm{S}_{1/2}, F = 1\right\rangle$ manifold and the $|0\rangle$ state are eigenstates of the measurement operator $\hat{A}$ (see subsection 3.1.3). However, off-resonant scattering on the $\left|{}^2\mathrm{P}_{1/2}, F' = 1\right\rangle$ levels induce a coupling between the states, such that the eigenstate assumption is violated for long measurement times (see subsection 6.2.2). We collect photons emitted by the ion into free space using an objective with a geometric numerical aperture of NA = 0.48 and a single photon counter (SPC) according to subsection 3.2.3 and Figure 6.3 b).

For the sake of simplicity, we introduced the bright state as a single state $|B\rangle$ so far. In the experiment, however, the 'bright state' is given by the $\left|{}^2\mathrm{S}_{1/2}, F = 1\right\rangle$ manifold as can be seen in Figure 6.3 c) and we cannot distinguish between the orthonormal Zeeman states $|g^+\rangle$, $|g^-\rangle$ and $|g^0\rangle$. This corresponds to a number of eigenstates sharing the common eigenvalue λ_B. The probability for the observation of a bright ion is then given by [9]

$$P(\lambda_B) = \mathrm{Tr}(\hat{\rho}\hat{P}_B) \quad \text{with} \quad \hat{P}_B = \left|g^+\right\rangle \left\langle g^+\right| + \left|g^0\right\rangle \left\langle g^0\right| + |g^-\rangle \langle g^-|. \tag{6.7}$$

We have to be aware that using the fluorescence state detection, we project a pure state $|\Psi\rangle$ onto the bright state manifold population as

$$|\langle\Psi|F = 1\rangle|^2 \to |\left\langle\Psi|g^+\right\rangle|^2 + |\langle\Psi|g^-\rangle|^2 + |\left\langle\Psi|g^0\right\rangle|^2. \tag{6.8}$$

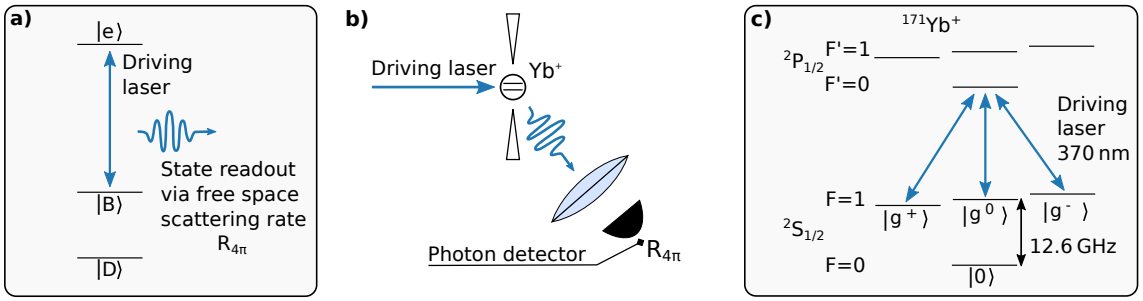

Figure 6.3: a) Conceptional sketch of fluorescence state detection of an atom with the relevant energy levels. **b)** Simplified sketch of the experimental implementation. **c)** Relevant energy levels and driven transitions of $^{171}Yb^{+}$.

6.2.1 Measurement of the expectation value

The state detection method presented this subsection makes use of multiple realisations of the same state $\hat{\rho}$ and averages the recorded data to an expectation value of the measurement operator $\left\langle \hat{A} \right\rangle$. For this purpose, we directly measure the population of the $(^2S_{1/2}, F = 1)$ manifold ρ_{bright} introduced in equation (6.6) using the rate of detected photons scattered by the ion into free space $R_{4\pi}$ according to Figure 6.3 b)+c). For this purpose, we need to normalise the detection rate $R_{4\pi}$ to the detection rate obtained during Doppler cooling R_{ref} as a reference for $\rho_{\text{bright}} = 1$, since we expect most of the ion's steady state population to be distributed among the cooling levels, i.e., the ion being '100 % bright' during cooling[53]. According to equation (6.6), the bright state population is then given as

$$\rho_{\text{bright}} = P(\lambda_B) = \frac{R_{4\pi}}{R_{\text{ref}}}. \tag{6.9}$$

An experimental sequence used for the measurement of ρ_{bright} in the context of an excitation pulse calibration is shown in Figure 6.4 as an example. It shows the binned SPC data collected during 20,000 repetitions of an atomic state readout for the same preparation of the state $\hat{\rho}$.

[53] We confirm this assumption to be valid up to a few percent in subsection 6.2.2

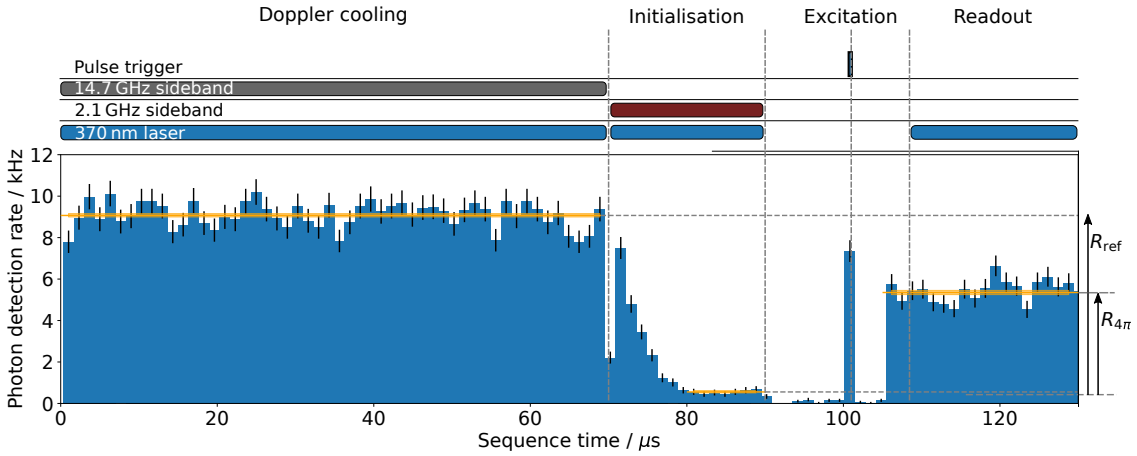

Figure 6.4: Evaluation of the ion's excited state population for one parameter set of an excitation pulse. Binned photon detection statistics for 20,000 repetitions of the same sequence are shown (blue bars, sequence sketched at the top). We initialise the ion to the $|0\rangle$ state at $\sim 70\,\mu$s. At $100\,\mu$s a laser pulse drives coherent Rabi-oscillations on the $|0\rangle \leftrightarrow |e\rangle$ transition. This is followed by a $20\,\mu$s readout of the excited state population. Due to the bin width being $1.3\,\mu$s, excitation and decay of the ion happens within one bin. The time windows used for determination of the rates R_{ref} and $R_{4\pi}$ and their values are shown as orange lines with the standard error of the rates indicated by the linewidth. The standard errors of the binned detection rates are given as error bars.

Since we use a $20\,\mu$s time window for measurement of the scattering rate $R_{4\pi}$ per sequence, we can neglect the decay of the ion to the $|0\rangle$ state during readout as described in the following subsection. The quality of the average state detection is given by the error on the measured rates, which gets improved for a higher number of repetitions.

6.2.2 Single shot readout

The measurement of $\left\langle \hat{A} \right\rangle$ as presented in the previous subsection makes use of multiple realisations of the same state. However, certain applications require a measurement of a single realisation of a quantum state generated in a single shot of an experiment, namely $\hat{A}\,|\Psi\rangle$. Reading out a single quantum state requires gaining enough information in a single shot of the experiment to allow discrimination between individual states. This makes a single shot readout generally more challenging than measuring the expectation value of a measurement operator on multiple implementations of the same state. In particular, when measuring an entangled two-qubit state, correlations between the measurement results of the individual qubits can only be observed for a particular realisation of the entangled state, while the expectation value averages out to $\left\langle \hat{A} \right\rangle = 0$ for each qubit state individually.

In order to determine the achievable contrast of the single-shot state detection in the experiment, we initialise the ion in the respective eigenstates of the measurement operator $\hat{A}$, which are $|0\rangle$ and $|F = 1\rangle$. Subsequently, we measure the number of detected photons N within a certain time window for a single shot of the experiment. By repeating this measurement over many shots, we obtain the statistics of detected photons per shot, which follows a Poisson distribution (see Figure 6.5 a)). The photon statistics depend on the interplay of several factors such as magnetic field (formation of coherent dark states),

driving laser intensity (scattering rate of the photons, also at unwanted transitions), readout time and initialisation fidelity. We discuss all these points in this and the following subsection 6.2.3.

It is important to note that the following results do not distinguish between the initialisation fidelity of the respective initial states and the detection fidelity, i.e. the errors introduced by the state detection itself. However, we take this into account later in this subsection and present a method in subsection 6.2.3 to extrapolate the results to a perfect initialisation.

For the measured photon statistics, we define the corresponding mixed states $\hat{\rho}_{\text{bright/dark}}$ as

$$\hat{\rho}_{\text{bright}} = a \cdot |F=1\rangle\langle F=1| + c \cdot |0\rangle\langle 0| \quad \text{and} \quad \hat{\rho}_{\text{dark}} = b \cdot |0\rangle\langle 0| + d \cdot |F=1\rangle\langle F=1|\,, \tag{6.10}$$

where we distinguish between an initial preparation of the ion in a bright/dark state. These states are not meant to describe the prepared initial state, but the overall detected state and, as mentioned, include preparation and measurement imperfections, both of which mix a portion of the 'wrong' state into the detected state. This is reflected by the coefficients c and d. The factors a and b denote the probabilities for detecting the 'correct' state. Figures 6.5 b)+c) show statistics of the number of photon detection events obtained in each of the single-shot readouts for a dark and a bright state preparation. For $\hat{\rho}_{\text{bright}}$, we observe a significant contribution of a second Poisson distribution with amplitude $\eta = 0.05(1)$ (dark contribution), where the bright contribution has an amplitude of $(1-\eta)$.

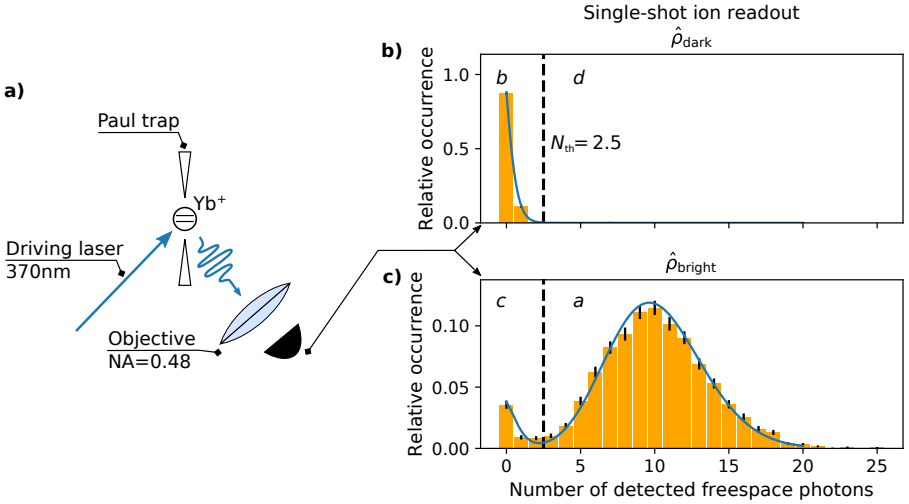

Figure 6.5: a) Sketch of the experimental implementation of the single shot atomic state readout. We detect photons emitted into free-space while driving the ion near resonant on the $|^2S_{1/2}, F=1\rangle \leftrightarrow |^2P_{1/2}, F'=0\rangle$ transition. **b)** Photon statistic for the detected state $\hat{\rho}_{\text{dark}}$ obtained from multiple repetitions of single-shot readouts of an initial dark prepared ion during a detection time window of 400 μs and with $I/I_0 \approx 0.25$. The shown data includes 6,000 readout shots. The optimal discrimination threshold of $N_{\text{th}} = 2.5$ between dark and bright ion is shown as dashed line. The solid line is a fit according to a Poisson distribution of probabilities. **c)** Same as in b) for $\hat{\rho}_{\text{bright}}$ and 18,0000 shots. The values of a, b, c, d are given in Table 3 for both graphs. The standard error on the bins shown in b)+c) are calculated according to Appendix A. The data in b)+c) have also been published in [92].

We define the discrimination fidelity of states as the average detected fidelity of each qubit state with

$$\mathcal{F} = \frac{\langle F=1|\,\hat{\rho}_{\text{bright}}\,|F=1\rangle + \langle 0|\,\hat{\rho}_{\text{dark}}\,|0\rangle}{2} = \frac{a+b}{2}. \tag{6.11}$$

The contrast of the readout is calculated as

$$\begin{aligned} C_{\text{readout}} = & \left[\underbrace{P(N > N_{\text{th}}\,|\,F=1)}_{a} + \underbrace{P(N < N_{\text{th}}\,|\,0)}_{b}\right]/2 \\ - & \left[\underbrace{P(N < N_{\text{th}}\,|\,F=1)}_{c} + \underbrace{P(N > N_{\text{th}}\,|\,0)}_{d}\right]/2, \end{aligned} \tag{6.12}$$

where $P(\alpha\,|\,\beta)$ is the probability of measuring condition α while preparing the ion into state $|\beta\rangle$. For the conditions α the expression $N > N_{\text{th}}$ denotes the probability of detecting more photons in a single shot of the readout sequence than the bright-to-dark discrimination threshold N_{th}. The readout contrast C is related to the discrimination fidelity F through equation (6.11) as

$$C = \frac{a+b-c-d}{2} = \left(\mathcal{F} - \frac{1}{2}\right)\cdot 2. \tag{6.13}$$

For a high contrast readout, the distribution of detected photons have to separate clearly for a dark and a bright ion in order to reduce the erroneous state detections c and d. Due to off-resonant scattering, longer readout time windows do not improve the readout contrast because $|0\rangle$ and $|F=1\rangle$ can no longer be considered as eigenstates of the measurement operator $\hat{A}$. However, a higher collection efficiency of the scattered photons supports the contrast of the state discrimination. This can also allow for shorter readout times to improve the contrast.

For the measurements shown in Figure 6.5, we achieve a contrast of

$$C_{\text{meas}} = 0.938(8) \tag{6.14}$$

including the preparation imperfections of the initial states. The conditional probabilities obtained for this particular measurement are shown in Table 3 for a 400 μs readout window.

	Preparation bright	Preparation dark
Above threshold $N > N_{\text{th}}$	0.947(4)	0.009(3)
Below threshold $N < N_{\text{th}}$	0.053(4)	0.991(4)

Table 3: Measured conditional probabilities for a single shot bright/dark hyperfine state discrimination at 4.6 G, $I/I_0 \approx 0.25$ and 400 μs readout.

Using the data shown in Figures 6.5 b)+c), we can assign an expectation value to the distribution of detected photons for a dark ion $\overline{N}_{\text{dark}}$ and a bright ion $\overline{N}_{\text{bright}}$ respectively. From the fitted Poisson distributions, we obtain for this particular measurement

$$\overline{N}_{\text{dark}} = 0.13(1) \text{ and } \overline{N}_{\text{bright}} = 10.2(1), \tag{6.15}$$

which we use in the following to calculate the initialisation fidelity of the bright manifold.

Initialisation fidelity of the bright state population

To get the pure detection fidelity of a state, we have to consider the non-perfect preparation fidelity f of the ion state to the bright $(^2\mathrm{S}_{1/2}, F = 1)$ manifold. This originates from the initialisation of the population in the $(^2\mathrm{S}_{1/2}, F = 1)$ manifold by applying continuous Doppler cooling. For this purpose, repumping fields from the $^2\mathrm{D}_{3/2}$ dark states (935 nm) as well as from the $|0\rangle$ dark state (14.7 GHz) are applied. Due to a finite probability of the ion population to be in one of these dark levels, the initialisation fidelity of the bright $\left|^2\mathrm{S}_{1/2}, F = 1\right\rangle$ manifold is worse than for the dark state $|0\rangle$, where we reach initialisation fidelities exceeding 99 % (see section 6.1). In addition, a fraction of the population of the $\left|^2\mathrm{S}_{1/2}, F = 1\right\rangle$ manifold could also be trapped in a coherent dark state (see subsection 3.1.3).

From a measurement as shown in Figure 6.5 b)+c), we can extract the photon statistic obtained for the single-shot readouts. From the expectation values of the Poisson-statistics for a dark and a bright ion $\bar{N}_{\mathrm{dark}}$ and $\bar{N}_{\mathrm{bright}}$, we can compute the corresponding detection rates $\bar{R}_{\mathrm{dark}} = \bar{N}_{\mathrm{dark}}/\Delta t_{\mathrm{readout}}$ and $\bar{R}_{\mathrm{bright}} = \bar{N}_{\mathrm{bright}}/\Delta t_{\mathrm{readout}}$ considering a readout time window $\Delta t_{\mathrm{readout}}$. The free-space detection rate of photons expected from the steady state fluorescence of the ion during Doppler cooling can then be calculated as

$$R_{\mathrm{cooling}} = f \cdot \bar{R}_{\mathrm{bright}} + (1 - f) \cdot \bar{R}_{\mathrm{dark}}. \tag{6.16}$$

The free parameter f is the fraction of population, which we expect to be in the bright manifold and therefore, f is the fidelity of the initialisation of the bright states. We extract R_{cooling} from the average measured detection rate of scattered photons during the cooling part of all 6,000 readout sequences (similar to R_{ref} in Figure 6.4). We obtain for the presented measurement with $I/I_0 \approx 0.25$ and the parameters from equation (6.15) a bright state initialisation fidelity of $f = (94 \pm 2)\,\%$. In subsection 6.2.3 we use this method to: i) reproduce the data we measured in the experiment by implementing the measured value of f into a simulation and ii) by running a second simulation where we set $f = 1$ and from there can infer the pure detection fidelity. In order to realise such a simulation, we first need to investigate the mechanism of off-resonance scattering, as done in the following paragraph.

Off-resonant scattering on the $\left|^2P_{1/2}, F' = 1\right\rangle$ level

In principle, measuring the fluorescence over a longer time range should improve the separation of the Poisson distributions and thus the detection fidelity. However, this is only partially true since off-resonant scattering on the $\left|^2P_{1/2}, F' = 1\right\rangle$ level introduces a weak coupling between bright and dark state which becomes important for longer readout times. Since the detuning of the readout laser to the $\left|^2S_{1/2}, F = 1\right\rangle \leftrightarrow \left|^2P_{1/2}, F' = 1\right\rangle$ transition is $\Delta_b \sim 2\pi \cdot 2.1\,\mathrm{GHz}$, the transfer of bright population to the dark states happens more likely than a dark ion to become bright. Here, the detuning is $\Delta_d \sim 2\pi \cdot 14.7\,\mathrm{GHz}$ (Figure 6.6 a)). This implies that in addition to the initialisation fidelity, the errors of the state detection itself contribute to the occurrence of two Poisson distributions for the bright state detection, as shown in Figure 6.5 c).

For a weak coupling, i.e. $\Delta_{\mathrm{b/d}} \gg \Gamma$, the rate of scattering a photon on the $\left|^2P_{1/2}, F' = 1\right\rangle$

level can be calculated according to equation (6.28) as

$$R_{\mathrm{b/d}} = \frac{\Gamma}{2} \cdot \frac{I/I_0}{1 + I/I_0 + 4\left(\frac{\Delta_{b/d}}{\Gamma}\right)^2}, \tag{6.17}$$

with the intensity of the 370 nm readout laser I, the saturation intensity I_0 and the natural transition linewidth $\Gamma = 2\pi \cdot 19.6\,\mathrm{MHz}$. Due to the high detuning $\Delta_{\mathrm{b/d}} \gg \Gamma$, the off-resonant scattering rate depends critically on the power of the readout laser. The effect of a potential driving laser detuning $\Delta_{\mathrm{readout}}$ is negligible for the off-resonant scattering rate $R_{b/d}$, since $\Delta_{\mathrm{readout}} \ll \Delta_{b/d}$ (see Figure 6.6 a)).

Due to the weak coupling, the population of the bright manifold $|F = 1\rangle$ on average approaches a steady state $\rho_{\mathrm{bright,ss}} \ll 1$ when driving the ion on the $\left|^2S_{1/2}, F = 1\right\rangle \leftrightarrow \left|^2P_{1/2}, F' = 0\right\rangle$ transition. We determine this mixing effect of bright and dark state to be the limiting factor of the atomic state readout.

The steady state population is determined by the ratio of the off-resonant scattering rates R_b and R_d for a bright and a dark ion respectively. Using equation (6.17) we compute

$$\rho_{\mathrm{bright,ss}} = \frac{2/3}{1/3} \cdot \frac{R_b}{R_d} \approx 4\,\%. \tag{6.18}$$

The additional factor of $\frac{2/3}{1/3}$ in equation (6.18) comes from the Clebsch-Gordan coefficients of the involved transitions. On average, the ion state is transferred to a statistical mixture of states with $\sim 96\,\%$ occurrence of the $|0\rangle$ state during readout. We verify this experimentally by measuring the transfer into the dark state over many repetitions of the same experimental sequence as shown in Figure 6.6 b)). We obtain a decay constant of $\tau = 2.8(2)\,\mathrm{ms}$ for the bright state to approach the steady state at $I/I_0 \approx 0.8$.

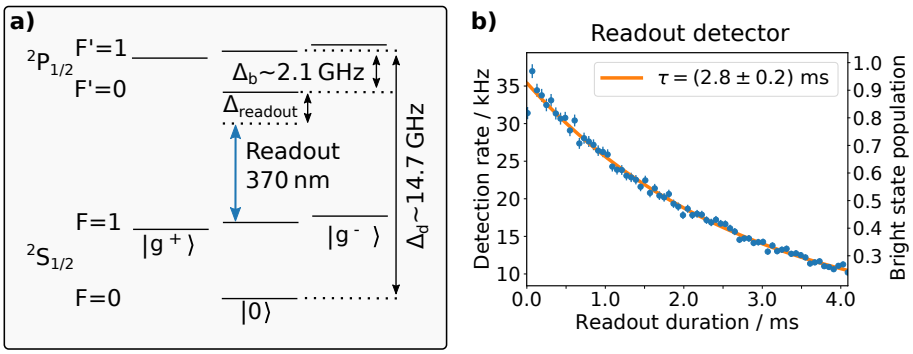

Figure 6.6: a) Relevant energy levels of $^{171}\mathrm{Yb}^+$ including the definitions of the detunings. **b)** Measured time dependence of the average population of the $|F = 1\rangle$ manifold which couples to the readout laser for a driving laser saturation parameter of $I/I_0 \approx 0.8$. We obtain the decay time τ from fitting an exponential decay (orange solid line) to the time-binned measured detection rates of photons scattered into free-space (blue dots) for 18,000 readout sequences. The standard errors are given as error bars.

Note, that the steady state is only defined for an average of measurements. Within a single experimental shot the ion can only switch between fully dark and fully bright as described at the beginning of this section.

6.2.3 Monte-Carlo simulation

In order to better understand what determines the readout fidelity of the fluorescence state detection in the experiment, we employ a Monte-Carlo simulation of the single shot ion readout. From the simulation, we obtain the statistic of detected scattered photons as introduced in subsection 6.2.2. We include the weak coupling between bright and dark state as described in equation (6.17) and the experimental fluorescence parameters achieved for high and for low magnetic field respectively. We perform the simulation for two different settings of the relative readout laser intensity $I/I_0 = 0.25$ and $I/I_0 = 0.8$. During the measurements of the entangled state correlations, we had to switch from $I/I_0 \approx 0.25$ ($\hat{\sigma}_z$-basis) to $I/I_0 \approx 0.8$ (others) in order to improve cooling and trapping stability of the ion.

The simulation reproduces a single readout of the ion in small time steps while calculating the probabilities of going dark or bright for each time step from equation (6.17), respectively. Repeating this readout simulation 20,000 times results in the photon statistics of the detected ion fluorescence for an initial state set to the beginning of each readout. The simulated and measured readouts are compared in Figure 6.7 for different readout time windows. In Figure 6.7 a) the readout fidelity dependence on the readout time window is shown for different driving laser and fluorescence conditions in accordance with the conditions achieved during the correlation measurements of chapter 7. We have found that we need to consider non-perfect state initialisation for the bright state, described by the initialisation fidelity f as introduced in subsection 6.2.2, in order to consistently reproduce the measured data of subsection 6.2.2. Taking this into account, we found the simulated values to be in excellent agreement with the measured data. The dark-to-bright threshold, which is shown as dashed line in Figure 6.7 b)+c) is adjusted to the optimal value for each readout time window in terms of achievable contrast (simulation and experiment).

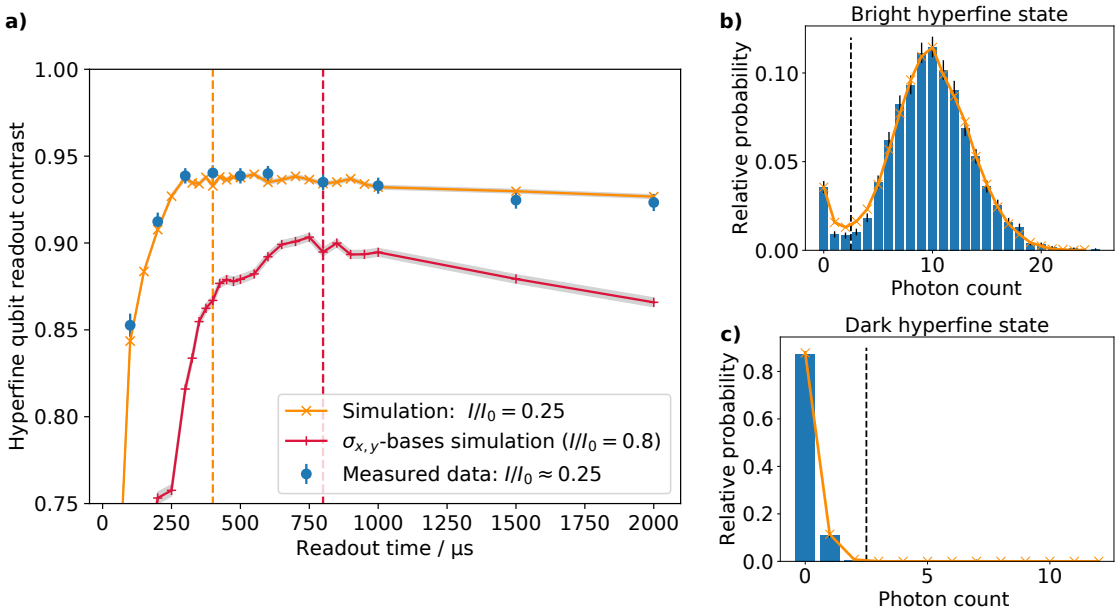

Figure 6.7: Measured and simulated contrast of the atomic fluorescence state detection. The solid lines are linear interpolations between the discrete results of a Monte-Carlo simulation comprising of 20,000 atomic readouts (per data point in a)). **a)** The blue dots denotes the measured experimental data. The orange "x" are values obtained from the simulation based on the same parameters: 4.6 G magnetic field and bright state preparation fidelity of $f = 0.94(2)$. The red crosses represents simulated data for the lower magnetic field parameters ($\sim 600\,\mathrm{mG}$) and $f = 1$. Standard errors of the simulation are given as grey shaded areas around the curves. The dashed lines denote the corresponding readout lengths which were used for correlation measurements in chapter 7. **b)/c)** Simulated occurrence of the number of detected photons for a $400\,\mu\mathrm{s}$ readout at $I/I_0 = 0.25$ and $f = 0.94(2)$ (orange "x"). The measured probabilities are given as blue bars with the standard error as black bars (same data as in Figure 6.5 c)/b)). The optimal discrimination threshold is given as dashed line.

We can confirm the considerations of subsection 6.2.2 that off-resonant scattering on the $\left|{}^2\mathrm{P}_{1/2}, F' = 1\right\rangle$ manifold mixes a significant contribution of the dark state to an initial bright ion (Figure 6.7 b)), whereas for an ion initially prepared to the dark state, the bright state contribution is small (Figure 6.7 c)).

Due to the excellent agreement of the simulated photon detection probabilities with the experimental measured data, we use the simulation in the following to compute the achieved readout contrast for the correlation measurements presented in chapter 7 with the corresponding experimental parameters. We cannot use experimental data for this purpose, since our preparation fidelity for the excited state is $f < 1$ (see subsection 6.2.2).

We achieve a dark count rate of $(500 \pm 50)\,\mathrm{counts/s}$ and a bright ion fluorescence of $(29,750 \pm 750)\,\mathrm{counts/s}$ in the optimal case in the experiment for high magnetic field ($4.6\,\mathrm{G}$) and $I/I_0 \sim 0.25$. According to the Monte-Carlo simulation with $f = 1$, the readout contrast using a $\Delta t_{\mathrm{readout}} = 400\,\mu\mathrm{s}$ time interval is given by

$$C_{\mathrm{readout},z} = 96.5(12)\,\%. \tag{6.19}$$

This result is on par with the values achieved previously on the $^{171}\mathrm{Yb}^+$ hyperfine qubit [129, 46], where also the main limitation was the off-resonant scattering of photons on the

$\left|{}^2P_{1/2}, F' = 1\right\rangle$ level.

For magnetic fields lower than 1 G ($\sim$ 3 MHz splitting of $|g^{\pm}\rangle$), we observe a drastic decrease of the ion fluorescence in the experiment resulting from formation of coherent dark states in the $\left|{}^2S_{1/2}, F = 1\right\rangle$ hyperfine levels [18, 119]. Decreasing the magnetic field into this range, however, is necessary to reduce the Larmor frequency and therefore improve timing precision for a readout in the rotated bases[54] $\bar{\hat{\sigma}}_{x/y}$ (see subsection 7.4.1). We are able to partly recover the fluorescence of the ion to $\sim$ 50 % by using a second cooling laser (see subsection 3.1.3). We achieve a dark count rate of (762 ± 25) counts/s and a bright ion fluorescence of $(12,000 \pm 500)$ counts/s in the optimal case for the correlation measurements in $\bar{\hat{\sigma}}_{x/y} \otimes \bar{\hat{\sigma}}_{x/y}$ basis. For the readout contrast in the rotated bases, we get from a Monte-Carlo simulation with $I/I_0 \sim 0.8$ and $f = 1$ a value of

$$C_{\text{readout},\bar{x}/\bar{y}} = 89.5(12)\,\%, \tag{6.20}$$

for $\Delta t_{\text{readout}} = 800\,\mu$s. Due to an increased cooling performance, $I/I_0 \sim 0.8$ was used for correlation measurements in the rotated bases (instead of $I/I_0 = 0.25$).

6.3 Pulsed excitation

For certain applications, the transfer of the population to an excited state is desired. In particular, the spontaneous decay of an atomic state with a finite lifetime via an optical transition enables the deterministic generation of a single photon. The emission probability of the photon naturally depends on the population of the excited state. We derive in subsection 6.3.1 that reaching unit excitation probability requires the excitation to be much faster than the decay of the excited state. These ultra-fast Rabi-flops for state preparation can be achieved using pico-second long laser pulses with high peak intensities [121].

In this section, we introduce the theoretical framework to describe pulsed excitation in general and derive an approximation to describe the dynamics of a two-level system driven by an arbitrarily shaped ultra-short laser pulse. Furthermore, we present the experimental implementation and the characterisation of the setup generating the pico-second long laser pulses.

6.3.1 Optical Bloch equations

Based on the semi-classical description of a driven two-level system in subsection 5.4.1, we derive in this subsection a set of coupled differential equations, which describe the time evolution of the driven two-level system. With the so-called optical Bloch equations we can geometrically represent the time evolution of any two-level state $|\Psi\rangle = c_g(t)\,|g\rangle + c_e(t)\,|e\rangle$ as a vector on the Bloch sphere (see section 2.1), which for a pure state with $|c_g(t)|^2 + |c_e(t)|^2 = 1$ always points to the surface of this unit sphere.

Here, we derive the formalism in the context of a driving electric field, however, the representation of states on the Bloch sphere can be made for any two-level system and the concept is used throughout this thesis to visualise two-level quantum states and their

[54] See equation (5.87) for a definition of $\bar{\hat{\sigma}}_{x/y}$

time dynamics. For a state representation on the Bloch sphere, we use the expectation values of the state projection to the eigenstates of the Pauli matrices as coordinates[55]:

$$\begin{aligned} x &= \langle\hat{\sigma}_x\rangle \quad \text{with eigenstates} \quad \frac{1}{\sqrt{2}}\left(|e\rangle \pm |g\rangle\right), \\ y &= \langle\hat{\sigma}_y\rangle \quad \text{with eigenstates} \quad \frac{1}{\sqrt{2}}\left(|e\rangle \pm i\,|g\rangle\right), \\ z &= \langle\hat{\sigma}_z\rangle \quad \text{with eigenstates} \quad |e\rangle\,, |g\rangle\,. \end{aligned} \tag{6.21}$$

This is similar to the definitions of equations (2.2) and (2.7) and Figure 2.1 b), but with different basis states $|e\rangle$ / $|g\rangle$ of the Hilbert space.

According to the Ehrenfest theorem, the time evolution of an operator's expectation value $\left\langle \hat{A} \right\rangle$ is given by

$$\frac{d}{dt}\left\langle \hat{A} \right\rangle = \frac{i}{\hbar}\left\langle \left[\hat{H}, \hat{A}\right] \right\rangle + \left\langle \frac{\partial A}{\partial t} \right\rangle. \tag{6.22}$$

Using the commutation relations of the Pauli matrices and the Hamiltonian of a driven two-level system in a semi-classical description (equation (5.39)), we derive following equations (Bloch equations):

$$\begin{aligned} \dot{x} &= \frac{d}{dt}\langle\hat{\sigma}_x\rangle = \frac{i}{\hbar}\frac{\hbar}{2}\langle[-\Delta\hat{\sigma}_z, \hat{\sigma}_x] + [\Omega_R\hat{\sigma}_x, \hat{\sigma}_x]\rangle = \Delta \cdot \langle\hat{\sigma}_y\rangle = \Delta \cdot y, \\ \dot{y} &= -\Delta \cdot x - \Omega_R \cdot z, \\ \dot{z} &= \Omega_R \cdot y. \end{aligned} \tag{6.23}$$

We can understand the evolution of a state on the Bloch sphere intuitively by rewriting these equations into a vector cross product

$$\begin{pmatrix} \dot{x} \\ \dot{y} \\ \dot{z} \end{pmatrix} = \begin{pmatrix} \Omega_R \\ 0 \\ -\Delta \end{pmatrix} \times \begin{pmatrix} x \\ y \\ z \end{pmatrix}. \tag{6.24}$$

The so-called optical Bloch equations can be obtained from equations (6.23) by including relaxation of the states. We differentiate between the decay of the excited state $|e\rangle$ with rate $\Gamma = 1/T_1$ and the decoherence of the superposition states given by the x- and y-components with rate $1/T_2$. The optical Bloch equations reads

$$\begin{pmatrix} \dot{x} \\ \dot{y} \\ \dot{z} \end{pmatrix} = \begin{pmatrix} \Omega_R \\ 0 \\ -\Delta \end{pmatrix} \times \begin{pmatrix} x \\ y \\ z \end{pmatrix} - \begin{pmatrix} 1/T_2 \cdot x \\ 1/T_2 \cdot y \\ 1/T_1\,(z+1) \end{pmatrix}. \tag{6.25}$$

Steady state solution

The calculation of the steady state solution of equations (6.25) with $\dot{x} = \dot{y} = \dot{z} = 0$ provides important insights into the driven two-level system. In particular, it provides the scattering rate of photons into 4π solid angle by a single driven two-level atom. For the spontaneous decay of the excited state into the three-dimensional electromagnetic vacuum $T_2 = 2 \cdot T_1$ holds [53]. We derive the steady state solution of equations (6.25) as

$$\begin{pmatrix} x^{ss} \\ y^{ss} \\ z^{ss} \end{pmatrix} = \frac{1}{4\Delta^2 + \Gamma^2 + 2\Omega_R^2} \cdot \begin{pmatrix} 4\Omega_R\Delta \\ 2\Omega_R\Gamma \\ -\Gamma^2 - 4\Delta^2 \end{pmatrix}. \tag{6.26}$$

[55] Note, that in literature the coordinates are often also named u, v, w

We calculate the steady state excited state population as

$$\rho_{ee}^{ss} = \frac{1+z^{ss}}{2} = \frac{0.5 \cdot I/I_0}{1 + I/I_0 + (2\Delta/\Gamma)^2} \quad \text{with} \quad \frac{I}{I_0} = 2\frac{|\Omega_R|^2}{\Gamma^2}, \tag{6.27}$$

where I_0 is also known as the saturation intensity. Subsequently this result gives the scattering rates of photons into free space as

$$R_{4\pi} = \Gamma \cdot \rho_{ee}^{ss}. \tag{6.28}$$

Furthermore, it follows from equation (6.27) that the population of the excited state ρ_{ee}^{ss} cannot exceed the population of the ground state in a driven steady state, i.e. $\rho_{ee}^{ss} < 0.5$ even for high driving field intensity $I/I_0 \gg 1$ and on resonance $\Delta = 0$. To achieve population inversion or even complete transfer of the population from the ground state $|g\rangle$ to the excited state $|e\rangle$, we must not reach the steady state regime and instead drive the two-level system coherently with $\Omega_R \gg \Gamma = 2\pi \cdot 19.6\,\text{MHz}$ on a time scale much shorter than $1/\Gamma$. This explicitly motivates the use of ultra-short laser pulses, as presented in the next paragraph.

Fast dynamics

For a pulsed excitation of the two-level system, we are particular interested in the excited state population

$$\rho_{ee}(t) = \frac{1+z(t)}{2}, \tag{6.29}$$

which can be obtained in a general case from a numerical solution of the equations (6.25) even for an arbitrarily shaped pulse. For an analytical solution, however, we constrain ourselves to a square pulse with a duration of τ_{pulse} and $\Gamma \ll 1/\tau_{\text{pulse}}$. Starting from the ground state ($\rho_{ee}(0) = 0$), we obtain the same preconditions as in subsection 5.4.2, where we assumed that the driving field has a time constant amplitude which results in a time constant Rabi frequency Ω_R (eq. (5.31)). We then write the excitation probability according to equation (5.40) as

$$\eta_{\text{exc}} = \rho_{ee}(\tau_{\text{pulse}}) = \frac{\Omega_R^2}{(\Omega')^2} \cdot \left(\frac{1}{2} - \frac{1}{2}\cos\left(\Omega'\tau_{\text{pulse}}\right)\right) \quad \text{with} \quad \Omega' = \sqrt{\Omega_R^2 + \Delta_{\text{pulse}}^2}. \tag{6.30}$$

For the general description of pulsed excitation, however, it would be advantageous if we could adapt the analytical solution to an arbitrarily shaped excitation pulse. In subsection 6.3.2 we derive a formalism, which accounts for the pulse-shape, but allows us to use equation (6.30) for the calculation of the excitation probability considering the entire pulse.

For the sake of completeness, we also have to mention that an alternative expression of equations (6.23) can be obtained without applying any of the standard approximations such as RWA by solving the coupled semi-classical Maxwell-Bloch system as done numerically by R.W. Ziolkowski et al. in [188]. This approach accounts for the exact electric field time dependence including the pulse envelope and therefore, provides a more resolved study of the driven two-level dynamics. However, the results in [188] can be well approximated with the optical Bloch equations derived in (6.25) even for ultra-short pulsed excitations if one is not interested in the oscillation cycles of the pulsed electric field.

6.3.2 Theory of pulse shapes

In general, a constant driving field amplitude $|\mathbf{E}_0|$ is not given for the envelope of a laser pulse. In particular, the pico-second laser pulses used here have an exponentially decreasing electric field envelope due to spectral filtering (see subsection 6.3.4). In general, the Rabi frequency of equation (5.31) as a function of the transition dipole moment $\mathbf{d}$ and the linearly polarised electric field with amplitude $\mathbf{E}_0(t)$ becomes time dependent

$$\Omega_R(t) = \frac{|\mathbf{d}| \cdot |\mathbf{E}_0(t)|}{\hbar} \cdot \cos(\theta), \tag{6.31}$$

with θ being the angle between the electric field vector and the dipole orientation.

Due to the short time profile of the pulses, their time resolved monitoring is experimental challenging and could be achieved using autocorrelation measurements. However, in this subsection, we derive a formalism which does not require the exact time dependence of a pulse, but a known scaling factor a of the pulse envelope. We use this scaling factor to compute the excited state population after the pulse has interacted with the two-level system. To this end, the pulse energy is a useful quantity, which we can obtain from a low bandwidth power measurement (equation (6.35)).

We separate the power $P_p(t)$ of a single pulse into a time dependent part $\alpha(t)$ and a constant envelope amplitude P_A of the pulse as

$$P_p(t) = P_A \cdot \alpha(t), \text{ where } 0 \leq \alpha(t) \leq 1. \tag{6.32}$$

Furthermore, we can define a pulse length τ_{pulse} for a pulse shape $\alpha(t)$ such that

$$\int_{-\infty}^{\infty} \alpha(t)dt = a \cdot \tau_{\text{pulse}}. \tag{6.33}$$

Combining equations (6.32)-(6.33), we can express the total energy carried by a single pulse u_p as

$$u_p = \int_{-\infty}^{\infty} P_{\text{p}}(t)dt = P_A \cdot a \cdot \tau_{\text{pulse}}, \tag{6.34}$$

which is the equivalent to a square pulse. The parameters a and τ_{pulse} depend on the corresponding time envelope of the pulse $\alpha(t)$. For an exponentially decaying time profile starting at $t = 0$, it is straight forward to show that $a = 1$ in equation (6.34) if τ_{pulse} is defined as the $1/e$-decay constant.

In the experiment, we measure the pulse energy u_p using the average deposit power of a train of pulses $\bar{P}_{\text{train}}$ with a repetition rate R according to

$$\bar{P}_{\text{train}} = u_p \cdot R, \tag{6.35}$$

where the bandwidth of the power measurement is much smaller than R.

Using equation (6.34), we can calculate the total spatial deposited energy per pulse considering the power P_A to be distributed according to a Gaussian beam shape [149] as

$$\begin{aligned} u_p = a \cdot \tau_{\text{pulse}} \cdot \underbrace{\int_0^{\infty} I(\rho, 0) \cdot 2\pi \cdot d\rho}_{P_A} = a \cdot \tau_{\text{pulse}} \cdot I_0 \cdot \frac{1}{2}\pi\omega_0^2 \\ \text{with } I(\rho, z) = I_0 \left(\frac{\omega_0}{\omega(z)}\right)^2 \exp\left(-\frac{2\rho^2}{\omega^2(z)}\right), \end{aligned} \tag{6.36}$$

where ω_0 is the $1/e^2$ radius of the beam intensity at the beam focus ($z = 0$).

Since the ion is located (ideally) in the centre of the Gaussian beam, the centre intensity $I_0(t) = \frac{1}{2}c_0\epsilon_0|E_0(t)|^2$ sets the Rabi frequency Ω_R. We can now use this expression of the electric field amplitude together with equation (6.36), where we have derived a time independent expression of I_0, to extract the time dependence of the pulse envelope from the electric field amplitude ($E_0(t) \to E_0$). In total, we find following expression for the Rabi frequency:

$$\Omega_R = \frac{|\mathbf{d}| \cdot \cos(\theta)}{\hbar} \cdot \sqrt{\frac{4u_p}{a\tau_{\text{pulse}}\pi\omega_0^2 c_0\epsilon_0}}. \tag{6.37}$$

For the investigated hyperfine transition, the computation of the transition matrix element $\langle 0|\,\hat{\mathbf{r}}\,|e\rangle$ depends on the polarisation of the driving field and the quantum numbers of ground and excited state (see Appendix B). As we intend to drive only the $\Delta m_F = 0$ transition of the ion, we align the linearly polarised electric field of the laser pulse parallel to the quantisation axis ($\theta = 0$). With the Clebsch-Gordan coefficient of the $|0\rangle \leftrightarrow |e\rangle$ transition of $c_\pi = \sqrt{\frac{1}{3}}$, the Rabi frequency for this particular π-transition becomes $\Omega_\pi = \sqrt{\frac{1}{3}}\Omega_R$. For simplicity, we denote Ω as the Rabi frequency in the following with $\Omega \equiv \Omega_\pi$. In summary, we get following dependency for the Rabi frequency on the pulse energy u_p and pulse duration τ_{pulse}:

$$\Omega \propto \sqrt{\frac{u_p}{\tau_{\text{pulse}}}}. \tag{6.38}$$

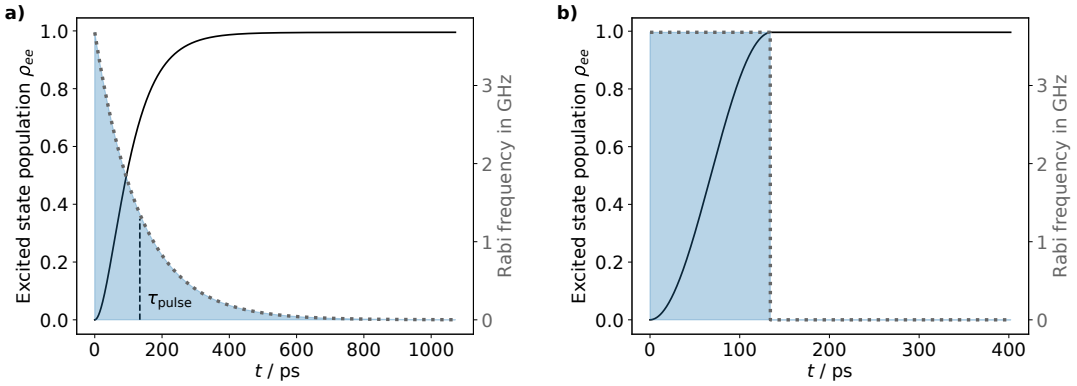

Figure 6.8: Numerical calculation of the time evolution of the excited state population ρ_{ee} (black solid curve) according to equations (6.25) and (6.29) for: **a)** an exponential decay pulse envelope with the decay constant $\tau_{\text{pulse}} = 134\,\text{ps}$ (see eq. (6.40)), which is on resonance with the atomic transition $\Delta_{\text{pulse}} = 0$ and **b)** the square equivalent pulse with a constant Rabi frequency according to equation (6.37) calculated with the experimental parameters of a). The excitation pulse electric field envelope is shown as blue coloured area in both cases with the corresponding Rabi frequency as grey dotted line. The chosen parameters correspond to those of the real experiment. Both pulses exhibit an energy of 3 pJ. Note the different scaling of the time axes.

Figure 6.8 illustrates the presented method using the example of an exponentially decaying time profile with an energy of $u_p = 3\,\text{pJ}$, where the parameters were chosen according to those of the real experiment. In Figure 6.8 a), a numerical solution to the optical Bloch equations (equations 6.25) is shown with the electric field amplitude and the Rabi

frequency of the excitation pulse following an exponential decay function with a decay constant of τ_{pulse}. For the same experimental parameters Figure 6.8 b) shows the response of the system to a square pulse with a constant Rabi frequency according to equation (6.37). Both pulses reach the same excited state population ρ_{ee} for large times t. Hence, we can treat the pulses as square pulses in the experiment using equation (6.37) in combination with equation (6.30) for the calculation of the excitation probability after the pulse was applied ($t \gg \tau_{\text{pulse}}$). This is particularly useful for the calibration of the pulse parameters as shown in subsection 6.3.5.

For the numerical simulation of the excited state population in Figure 6.8, we used typical values achieved in the experiment. We obtain peak powers around 22 mW for ~ 3 pJ pulses, after a spectral filtering of the pulses (see subsection 6.3.4). Together with a beam waist of $\sim 12\,\mu$m, we reach around $3.3\,\frac{\text{kV}}{\text{cm}}$ electric field amplitude at the position of the ion and $\Omega \sim 2\pi \cdot 3.5$ GHz [56].

6.3.3 Generation of pulses

The laser pulses are generated from a Kerr lens mode-locked Titanium-Sapphire laser[57] near 740 nm and are subsequently frequency doubled to 370 nm using a plane-cut Bismuth Triborate (BiBO) crystal [80]. The high peak intensities of the laser pulses support the second-harmonic generation which enables conversion efficiencies around 30 % [80]. In the following, we present the basic parameters of the pulses, namely energy, timing, centre frequency and spatial mode. A sketch of the setup is presented in the context of frequency adjustment in Figure 6.10 as this involves multiple stages.

Pulse energy

The Ti:sapphire laser consists of a ring resonator pumped by 5–6 W of laser light[58] at 532 nm. For a deterministic extraction of single pulses, we extend the ring cavity with a commercial available Bragg cell module[59]. This allows for controlled extraction of pulses by applying a 7.5 ns long RF-pulse to the acousto-optic modulator. The amplitude of the applied RF-signal determines the energy of the diffracted pulse.

Timing of the pulses

The RF-pulse to the Bragg cell is triggered by a TTL signal, which originates from the fast experimental control system (FECS) (see Figure 6.9 a) and subsection 3.2.4). Due to the round trip time of the ring resonator, a pulse cannot be extracted from the resonator immediately, but the next available pulse is extracted. The mode-locked Ti:Sapphire laser exhibits a resonator round trip frequency of ~ 54 MHz. Using the built in fast photo diode of the pulsed laser, a seed signal is generated which reflects the exact cavity round trip time. This signal is used internally to extract the next available pulse. However, the maximum relative timing uncertainty between the extraction time of the pulse with respect to the pulse request of the FECS is $\sim 1/54\,\text{MHz} = 18.5$ ns. By synchronising the

[56] $|\mathbf{d}|_\pi = c_\pi \cdot e\sqrt{\frac{3c_0^2}{4\alpha\omega_a^3} \cdot A_{0e}}$ [52] with the Einstein A-coefficient for unpolarised light of $A_{0e} = 1.23 \times 10^8$ ($^2\text{S}_{1/2} \leftrightarrow {}^2\text{P}_{1/2}$ transition) [96]

[57] Mira optima 900 from Coherent

[58] generated by a Verdi V12 from Coherent

[59] Pulse switch from APE

acquisition of data only to the FECS, the resulting jitter of the pulse arrival times at the ion's position blurs out time dynamics happening in the same order of magnitude, in particular the decay of the $|e\rangle$ state with a lifetime of $\tau \sim 8\,\text{ns}$ (see Figure 6.9 b)).

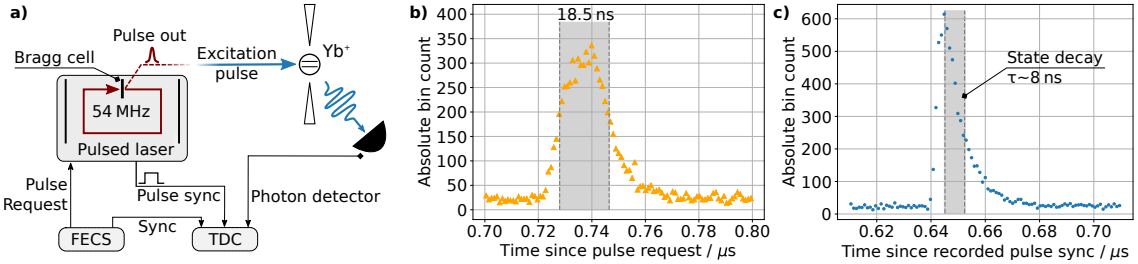

Figure 6.9: a) Sketch of the experimental setup used for synchronisation of the photon detection time stamps to the pulsed laser round trip frequency. The internal cavity of the pulsed laser is sketched as two mirrors confining the locked modes. **b)** Recorded time stamps of $\sim 3,000$ photon detection events extracted through the fibre cavity (to suppress pulse stray light). The detection timestamps are binned without a correction applied. **c)** Same data as in b) using the extraction times of the excitation pulses timestamp-wise as an offset for the photon detection timestamps. The x-axis of a) and b) shows the same scale to enable a comparison. The bin width is 1 ns.

The effect of blurred pulse arrival times can be reduced to an accuracy of 50 ps[60] in post analysis by using the 54 MHz seed signal to generate a sync pulse that synchronises each recorded photon timestamp on the TDC to the precise extraction time of the laser pulse for this particular timestamp. Figure 6.9 c) shows binned detection timestamps that were corrected by the recorded sync pulse. This data allow us to resolve the excited state decay.

Pulse centre frequency

For a coarse setting of the pulse centre frequency, we use a birefringent filter located within the internal ring cavity of the laser (accuracy $\sim 20\,\text{GHz}$). More accurate tuning of the frequency ($\sim 2\,\text{GHz}$) is achieved via a Gires-Tournois interferometer, which also generates the required group velocity dispersion for the 6 ps long pulses [34]. The fine tuning of the pulse centre frequency is done by a self-built filter cavity cutting out $\sim 1\,\text{GHz}$ of spectral intensity from the $\sim 100\,\text{GHz}$ wide frequency-doubled pulse (see Figure 6.10 a)). We discuss the spectral filtering of pulses in more detail in the next subsection. For now, we focus on the stabilisation of the filter-cavity to the atomic excitation transition $|0\rangle \leftrightarrow |e\rangle$. For this purpose, we use a 780 nm reference laser locked in a Pound-Drever-Hall (PDH) scheme [43] to a ultra stable reference-cavity with a maximal frequency change of 0.5 MHz/h [104] (see Figure 6.10 a)+b)). The filter-cavity mirrors exhibit a finite reflectivity at 780 nm, which allows for the length stabilisation of the filter-cavity using the 780 nm reference laser in a second PDH locking scheme. We calibrate the length of the filter-cavity using a backwards-coupled reference laser resonant to the $|0\rangle \leftrightarrow |e\rangle$ transition of $^{171}\text{Yb}^+$ (see next paragraph).

[60] According to APE

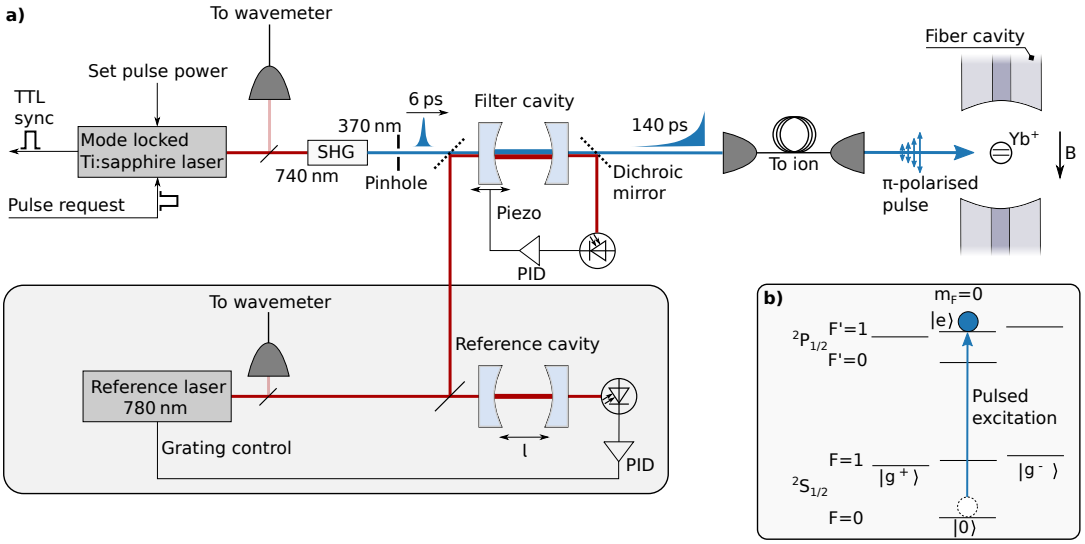

Figure 6.10: a) Important elements of the pulsed laser setup. The generated pulses are frequency doubled using second-harmonic generation (SHG). The pulse width of $\sim 100\,\mathrm{GHz}$ is spectral filtered by a stabilised cavity with linewidth $\Delta\nu_{\mathrm{fwhm}} \approx 2\pi \cdot 1.19(1)\,\mathrm{GHz}$. A second laser at 780 nm is locked to a length stabilised reference cavity and serves as reference for the centre frequency of the filter cavity. **b)** Relevant hyperfine energy level scheme of $^{171}\mathrm{Yb}^+$. The ion is initialised in the $|0\rangle$ ground state. We adjust power, frequency and polarisation of the laser pulse to coherently excite the ion to the $|e\rangle$ state.

Further adjustments

Due to the pulse spectral width being $\sim 100\,\mathrm{GHz}$ before the filter cavity, the pulse couples to multiple transversal modes of the cavity and the transmitted spatial shape of the pulse is a mixture of TEM modes. The pulses are spatial filtered on a pinhole with $\sim 50\,\%$ transmission in advance, however, the higher order mode coupling cannot be fully suppressed. Due to their frequency spacing, only one of the transverse modes can be tuned into resonance with the ion.

We guide the pulses to the ion using a 10 m polarisation maintaining fibre[61]. The best spatial coupling of the pulses to the single mode fibre can be achieved for the TEM_{00} mode of the filter-cavity. However, the coupling between TEM_{00} mode and fibre cannot be optimised using the transmitted pulses. Due to the mixture of spatial modes, there are several local maxima in the transmission efficiency, which one could mistakenly assume to be the optimum coupling of the TEM_{00} mode to the fibre. Instead, we couple a narrow bandwidth laser from the ion-trap side backwards through the fibre and optimise the coupling of the fibre's TEM_{00} mode to the filter cavity TEM_{00} mode in transmission[62], where we achieve $\sim 60\,\%$ transmission of intensity.

Finally, we adjust the polarisation of the excitation pulse to be parallel to the quantisation axis at the place of the ion in order to drive the $\Delta m_F = 0$ transition (see Figure 6.10 a)+b)). In total, we reach around 4 pJ pulse energy at maximum at the ion's position focused down to a beam waist of $\sim 12\,\mu\mathrm{m}$.

[61] S405-XP from Thorlabs with a damping of 0.8(5) dB/m
[62] Which was also done in [6]

6.3.4 Spectral filtering of the pulses

From previous experiments we know that stray photons originating from an illuminating laser beam could be scattered into the fibre cavity mode by elements of the trap setup and subsequently cause accidental photon detection events on the cavity SPCs. This holds even for a laser beam which impinges perpendicular to the cavity axis [157]. The ultrafast laser pulses with which we excite the ion cause noticeable stray photons at the trap structure due to their comparably large peak powers ($\sim 20\,\mathrm{mW}$). Moreover, due to the excited state lifetime of the ion of $\sim 8\,\mathrm{ns}$ and the cavity decay time of $1.4(1)\,\mathrm{ns}$, these stray-photons mix up with photons emitted spontaneously by the ion on the SPCs. Adaption of the post-processing acceptance window of the detected cavity photons could potentially filter out these stray photons but at the cost of the travelling qubit detection efficiency (see subsection 5.5.2). A more elegant approach is the reduction of the excitation pulse linewidth, such that the photons are far detuned from the cavity resonance frequency. At the same time, a reduction of the pulse energy reduces the pulse-broadening due to non-linear effects in the guiding fibre [6].

We reduce the bandwidth of the pulses which exit the pulsed laser at a spectral bandwidth of $\sim 100\,\mathrm{GHz}$ using a filter cavity resonant to the atom and having a linewidth of $\sim 1\,\mathrm{GHz}$. The spectral bandwidth of the filtered pulses is small against the separation of $\sim 12.6\,\mathrm{GHz}$ between cavity resonance frequency ($\left|^2\mathrm{S}_{1/2}, F = 1\right\rangle \leftrightarrow |e\rangle$) and atomic transition for pulsed excitation ($|0\rangle \leftrightarrow |e\rangle$). We proof experimentally that this reduces the level of stray photons on the cavity single photon detectors below their noise level (~ 100 counts per second).

We built the symmetric filter-cavity from two concave mirrors with 98.5% reflectivity (at 370 nm) and 100 mm radius of curvature. This places the finesse of the cavity to $F \approx 200$. The mirrors are separated by a few micrometres and allow for smooth cavity length adjustment using a ring piezo actuator glued to the backside of one mirror.

Influence of the spectral filtering to the time profile of the pulse

The time profile of the pulse is particularly interesting for the theoretical description of the ion-pulse interaction (see subsection 6.3.2). The filter-cavity determines the time profile of the spectral filtered pulse and we obtain the characteristic decay time of a light field within the cavity by measuring the linewidth of the cavity. To this end, we stabilise the cavity length to the reference laser at 780 nm while tuning the frequency of a second laser coupled through the cavity at the TEM_{00} mode and running at 370 nm (see Figure 6.11).

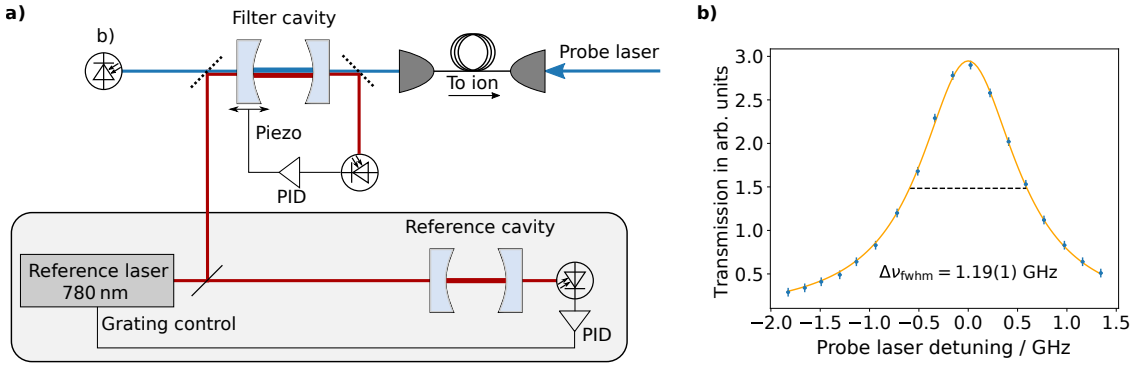

Figure 6.11: Linewidth measurement of the filter-cavity stabilised to a 780 nm reference laser. **a)** We probe the transmission of the cavity using a frequency scanned 370 nm probe laser coupled to the TEM_{00} mode of the cavity. **b)** The linewidth is extracted from the Lorentzian-profile (solid line) of the measured transmission (blue dots). The standard deviations are given as error bars.

We measure a linewidth of the filter cavity at 370 nm of

$$\Delta\nu_{\mathrm{fwhm}} = 1.19(1)\,\mathrm{GHz}. \tag{6.39}$$

For a pulse emitted by the Ti:Sapphire laser, the envelope of the electric field has a sech-function time profile due to the optical Kerr-effect, which enables the mode-locking of the laser in our case [97, 34]. The spectral filtering of the pulse changes the envelope to an exponential decay since the length of the generated pulse of 6 ps (according to the manufacturer) is much smaller than the cavity decay time of

$$\tau_{\mathrm{cavity}} = \frac{1}{2\pi \cdot \Delta\nu_{\mathrm{fwhm}}} = (134 \pm 1)\,\mathrm{ps}. \tag{6.40}$$

Due to the approximately instant excitation of the cavity mode, the length of the spectral filtered pulse is $\tau_{\mathrm{pulse}} = \tau_{\mathrm{cavity}}$.

6.3.5 Calibration of pulse parameters

We calibrate intensity and centre frequency of the laser pulses on a daily basis by driving resonant Rabi oscillations on the $|e\rangle \leftrightarrow |0\rangle$ transition after initialising the ion to the $|0\rangle$ state as described in section 6.1. We measure the excitation probability of the ion using the population of the $(^2\mathrm{S}_{1/2}, F = 1)$ manifold ρ_{bright} after the excited state decay happened (see Figure 6.12 a)+b)). To this end, we measure the rate of detected photons scattered by the ion into free space $R_{4\pi}$ while driving the ion on the cooling transition $\left|^2\mathrm{S}_{1/2}, F = 1\right\rangle \leftrightarrow \left|^2\mathrm{P}_{1/2}, F' = 0\right\rangle$ as described in subsection 6.2.1.

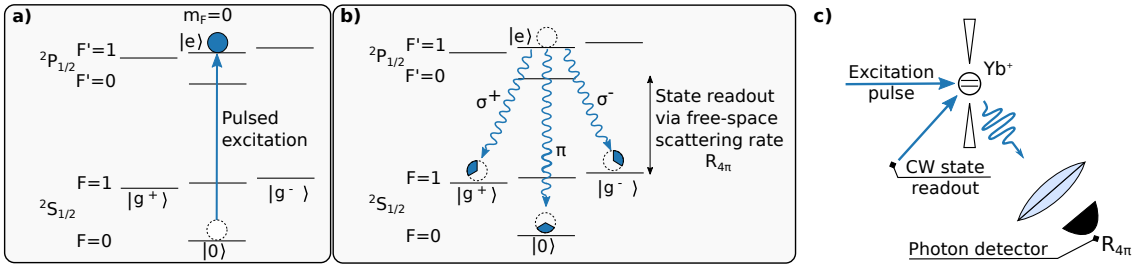

Figure 6.12: a) Experimental sequence for measuring the excitation probability of the $|e\rangle$ state. We initialise the ion to the $|0\rangle$ state as described in section 6.1. Subsequently, the laser pulse drives coherent Rabi-oscillations on the $|0\rangle \leftrightarrow |e\rangle$ transition. **b)** From the excited state $|e\rangle$, the ion decays to the $^2S_{1/2}$ manifold. **c)** Important elements of the experimental setup used for the measurement of ρ_{bright}. CW: continuous wave.

Considering the Clebsch-Gordan coefficients of the involved transitions of the excited state decay, we extract the excitation probability η_{exc} from the branching ratios of Figure 6.12 c) as

$$\eta_{\text{exc}} = \frac{3}{2} \cdot \rho_{\text{bright}}. \tag{6.41}$$

It follows from equation (6.30) that the coherent transfer of population to the excited state can only happen with unit probability, if the pulse centre frequency is resonant to the atomic transition ($\Delta_{\text{pulse}} = 0$). We hold the laser pulse resonant to the atomic transition using the stabilised filter–cavity (see Figure 6.10 a)). For a calibration of the pulse centre frequency, we monitor the excitation probability of the ion, while varying the length of the filter-cavity. A calibration of the pulse frequency is shown in Figure 6.13 a), where we achieve $\Delta_{\text{pulse}} = 0$ at the maximum excitation.

Furthermore, it follows from equation (6.30) that a full transfer of population to the excited state with a resonant pulse requires $\Omega \cdot \tau_{\text{pulse}} = \pi \cdot (2n + 1)$, $n \in \mathbb{N}$. Due to a fixed pulse length τ_{pulse}, we have to tune the Rabi frequency Ω in order to fulfil this condition. We control the Rabi frequency Ω by changing the pulse energy according to subsection 6.3.3. A measurement of the pulse energy $u_{\pi,p}$ corresponding to a full population transfer from the ground state $|0\rangle$ to the excited state $|e\rangle$ (π-rotation) is shown in Figure 6.13 b). We achieve an excitation probability of

$$\eta_{\text{exc},\pi} = (99 \pm 1)\,\% \tag{6.42}$$

for a calibrated π-pulse with an energy of $u_p \sim 3\,\text{pJ}$.

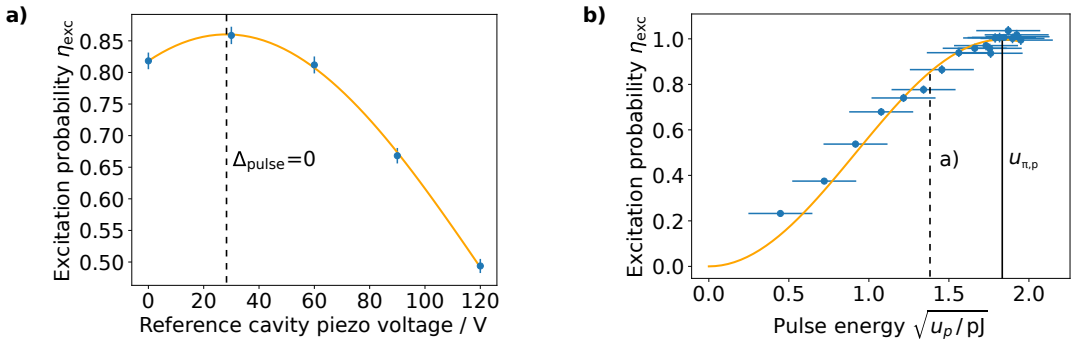

Figure 6.13: Measured excitation probability of the $|e\rangle$ state while driving ultra-fast Rabi flops on the $|0\rangle \leftrightarrow |e\rangle$ transition. The solid line is a fit according to equation (6.30). **a)** Calibration of the pulse centre frequency performed at a pulse energy smaller than the energy required for a π-pulse ($u_{\pi,p}$). We scan the centre frequency of the pulse by varying the length of the reference cavity using a piezo actuator. Blue dots are measured data with the standard errors given as error bars. **b)** Calibration of the pulse energy u_p (blue dots). The standard deviation of the pulse energy is given as horizontal error bars, the standard error of the excitation probability is given as vertical bars. The centre frequency of the pulse is adjusted to be resonant with the atomic transition, i.e. $\Delta_{\mathrm{pulse}} = 0$ according to the measurement in a). We are able to drive a π-rotation on the atomic two-level system at an energy of $u_{\pi,p} \sim 3\,\mathrm{pJ}$. The x-axis accounts for the square-root dependence of Ω on the pulse energy u_p (see eq. (6.38)). From the fit we extract $\eta_{\mathrm{exc}}(u_{\pi,p}) = (99 \pm 1)\,\%$. The pulse energy used for the calibration of the pulse centre frequency in a) is denoted with a dashed line.

6.3.6 Deterministic generation of single photons

The quantum nature of many systems becomes particularly dominant for low excitation states. Since a photon represents the lowest excited quantum state of a radiation field, exploiting the quantum nature of light becomes possible with single photons. Therefore, the realisation of single photon sources plays an important role across multiple fields of quantum information. Examples are provably secure quantum communication [176] or quantum information processing in linear optics, where single photons are needed as qubits [88].

In order to generate single photons, ion-cavity systems are beneficial due to the localised single emitter coupled to a defined mode of the optical fibre cavity. This allows for the generation of photons with a defined profile and timing and has been realised in several experiments using macroscopic cavities [82, 177, 111, 10]. The generation of single photons from a fibre cavity by a continuously driven ion in the UV spectral range [7] and by a deterministically excited ion in the IR spectral range [159] has also been demonstrated. In this subsection, we present the on-demand generation of a single photon out of a fibre cavity in the UV spectral range using ultra-short pulsed excitation of the trapped ion. Using the detection times for a stream of emitted photons and the second-order temporal correlation function $g^{(2)}(\tau)$, we verify the emission of only one photon from the ion at a time.

The normalised second-order temporal correlation function $g^{(2)}(\tau)$ provides insight into

the photon statistic of a source. In terms of intensity it is defined as

$$g^{(2)}(\tau) = \frac{\langle I(t)I(t+\tau)\rangle}{\langle I(t)\rangle \langle I(t+\tau)\rangle}, \tag{6.43}$$

where for a source with constant average intensity $\langle I(t)\rangle = \langle I(t+\tau)\rangle$ [53]. In a quantum mechanical description, where the intensity is proportional to the expectation value of the photon number operator $\langle I\rangle \propto \langle \hat{n}\rangle = \left\langle \hat{a}^\dagger \hat{a}\right\rangle$, we can rewrite equation (6.43) as [118]

$$g^{(2)}(\tau) = \frac{\left\langle \hat{a}^\dagger(t)\hat{a}^\dagger(t+\tau)\hat{a}(t+\tau)\hat{a}(t)\right\rangle}{\langle \hat{a}^\dagger(t)\hat{a}(t)\rangle^2}. \tag{6.44}$$

Using the commutation relation $\left[\hat{a}, \hat{a}^\dagger\right] = 1$, we can find in the case of $\tau = 0$ an expression of equation (6.44) in terms of photon number operators which reads

$$g^{(2)}(0) = \frac{\langle \hat{n}^2\rangle - \langle \hat{n}\rangle}{\langle \hat{n}\rangle^2} = 1 + \frac{\left\langle (\hat{n} - \langle \hat{n}\rangle)^2\right\rangle - \langle \hat{n}\rangle}{\langle \hat{n}\rangle^2}. \tag{6.45}$$

We find $\langle \hat{n}\rangle$ to be the mean photon number of the investigated mode and $\left\langle (\hat{n} - \langle \hat{n}\rangle)^2\right\rangle$ to be the variance of the photon number. Considering non-classical sources of light without any fluctuation, i.e. $\left\langle (\hat{n} - \langle \hat{n}\rangle)^2\right\rangle = 0$, above expression reads

$$g^{(2)}(0) = 1 - \frac{1}{\langle \hat{n}\rangle} < 1, \tag{6.46}$$

which becomes $g^{(2)}(0) = 0$ only for a true single photon source with $\langle \hat{n}\rangle = 1$. Therefore, we can use equation (6.46) to test a light source for the emission of single photons.

In subsection 6.3.5, we presented the excitation of the ion with $(99 \pm 1)\,\%$ probability by driving ultra-fast Rabi flops and in subsection 5.5.2, we verified that the spontaneous decay of the excited state generates deterministic photon pulses with a defined time profile. In order to verify that these light pulses each consist of a single photon, we use a measurement setup similar to the Hanbury Brown and Twiss experiment [30], where we detect the emitted photons on two single photon counters (SPCs) (see Figure 6.14 a)).

We perform in total $N = 20 \times 10^6$ excitations of the ion, separated by $61\,\mu$s. The train of emitted photons is chunked into sequences containing 200,000 excitation events with $\sim 1\,$sec interruptions in between the sequences, where we download the data. We reloaded the ion once for this measurement which caused an interruption of $\sim$ 2 minutes. The arrival times were binned with $1\,\mu$s bin width and the cross-correlations were evaluated between the two SPCs for each of the 100 streams containing 200,000 photon generation attempts. The resulting second-order correlations are shown in Figure 6.14 b). We perform the noise level correction of both detectors according to [82] by recording $2,000$ sets of dark count detection sequences in order to reduce the shot noise. We use cross-correlations between noise-noise and noise-signal sequences to perform the adjustment of the signal-signal correlation baseline. This allows us to give a specific value for $g^{(2)}(0)$ of

$$g^{(2)}(0) = 0.00(5), \tag{6.47}$$

which is limited in accuracy by the standard deviation of the noise baseline (see Figure 6.14 c)). This enables us to use the photons produced in this setup for a secure transfer of information by laws of quantum mechanics [182] (see chapter 8).

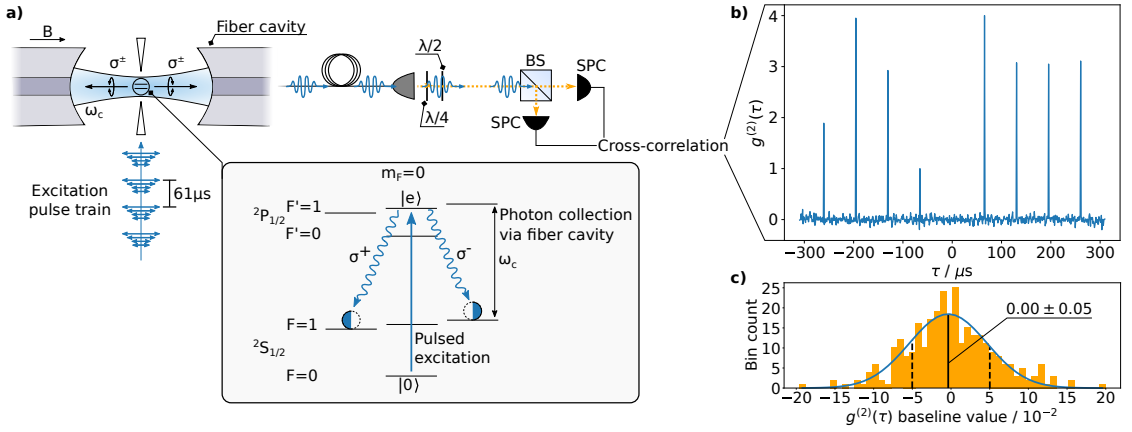

Figure 6.14: a) Sketch of the experimental setup for single photon generation and verification. The inset shows the relevant energy levels of $^{171}Yb^{+}$ with annotated processes. A sequence of atomic initialisation and excitation is repeated every 61 μs. Emitted photons that are collected by the fibre cavity are detected on two single photon counters (SPCs) and time stamps are assigned to the detection events using a time-to-digital converter (TDC) **b)** Temporal second-order cross-correlations of the photon arrival times on the two detectors with detector dark count correction applied according to [82]. **c)** Binned values of the correlation baseline of b), where we extract the mean (black solid line) and the standard deviation (black dashed lines) of the Gaussian noise (blue curve as a fit) and finally obtain $g^{(2)}(0) = 0.00(5)$.

Together with the results of subsection 5.5.2, we can now confirm the on-demand generation of a single photon from the ion-cavity system with a short time profile of 9.3(9) ns width.

6.3.7 Impact of the pulsed laser calibration on the generation of an entangled spin-photon state

In this subsection, we discuss the role of the pulsed laser calibration on the generation of the entangled ion-photon state conceptually. We consider the observation of the emitted photon along the quantisation axis as sketched in Figure 6.15 a). A detailed analysis including the numbers of a particular implementation of an ion-photon state measurement can be found in subsection 7.3.2. In the following, we split our discussion into two parts: i) the pulse detuning Δ_{pulse} and pulse power u_{p} and ii) the polarisation alignment.

Detuning and power

Detuning and power influence the emission probability of a photon in the first place and thus the generation rate of entanglement. The emission probability depends linearly on the excitation probability η_{exc} of the atomic $|e\rangle$ state. If the ion gets not exited, no spontaneous decay happens and no emitted photon can be detected for this attempt of entanglement generation.

However, dark count noise on the single photon counters (SPCs) can trigger false-positive detection events. These events contribute to the analysis of the state correlations between atom and photon. Higher excitation probabilities lower the false-positive ratio on the SPCs and therefore can enhance the detection fidelity of the entangled atom-photon state.

Polarisation

In contrast to power and detuning, the polarisation alignment determines directly the preparation fidelity of the excited state $|e\rangle$. For a high preparation fidelity, the pulsed laser light has to be purely linearly polarised and parallel to the atomic quantisation axis (see Figure 6.15 a)). Otherwise, the accidental driving of atomic transitions with $\Delta m_F = \pm 1$ has direct consequences on the fidelity of the generated atom-photon state (see Figure 6.15 b)). In Figure 6.15 c) the desired decay of the ion from the $|e\rangle$ state is shown. The decay from the $|e\rangle$ state happens in a superposition of decay channels. If the emitted photon is collected along the quantisation axis, the atom-photon state can be written as

$$|\Psi_{\text{atom-photon}}\rangle = \frac{1}{\sqrt{2}} \left(\left|\sigma^+\right\rangle \left|g^+\right\rangle - |\sigma^-\rangle \, |g^-\rangle \right) \tag{6.48}$$

because only circularly polarised photons can be observed. However, accidental excitation of the $|F' = 1, m_F = \pm 1\rangle$ states enables additional decay channels that reduce the generation fidelity of the desired entangled state.

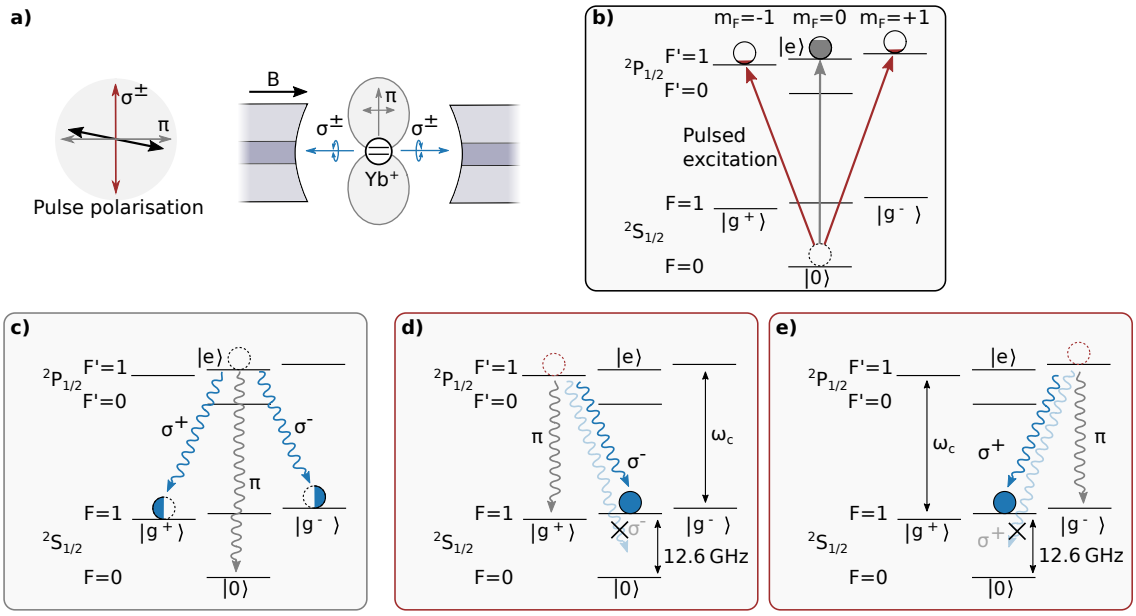

Figure 6.15: a) Definition of the polarisation axes within the setup. Due to the magnetic field, the quantisation axis is parallel to the cavity axis. Misalignment of the driving electric field (black arrow) from an ideal π polarised driving field (grey arrow) results in a fractional driving of $\Delta m_F = \pm 1$ transitions (red arrow). **b)** The circularly polarised fraction of the pulse populates the $|F' = 1, m_F = \pm 1\rangle$ states (red arrows). **c)** Desired decay of the ion for the generation of atom-photon entanglement. **d)+e)** Decay channels of the accidentally excited states. The transition to the $|0\rangle$ state is off-resonant by $\sim 12.6\,\text{GHz}$ to the resonance frequency of the fibre cavity mode ω_c, which suppresses this decay channel for a photon emission into the cavity mode.

For a right-angled beam path with respect to the quantisation axis, the accidental excitation probabilities of these two levels are equal. Photons emitted by a decay of these states and collected by the resonant fibre cavity lead to a population of the $|F = 1, m_F = 0\rangle$ state (see Figure 6.15 d)+e)). This state is detected as bright state in the fluorescence-based readout of the ion in any case (subsection 6.2.2). During the atomic readout sequence, the $|g^-\rangle$ state is mapped to the dark state $|0\rangle$ (see subsection 6.4.2). This results subsequently

in an accidental state attribution of $|F = 1, m_F = 0\rangle$ to $|g^+\rangle$ (bright ion) and a higher probability of measuring a bright ion than a dark ion. This can be expressed in terms of conditional probabilities for a state detection in $\hat{\sigma}_z \otimes \hat{\sigma}_z$ basis as

$$P(g^+|\sigma^-)P(g^+|\sigma^+) > P(0|\sigma^+)P(0|\sigma^-), \tag{6.49}$$

where $P(a|b)$ is the probability of detecting state a for a detection of state b. From the error estimation of the $\hat{\sigma}_z \otimes \hat{\sigma}_z$ correlation measurements presented in subsection 7.3.2, we calculate the preparation fidelity to be $(92 \pm 5)\,\%$.

In terms of $\lambda/2$ wave plate alignment this corresponds to an accidental rotation of the polarisation axis of $(16 \pm 5)^\circ$ for a perfect linear polarisation impinging on the $\lambda/2$ wave plate. We adjusted the polarisation angle of the beam using a polarising beam splitter (PBS) at the beam exit port of the vacuum chamber. Therefore, alignment errors up to some degrees seem reasonable, however, it is also likely that imperfect optical elements such as wave plates and mirrors cause the circular polarisation components to be more present. This assumption is supported by the observation that we cannot completely suppress the intensity of the pulsed laser beam on one arm of the PBS at the exit of the vacuum chamber. However, as long as the quantisation axis and the wave vector of the pulsed laser beam enclose a 90 degree angle, this does not affect our assumption of equal strengths of the circular polarisation components. Any other then a right-angled alignment could cause one of the circular polarisations to become dominant resulting in a violation of the assumptions made. However, we are able to verify this dependence on a large scale, since we have designed the setup according to the required perpendicular dependence between the two axes and conclude that the error in the alignment of the beam axis is negligible compared to the alignment of the polarisation axis.

6.3.8 Summary

We have shown the experimental realisation of an ultra-fast transfer of an atomic ground state population to an excited state with $(99 \pm 1)\,\%$ probability using a laser pulse with a length of $\tau_{\text{pulse}} = (134 \pm 1)\,\text{ps}$. Furthermore, we discussed the generation and application of the laser pulses. We presented how to control and to calibrate the power, centre frequency, spectral bandwidth, polarisation and timing of the pulses at the ion's position.

We have demonstrated that the decay of the deterministically excited ion allows for the on-demand generation of a single photon. We tested this method for the occurrence of two photon events using a second-order correlation measurement, where we obtained $g^{(2)}(0) = 0.00(5)$. The timescale on which the atomic excitation takes place is much shorter than the lifetime of the excited state. Therefore, the time shape of the photons emitted during the decay of the excited state is determined by the natural linewidth of the transition (see subsection 5.5.2). The resulting short photon time shape is particularly useful for a low-noise detection of the entangled ion-photon state in chapter 7. In this context, we discussed how a non-optimal calibration of one of the experimental pulse parameters can affect the measurement of the entangled two-qubit state.

We derived an approximation that allows the application of an analytical solution for the description of the measured excitation probabilities, on which we then based the calibration of the pulse parameters.

6.4 Hyperfine qubit manipulation

The coherent manipulation of information stored in a qubit is an essential part of quantum information processing. The whole concept of universal quantum computation relies on the application of high fidelity gate operations. Also in the context of quantum communication, the ability to rotate a qubit state enables quantum information to be read out in a controlled basis, which is, for example, the basic requirement for provably secure entanglement-based communication [110, 89].

In this section, we first provide a theoretical framework before addressing the technical implementation of qubit rotation operators.

6.4.1 Theory

The energy levels used for the encoding of quantum information are located within the $^2S_{1/2}$ manifold of $^{171}Yb^+$ (see Figure 6.1). Due to the separation of 12.6 GHz between the $F = 1$ and $F = 0$ hyperfine levels, we can coherently manipulate information encoded in this states using microwave radiation. In particular, we focus on the $|F = 0, m_F = 0\rangle$ state and the $|F = 1, m_F = \pm 1\rangle$ states. The $|F = 1, m_F = \pm 1\rangle$ states are important since they contain the phase information of the entangled atom-photon state after decay (see chapter 7) and the $|F = 0, m_F = 0\rangle$ state is added to the system for initialisation and readout purposes. Together, they form a so-called (inverted) lambda-system, which we generalise using the orthogonal states $|0\rangle, |1\rangle$ and $|2\rangle$ in the following (see Figure 6.16). In this subsection, we derive the Hamiltonian of the lambda-system, which can be used in the form of a Master equation to numerical simulate the time dependence of the system using a Lindblad master equation solver[63].

In the experiment, we set the quantisation axis of the system using a static magnetic field $\vec{B_0}$ applied along the z-axis (cavity-axis). The field lifts the degeneracy between the $|F = 1, m_F = \pm 1\rangle$ states by $\omega_L = 2\pi \cdot 2 \cdot 1.4 \frac{\text{MHz}}{G}$ according to equation (6.88), which results in a precession of the atomic spin in the laboratory frame for superposition states of these levels according to the Larmor-precession. In our model, we consider the static magnetic field $\vec{B_0}$ by introducing an energy splitting between $|1\rangle$ and $|2\rangle$ resulting from the static magnetic field as $\hat{H}_{B_0} = -\hat{\vec{\mu}} \cdot \vec{B_0}$.

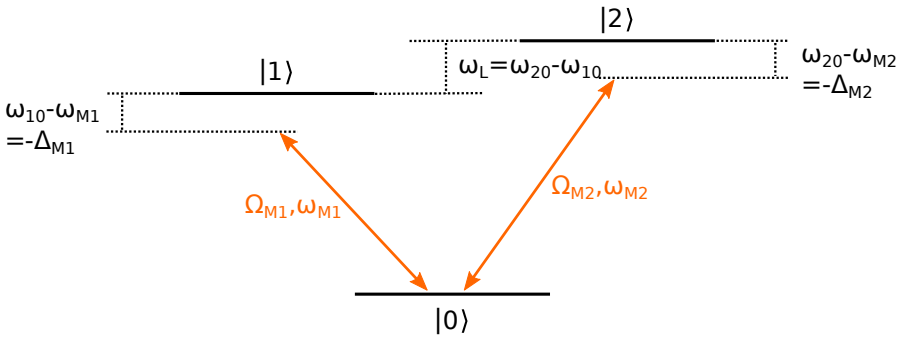

Figure 6.16: Energy levels and relevant frequencies of a driven three-level system.

[63] We use the package QUTIP in PYTHON for a numerical solving

We describe a driving RF microwave field at the ion's position by a time varying magnetic field $\vec{B}(t)$ with frequency ω_M. The interaction of $\vec{B}(t)$ with the magnetic dipole moment $\vec{\mu}$ of the atomic spin is given by the dipole interaction Hamiltonian $\hat{H}_I$ as

$$\hat{H}_I(t) = -\hat{\vec{\mu}} \cdot \vec{B}(t) = g\frac{\mu_B}{\hbar}\hat{\vec{S}} \cdot \vec{B}(t) \qquad \text{with} \qquad \hat{\vec{S}} = \frac{\hbar}{2}\begin{pmatrix} \hat{\sigma_x} \\ \hat{\sigma_y} \\ \hat{\sigma_z} \end{pmatrix}. \tag{6.50}$$

Here, μ_B is the Bohr magneton, g is the dimensionless g-factor and $\hat{\sigma}_{x/y/z}$ are the Pauli matrices forming the spin operator $\hat{\vec{S}}$. Without loss of generality, we assume the magnetic field $\vec{B}(t)$ of the microwave RF radiation to oscillate along the x-axis of the spatial coordinate system with a phase offset ϕ. We write the magnetic field as

$$\vec{B}(t) = B_x \cdot \cos\left(\omega_M t + \phi\right). \tag{6.51}$$

With $\vec{B}(t)$ from equation (6.51), the interaction Hamiltonian of equation (6.50) reads

$$\hat{H}_I = \hbar\Omega_M \cdot \hat{\sigma_x} \cos\left(\omega_M t + \phi\right) \quad \text{with} \quad \Omega_M = \frac{\mu_B g B_x}{2\hbar} \tag{6.52}$$

being the Rabi-frequency.

Using equation (6.52), we derive the Hamiltonian of the driven lambda-system with energy states $|0\rangle, |1\rangle, |2\rangle$ and two driving fields $\vec{B}_k(t)$, $k \in 1, 2$ as

$$\hat{H} = \sum_{i=1}^{2} \hbar\omega_{i0} \left|i\right\rangle \left\langle i\right| + \sum_{k=1}^{2} \hat{H}_{I,k} \tag{6.53}$$

with

$$\hat{H}_{I,k} = \hbar\Omega_{Mk} \cdot \left(\hat{\sigma}_{x,k} \cdot \cos\left(\omega_{Mk} t + \phi_k\right)\right), \tag{6.54}$$

where we set the zero point of the energy scale to the $|0\rangle$ state by defining $\omega_0 = 0$. Furthermore, we introduced the transition frequencies ω_{i0} for the two investigated atomic transitions $|i\rangle \leftrightarrow |0\rangle$ with $i \in \{1, 2\}$.

In equation (6.53), we assumed each magnetic field to interact near resonant with the corresponding atomic transition and neglected cross-interactions of the fields with the transitions. This is a valid assumption, since the energy splitting ω_L between the $|1\rangle$ and $|2\rangle$ states is much higher than the full width at half maximum γ_M of the central excitation peak of the corresponding driven transition for $\Omega_{Mk} \cdot t \leq \pi$ (see Figure 6.23 b)). The corresponding values in the experiments are

$$\gamma_M = 2\Omega_M \sim 2\pi \cdot 30\,\text{kHz} \ll \omega_L = 2\pi \cdot 1.690(2)\,\text{MHz}. \tag{6.55}$$

Therefore, each field $\vec{B}_k(t)$ only applies to the corresponding transition and is far detuned from the other transition.

In equation (6.53), the timescale of the described system dynamics is dominated by the fast oscillating terms of $O(\omega_{i0}) \sim O(\omega_{Mk}) \sim 12.6\,\text{GHz}$. Investigation of the system becomes easier when transforming into a frame rotating at $\sim 12.6\,\text{GHz}$. In analogy to the transformation into a rotating frame in subsection 5.4.2 for a two-level system, we apply a transformation for the presented three level system using the unitary transformation

$$T = e^{i\omega_{M1}t|1\rangle\langle 1| + i\omega_{M2}t|2\rangle\langle 2|} \tag{6.56}$$

to the Hamiltonian of equation (6.53) according to equation (5.37) [64]. Neglecting all terms oscillating with $O(2\omega_{i0})$, we end up with the following expression of the transformed Hamiltonian $\hat{H}'$ in the rotating wave approximation (RWA):

$$\begin{aligned}\hat{H}' = &-\hbar\left(\omega_{M1}-\omega_{10}\right)|1\rangle\langle 1| - \hbar\left(\omega_{M2}-\omega_{20}\right)|2\rangle\langle 2| \\ &+\frac{\hbar}{2}\Omega_{M1}\left[e^{i\phi_1}|1\rangle\langle 0| + e^{-i\phi_1}|0\rangle\langle 1|\right] \\ &+\frac{\hbar}{2}\Omega_{M2}\left[e^{i\phi_2}|2\rangle\langle 0| + e^{-i\phi_2}|0\rangle\langle 2|\right].\end{aligned} \tag{6.57}$$

Since the atomic resonance frequencies ω_{i0} depend on the offset magnetic field in the experiment, they vary with the magnetic field noise. We can account for the magnetic field noise in our model by defining the detuning of the driving fields with respect to the corresponding atomic transition as time dependent. The detuning then reads

$$\Delta_{Mi}(t) = \omega_{Mi} - \omega_{i0}(t). \tag{6.58}$$

Since the RF sources are locked to a 10 MHz reference, it is intuitive to choose the driving field frequencies ω_{Mi} as time stable. From a pure physical point of view, it does not matter which system (atom or microwave) is defined to be frequency stable.

The expression $\frac{\hbar}{2}\Omega_{Mk}\left[e^{i\phi_k}|k\rangle\langle 0| + e^{-i\phi_k}|0\rangle\langle k|\right]$ of equation (6.57) with $k \in 1,2$ describes a coupling between the $|k\rangle$ and the $|0\rangle$ state at rate $\Omega_{Mk}/2$.. By rewriting equation (6.57) in matrix representation as

$$\hat{H}' = \hbar\begin{pmatrix} 0 & \frac{\Omega_{M1}}{2}\left[\cos(\phi_1) - i\sin(\phi_1)\right] & \frac{\Omega_{M2}}{2}\left[\cos(\phi_2) - i\sin(\phi_2)\right] \\ \frac{\Omega_{M1}}{2}\left[\cos(\phi_1) + i\sin(\phi_1)\right] & -\Delta_{M1}(t) & 0 \\ \frac{\Omega_{M2}}{2}\left[\cos(\phi_2) + i\sin(\phi_2)\right] & 0 & -\Delta_{M2}(t) \end{pmatrix}, \tag{6.59}$$

we are able to identify the rotation axis of the coupling between the $|k\rangle$ and the $|0\rangle$ state on resonance ($\Delta_{Mk} = 0$) as

$$\vec{r}_k(\phi_k) = \cos(\phi_k)\,\hat{\sigma}_x + \sin(\phi_k)\,\hat{\sigma}_y \tag{6.60}$$

using equation (2.9).

The phase ϕ_k of the driving field $\vec{B}_k(t)$ is an important parameter, since it defines the orientation of the rotation axis $\vec{r}_k$ in the equatorial plane of the Bloch-sphere upon application of a resonant driving field (see Figure 6.17). The phase ϕ_k is measured in the same reference frame as the phase β_k of superposition states. Such a state on the $|0\rangle$ / $|k\rangle$ qubit reads

$$|\Psi\rangle(\theta,\beta_k) = \cos(\theta/2)\,|k\rangle + e^{i\beta_k}\sin(\theta/2)\,|0\rangle \;\text{ with } 0 \le \theta \le \pi \text{ and } 0 \le \beta_k \le 2\pi \tag{6.61}$$

according to equation (2.6). The state $|\Psi\rangle(\theta = \pi/2, \beta_1 = 0) = \frac{1}{\sqrt{2}}(|1\rangle + |0\rangle)$ points along the x-axis of the Bloch sphere and so does $\vec{r}_1(\phi_1 = 0)$.

The orientation of the driving magnetic field vector defines the offset of the phase ϕ_k. If we perform the previous calculations starting from equation (6.51) by solely changing the magnetic field to oscillate along the y-axis instead of the x-axis, we end up with a similar

[64] We used MATHEMATICA 11.3 for this purpose

result of equation (6.59) and equation (6.60) but with ϕ_k having a phase offset of $\pi/2$. In particular, we can simply adapt both equations to a magnetic field oscillating along the y-axis by substituting $\phi_k \to \phi_k + \pi/2$. We discuss two applications of the above findings in the following.

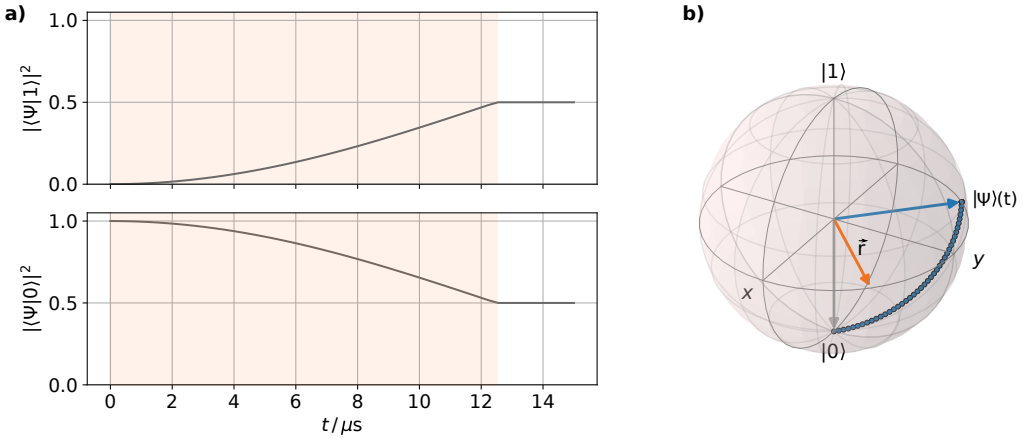

Figure 6.17: Simulated time evolution of a state $|\Psi\rangle(t=0) = |0\rangle$ upon application of a resonant microwave pulse on the $|0\rangle \leftrightarrow |1\rangle$ transition with $\Delta_{M1} = 0$, $\Omega_{M1} = 2\pi \cdot 20\,\text{kHz}$ and $\hat{R}_{\vec{r}(\phi_1=\pi/4)}\left(\frac{\pi}{2}\right)$ (see eq. (6.62)). **a)** Time evolution of the expectation values of a state projection to the basis states $|0\rangle$ and $|1\rangle$. For simplicity, the $|2\rangle$ state is not shown since its expected population is zero at all times. The duration of the pulse is visualised as coloured area. **b)** Evolution of the state $|\Psi\rangle(t)$ on the Bloch-sphere of the two-level sub-system $\{|0\rangle, |1\rangle\}$. The initial state $|\Psi\rangle(t=0)$ is shown as grey arrow and the final state $|\Psi\rangle(t > 12.5\,\mu\text{s}) = |\Psi\rangle(\theta = \pi/2, \beta_1 = 3\pi/4)$ as blue arrow. The trace of the state $|\Psi\rangle(t)$ on the Bloch-sphere is shown as blue points. The rotation axis of the microwave pulse $\vec{r}(\phi_1 = \pi/4)$ is shown as orange arrow.

Driving one qubit transition at a time

For a microwave pulse resonant to a single qubit transition, the interaction time t_M of the radiation with the atomic qubit leads to a rotation of the qubit state. We are able to assign a rotation operator $\hat{R}_{\vec{r}(\phi)}(\alpha)$ to the microwave pulses according to equations (2.9) and (6.59) as

$$\hat{R}^{\alpha}_{\vec{r}(\phi)} = \hat{R}^{\Omega_M \cdot t_M}_{\vec{r}(\phi)}, \tag{6.62}$$

with $\vec{r}(\phi)$ defined according to equation (6.60). The rotation axis $\vec{r}(\phi)$ becomes particularly important when considering a sequence of rotations. A sequence can include rotation operators for a single transition $|0\rangle \leftrightarrow |k\rangle$ or rotations performed one after the other on both transitions. We discuss this in detail in subsection 6.4.2, where we consider the readout of the atomic part of an entangled spin-photon state.

For the less general case of near resonant driving of only one atomic transition with an initial state $|0\rangle$, we can write the probability of finding the atom in the corresponding excited state $|k\rangle$ as

$$\eta_{\text{exc}}(t) = |\langle k|\Psi(t)\rangle|^2 = \frac{\Omega_M^2}{(\Omega'_M)^2} \cdot \left(\frac{1}{2} - \frac{1}{2}\cos\left(\Omega'_M t\right)\right), \tag{6.63}$$

with $\Omega'_M = \sqrt{\Omega_M^2 + \Delta_M^2}$ being the generalised Rabi frequency[65]. We have seen this

[65] We omit the index k for the Rabi frequency and detuning Ω_{Mk}, Δ^2_{Mk} of the transition $|k\rangle \leftrightarrow |0\rangle$

expression in the context of a driven two-level system in equation (5.40) and indeed, driving only a two-level sub-system of the lambda-system gives the same result. We use this feature for the calibration of the individual microwave driving fields in subsection 6.4.4.

In this case of driving only a sub two-level system, we can derive the equivalent of the Bloch-equations (eq. 6.24) as

$$\begin{pmatrix} \dot{x} \\ \dot{y} \\ \dot{z} \end{pmatrix} = \underbrace{\begin{pmatrix} \cos(\phi) \cdot \Omega_M \\ \sin(\phi) \cdot \Omega_M \\ -\Delta_M \end{pmatrix}}_{\vec{r}(\Delta_M, \Omega_M, \phi)} \times \begin{pmatrix} x \\ y \\ z \end{pmatrix}, \tag{6.64}$$

where we obtain the interesting expression of the rotation axis $\vec{r}(\Delta_M, \Omega_M, \phi)$ of a microwave pulse, which is not resonant to the atomic transition.

Simultaneous driving of both qubit transitions

Equation (6.63) leads to the Rabi oscillations which are well known for a two-level subsystem. However, we can achieve something similar when driving the lambda-system on both transitions $|1\rangle \leftrightarrow |0\rangle$ and $|2\rangle \leftrightarrow |0\rangle$ simultaneously (see Figure 6.18). For equal driving power on resonance, i.e. $\Omega_{M1} = \Omega_{M2} \equiv \Omega_M$ and $\Delta_{M1} = \Delta_{M2} = 0$, the effective frequency Ω_{eff} of the oscillation between a superposition state $\frac{1}{\sqrt{2}}\left(|2\rangle + e^{i(\phi_2 - \phi_1)}|1\rangle\right)$ and $|0\rangle$ is given by $\Omega_{\text{eff}} = \sqrt{2} \cdot \Omega_M$.

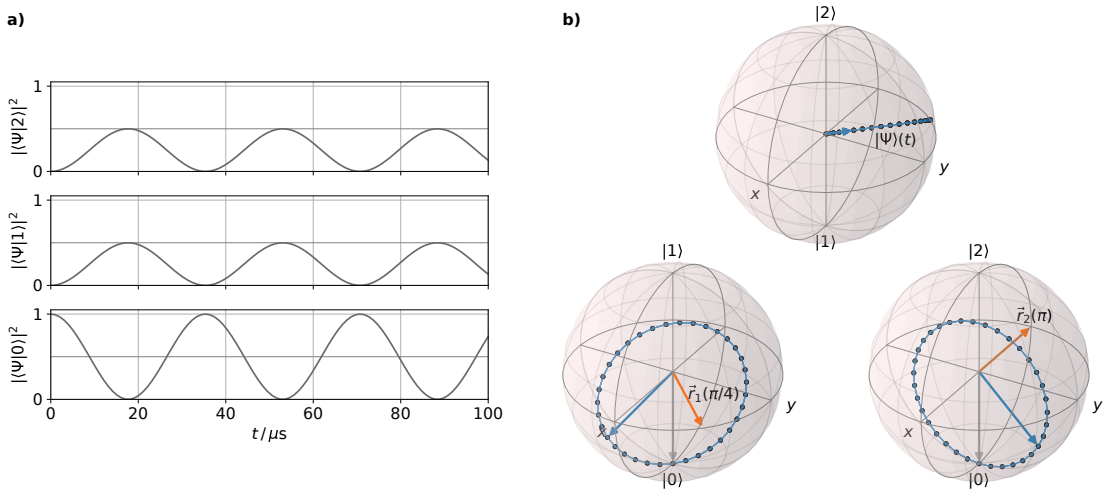

Figure 6.18: Simulation of simultaneous driving of two atomic qubit transitions using $\vec{B}_1(t)$ and $\vec{B}_2(t)$ with $\Omega_{M1} = \Omega_{M2}$ and $\Delta_{M1} = \Delta_{M2} = 0$. The driving field phases are set to $\phi_1 = \pi/4$ and $\phi_2 = \pi$. **a)** Time evolution of the expectation values of the state projections to the basis states $|0\rangle, |1\rangle, |2\rangle$. **b)** Bloch sphere representation of the state evolution on all three two-level subsystems. The rotation axis $\vec{r}_1(\phi_1)$ and $\vec{r}_2(\phi_2)$ of the microwave driving is shown as orange arrows. The initial state $|\Psi\rangle(t = 0) = |0\rangle$ is shown as grey arrow, the final state $|\Psi\rangle(t = 100\,\mu\text{s})$ as blue arrow and the state evolution as blue dots.

This effect can be particular interesting when considering a readout strategy for a superposition state

$$|\Psi\rangle(t = 0) = \frac{1}{\sqrt{2}}\left(|2\rangle + e^{i\beta}|1\rangle\right). \tag{6.65}$$

For a phase difference of the driving fields of

$$\beta = \phi_2 - \phi_1 \tag{6.66}$$

the superposition state can be rotated to $|0\rangle$ for $\Omega_{\text{eff}} \cdot t_M = \pi$. However, for $\beta = \phi_2 - \phi_1 + \pi$ the superposition state remains unaffected from the driving fields. Considering the Zeeman qubit $|g^{\pm}\rangle$, this allows an eigenstate of a rotated basis to be mapped to the $|0\rangle$ dark state while the orthogonal eigenstate remains 'bright', which subsequently allows projective fluorescence state detection. This requires two phase stable driving fields $\vec{B}_k(t), k \in \{1, 2\}$ which are applied simultaneously. We explored this strategy in an earlier stage of the experiment, but found that phase stability was easier to achieve for distinct microwave pulses in our setup. Therefore, for the results presented in this thesis, we used an alternative readout strategy that uses two pulses, as described in the next subsection.

6.4.2 Basis selection of the atomic qubit readout

In this subsection, we present the readout of the atomic part of the entangled atom-photon state. In particular, we focus on the atomic qubit manipulation, which has to be done in advance to the projective fluorescence state detection (see subsection 6.2.2). We present the mapping of the eigenstates of a desired readout basis to the eigenstates of the projective state measurement.

Due to the entanglement generation scheme, the atomic part of the atom-photon state is encoded in the Zeeman qubit $\left|{}^2\mathrm{S}_{1/2}, F = 1, m_F = \mp 1\right\rangle \equiv |g^{\pm}\rangle$, as described in subsection 7.1.3. The projective measurement of the ion state, however, happens to the $\left|{}^2\mathrm{S}_{1/2}, F = 0\right\rangle \equiv |0\rangle$ state and the $\left|{}^2\mathrm{S}_{1/2}, F = 1\right\rangle$ manifold as presented in section 6.2. In other words, both Zeeman qubit states $|g^+\rangle$ and $|g^-\rangle$ couple to the driving laser field of the state readout (see Figure 6.19). Therefore, we have to map the Zeeman qubit $|g^+\rangle \leftrightarrow |g^-\rangle$ to one of the hyperfine qubits $|g^{\pm}\rangle \leftrightarrow |0\rangle$.

In principle, any of the two states $|g^{\pm}\rangle$ can be mapped to the $|0\rangle$ state. However, due to the microwave antenna alignment, we have a slightly higher driving Rabi-frequency on the $|0\rangle \leftrightarrow |g^-\rangle$ transition. Therefore, we apply a microwave π-pulse with rotation operator $\hat{R}^{\pi}_{\vec{r}(\phi)}$ (see equation (6.62)) on this transition, which coherently transfers the information from the Zeeman qubit to the hyperfine qubit $|0\rangle \leftrightarrow |g^+\rangle$ (see Figure 6.19).

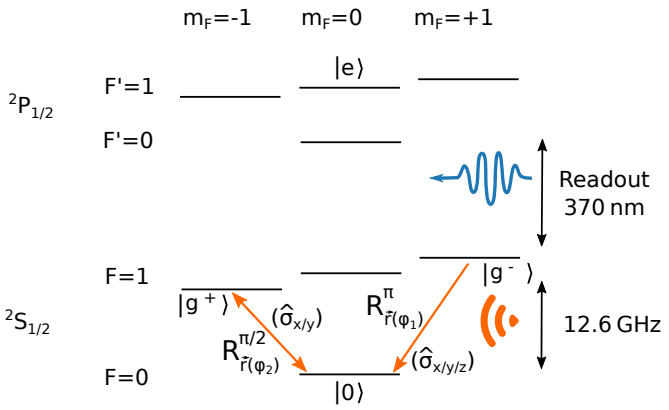

Figure 6.19: Illustration of the coherent state manipulation of the atom in advance to a fluorescence state detection at 370 nm. The relevant energy levels of $^{171}Yb^+$ are shown. The applied rotations are indicated at the corresponding transitions. The bases for which they are applied are given in brackets.

After the mapping π-pulse, the states $|g^+\rangle$ and $|0\rangle$ are eigenstates of the operator $\hat{\sigma}_z$ acting on the hyperfine qubit $|g^+\rangle / |0\rangle$ and also eigenstates of the fluorescence state detection[66]. Therefore, at this stage, a fluorescence state readout projects to the $\hat{\sigma}_z$ basis on the atomic side.

Also, for a state projection to one of the bases orthogonal to $\hat{\sigma}_z$ (e.g. $\hat{\sigma}_{x/y}$), we need to map the eigenstates of this measurement basis to the eigenstates of the fluorescence state detection. But here, the eigenstates of the rotated bases are superposition states of the Zeeman qubit basis states $|g^+\rangle$ and $|g^-\rangle$. Therefore, we have to care about the phases of the mapping pulses with respect to the phase of the superposition state.

To develop a state mapping strategy, we consider the general Zeeman qubit superposition state

$$|\Psi\rangle(\alpha) = \frac{1}{\sqrt{2}}\left(|g^+\rangle + |g^-\rangle \cdot e^{i\alpha}\right), \tag{6.67}$$

which we define as an eigenstate of one of the rotated bases $\hat{\sigma}_k$ with

$$\hat{\sigma}_k |\Psi\rangle(\alpha) = +1 |\Psi\rangle(\alpha) \tag{6.68}$$

according to equation (2.3). The second eigenstate of the basis $\hat{\sigma}_k$ with eigenvalue $\lambda = -1$ is $|\Psi\rangle(\alpha + \pi)$. Examples are given by

$$\begin{aligned} &\hat{\sigma}_x \text{ basis:} && \alpha = 0, \\ &\hat{\sigma}_y \text{ basis:} && \alpha = \pi/2, \\ &\left[(-\hat{\sigma}_x + \hat{\sigma}_y)/\sqrt{2}\right] \text{ basis:} && \alpha = 3\pi/4. \end{aligned} \tag{6.69}$$

For readout purposes, a $\pi/2$ rotation operation could map the state $|\Psi\rangle(\alpha)$, to the corresponding eigenstate of the $\hat{\sigma}_z$ basis $|g^+\rangle$. The corresponding rotation operator $\hat{R}^{\pi/2}_{\vec{r}(\phi=\alpha-\pi/2)}$ with rotation axis $\vec{r}(\alpha - \pi/2)$ rotates the state as

$$\hat{R}^{\pi/2}_{\vec{r}(\phi)} |\Psi\rangle(\alpha) \quad \overset{\phi=\alpha-\pi/2}{\longrightarrow} \quad |g^+\rangle. \tag{6.70}$$

[66] Strictly speaking, the state $|g^+\rangle$ is not an eigenstate of the fluorescence state detection because it projects to the manifold $|F = 1\rangle$ according to the projection operator $\hat{P}_B$ of equation (6.7). This has no influence on the methods presented here, but should be mentioned.

The second eigenstate of the rotated basis $|\Psi\rangle(\alpha+\pi)$ is mapped to $|g^-\rangle$ during this pulse (see Figure 6.20). At this stage, projection and readout as described previously for the $\hat{\sigma}_z$ basis can be performed in principle. However, the realisation of $\hat{R}^{\pi/2}_{\vec{r}(\phi=\alpha-\pi/2)}$ on the $|g^{\pm}\rangle$ qubit would require a phase stable RF-pulse with respect to the generation time of the entangled state, which in addition has to be resonant to the $|g^{\pm}\rangle$ qubit energy splitting ($\sim 1.6\,\mathrm{MHz}$). This is experimentally challenging, as it requires the real-time synchronisation of the pulse phase for each readout attempt with the generation time of the entanglement. This approach is currently explored in the research group of J. Eschner in Saarbrücken.

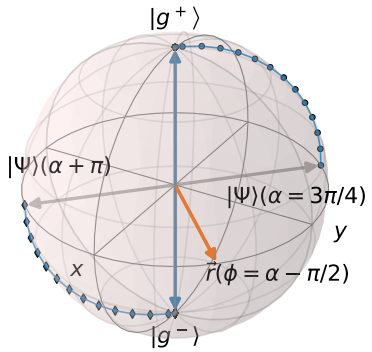

Figure 6.20: Mapping of eigenstates of an example basis $(-\hat{\sigma}_x+\hat{\sigma}_y)/\sqrt{2}$ to the eigenstates of the $\hat{\sigma}_z$ basis. The Bloch sphere representation of the rotation $\hat{R}^{\pi/2}_{\vec{r}(\phi=\alpha-\pi/2)}$ described in equation (6.70) is shown. The rotation axis $\vec{r}$ is shown as orange arrow. The two basis states are shown as grey arrows. The traces of the transformations are shown as blue dots whereas the final states are shown as blue arrows.

A more convenient solution is to first map the superposition state to one of the hyperfine qubits, where the mapping π-pulse again can act on one of the two transitions $|0\rangle \leftrightarrow |g^{\pm}\rangle$ and we again choose the $|0\rangle \leftrightarrow |g^-\rangle$ transition (see Figure 6.19). A following $\pi/2$-pulse maps the superposition state encoded in the hyperfine qubit $|0\rangle / |g^+\rangle$ subsequently to the eigenstates of the fluorescence state detection. We present in the following that this method has the advantage that we only need relative phase stability between the two pulses [67] [68].

We again start with the general Zeeman qubit superposition state $|\Psi\rangle(\alpha)$ from equation (6.67). The first pulse acting on the $|0\rangle \leftrightarrow |g^-\rangle$ transition with $\hat{R}^{\pi}_{\vec{r}(\phi_1)}$ maps the state encoded in the $|g^{\pm}\rangle$ qubit to the $|0\rangle / |g^+\rangle$ hyperfine qubit and we obtain the state

$$|\Phi\rangle(\alpha) = \frac{1}{\sqrt{2}}\left(\left|g^+\right\rangle + |0\rangle \cdot e^{i(\alpha-\pi/2+\phi_1)}\right). \tag{6.71}$$

The second pulse with operator $\hat{R}^{\pi/2}_{\vec{r}(\phi_2)}$, which subsequently acts on the $|0\rangle \leftrightarrow |g^+\rangle$ transi-

[67] As an alternative, one could also drive both transitions simultaneously as described to the end of subsection 6.4.1.

[68] Note that in deviation from subsection 6.4.1, we name the phase $\phi_i, i \in \{1,2\}$ of a pulse according to the order of the applied microwave pulses instead of the corresponding atomic transition. We refer to the atomic transition in the context of the corresponding rotation operator $\hat{R}$.

tion has to have a phase of

$$\phi_2 = (\alpha - \pi/2 + \phi_1) - \pi/2 \tag{6.72}$$

in order to map the state of equation (6.71) to the $\left|g^+\right\rangle$ state (similar to equation (6.70)). For the state mapping, it is important to rotate the eigenstates of the $\hat{\sigma}_{x/y/z}$ operator $\left|\Psi_{\pm x/\pm y/\pm z}\right\rangle$ as follows:

$$\begin{aligned} \left|\Psi_{x/y/z}\right\rangle &\rightarrow \left|g^+\right\rangle \\ \left|\Psi_{-x/-y/-z}\right\rangle &\rightarrow |0\rangle\,. \end{aligned} \tag{6.73}$$

This mapping of the eigenstates preserves the corresponding eigenvalue $\lambda = \pm 1$ for the eigenstate $|\Psi_{\lambda\cdot j}\rangle$ of all bases $\hat{\sigma}_j$ with $j \in \{x, y, z\}$ (equation (2.3)). This is similar to the photon state mapping described in equations (5.82) and (5.86).

From equation (6.72), we finally obtain the important expression of the relative pulse phase difference to realise above mapping for the rotated bases in the equatorial plane of the Bloch sphere, which reads

$$\Delta\phi = \phi_2 - \phi_1 = \alpha - \pi. \tag{6.74}$$

For the sake of completeness, we point out again that the state mapping for a readout in $\hat{\sigma}_z$ basis only requires the first π-pulse with an arbitrary[69] phase ϕ_1.

A simulation of a whole state mapping sequence is shown in Figure 6.21 for the basis $(-\hat{\sigma}_x + \hat{\sigma}_y)/\sqrt{2}$ with eigenstates $|\Psi\rangle\,(\alpha = 3\pi/4)$ and $|\Psi\rangle\,(\alpha + \pi)$ as an example to clarify the presented method. It is important to understand that the solution of equation (6.74) does not require constant phases $\phi_{1/2}$ as long as they exhibit relative stability. In the experiment, we program the relative phase into the arbitrary waveform generator generating the pulses, see subsection 6.4.3. As we mix these pulses to the same carrier, the relative phase is preserved. However, the carrier phase exhibits no fixed relation to the experimental sequence and consequently, no fixed relation to the phase of the generated entangled atom-photon state. In total ϕ_1 and ϕ_2 indeed have different values for every experimental shot of the state readout, but are stable in their relative difference $\Delta\phi$. Figure 6.21 b) shows a possible rotation axis of the first pulse with $\phi_1 = \pi/4$ with the corresponding phase of the second pulse ϕ_2, but any other rotation axis for the first pulse located in the equatorial plane of the Bloch sphere also works.

[69] Here, the phase ϕ_1 appears only global for the eigenstates of the $\hat{\sigma}_z$ basis ($\left|g^+\right\rangle$ and $\left|g^-\right\rangle$), since no superposition states are involved

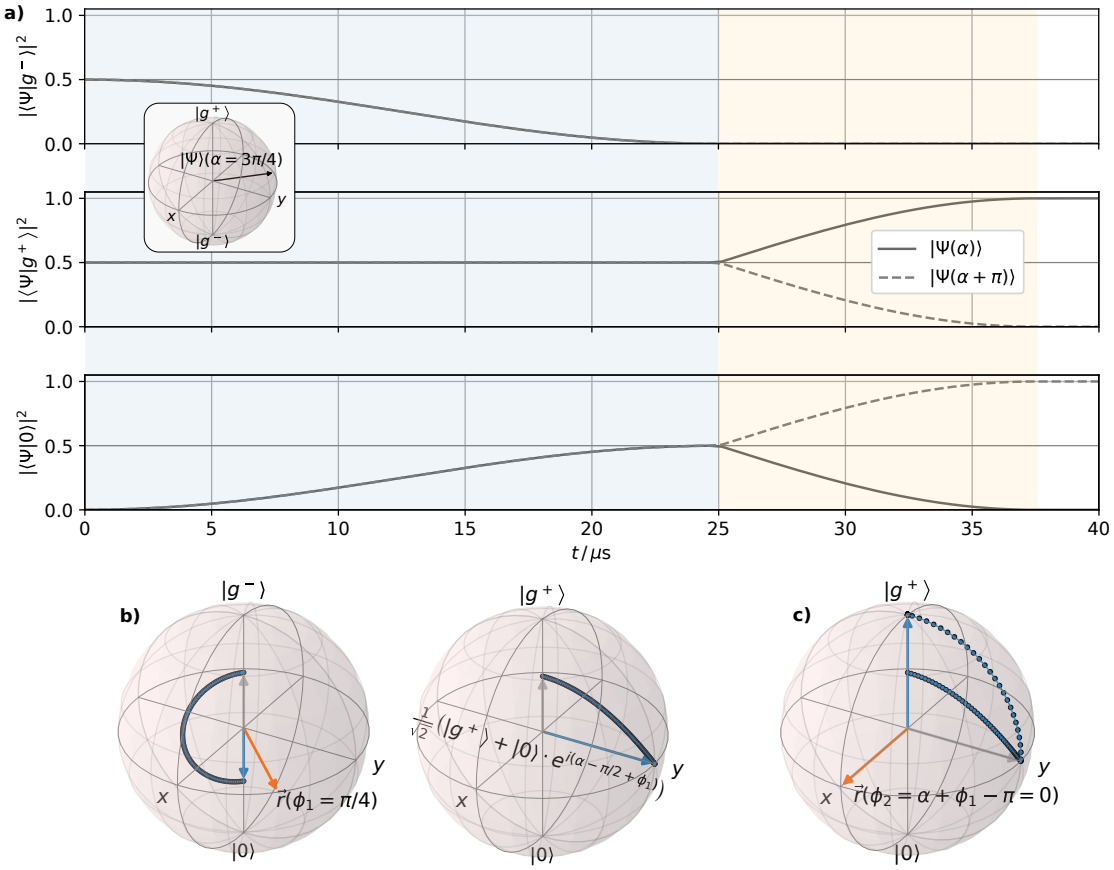

Figure 6.21: Example of a coherent qubit state manipulation to map the eigenstates $|\Psi\rangle\,(\alpha = 3\pi/4)$ and $|\Psi\rangle\,(\alpha + \pi)$ of the $(-\hat{\sigma}_x + \hat{\sigma}_y)/\sqrt{2}$ basis according to equation (6.67) to the eigenstate $|g^+\rangle$ and $|0\rangle$ of the fluorescence state detection according to equation (6.73). **a)** Time evolution of the expectation values of the state projections to the basis states $|0\rangle, |g^-\rangle$ and $|g^+\rangle$ (solid line: $|\Psi\rangle\,(\alpha)$, dashed line: $|\Psi\rangle\,(\alpha + \pi)$). For the time of the blue shaded area the rotation operator $\hat{R}^{\pi}_{\vec{r}(\phi_1)}$ is applied on the $|g^-\rangle \leftrightarrow |0\rangle$ transition. For the time of the yellow shaded area $\hat{R}^{\pi/2}_{\vec{r}(\phi_2)}$ is applied on the $|g^+\rangle \leftrightarrow |0\rangle$ transition. The orientation of the initial superposition state $|\Psi\rangle\,(\alpha = 3\pi/4)$ on the $|g^{\pm}\rangle$ Bloch-sphere is shown as inset. **b)** Bloch-sphere representations of the first rotation (blue area in a)) with the trace of the state shown as blue points. The initial state $|\Psi\rangle\,(\alpha)$ is shown as grey arrow, the final state is shown as blue arrow. The rotation axis is depicted with an orange arrow. **c)** Second rotation (yellow area in a)) represented on the Bloch-sphere with same colour-coding as in b). Here, the blue dots represent the state trace during the whole sequence.

Specifically for $\alpha = \pi/2$, we deal with the eigenstates of the $\hat{\sigma}_y$ basis: $|\Psi_y\rangle = |\Psi\rangle\,(\pi/2)$ and $|\Psi_{-y}\rangle = |\Psi\rangle\,(\pi/2 + \pi)$. They map for $\Delta\phi = -\pi/2$ to $|g^+\rangle$ and $|0\rangle$ respectively. The mapping of the eigenstates of the $\hat{\sigma}_x$ basis can be obtained in a similar way by setting $\alpha = 0$.

Timing of the pulses

In order to end up with the same superposition phase α for all experimental shots, we need a precise timing of the microwave pulses, since the investigated superposition states evolve with a time depended phase $\alpha(t)$ in the laboratory frame. The timing uncertainty of the pulses needs to be much smaller than the time constant of the state evolution, which is determined by the energy splitting of the Zeeman states given in terms of frequency as

$\omega_L = 2\pi \cdot 1.690(2)\,\mathrm{MHz}$ (see subsection 7.4.1). The impact of the microwave pulse timing on the entangled state measurement is considered quantitatively in subsection 7.4.2.

6.4.3 Microwave setup

In this subsection, we discuss the setup that generates the microwave pulses. Since we need to apply sequences of atomic state rotations, we need a setup that can switch between the two transition frequencies of the ion $|g^+\rangle \leftrightarrow |0\rangle$ and $|g^-\rangle \leftrightarrow |0\rangle$ on a fast timescale. In addition, a stable and tunable phase relationship $\Delta\phi$ between the RF oscillations of the applied pulses is required in order to set the correct rotation axes (see previous subsection). A fast rise/fall time of the pulses and a low timing jitter completes the list of requirements.

We generate the pulses using an arbitrary waveform generator[70] (AWG) which is locked to a 10 MHz reference signal. However, we do not generate pulses which are resonant to the atomic transition, but at a frequency $\omega_p \sim 8\,\mathrm{MHz}$. These pulses get mixed to a carrier signal at $\omega_c \sim 12.6\,\mathrm{GHz}$, which is red detuned from the frequencies $\omega_{|i\rangle\leftrightarrow|0\rangle}$, $i \in \{g^+, g^-\}$ of the atomic microwave transitions such that for the sideband of the $+1$ mixing order following applies:

$$\omega_{|i\rangle\leftrightarrow|0\rangle} = \omega_c + \omega_{p,i} - \Delta_{Mi}, \tag{6.75}$$

where $\Delta_{M,i}$ is a controllable detuning of the sideband to the atomic resonance frequency. The carrier is far detuned from the three hyperfine transitions of $^2\mathrm{S}_{1/2} \leftrightarrow {}^2\mathrm{P}_{1/2}$ with $8\,\mathrm{MHz} \gg 2\Omega_M \sim 2\pi \cdot 30\,\mathrm{kHz}$.

Mixing the pulses to the same carrier preserves the relative phase $\Delta\phi$ between the pulses. This method has the advantage of needing only one high frequency source[71] at 12.6 GHz, which itself needs not be phase locked, but frequency locked to the 10 MHz reference. Furthermore, the fast switching of pulses is technically cheaper in a MHz frequency regime.

We program the AWG using the maximum available sample rate of 1 GHz, which results in a rise/fall time of a pulse of 2.9 ns according to the manufacturer. The programmed sequence of RF pulses is output upon the arrival of an external trigger[72]. The generated pulses exhibit a timing jitter of $< 320\,\mathrm{ps}$ according to the manufacturer.

For pulsed application of the microwave carrier signal, we use a slower switch with a rise/fall time of 100 ns according to the manufacturer[73]. In the experiment, we switch the carrier signal on and off with more than 200 ns buffer with respect to the AWG pulses. A block diagram of the setup including a sketch of the pulse timing is shown in Figure 6.22.

[70] Keysight 33600A
[71] N5183A from Agilent
[72] The jitter on the trigger arrival time is 50 ps according to subsection 6.3.3
[73] RF-Lambda

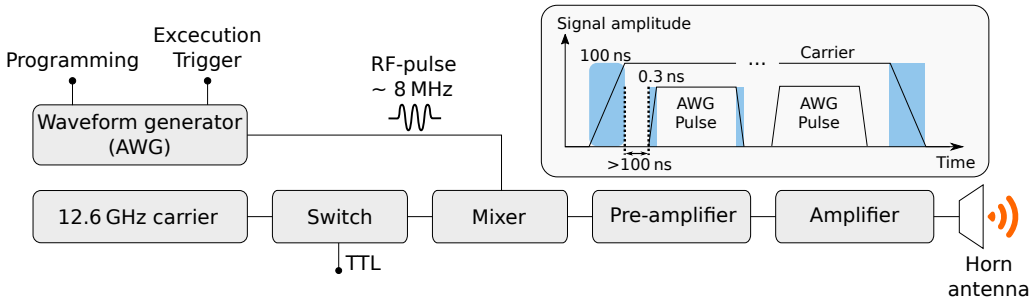

Figure 6.22: Sketch of the setup used for generation and application of microwave pulses. Pulses are generated by a waveform generator (AWG) and modulated to a carrier using a mixer. Timing of the carrier and AWG-pulses as well as the corresponding jitter of the pulse edges are shown as inset (blue shaded areas). Inset: times and amplitudes are not to scale

6.4.4 Calibration of the microwave experimental parameters

For the driving microwave pulses, we need to calibrate radiation power, pulse length and frequency. To this end, we initialise the ion into the $|0\rangle$ state and subsequently apply a (near) resonant microwave pulse to one of the transitions $|i\rangle \leftrightarrow |0\rangle$, $i \in \{g^+, g^-\}$. We aim for the radiation frequency of the pulse to be on resonance with the respective atomic transition, i.e. $\Delta_{Mi} = 0$ (see subsection 6.4.1). Subsequently, we measure the Rabi-frequency Ω_M for both transitions. We make use of equation (6.63) describing the excitation probability under the assumption of distinct atomic transitions (see equation (6.55)) and driving of only one transition at a time. Using fluorescence state detection with a near resonant laser as described in section 6.2, we are able to distinguish between the $\left|^2\mathrm{S}_{1/2}, F = 1\right\rangle$ manifold and the dark state $|0\rangle$. Using the same technique as described in subsection 6.2.1 for a measurement of the bright state population ρ_{bright}, we obtain the excitation probability of a microwave pulse as

$$\eta_{\mathrm{exc}} = \rho_{\mathrm{bright}} = \frac{R_{4\pi}}{R_{\mathrm{ref}}}, \tag{6.76}$$

where we use a time window of $50\,\mu$s per sequence for the determination of the scattering rates $R_{4\pi}$ and R_{ref} over multiple repetitions of a sequence.

Figure 6.23 a) shows a simulation of the expected excitation probability according to equation (6.63) in a two-dimensional parameter space, namely detuning to the atomic transition frequency Δ_M and duration of the applied microwave pulse t_M. We program duration and frequency of the microwave pulse into an arbitrary waveform generator (AWG) which together with a 12.6 GHz carrier forms a (near) resonant pulse (see subsection 6.4.3). We operate the entire microwave setup at the maximum available power[74] to keep the time for the qubit manipulations as short as possible, which mitigates the phase decoherence (see next section). For each set of parameters, we perform $\sim 10,000$ repetitions of the same experimental sequence from which we obtain a measurement of the excitation expectation value η_{exc} for this set of pulse parameters.

In Figure 6.23 b)+c), the pulse parameters were scanned one by one for the $\left|g^+\right\rangle \leftrightarrow |0\rangle$ transition. We extract the resonance frequency $\Delta_M = 0$ and Rabi-frequency Ω_M of the corresponding transition. For calibration of the resonance frequency we choose the rising edge of the first excitation maximum of the Rabi-oscillations, i.e. $\Omega_M \cdot t_M \leq \pi$, such that

[74] Without saturating the involved devices, e.g. amplifiers

we get a clear maximum at $\Delta_M = 0$. The Rabi-frequency Ω_M is measured subsequently at resonance by driving Rabi-oscillations. From these measurements, we can identify the pulse parameters in order to form an arbitrary qubit rotation operator $\hat{R}_{\vec{r}(\phi)}(\Omega_M \cdot t_M)$ as described in equation (6.62).

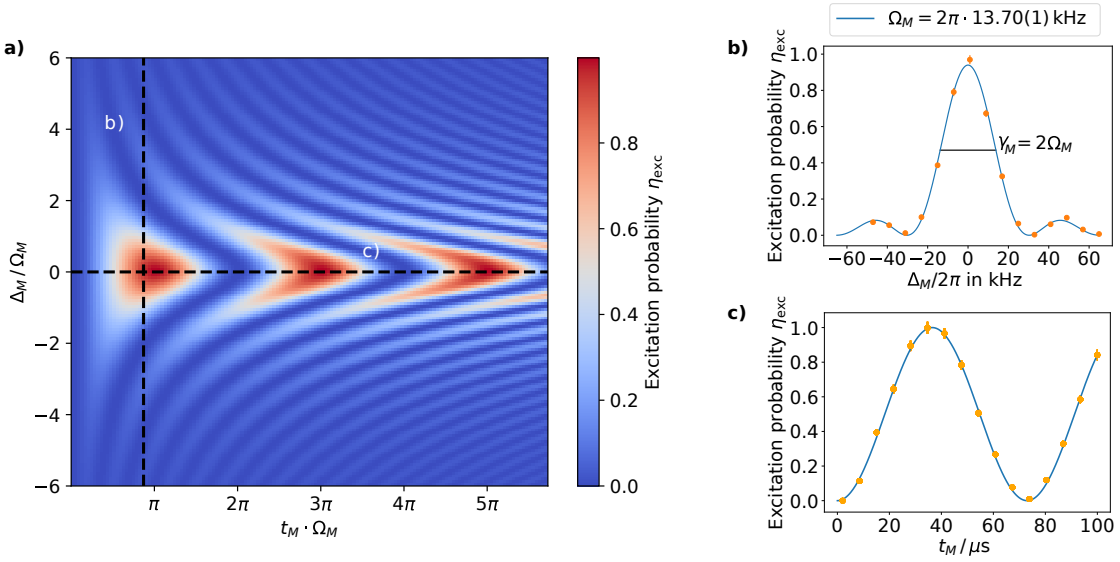

Figure 6.23: a) Calculated excitation probability according to equation (6.63). The traces of the calibration measurements for Δ_M and $\Omega_M \cdot t_M$ are shown as dashed lines. **b)** Calibration of the frequency of the applied microwave pulse by measuring the excitation probability $\eta_{\text{exc}}(\Delta_M)$ for a fixed $\Omega_M \cdot t_M \leq \pi$ while varying the detuning Δ_M to the atomic transition $|g^+\rangle \leftrightarrow |0\rangle$. The FWHM of the central peak is $\gamma_M = 2\Omega_M$. **c)** Calibration of the applied microwave pulse duration t_M by driving Rabi-oscillations at resonance ($\Delta_M = 0$) and measuring $\eta_{\text{exc}}(t_M)$. For a π-pulse, we obtain from the fit $\eta_{\text{exc}} = 100.0(4)\,\%$. For b)+c), the measured data is shown as orange dots with the theory according to a) as blue lines. Error bars show the standard error in b), c).

6.5 Coherence time

For the storage of coherent information in qubits, the time interval in which the information can be retrieved from the qubit with an acceptable error is a crucial property and is called the coherence time. Much effort is put into achieving long coherence times of memory qubits [101, 178]. In quantum communication, the use of memory qubits at the nodes of a network can enable better scaling of the network. The link efficiency in a quantum network $\eta_{\text{Link}} = R_{\text{entanglement}}/R_{\text{decoherence}}$ gives the ratio of entanglement rate, i.e. information distribution, and decoherence rate, i.e. information loss [68, 172]. The link efficiency directly depends on the characteristic coherence time τ of the nodes with $R_{\text{decoherence}} = 1/\tau$.

In this section, we investigate the coherence time of the Zeeman qubit $|g^{\pm}\rangle$ and the hyperfine qubits $|0\rangle$ / $|g^+\rangle$ and $|0\rangle$ / $|g^0\rangle$. To keep the following considerations general, we call the basis states of the investigated qubit $|0\rangle$ and $|1\rangle$. We determine the coherence time of the qubit using a Ramsey sequence with variable hold times t_{hold}, as shown in Figure 6.24 a). To this end, we prepare the system into the state $|0\rangle$ and rotate it to the

equatorial plane of the Bloch-sphere using a resonant microwave pulse with rotation axis[75] $\vec{r}(\phi_1)$ (see Figure 6.24 b)), which can be expressed through the qubit rotation operator $\hat{R}^{\pi/2}_{\vec{r}(\phi_1)}$. Subsequently, we let the superposition state evolve for the time t_{hold}. For each hold time, we obtain the remaining coherence fraction by the visibility of a full scan of the relative phase $\Delta\phi$ between the pulses.

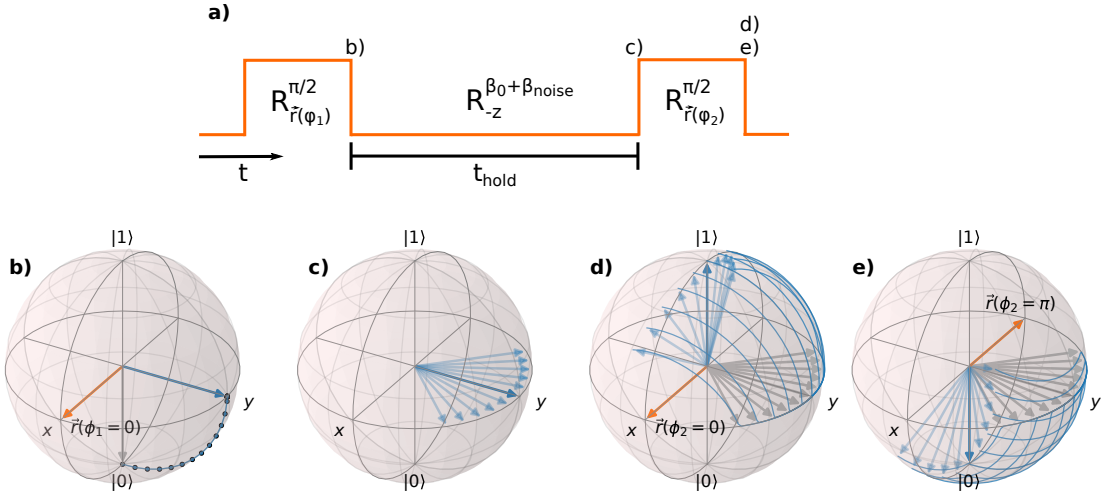

Figure 6.24: a) Ramsey-like pulse sequence creating a superposition state that accumulates phase during a hold time t_{hold} according to equation (6.77). The second pulse probes the time evolution of the state. **b)** Bloch-sphere representation of the generation of the superposition state. The orange arrow depicts the rotation axis $\vec{r}(\phi)$ of the rotation operator of the applied pulse. The grey arrow is the initial state. The final state after applying the rotation operator is shown as a blue arrow. **c)** Time evolution of the superposition state on the Bloch-sphere for 11 different manifestations of $\beta_{\text{noise},k}$ (blue arrows). The dark blue arrow represents the state evolution for vanishing magnetic field noise, i.e. $\beta_{\text{noise}} = 0$. The second probing pulse is visualised for **d)** a maximum average excitation $\Delta\phi_{\text{max}} = 0$ and **e)** for minimum average excitation $\Delta\phi_{\text{min}} = \pi$. Same colour coding of the vectors as in b). For all Bloch-sphere representations, we assumed a vanishing detuning of the driving field to the resonance frequency, i.e. $\Delta_M = 0$.

We consider the system in a rotating frame according to section 6.4. We write the phase β_k accumulated by a qubit superposition state within the hold time t_{hold} of sequence k as

$$\beta_k = \int_0^{t_{\text{hold}}} [\Delta_M + \delta_{M,k}(t)]\, dt = \underbrace{\Delta_M \cdot t_{\text{hold}}}_{\beta_0} + \beta_{\text{noise},k} \tag{6.77}$$

where Δ_M takes into account a potential detuning of the driving field to the atomic transition determined by the static offset field B_0 as described in subsection 6.4.1. The offset field B_0 and Δ_M are defined to be time independent. We assume that the noise contribution $\beta_{\text{noise},k}$ is caused by an additional detuning $\delta_{M,k}(t)$ resulting from the magnetic field noise $B_{\text{noise,k}}(t)$ which has affected the energy splitting of the qubit states during the sequence k. Figure 6.25 shows an illustration of the above definitions.

[75] We name the phase $\phi_i, i \in \{1, 2\}$ of a pulse according to the order of the applied microwave pulses. We refer to the atomic transition in the context of the corresponding rotation operator $\hat{R}$

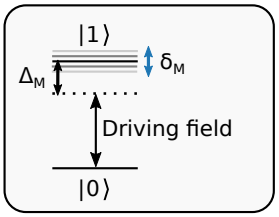

Figure 6.25: Detunings for different origins of frequency mismatch between driving field and atomic transition $|0\rangle \leftrightarrow |1\rangle$ according to equation (6.77).

The phase evolution of 11 different $\beta_{\text{noise},k}$ is shown in Figure 6.24 c) for $\Delta_M = 0$. The second microwave pulse rotates the state around an axis $\vec{r}(\phi_2)$. After the second pulse, we measure the excitation probability P_e of the state $|1\rangle$. For a sequence k, the excitation probability is given as a function of the phase difference of the microwave pulses $\Delta\phi = \phi_2 - \phi_1$ as

$$P_{e,k}(\Delta\phi) = \cos^2\left(\frac{\Delta\phi + \beta_k}{2}\right). \tag{6.78}$$

However, we cannot measure the excitation probability in a single-shot. As described in subsection 6.2.1, the excitation probability is measured over multiple implementations of the same measurement sequence. For each $\Delta\phi$ we run $\sim 10,000$ sequences and the excitation probability averages over all sequences k and all $\beta_{\text{noise},k}$. For a specific $\Delta\phi$ we obtain the measurement result

$$\bar{P}_e(\Delta\phi) = \frac{1}{N}\sum_{k=1}^{N} P_{e,k}(\Delta\phi). \tag{6.79}$$

The average excitation $\bar{P}_e$ reaches its maximum at $\Delta\phi_{\max} = -\Delta_M \cdot t_{\text{hold}} + 2n\pi$ (see Figure 6.24 d)) and its minimum at $\Delta\phi_{\min} = -\Delta_M \cdot t_{\text{hold}} + (2n+1)\pi$ (see Figure 6.24 e)) with $n \in \mathbb{N}_0$. However, the achievable excitation probability is reduced by summation over the $\beta_{\text{noise},k}$, which cause the phases β_k to evolve faster or slower in some of the sequences (see equation (6.77)). For increasing hold times, $\beta_{\text{noise},k}$ blurs out the phases β_k over multiple sequences and the maximal/minimal achievable excitation probabilities approaching $\bar{P}_e(\Delta\phi_{\max/\min}) = 0.5$.

We measure the visibility

$$V = \frac{\bar{P}_e(\Delta\phi_{\max}) - \bar{P}_e(\Delta\phi_{\min})}{\bar{P}_e(\Delta\phi_{\max}) + \bar{P}_e(\Delta\phi_{\min})} \tag{6.80}$$

for several hold times t_{hold} and extract the coherence time τ from the decreasing visibility V as shown in Figure 6.26 for the Zeeman qubit $|g^{\pm}\rangle$ as

$$\tau_{|g^{\pm}\rangle} = (496 \pm 42)\,\mu\text{s} \tag{6.81}$$

and for the hyperfine qubit $|0\rangle \leftrightarrow |g^{+}\rangle$ as

$$\tau_{|0\rangle\leftrightarrow|g^{+}\rangle} = (1020 \pm 278)\,\mu\text{s}. \tag{6.82}$$

Due to the contrary Zeeman shift of the two states $\left|^2\text{S}_{1/2}, F = 1, m_F = \mp 1\right\rangle \equiv |g^{\pm}\rangle$, the energy splitting of this qubit is twice as sensitive to magnetic field fluctuations as for the

$|0\rangle$ / $|g^+\rangle$ hyperfine qubit, where only the energy of the $|g^+\rangle$ state depends on the magnetic field at first order. Consequently, if magnetic field noise is the main source of decoherence, we expect the coherence time of the $|g^\pm\rangle$ qubit to be half as long as that of the $|0\rangle$ / $|g^+\rangle$ qubit. The given values of $\tau_{|g^\pm\rangle}$ and $\tau_{|0\rangle\leftrightarrow|g^+\rangle}$ indicate that.

We can confirm the strong influence of the magnetic field by investigating the coherence time of the first-order magnetic field insensitive qubit $|0\rangle$ / $|g^0\rangle$, where both states have the quantum number $m_F = 0$. For this transition, we obtain

$$\tau_{|0\rangle\leftrightarrow|g^0\rangle} = (12.4 \pm 2.5)\,\text{ms}. \tag{6.83}$$

The coherence time of the $|0\rangle \leftrightarrow |g^0\rangle$ transition is by one order of magnitude longer as for the magnetic field dependent transitions.

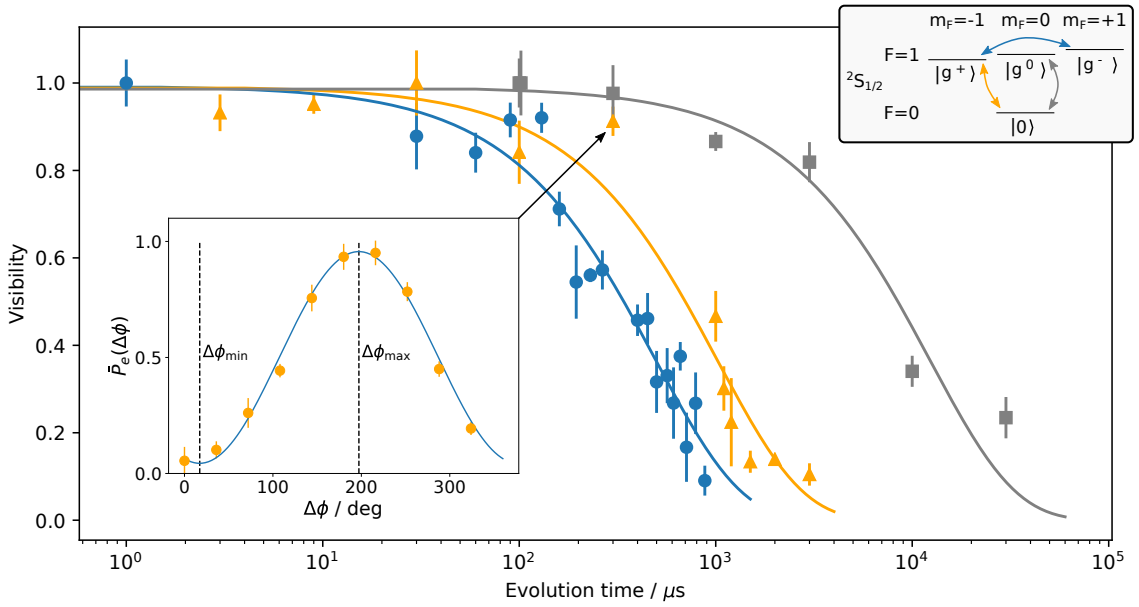

Figure 6.26: Coherence time measurements with magnetic field shielding in place (see subsection 6.6.2). The experimental data show the decreasing visibility for different evolution times between the two $\pi/2$-pulses of a Ramsey like sequence. The visibility for a certain evolution time t_{hold} is determined by scanning the relative phase $\Delta\phi$ between the pulses (inset). Blue circles: Zeeman qubit $|g^\pm\rangle$. Yellow triangles: hyperfine qubit $|g^+\rangle$ / $|0\rangle$. Grey squares: First order magnetic field decoupled qubit $|g^0\rangle$ / $|0\rangle$. Coherence times are extracted from fits (solid lines) with the function $\exp(-(t/\tau))$. Error bars show the standard error. Parts of the data have also been published in [92].

Details on the coherence time measurement of the Zeeman $|g^\pm\rangle$ qubit

The methods and analyses shown above are already applicable to the Zeeman qubit. Only the concrete experimental implementation of generating and reading out superposition states differs in detail from the sequences presented above for the hyperfine qubits and should be listed here for the sake of completeness. To determine the visibility V for the Zeeman qubit, we require the experimental generation (and readout) of superposition states having the form $|\Psi\rangle = \frac{1}{\sqrt{2}}(|g^-\rangle + |g^+\rangle \cdot e^{i\alpha})$, which we cannot realise from the $|0\rangle$

initial state using a single microwave pulse with operator $\hat{R}^{\pi/2}_{\vec{r}(\phi=\alpha-\pi/2)}$. In order to realise a $\hat{R}^{\pi/2}_{\vec{r}(\phi)}$ operation on this qubit, we use two distinct microwave pulses on the two transitions $|0\rangle \leftrightarrow |g^{\pm}\rangle$. The first pulse is doing a $\pi/2$-rotation $\hat{R}^{\pi/2}_{\vec{r_1}(\psi_1)}$ on the transitions $|0\rangle \leftrightarrow |g^{+}\rangle$ with the initial state being $|0\rangle$. The second pulse transfers the remaining population to the $|g^{-}\rangle$ state with $\hat{R}^{\pi}_{\vec{r_2}(\psi_2)}$ acting on the $|0\rangle \leftrightarrow |g^{-}\rangle$ transition. The superposition state is then given by $|\Psi\rangle = \frac{1}{\sqrt{2}}\left(|g^{-}\rangle + |g^{+}\rangle \cdot e^{i(\psi_2-\psi_1)}\right)$. The rotation operator on the $|g^{\pm}\rangle$ qubit resulting in this particular state is $\hat{R}^{\pi/2}_{\vec{r_1}(\phi=\psi_2-\psi_1-\pi/2)}$. For the readout, we apply the reversed sequence with phases ψ_3 and ψ_4. In equation (6.78) one has to consider that the phases $\phi_1(\psi_1, \psi_2)$ and $\phi_2(\psi_3, \psi_4)$ are determined by the phases of the sub-pulses.

6.6 Magnetic field control

High precision control of the magnetic field at the ion's position is crucial for the usage of the trapped ion as a memory qubit. The magnitude of the magnetic field determines the energy splitting of the information encoding hyperfine states and therefore the stability of the field is decisive for the time with which coherent information can be stored in the Zeeman and the hyperfine qubits (see previous section). For the presented setup, we can assume that the magnetic field noise is the main source of decoherence for the atomic qubits. Moreover, the direction of the magnetic field vector sets the quantisation axis and its orientation has to be controlled such that it precisely points along the cavity axis. The applied spin-photon entanglement scheme relies on the suppression of emission of π-polarised light into the cavity mode (section 7.2).

We discuss the stability of the magnetic field generation on a technical level in Appendix D. In this section, we present the calibration of the static magnetic field and shielding of the magnetic field noise.

6.6.1 Orientation and magnitude of the magnetic field

The total magnetic field vector $\vec{B}_s$ at the position of the ion can be written as a static offset field $\vec{B}_{\text{off}}$ superimposed with the generated magnetic field $\vec{B}_c$ originating from the coils as

$$\vec{B}_s = \vec{B}_c + \vec{B_{\text{off}}} = \begin{pmatrix} B_{c,x} \\ B_{c,y} \\ B_{c,z} \end{pmatrix} + \begin{pmatrix} B_{\text{off},x} \\ B_{\text{off},y} \\ B_{\text{off},z} \end{pmatrix}. \tag{6.84}$$

Due to the alignment of the coils, the magnetic field $\vec{B}_c$ can be expressed through the current I_k running through the corresponding coil $k \in x, y, z$ as

$$\vec{B}_c = \begin{pmatrix} a_x \cdot I_x \\ a_y \cdot I_y \\ a_z \cdot I_z \end{pmatrix}, \tag{6.85}$$

where a_k is a factor including the specific properties of the coil. The magnitude of the total magnetic field is

$$|\vec{B}_s| = \sqrt{\sum_{i\in\{x,y,z\}} (a_i \cdot I_i + B_{\text{off},i})^2}, \tag{6.86}$$

which we can rewrite as a function of the current through the coil k as

$$|\vec{B}_s(I_k)| = \sqrt{(a_k \cdot I_k + B_{\text{off},k})^2 + \underbrace{\sum_{i\in\{x,y,z\}\wedge i\neq k} (a_i \cdot I_i + B_{\text{off},i})^2}_{R}}. \tag{6.87}$$

For a single coil $k \in \{x, y, z\}$ and $R \neq 0$, equation (6.87) has the form of a parabola with the minimum being at $I_{0,k} = -B_{\text{off},k}/a_k$ and an offset of R at this point. The offset R results from the offset magnetic field along the remaining two spatial directions.

Using the ion as a sensor, we can probe the absolute value of the static magnetic field $|\vec{B}_s(I_k)|$ using the Zeeman shift of the $|g^{\pm}\rangle$ state which is given by

$$\Delta\nu^{\pm} = \mp 1 \cdot \mu_B \cdot g_F \cdot |\vec{B}_s(I_k)|. \tag{6.88}$$

For the investigated states the Landé factor is $g_F = 1$ and the shift is given by the Bohr magneton in terms of frequency $\mu_B \approx 1.4\,\text{MHz/G}$. We measure the shift $\Delta\nu^{\pm}$ by determining the resonance frequency of the $\omega_{|g^{\pm}\rangle\leftrightarrow|0\rangle}$ transition as shown in Figure 6.23 b) and subsequently computing

$$\Delta\nu^{\pm} = \omega_{|g^{\pm}\rangle\leftrightarrow|0\rangle} - \omega_{|g^{0}\rangle\leftrightarrow|0\rangle}. \tag{6.89}$$

We hereby neglect the second-order magnetic field dependence of the $|g^0\rangle \leftrightarrow |0\rangle$ transition[76]. Figure 6.27 a) shows the expected parabolic behaviour of the Zeeman shift $\Delta\nu^-$. We use equation (6.87) to do a best fit to the measured data and extract $I_{0,x} = -B_{\text{off},x}/a_x$ for the x-axis. We performed a similar measurement also for the y-axis. Applying the offset current values $I_{0,x}$ and $I_{0,y}$ to the corresponding coils cancels out the offset magnetic field along these directions. Figure 6.27 b) shows the expected linear behaviour of the magnetic field value $|\vec{B}_s(I_{k=z})|$ on the current I_z for a vanishing magnetic field offset, i.e. $R = 0$.

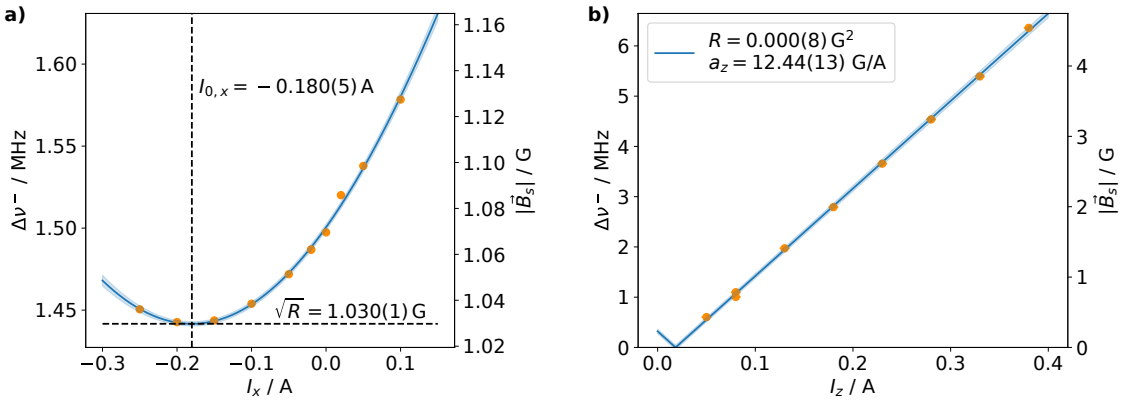

Figure 6.27: Calibration of the magnetic field **a)** along the x-axis **b)** along the z-axis (cavity axis). The latter was performed with zeroed field along the remaining directions ($R = 0$). All data has been recorded without the magnetic field shielding (cobalt foil) in place. The orange points are measured values of $\Delta\nu^-$ with the standard errors depicted as bars (mostly not visible on this scale). The blue solid lines are fits to the measured Zeeman shifts according to equations (6.87) and (6.88). The linewidth depicts the standard deviation of the parameters of the fits.

[76] $\sim 300\,\text{Hz/G}^2$ [186]

For the measurements presented in this thesis, we apply magnetic fields of $|\vec{B}_s(I_z)| \gtrsim 600\,\mathrm{mG}$ along with $R = 0$ in order to set the quantisation axis parallel to the cavity axis. We also refer to this field as B_0.

After wrapping the vacuum chamber in a magnetic field shield consisting of cobalt foil (subsection 6.6.2), we had to repeat the magnetic field calibration due to changing environmental conditions. The results of both calibrations are summarised in Table 4.

	Bare setup	Cobalt foil
$I_{0,z}$/A	0.018(3)	−0.005(2)
$I_{0,x}$/A	−0.180(5)	0.069(4)
$I_{0,y}$/A	−0.036(6)	0.011(1)

Table 4: Applied coil current for a compensation of the magnetic offset field.

6.6.2 Stability of the magnetic field

In this subsection, we present the detection and the mitigation of magnetic offset field fluctuations. To this end, we employed the ion as a precise magnetic field sensor in the low frequency regime of 50 Hz with an accuracy of $\sim 100\,\mu$G.

We describe the magnetic field at the ion's position as

$$\vec{B}(t) = \vec{B_0} + \vec{B}_\sim(t), \tag{6.90}$$

where $\vec{B}_0$ is the static magnetic field we apply to define the quantisation axis along the cavity axis (see subsection 6.6.1) and $\vec{B}_\sim(t)$ is a time dependent part describing the field noise. Not only an imperfect generation of the custom magnetic field at the position of the ion could cause the magnetic field vector to vary over time, but also external sources of noise such as inductive transformers in power supplies.

The noise $\vec{B}_\sim(t)$ changes orientation and magnitude of the total magnetic field $\vec{B}(t)$. The orientation of the quantisation axis is important for the definition of polarisation modes. However, the orientation change happens to a sub degree level with $\arctan\left(|\vec{B}_\sim(t)|/|\vec{B}_0|\right) \lesssim 10^{-2}$, which we can neglect. In contrast, the length change of the magnetic field vector directly has influence to the Zeeman splitting of the hyperfine states, where a relative change of 10^{-2} is in the order of a few kHz, which is noticeable for the transition frequencies of the qubits. We find that

$$|\vec{B}(t)| = \sqrt{|\vec{B_0}|^2 + |\vec{B}_\sim(t)|^2} \approx |\vec{B_0}| + \frac{|\vec{B}_\sim(t)|^2}{2|\vec{B_0}|} \quad \text{for} \quad \vec{B}_0 \perp \vec{B}_\sim(t) \text{ and } |\vec{B}_\sim(t)| \ll |\vec{B}_0|, \tag{6.91}$$

which is small compared to a direct length change of

$$|\vec{B}(t)| = |\vec{B_0}| + |\vec{B}_\sim(t)| \quad \text{for} \quad \vec{B}_0 \parallel \vec{B}_\sim(t). \tag{6.92}$$

From above equations, we conclude that the magnetic field noise has most effect along the axis of $\vec{B}_0$ (z-axis). Furthermore, we define

$$|\vec{B}(t)| = |\vec{B_0}| + B_{\mathrm{noise}}(t), \tag{6.93}$$

with $B_{\text{noise}}(t)$ being the length change of the magnetic field vector caused by noise and $B_{\text{noise}}(t) \approx B_{\sim,z}(t)$ with $B_{\sim,z}(t)$ being the noise component along the cavity axis.

To get an estimate of the magnetic field noise, we measure the magnetic field at a distance of $\sim$ 10 cm from the position of the ion using a fluxgate sensor[77] outside the vacuum chamber. The sensor measures the field along the cavity axis ($B_z(t)$). At the beginning of our noise investigations, we measured $\sim$ 10 mG peak-to-peak noise at this place which seems to be mainly 50 Hz noise with a 150 Hz harmonic on top (see Figure 6.28).

For the first approach of noise cancellation, we used the DC-suppressed sensor signal as an input for a PID-feedback loop with set point zero (see Figure 6.28). The output of the PID-controller was amplified using an audio-amplifier, which is well suited for high current output and low impedance loads. By using a feedback coil with only 5 windings and thus a higher bandwidth than the coils generating the static magnetic field B_0, we applied a magnetic field feedback. We observe that this method allows in principle for an accurate real-time cancellation of the magnetic field fluctuations at the position of the sensor at 50–150 Hz. However, at the position of the ion, the phases of the 50 Hz and the 150 Hz noise contributions slightly differ, which results in a different total noise manifestation. Consequently, the magnetic field noise at the ion's position was not cancellable using a single sensor with a distance of 10 cm from the ion[78].

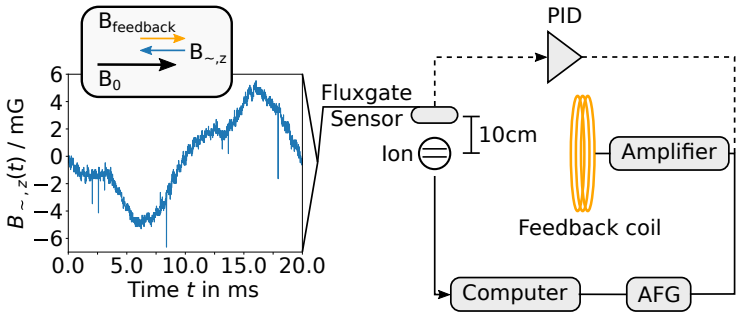

Figure 6.28: Active cancellation of magnetic field noise $B_{\sim,z}(t)$ along the the axis of the static magnetic field B_0. Dashed line: Method 1 uses a Fluxgate sensor, which measures the field along this axis and applies a DC-suppressed feedback via a PID regulator to a feedback coil. The magnetic field fluctuations of one noise period recorded on the Fluxgate sensor along the z-axis are shown versus time. The data was recorded without any feedback applied. Solid line: Method 2 uses the ion for magnetic field sensing.

In principle, the ion itself can be used as a precise magnetic field sensor by utilising the Zeeman energy splitting of the $\left|{}^2\mathrm{S}_{1/2}, F = 1, m_F = \pm 1\right\rangle$ levels. However, the sensing is not real-time and requires measurement cycles of a few seconds in order to gain enough statistic. If the magnetic field noise is time periodic and stable in its periodicity over time, we can measure the signal by reordering the measurement sequences to match the periodicity (and higher harmonics) in post-analysis. Therefore, we have to assume that the duration of one measurement sequence is much shorter than the change of the magnetic field noise B_{noise}. Since we know that the dominant noise occurs in the $\sim$ 50 Hz frequency

[77] Mag-03IEL70 from Bartington

[78] The use of further sensors distributed around the trap could allow extrapolation of the noise manifestation at the position of the ion

regime, we can assume the magnetic field amplitude $|\vec{B}| = |\vec{B_0}| + B_{\text{noise}}$ to be constant within the duration of $\lesssim 1\,\text{ms}$ of one measurement sequence.

For a measurement of the magnetic field noise, we use the detuning that occurs between the driving microwave radiation and the atomic resonance transition $|0\rangle \leftrightarrow |g^-\rangle$ as the energy splitting between the two states changes. To this end, we use a variation of the Ramsey-like sequence of section 6.5 with a fixed hold time $t_{\text{hold}} = 50\,\mu\text{s}$ between the two $\pi/2$ rotations on the $|0\rangle \leftrightarrow |g^-\rangle$ transition. Accordingly, we describe the accumulated phase of a superposition state within the hold time of the kth sequence as

$$\beta_k = (\Delta_M + \delta_{M,k}) \cdot t_{\text{hold}}, \tag{6.94}$$

where Δ_M is the detuning of the driving field to the atomic transition given by B_0. Since the duration of the kth measurement sequence is much shorter than the variation of the magnetic field noise, we can write the time dependent detuning $\delta_M(t)$ resulting from the noise as discrete values[79] $\delta_{M,k} = -1.4\,\frac{\text{MHz}}{\text{G}} \cdot B_{\text{noise},k}$ during the sequence k. The sensitivity of the magnetic field measure depends on the hold time in which the phase of the superposition state can evolve.

In analogy to section 6.5, we measure the excitation probability $P_e(\Delta\phi)$ for a given $\Delta\phi = \phi_2 - \phi_1$ by repeating the Ramsey-sequence $\sim 10,000$ times. Also here, the sequence k contributes as

$$P_{e,k}(\Delta\phi) = \cos^2\left(\frac{\Delta\phi + \beta_k}{2}\right) \tag{6.95}$$

to the measured excitation probability (see equation (6.78)).

In contrast to section 6.5, here we reorder all sequences in a 25 ms time frame, since we know that the periodicity of the magnetic field noise is an integer multiple of 50 Hz. To this end, we bin all sequences according to their relative time distance to a 50 Hz power grid synchronisation trigger, which we record during the measurements (see Figure 6.29 a)). For the sequences contained in the ith bin, the average excitation probability $\bar{P}_e(\Delta\phi, \bar{t}_i)$ is computed, where $\bar{t}_i$ is the bin average time elapsed for the containing sequences since the grid synchronisation trigger was recorded.

[79] Note that an increasing magnetic field amplitude results in a more negative detuning for the $|0\rangle \leftrightarrow |g^-\rangle$ transition according to equation (6.58)

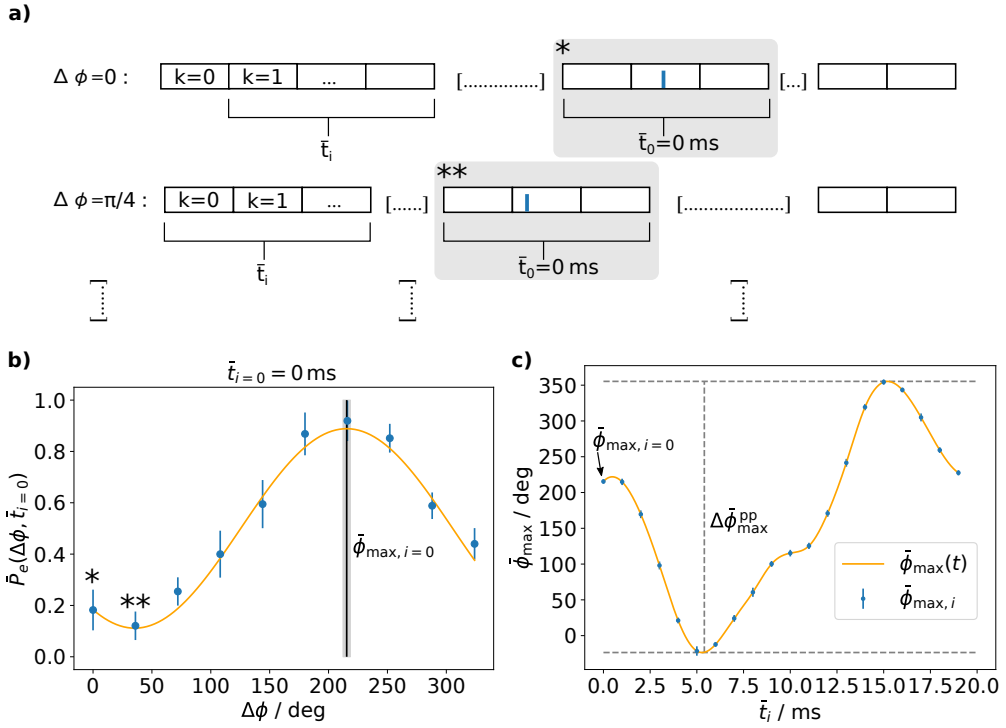

Figure 6.29: Reconstruction of the time dependence of the magnetic field noise. **a)** The rearrangement of measured sequence data (black boxes) is illustrated for two specific phase differences of the microwave pulses $\Delta\phi$. A block of sequence data is combined within a bin i according to the distance to a 50 Hz synchronisation trigger (blue bar). Two example blocks, each giving a data point in b), are highlighted (*, **). **b)** The average excitation probability $\bar{P}_e(\Delta\phi, \bar{t}_i)$ is shown for the sequences contained within the bin $i = 0$ (blue points, with standard errors as bars). The point of maximal excitation $\bar{\phi}_{\mathrm{max,i=0}}$ is extracted from a cosine fit (solid yellow line) and shown as black vertical line with the standard error indicated as grey shaded area. **c)** Measured values of $\bar{\phi}_{\mathrm{max},i}$ for the discrete time bins $\bar{t}_i$ (blue dots). Using cubic interpolation of the data points, the continuous function $\bar{\phi}_{\mathrm{max}}(t)$ is derived (yellow line). The correction $\bar{\phi}_{\mathrm{max}}(t = 0) \stackrel{!}{=} 0$ is not yet applied to the shown data for the sake of simplicity. The peak-to-peak amplitude of the magnetic field noise $B_{\mathrm{noise}}(t)$ can be inferred from the peak-to-peak amplitude of the acquired phase $\bar{\phi}^{\mathrm{pp}}_{\mathrm{max}}$ during state evolution.

The number of bins has to be sufficiently large to provide an accurate time sampling, but also sufficiently small for the bins to contain enough sequences for an acceptable statistical error. For each time bin i, we extract the phase difference $\bar{\phi}_{\mathrm{max},i}$ for which the excitation probability $\bar{P}_e(\Delta\phi = \bar{\phi}_{\mathrm{max},i}, \bar{t}_i)$ has reached its maximum (see Figure 6.29 b)+c)). According to equation (6.95) this is the case at

$$\bar{\phi}_{\mathrm{max},i} = -\Delta_M \cdot t_{\mathrm{hold}} - \bar{\delta}_{M,\bar{t}_i} \cdot t_{\mathrm{hold}} + 2n\pi \tag{6.96}$$

The detunings $\delta_{M,k}$ for all sequences k contained within the bin i average to discrete values $\bar{\delta}_{M,\bar{t}_i}$.

The discrete mapping of the average elapsed time to the average accumulated phase

$$\bar{t}_i \longrightarrow \bar{\phi}_{\mathrm{max},i} \tag{6.97}$$

is done according to Figure 6.29 c). Full rotations of the state vector on the Bloch-sphere

($n \to n \pm 1$ in equation (6.96)) are considered by ensuring continuity[80] of the mapping. We subsequently perform a cubic interpolation[81] of the discrete data points from the mapping of equation (6.97) and obtain a continuous function $\bar{\phi}_{\max}(t)$.

From Figure 6.29 c), we infer a peak-to-peak difference of the Bloch-vector evolution of $\Delta\bar{\phi}^{\mathrm{pp}}_{\max} \approx 380\,\mathrm{deg} = 2.1\pi\,\mathrm{rad}$ within a hold time of $t_{\mathrm{hold}} = 50\,\mu\mathrm{s}$. The corresponding detuning induced by the magnetic field noise is

$$\Delta\bar{\delta}^{\mathrm{pp}}_{M,\bar{t}_i} = \frac{\Delta\bar{\phi}^{\mathrm{pp}}_{\max}}{2\pi \cdot t_{\mathrm{hold}}} \approx 20\,\mathrm{kHz}, \tag{6.98}$$

which corresponds to $\frac{20\,\mathrm{kHz}}{1.4\,\mathrm{MHz/G}} \approx 14\,\mathrm{mG}$ peak-to-peak ripple of $B_{\mathrm{noise}}(t)$. This result is consistent to the fluxgate measurement of the magnetic field noise described earlier in this subsection.

For the sake of field noise cancellation, we programmed the obtained shape of $B_{\mathrm{noise}}(t)$ into an arbitrary function generator (AFG), which applied the waveform to the feedback coil (see Figure 6.28). To this end, we defined $\bar{\phi}_{\max}(t = 0) \stackrel{!}{=} 0$, which corresponds to a vanishing noise contribution at the zero crossing of the power grid AC voltage. We iteratively optimised the amplitude and timing of the output signal to achieve maximum noise compensation while repeating the measurement of $\bar{\phi}_{\max}(t)$ to obtain $\Delta\bar{\phi}^{\mathrm{pp}}_{\max}$ for each step. In the optimised case, we obtained $\Delta\bar{\phi}^{\mathrm{pp}}_{\max} = (58 \pm 11)\,\mathrm{rad}$. From this (peak-to-peak) ripple of the Bloch-vector oscillations, we calculated a residual magnetic field ripple of 2.3(4) mG as the lower limit of this active noise cancellation method while maintaining an acceptable measurement effort. The limitations on the accuracy of the active cancellation are given by the bandwidth of the feedback (amplifier and coil), precision of the feedback signal itself and fluctuations in the power grid frequency around the nominal frequency of 50 Hz.

In addition, we performed passive magnetic field stabilisation by identifying devices with a high magnetic field noise amplitude in the first step and moving them as far away from the vacuum chamber as possible. These were primarily devices in which AC transformers were installed, in particular a digital-to-analogue converter that we built. At this point, we reached already a remaining peak-to-peak ripple of the magnetic field of 3.0(6) mG at the ion's position without active stabilisation. Since this was close to the limit of the active cancellation, we refrained from this method in the following. In a second step, we surrounded the vacuum chamber with 3 layers of laminated cobalt foil[82]. In a separate measurement, we found that this foil is able to damp magnetic field oscillations by a factor of up to 20 in the regime of 50–150 Hz. However, we are only able to put the shielding on 5 out of 6 sides of the experiment, since the bottom side is occupied with cooling laser optics. With the shielding in place, we achieve a damping of the 50–150 Hz magnetic field noise by a factor of 3 and end up with 0.9(1) mG remaining peak-to-peak ripple. We double check this result using the fluxgate sensor located outside the vacuum chamber but inside the shielding, where we measure $\sim 0.7\,\mathrm{mG}$ noise amplitude. A summary of the achieved noise suppression methods and the achieved residual noise amplitudes at 50 Hz at the ion's position can be found in Table 5.

[80] The absolute point-to-point difference has to be smaller than 180 deg
[81] Using the Python package scipy.interp1d
[82] MCL61

	$B_{\mathrm{noise,pp}}$ / mG
No cancellation	~ 14
Active cancellation	2.3(4)
Noise source identification	3.0(6)
Shielding + source identification	0.9(1)

Table 5: Comparison of magnetic field noise cancellation methods. The remaining peak-to-peak amplitude of the noise $B_{\mathrm{noise,pp}}$ at the ion's position is compared.

6.7 Summary

We presented the central methods for the realisation of a quantum network node with a single trapped ^{171}Yb ion as a memory qubit. We demonstrated phase coherent storage of a superposition state in the $|0\rangle / |g^0\rangle$ qubit for a maximum time interval of around 12 ms. Furthermore, we demonstrated state initialisation of the ion within 3.1(1) μs using optical pumping with fidelities exceeding 99 %. Subsequently, we presented the ability of quantum information processing on the atomic hyperfine qubits using phase coherent microwave pulses to implement high fidelity gate operations. To understand the state manipulation of the atomic spin and the mapping of information between the qubits, we derived the full Hamiltonian of the system. This allows us to describe a sequence of arbitrary state rotations on the system taking into account the phases of the driving fields. We presented the mapping of the eigenstates of any basis to the eigenstates of the projective state measurement. Based on free-space fluorescence detection, we achieved a projective readout of the qubit state with a fidelity of 98.2(6) %. This value is on par with similar experimental implementations using the hyperfine qubit of ^{171}Yb$^+$ [129, 46].

By employing the ion as a high precision magnetic field sensor at 50 Hz with an accuracy of $\sim 100\,\mu$G, we stabilised the magnetic field noise actively and passively and achieved a residual magnetic field noise of 0.9(1) mG at best.

In the context of quantum communication, we presented the generation of a single photon on demand with (99 ± 1) % success probability by driving ultra-fast Rabi flops on the atomic transition $|0\rangle \leftrightarrow |e\rangle$ using a picosecond laser pulse and employing the spontaneous decay of the $|e\rangle$ level. For the ion as triggered single photon source, we measured the temporal second-order correlation of photons emitted into the fibre cavity mode to be $g^{(2)}(0) = 0.00(5)$.

The combination of the trapped ion as a memory qubit with the fibre cavity as an interface between light and matter (see chapter 5) gives us the basic tools for quantum communication at hand and we continue with the generation and characterisation of an entangled two-qubit state in chapter 7.

7 Spin-photon entanglement

Contents

7.1 Generation of deterministic atom-photon entanglement 140
7.2 Experimental sequence 146
7.3 Correlation measurements in the $\hat{\sigma}_z \otimes \hat{\sigma}_z$ basis 149
7.4 Correlation measurements in the rotated bases $\hat{\sigma}_{x/y}$ 153
7.5 Full quantum state tomography 160
7.6 Summary 166

Inextricably linked to quantum phenomena, entanglement not only enables communication between distant quantum systems [121] but is also used, for example, for quantum computation [77] and quantum metrology [42]. Particularly for the purpose of quantum communication, the entanglement between an atom and a photon as two different types of qubits is beneficial because it allows to combine the advantages of information storage (atom) with those of long-range distribution of quantum information (photon).

In this chapter, we present the realisation of a quantum network node that combines the stable trapping and the quantum memory properties of the ion (chapters 3, 4 and 6) with the capabilities of the fibre cavity as an efficient light-matter interface (chapter 5). We demonstrate the generation and detection of entanglement between the trapped $^{171}Yb^{+}$ ion and a photon emitted into the fibre cavity mode. So far, only macroscopic cavities have been used as light-matter interfaces in this context. As a basic building block also for future fibre-cavity based experiments, we characterise the achieved entangled state in detail.

In section 7.1, we focus on the theoretical description of entanglement generation between the internal state of an atom and the polarisation degree of freedom of an emitted photon. Subsequently, we introduce the corresponding experimental implementation in section 7.2. We use the notation $\hat{\sigma}_i \otimes \hat{\sigma}_j$ for discussion, which refers to a measurement of the atomic part of the combined atom-photon state in $\hat{\sigma}_i$ basis, while the readout of the photonic part is performed in $\hat{\sigma}_j$ basis. In contrast to a statistical mixture of states, the entangled state of two qubits exhibits a definite phase relation between them and quantum correlations between the two qubit states are visible in any basis $\hat{\sigma}_i \otimes \hat{\sigma}_i$, which cannot be explained classically. We present correlations between atom and photon state measured in $\hat{\sigma}_z \otimes \hat{\sigma}_z$ basis in section 7.3 and in order to verify the occurrence of correlations in different bases orthogonal to $\hat{\sigma}_z$, we rotated both qubits into the equatorial plane of the Bloch sphere as presented in section 7.4. We perform a full quantum state tomography in section 7.5, which gives us the density matrix of the two-qubit state, from which we extract the detection fidelity and purity of the entangled state.

7.1 Generation of deterministic atom-photon entanglement

In this section, we introduce the spontaneous decay of an excited atomic level into several ground states under emission of a single photon as a method for generating atom-photon entanglement. Spontaneous decay of an excited level is a common technique for generating light-matter entanglement with ions [23, 24, 161, 37] and neutral atoms [175] and

has also been used with quantum dots [40] and NV centres [167]. We present in the subsections 7.1.1 and 7.1.2 that the single photon is emitted deterministically with a time constant determined by the lifetime of the excited state. We have already given the experimental verification of this result in subsection 5.5.2. We derive the entangled two-qubit state for the presented system according to a decay to multiple ground states in subsection 7.1.3 and present the experimental implementation in subsection 7.1.4.

7.1.1 Spontaneous decay in a two-level system

As discussed in subsection 6.3.1, a two-level system can undergo transitions when a driving field is applied, but even without the applied field, the system relaxes towards a ground state. However, we added the relaxation of an excited state towards the ground state only phenomenologically to the optical Bloch equations (eq. (6.25)). For an appropriate description of spontaneous emission of a photon, we need to consider the decay of an excited state into a continuum of modes (free-space or cavity modes).

The Hamiltonian of equation (5.43) describes the coupling of a two-level system to a continuum of modes and reads in the interaction picture [152]

$$\mathcal{V} = \hbar \sum_{\mathbf{k}} \left[g_{\mathbf{k}}^{*} \hat{\sigma}^{+} \hat{a}_{\mathbf{k}} e^{i(\omega_a - \omega_{\mathbf{k}})t} + \text{H.c.} \right]. \tag{7.1}$$

The time dynamics of the two-level system's excited state $|e\rangle$ can be derived using the so-called probability amplitude method, where we write the time dependent state of the whole system as

$$|\Psi(t)\rangle = c_e(t)\,|e,0\rangle + \sum_{\mathbf{k}} c_{g,\mathbf{k}}(t)\,|g,1_{\mathbf{k}}\rangle\,. \tag{7.2}$$

The system starts with the atom being in the excited state $|e\rangle$ and the electromagnetic field being in the vacuum state $|0\rangle$, i.e. $c_e(t=0) = 1$ and $c_{g,\mathbf{k}}(0) = 0, \forall \mathbf{k}$. Using the Schrödinger equation

$$\frac{\partial}{\partial t}|\Psi(t)\rangle = \frac{i}{\hbar}\mathcal{V}\,|\Psi(t)\rangle\,, \tag{7.3}$$

we obtain $\dot{c}_e(t)$ and $\dot{c}_{g,\mathbf{k}}(t)$ from equations (7.1) and (7.2) . By substituting the time integral of $\dot{c}_{g,\mathbf{k}}(t)$ into the expression of $\dot{c}_e(t)$, the time evolution of the excited state population is given by the exact equation

$$\dot{c}_e(t) = -\sum_{\mathbf{k}} |g_{\mathbf{k}}|^2 \int_0^t \mathrm{d}t' e^{i(\omega_a - \omega_k)(t-t')} c_e(t'). \tag{7.4}$$

The time evolution of the excited state population can be approximated by rewriting the sum over $\mathbf{k}$ as an integral[83] under the assumption of closely spaced modes and a linear polarisation basis of the radiation field as [152]

$$\dot{c}_e(t) = -\frac{4|\mathbf{d}_{eg}|^2}{(2\pi)^2 6\hbar\epsilon_0 c^3} \int_0^{\infty} \mathrm{d}\omega_{\mathbf{k}} \cdot \omega_{\mathbf{k}}^3 \int_0^t \mathrm{d}t' \cdot e^{i(\omega_a - \omega_{\mathbf{k}})(t-t')} c_e(t'), \tag{7.5}$$

where $|\mathbf{k}| = \omega_{\mathbf{k}}/c$ and the integral over the angular part has already been carried out. Computing the remaining integrals in the Weisskopf-Wigner approximation ($\omega_a \approx \omega_{\mathbf{k}}$)

[83] $\sum_k \to 2\frac{V}{(2\pi)^3}\int_0^{2\pi} d\phi \int_0^{\pi} d\theta \sin\theta \int_0^{\infty} dk\, k^2$

yields [152]

$$\dot{c}_e(t) = -\frac{1}{2}\underbrace{\frac{1}{4\pi\epsilon_0}\frac{4\omega_a^3|\mathbf{d}_{eg}|^2}{3\hbar c^3}}_{\Gamma}\cdot c_e(t), \tag{7.6}$$

with the same expression of Γ as obtained from Fermi's golden rule (see equation (5.52)). This is a well known differential equation leading to the exponential decay of the population in the excited state $|e\rangle$ towards the ground state. We can assign a lifetime $\tau = 1/\Gamma$ to the excited state population.

Carrying out the time integral for $\dot{c}_{g,\mathbf{k}}(t)$ leads to the following form of equation (7.2) [152][84]:

$$|\Psi(t)\rangle = e^{-\frac{\Gamma}{2}\cdot t}\,|e,0\rangle + |g\rangle\sum_{\mathbf{k}} g_{\mathbf{k}}\left[\frac{1-e^{-i(\omega_a-\omega_{\mathbf{k}})t-\frac{\Gamma}{2}t}}{(\omega_{\mathbf{k}}-\omega_a)+i\frac{\Gamma}{2}}\right]|1_{\mathbf{k}}\rangle\,. \tag{7.7}$$

Above expression becomes for long times $t \gg 1/\Gamma$

$$|\Psi(t\to\infty)\rangle = |g\rangle\sum_{\mathbf{k}} g_{\mathbf{k}}\left[\frac{1}{(\omega_{\mathbf{k}}-\omega_a)+i\frac{\Gamma}{2}}\right]|1_{\mathbf{k}}\rangle\,, \tag{7.8}$$

which constitutes a combined atom photon state with the photon being in a linear superposition state of different modes $\mathbf{k}$ with the probability amplitudes given by the mode coupling $g_{\mathbf{k}}$ of equation (5.44) (with $g_{\mathbf{k}}^{eg} = g_{\mathbf{k}}^{ge} = g_{\mathbf{k}}$).

7.1.2 Photon detection probability

For an experimental observation of the spontaneous decay in a two-level system, we can get access to the atom-photon system via the detection of the emitted photon. The probability of detecting a photon at time t on a detector at position $\mathbf{r}$ (with the atom at position $\mathbf{r}_0 = 0$) is then given by the first-order correlation function [152]

$$G^{(1)}(\mathbf{r},\mathbf{r};t,t) = \langle\Psi|\,E^{(-)}(\mathbf{r},t)E^{(+)}(\mathbf{r},t)\,|\Psi\rangle = \frac{\omega_a^4|\mathbf{d}_{eg}|^2\sin^2\theta}{(4\pi\epsilon_0 c^2)^2}\frac{1}{|\mathbf{r}|^3}\cdot\Theta\left(t-\frac{|\mathbf{r}|}{c}\right)e^{-\Gamma\left(t-\frac{|\mathbf{r}|}{c}\right)}, \tag{7.9}$$

where $E^{(+)}(\mathbf{r},t) = \sum_{\mathbf{k}}\mathbf{e}_{\mathbf{k}}\epsilon_{\mathbf{k}}a_{\mathbf{k}}e^{-i\omega_k t+i\mathbf{kr}}$ with the hermitian conjugate $E^{(-)}(\mathbf{r},t)$ and Θ is the step function ensuring that the signal cannot move faster than c. Above equation describes the angular dependence of the detection probability of an emitted linearly polarised photon[85] with $G^{(1)}(\mathbf{r},\mathbf{r};t,t)\propto\sin^2\theta$, where θ is the angle between the dipole axis and the emission direction of the photon.

Furthermore, equation (7.9) describes an exponential decay of the detection probability in time with $\tau = 1/\Gamma$. Given here in the context of a two-level system coupled to a linearly polarised radiation field mode, the time dependent part of equation (7.9) can also be transferred to a decay to multiple ground states as introduced in subsection 7.1.3. We have confirmed this statement in subsection 5.5.2 from the measured time profile of the spontaneously emitted photons for an atomic decay to multiple ground states.

[84] The authors of [152] state $e^{+i(\omega_a-\omega_{\mathbf{k}})t-\frac{\Gamma}{2}t}$ in their final expression. However, from their derivations it should be $e^{-i(\omega_a-\omega_{\mathbf{k}})t-\frac{\Gamma}{2}t}$

[85] Note, that we started with the Hamiltonian of equation (5.43) where we assumed a linear polarisation of the radiation mode

7.1.3 Spontaneous decay to multiple ground states

The coupling of a two-level system to a continuum of modes already leads to the spontaneous decay of the excited atomic state with the emitted photon being in a superposition state of modes (subsection 7.1.1). However, in order to generate entanglement between the atomic state and the photonic state, we have to consider multiple ground states of the atom offering additional decay channels (see Figure 7.1).

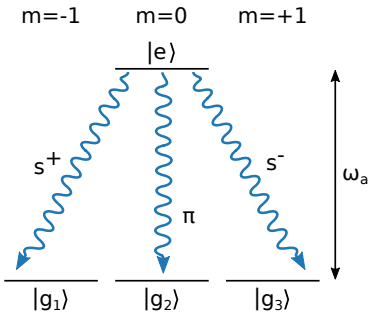

Figure 7.1: Sketch of the decay of an atomic excited state into several ground states $|g_j\rangle, j \in \{1,2,3\}$, where we focus on the quantum number m. The emitted photons couple to different polarisation modes according to angular momentum and parity conservation. Linear polarisation is denoted with π while the circular polarisation modes (usually denoted with $\sigma^{\pm}$) are named $s^{\pm}$ in order to avoid confusion with the atomic raising/lowering operators.

We can derive the state of the atom-photon system analogous to subsection 7.1.1 as

$$|\Psi(t)\rangle = c_e(t)\,|e,0\rangle + \sum_{\mu}\sum_{\mathbf{k}}\left[c_{g_1,\mathbf{k},\mu}(t)\,|g_1,1_{\mathbf{k},\mu}\rangle + c_{g_2,\mathbf{k},\mu}(t)\,|g_2,1_{\mathbf{k},\mu}\rangle + c_{g_3,\mathbf{k},\mu}(t)\,|g_3,1_{\mathbf{k},\mu}\rangle\right], \tag{7.10}$$

where $\sum_{\mu}$ constitutes the summations over the polarisation modes. The interaction Hamiltonian of equation (7.1) reads

$$\mathcal{V} = \hbar\sum_{\mathbf{k},\mu}\left[g^{1*}_{\mathbf{k},\mu}\hat{\sigma}_1^{+}\hat{a}_{\mathbf{k},\mu}e^{i(\omega_a-\omega_{\mathbf{k}})t} + g^{2*}_{\mathbf{k},\mu}\hat{\sigma}_2^{+}\hat{a}_{\mathbf{k},\mu}e^{i(\omega_a-\omega_{\mathbf{k}})t} + g^{3*}_{\mathbf{k},\mu}\hat{\sigma}_3^{+}\hat{a}_{\mathbf{k},\mu}e^{i(\omega_a-\omega_{\mathbf{k}})t} + \text{H.c.}\right], \tag{7.11}$$

where we define $\hat{\sigma}_j^{+} = |e\rangle\langle g_j|$ and neglect energy splitting between the ground level states, i.e. $\omega_{e\leftrightarrow g_j} = \omega_a$, $\forall j \in \{1,2,3\}$. We define $g^j_{\mathbf{k},\mu} = \mathbf{d}_{ej}\cdot\mathbf{e}_{\mathbf{k},\mu}\cdot\epsilon_{\mathbf{k}}/\hbar$ as the coupling between the atomic transition $|e\rangle \leftrightarrow |g_j\rangle$ and the radiation field state with wave vector $\mathbf{k}$ and polarisation mode μ with the unit vector $\mathbf{e}_{\mathbf{k},\mu}$. This becomes especially important when computing the coupling of a specific polarisation mode to an atomic transition under conservation of angular momenta and parity (see Clebsch-Gordan coefficients in Appendix B). Using Schrödinger's equation (7.3) with above definitions, one can derive an expression for $\dot{c}_e(t)$ analogous to equation (7.4) as

$$\dot{c}_e(t) = -\sum_{\mathbf{k},\mu,j}\left[|g^j_{\mathbf{k},\mu}|^2\int_0^t \mathrm{d}t' e^{i(\omega_a-\omega_k)(t-t')}c_e(t')\right]. \tag{7.12}$$

By carefully evaluating the coupling coefficients $|g^j_{\mathbf{k},\mu}|^2$, one can derive an expression of the atom-photon state $|\Psi(t)\rangle$ for large t analogous to equation (7.8) as

$$|\Psi(t\to\infty)\rangle = |g_1\rangle\left|s^{+}\right\rangle\sum_{\mathbf{k}} g^1_{\mathbf{k},s^+}A_{\mathbf{k}}\,|1_{\mathbf{k}}\rangle + |g_2\rangle\,|\pi\rangle\sum_{\mathbf{k}} g^2_{\mathbf{k},\pi}A_{\mathbf{k}}\,|1_{\mathbf{k}}\rangle + |g_3\rangle\left|s^{-}\right\rangle\sum_{\mathbf{k}} g^3_{\mathbf{k},s^-}A_{\mathbf{k}}\,|1_{\mathbf{k}}\rangle, \tag{7.13}$$

where we already executed the summation over the polarisation modes considering the system sketched in Figure 7.1 and absorbed remaining factors in the coefficient $A_{\mathbf{k}}$. The angular dependence of the observation of the atom-photon state is encoded in the coupling coefficients $g^j_{\mathbf{k},\mu}$. The radiation intensity profile is shown in Figure 7.2 derived according to Appendix C using the spatial emission characteristics of a radiating dipole in a classical picture.

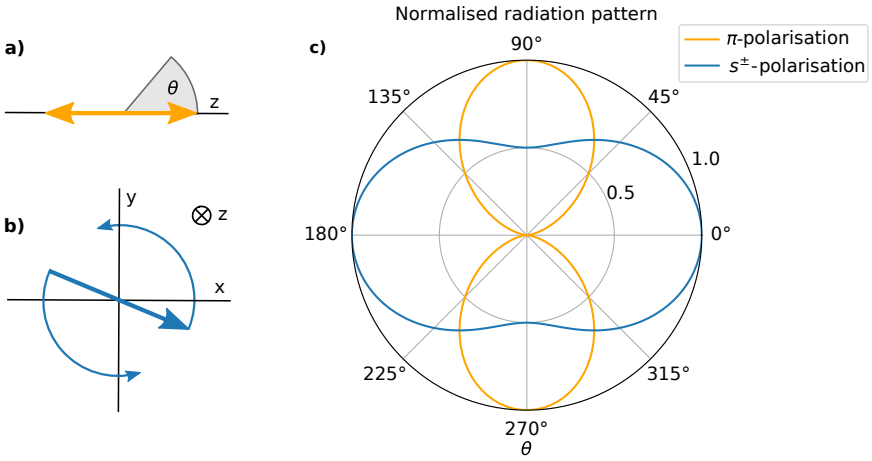

Figure 7.2: Emission characteristics of a radiating dipole in a classical picture. **a)** A localised charge oscillating along the z-axis results in a time varying dipole moment. The electric field of the emitted radiation is linearly polarised along the z-axis (π-polarised). **b)** The dipole moment rotates in the x, y-plane. The electric field of the radiation is called to be circularly polarised according to the direction of rotation ($s^{\pm}$). **c)** Emission characteristics of π- and s-polarised light. The average radiation power per unit solid angle is normalised considering the total average power of the corresponding radiation mode.

The spatial photon emission patterns are given by the vector spherical harmonics [37] and we can define the (un-normalised) polarisations states of the emitted photon according to [23] as

$$\begin{aligned} |\mathcal{P}_0\rangle &= -\sin(\theta)\,|\mathbf{e}_\theta\rangle && \text{for} \quad \Delta m = 0 \ (\pi\text{-polarisation}), \\ |\mathcal{P}_{\pm1}\rangle &= \frac{1}{\sqrt{2}} e^{\pm i\phi}\left[\cos(\theta)\,|\mathbf{e}_\theta\rangle \pm i\,|\mathbf{e}_\phi\rangle\right] && \text{for} \quad \Delta m = \pm 1 \ (s^{\mp}\text{-polarisation}) \end{aligned} \tag{7.14}$$

with the spherical polar/azimuthal angles θ/ϕ of the photon observation direction. Here, the spherical coordinate unit vectors are named $\mathbf{e}_{\theta/\phi}$ and the dipole axis points along $\mathbf{e}_z$ in accordance with Figure 7.2.

Using the polarisation states from equations (7.14), the state of equation (7.13) can be expressed as a sum over all possible decay channels to the ground states $|g_{1,2,3}\rangle$ as [23]

$$|\Psi(t\to\infty)\rangle = \textstyle\sum_{\Delta m_i} c_{\Delta m_i}\,|\mathcal{P}_{\Delta m_i}\rangle\,|\Delta m_i\rangle \quad \text{with} \quad \begin{aligned} |\Delta m_i = -1\rangle &\equiv |g_1\rangle \\ |\Delta m_i = 0\rangle &\equiv |g_2\rangle \\ |\Delta m_i = +1\rangle &\equiv |g_3\rangle \end{aligned} \tag{7.15}$$

and $c_{\Delta m_i}$ being the Clebsch-Gordan coefficients of the corresponding transition.

We can apply above derivations to the spontaneous decay of $^{171}Yb^+$ with levels:

$$\begin{aligned} |g_1\rangle \equiv \left|g^+\right\rangle &= \left|^2S_{1/2}, F=1, m_F=-1\right\rangle, \qquad |g_2\rangle \equiv \left|^2S_{1/2}, F=0, m_F=0\right\rangle, \\ |g_3\rangle \equiv |g^-\rangle &= \left|^2S_{1/2}, F=1, m_F=+1\right\rangle \text{ and } \quad |e\rangle \equiv \left|^2P_{1/2}, F'=1, m_F=0\right\rangle. \end{aligned} \tag{7.16}$$

The Clebsch-Gordan coefficients of the transitions are derived in Appendix B as

$$\begin{aligned} c_{-1} = 1/\sqrt{3} \text{ for } |e\rangle \leftrightarrow \left|g^+\right\rangle, \; c_0 = 1/\sqrt{3} \text{ for } |e\rangle \leftrightarrow |g_2\rangle \\ \text{and } c_{+1} = -1/\sqrt{3} \text{ for } |e\rangle \leftrightarrow |g^-\rangle. \end{aligned} \tag{7.17}$$

Together with equation (7.15), we obtain for an observation of the state along the quantisation axis (dipole axis) with $\theta = 0$ deg an atom-photon state of

$$|\Psi(t\to\infty)\rangle = \frac{1}{\sqrt{2}}\left(\left|g^+\right\rangle\left|s^+\right\rangle - |g^-\rangle\,|s^-\rangle\right), \tag{7.18}$$

which is a maximally entangled Bell-state (see section 2.2).

7.1.4 Experimental implementation

For the concrete application of the results from subsection 7.1.3, the fibre cavity ensures photon collection in a defined spatial mode. For photons emitted into the cavity mode, the decay channel into the ground state $|0\rangle$ with $\Delta m = 0$ is suppressed due to the magnetic field along the cavity axis (see Figure 7.3)).

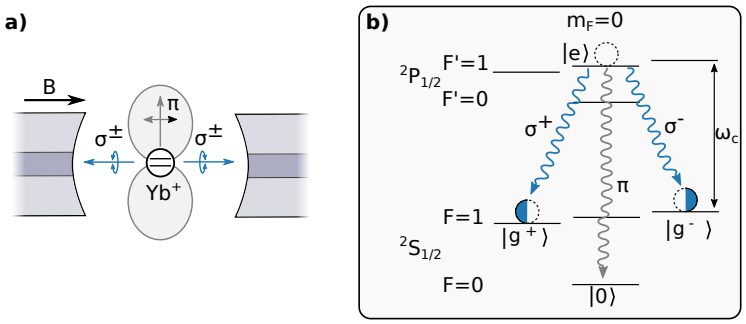

Figure 7.3: Spontaneous decay of the ion prepared in the $|e\rangle = \left|^2P_{1/2}, F'=1, m_F=0\right\rangle$ state under emission of a single photon at 370 nm. **a)** Due to the magnetic field applied along the fibre cavity axis, the emission of π-polarised photons into the cavity mode is suppressed. The angular emission profile of π-polarised photons is sketched as grey area. **b)** Relevant hyperfine energy levels of $^{171}Yb^+$. The ion decays in a superposition of decay channels from the excited state $|e\rangle$ under emission of a single photon into the Zeeman states $|g^+\rangle = \left|^2S_{1/2}, F=1, m_F=-1\right\rangle$ and $|g^-\rangle = \left|^2S_{1/2}, F=1, m_F=1\right\rangle$. The possible decay channels are reduced to the emission of circularly polarised light (blue) if photons are detected along the quantisation axis. In the ideal case, the centre frequency of the cavity mode ω_c is hold resonant to the atomic decay transition.

The external magnetic field leads to a level shift between the $|g^\pm\rangle$ states, however, the resulting frequency difference of $\omega_L \sim 2\pi \cdot 2\,\text{MHz}$ between the two polarisation modes of the emitted photon is much smaller than the atomic linewidth $\Gamma = 2\pi \cdot 19.6\,\text{MHz}$ and the cavity linewidth $\kappa = 2\pi \cdot (58 \pm 9)\,\text{MHz}$, which preserves the capability to decay in a superposition of channels.

From here on, we drop the notation $s^{\pm}$ for the circular polarisation modes and write the ideal maximally entangled atom-photon state for a photon emitted into the cavity mode as

$$|\Psi_{\text{atom-photon}}\rangle = \frac{1}{\sqrt{2}} \left(\left|\sigma^+\right\rangle \left|g^+\right\rangle - |\sigma^-\rangle\, |g^-\rangle \right). \tag{7.19}$$

7.2 Experimental sequence

The experimental sequence for generation and verification of ion-photon entanglement brings together the techniques discussed earlier in this thesis. We split the sequence into two parts: i) the initialisation and excitation of the trapped ion as described in sections 6.1 and 6.3 and ii) the projective state readout of the ion as described in sections 6.2 and 6.4. The execution of the readout part depends on whether we have successfully performed a projective state measurement on the photon state, as described in section 5.5.4. Since the photon is emitted spontaneously from the excited ion, we know the time frame of the photon's arrival at the SPCs to nanosecond precision (see subsection 5.5.2). In the data analysis, we consider the exact time frame with a length of $\sim 10\,\text{ns}$ to suppress false-positive detection events. However, within the experimental sequence, we use an acceptance window of $1\,\mu\text{s}$ for the real-time decision branching. If no photon is detected within a time window of $1\,\mu\text{s}$ after the excitation, the experimental sequence continues with a new initialisation and excitation of the ion (see Figure 7.4). Splitting the sequence and performing a conditional readout of the ion allows for higher repetition rates of the experiment, as the atomic readout takes the longest time and we can only perform a correlation analysis once both the photonic and atomic parts of the two-qubit state have been detected.

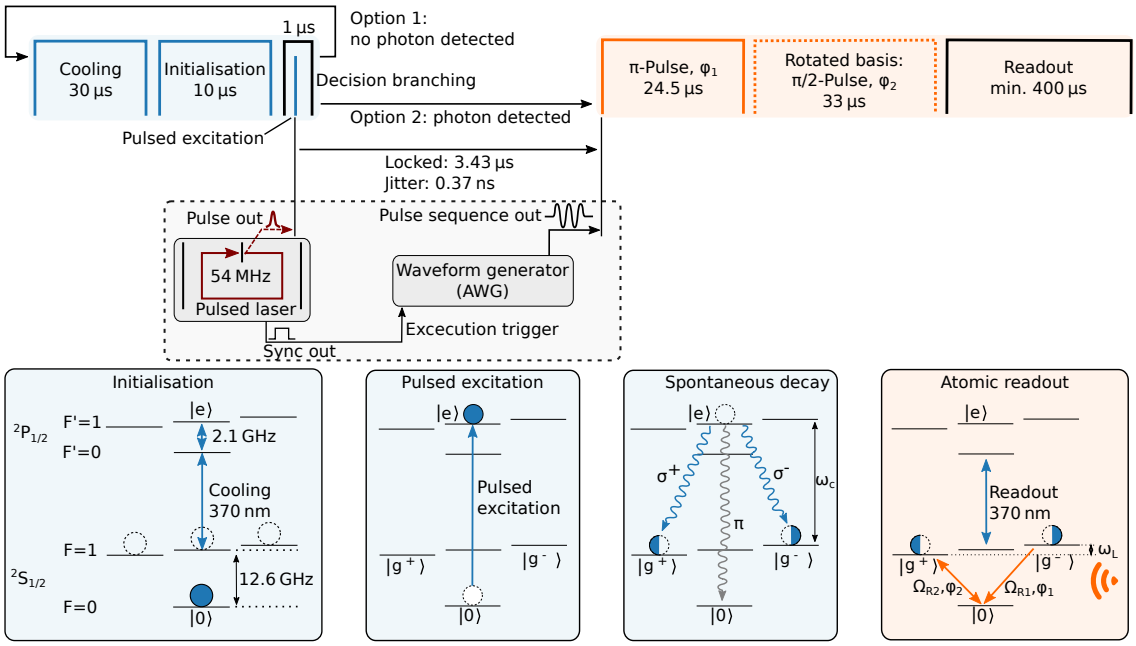

Figure 7.4: Experimental sequence for the generation of an entangled atom-photon state with subsequent detection. The energy level schemes corresponding to the subprocesses of the sequence are given in the bottom row and labelled accordingly. The sequence is split up into a state generation part (blue shaded) and state readout part of the atom (orange shaded). The latter is executed only for a successful state detection of the photon. The atomic state mapping is synchronised to the excitation laser pulse (dashed square inset).

Due to the phase evolution of the superposition spin states with a frequency of $\sim 2\,\mathrm{MHz}$ given by the energy splitting of $|g^{\pm}\rangle$, the readout of the atomic part has to be timed to a precision of $\sim 1\,\mathrm{ns}$ with respect to the generation of the entangled atom-photon state (for details see subsections 7.4.1 and 7.4.2). A lower timing precision results in a lower correlation contrast between atom and photon state, as sampling over multiple phases of the state evolution becomes noticeable. As pointed out in subsection 6.3.3, the arrival time of the excitation laser pulses and thus the generation time of the entangled state is blurred by 18.5 ns by the intra-cavity frequency of the pulsed laser. In order to mitigate this effect, we fix the starting time of the atomic state mapping to the extraction of the excitation laser pulse with a relative jitter of 0.37 ns (see Figure 7.4). This enables the mapping of the atomic state to start at a fixed phase of the state evolution in each repetition of the experiment. The state mapping is followed by a fluorescence state detection taking at least $400\,\mu\mathrm{s}$ (see subsection 6.2.2).

7.2.1 Experimental rate

As with classical communication, a high rate of information transmission is desired in quantum communication. However, in entanglement-based networks, the rate of entanglement generation affects the network as a whole. For entanglement-based communication, phase coherence is distributed across the network nodes and must be maintained to sustain the entanglement. For this purpose, the distribution of entanglement has to be faster than its loss in the network given by the characteristic decoherence rate $R_{\mathrm{decoherence}}$.

Hence, the characteristic distance of a network scales with the link efficiency

$$\eta_{\text{Link}} = R_{\text{entanglement,gen}}/R_{\text{decoherence}}, \tag{7.20}$$

which directly depends on the entanglement generation rate [172]. But also for the extension of networks to a higher number of nodes, the rate of entanglement generation must be higher than the loss rate of phase coherence [68]. Therefore, quantum network nodes with high bandwidth are particularly interesting for communication over long distances, e.g. using a quantum repeater (see Outlook), but also for the generation of multipartite entanglement, e.g. in distributed quantum computing.

We explicitly designed the light-matter interface of the presented network node for an application in a high bandwidth quantum network (see subsection 5.4.4). While maintaining a high collection efficiency of the emitted photons, the cavity design provides a fast extraction of the collected photons. The efficiency of entanglement detection depends on the excitation-, collection-, extraction-, mode-matching-, detector- and path-efficiencies (see subsection 5.5.2) as

$$P_{\text{d,eff}} = \underbrace{\eta_{\text{exc}} \cdot P_{\text{c,eff}} \cdot \eta_{\text{ext}} \cdot \epsilon_m}_{P_{\text{source}}} \cdot \eta_{\text{detector}} \cdot \eta_{\text{path+optics}} = 2.58(6) \times 10^{-3}, \tag{7.21}$$

while the efficiency of entanglement generation depends on the source efficiency $P_{\text{source}} = (1.9 \pm 0.6)\,\%$. Due to the minimum initialisation time of the atomic qubit of $\tau_{\text{init}} = 3.1(1)\,\mu\text{s}$, the fast extraction of the collected photons from the cavity mode ($1.4(1)\,\text{ns}$) has no influence on the achieved repetition rates, but is advantageous for the entanglement detection fidelity (see subsection 7.4.2). With the system presented, we can currently achieve a maximum ratio of entanglement generation rate to decoherence rate of

$$\frac{R_{\text{entanglement,gen}}}{R_{\text{decoherence}}} = \frac{\tau_{|0\rangle\leftrightarrow|g^0\rangle}}{\tau_{\text{init}}} \cdot P_{\text{source}} = \frac{(12,364 \pm 2,534)\,\mu\text{s}}{(3.1 \pm 0.1)\,\mu\text{s}} \cdot P_{\text{source}} = 76 \pm 29 \tag{7.22}$$

by assuming information encoding in the $|0\rangle \leftrightarrow |g^0\rangle$ transition on the atomic side with a coherence time of $\tau_{|0\rangle\leftrightarrow|g^0\rangle}$ (see section 6.5). This ratio is significantly larger than 1 and states that we can use the system as an efficient quantum communication node where the distribution of phase coherence dominates its losses.

We can calculate the expected entanglement detection rate $R_{\text{detection}}$ based on the sequence of Figure 7.4 using the probability P_{d} for a photon detection event per entanglement generation attempt. This directly gives the probability of performing an atomic state readout subsequently to an atomic excitation, where the readout lasts at least $\tau_{\text{a}} = 400\,\mu\text{s}$. We take into account a short cooling interval of the ion prior to its initialisation and excitation by defining the preparation time of the ion as $\tau_{\text{prep}} = \tau_{\text{init}} + \tau_{\text{cooling}}$. The maximum rate of entanglement generation attempts is then given as $1/\tau_{\text{prep}}$. In total, the average time per sequence is $\bar{\tau_s} = P_{\text{d}} \cdot \tau_{\text{a}} + \tau_{\text{prep}}$ and the experimental repetition rate is calculated as

$$R_{\text{exp}} = 1/\bar{\tau_s}. \tag{7.23}$$

The rate of detected entanglements is

$$R_{\text{detection}} = R_{\text{exp}} \cdot P_{\text{d}}. \tag{7.24}$$

The effective rates achieved in the experiment can be calculated considering the detection efficiency of a photon from equation (7.21) and the actual experimental parameters $\tau_\mathrm{a} = 1000\,\mu\mathrm{s}$ [86] and $\tau_\mathrm{prep} = 40\,\mu\mathrm{s}$. We obtain $R_\mathrm{detection} = (60 \pm 2)\,\mathrm{Hz}$, which is in good agreement with the maximum rate of 58 Hz we measured in the experiment. For comparison, the currently achieved success probability of detecting the atom-photon state per shot of $P_\mathrm{d} = 2.58(6) \times 10^{-3}$ is an order of magnitude lower than the success rate of [161], who, to our knowledge, reported the highest atom-photon entanglement measurement rate to date of $\gtrsim 500\,\mathrm{Hz}$.

There are two major improvements that can significantly increase our entanglement detection rate: first, we can use the shortest value allowed by atomic state initialisation of $3.1(1)\,\mu\mathrm{s}$ as the duration of the preparation sequence τ_prep (see section 6.1). This is to be understood as the lower limit of the ion preparation time, since the ion has to be cooled from time to time and thus the effective entanglement rate becomes smaller. Second, the actual detection efficiency suffers from an imperfect cavity stabilisation. Considering the theoretically achievable collection efficiency of the cavity design (see subsection 5.5.3), we compute an even higher rate of entanglement detection. For both cases mentioned, the achievable values are summarised in Table 6.

Experimental parameter	Current cavity lock	Stable cavity lock
$P_d\,/10^{-3}$	2.58 ± 0.06	21 ± 5
$R_\mathrm{exp}/\mathrm{kHz}$	242 ± 2	86 ± 14
$R_\mathrm{detection}/\mathrm{Hz}$	624 ± 15	1830 ± 520

Table 6: Maximal achievable rates of experimental repetition R_exp and entanglement detection $R_\mathrm{detection}$ for $\tau_\mathrm{a} = 400\,\mu\mathrm{s}$ and $\tau_\mathrm{prep} = 3.1(1)\,\mu\mathrm{s}$. The theoretical values for a stable cavity lock are calculated from the cavity design parameters according to subsection 5.5.3.

7.3 Correlation measurements in the $\hat{\sigma}_z \otimes \hat{\sigma}_z$ basis

The projective readout of the photon state is done by two single photon counters (SPCs), one on each exit path of a polarising beam splitter (PBS), projecting the photon state on $|H\rangle$ and $|V\rangle$ respectively as shown in Figure 5.17. For a photonic readout in $\hat{\sigma}_z$ basis, we map the circular polarisation modes $|\sigma^\pm\rangle$ to a linear polarisation basis $|H\rangle\,/\,|V\rangle$ (and vice versa) by a set of wave plates. According to subsection 5.5.4, the eigenstates of the $\hat{\sigma}_z$ basis transform as

$$\begin{aligned} \left|\sigma^+\right\rangle \quad &\rightarrow |V\rangle \\ \text{and} \quad \left|\sigma^-\right\rangle \quad &\rightarrow |H\rangle\,. \end{aligned} \tag{7.25}$$

The corresponding wave plate setting, where fibre, QWP and HWP act in total as a quarter wave plate, is obtained from Figure 5.20. After state mapping of the photonic part, the two-qubit state of equation (7.19) reads

$$|\Psi_\mathrm{atom\text{-}photon}\rangle = \frac{1}{\sqrt{2}} \left(|V_z\rangle \left|g^+\right\rangle - |H_z\rangle \left|g^-\right\rangle \right), \tag{7.26}$$

where we denote the mapped photon states with H_z/V_z for the corresponding wave plate setting.

[86] we shorten the readout window to $400\,\mu\mathrm{s}$ in post-analysis

Upon successful detection of a photon, we apply a microwave π-pulse on the atomic $|g^-\rangle \leftrightarrow |0\rangle$ transition in order to map the Zeeman qubit $|g^{\pm}\rangle$ to the hyperfine qubit $|g^+\rangle / |0\rangle$ (see subsection 6.4.2). We refer to these qubit basis states as the $\hat{\sigma}_z$ basis of the atomic qubit and write the combined atom-photon state after spin and polarisation mapping as

$$|\Psi_{\text{atom-photon}}\rangle = \frac{1}{\sqrt{2}} \left(|V_z\rangle \left|g^+\right\rangle - |H_z\rangle |0\rangle \right). \tag{7.27}$$

The two atomic states $|g^+\rangle$ and $|0\rangle$ separate in the fluorescence state detection for a 400 μs window according to Figure 7.5 a) as

$$\overline{N}_{\text{dark},\hat{\sigma}_z} = 0.20(2) \quad \text{and} \quad \overline{N}_{\text{bright},\hat{\sigma}_z} = 11.9(3), \tag{7.28}$$

where the subscript '$\hat{\sigma}_z$' denotes the experimental settings used for the $\hat{\sigma}_z$ basis correlation measurement.

In Figure 7.5 b), the correlations between atomic and photonic state in $\hat{\sigma}_z \otimes \hat{\sigma}_z$ basis are shown with an applied correction for cavity SPC dark counts (see subsection 7.3.2). We compute the correlation contrast as

$$\begin{aligned} C_{zz} &= P(0|H_z) \cdot P(H_z) + P(g^+|V_z) \cdot P(V_z) - P(g^+|H_z) \cdot P(H_z) - P(0|V_z) \cdot P(V_z) \\ &= (90.7 \pm 3.9)\,\%. \end{aligned} \tag{7.29}$$

The terms $P(\sigma|\lambda) \cdot P(\lambda)$ are the measured conditional probabilities for measuring the atomic qubit in state $|\sigma\rangle$ upon detection of a photon in state $|\lambda\rangle$ (see Table 7).

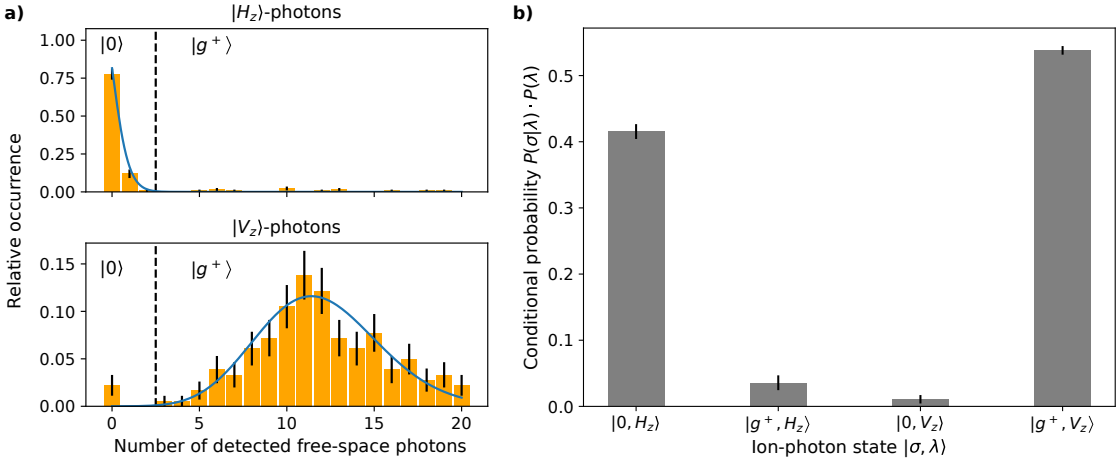

Figure 7.5: Spin-photon correlation in $\hat{\sigma}_z \otimes \hat{\sigma}_z$ basis. **a)** Histogram of free-space photons detected within a time window of 400 μs in the single shot atomic readouts of 315 entanglement events. The solid lines constitute fits to the Poisson distribution. **b)** Conditional probabilities corrected for detector dark counts as bar chart. The data in b) have also been published in [92]. Error bars show the standard error.

	H_z	V_z
g^+	0.036(11)	0.538(6)
0	0.415(11)	0.011(6)
$P(\|\lambda\rangle)$	0.451	0.549

Table 7: Conditional probabilities for a readout in $\hat{\sigma}_z \otimes \hat{\sigma}_z$ basis, corrected for detector dark counts. The photon states are $\lambda = \{H_z, V_z\}$.

7.3.1 Time dependence of the $\hat{\sigma}_z \otimes \hat{\sigma}_z$ basis

The time evolution of the basis states in the Schrödinger picture is given by:

$$\begin{aligned} \left|g^+\right\rangle(t) &= \left|g^+\right\rangle e^{-iE_{g^+}t/\hbar}, \\ \left|g^-\right\rangle(t) &= \left|g^-\right\rangle e^{-iE_{g^-}t/\hbar}, \\ \left|\sigma^+\right\rangle(t) &= \left|\sigma^+\right\rangle e^{-iE_{\sigma^+}t/\hbar}, \\ \left|\sigma^-\right\rangle(t) &= \left|\sigma^-\right\rangle e^{-iE_{\sigma^-}t/\hbar}. \end{aligned} \tag{7.30}$$

Inserting the time evolution of the eigenstates into equation (7.19) results in

$$|\Psi_{\text{atom-photon}}\rangle = \frac{1}{\sqrt{2}}\left(\left|\sigma^+\right\rangle\left|g^+\right\rangle - \left|\sigma^-\right\rangle\left|g^-\right\rangle \cdot e^{-i(E_{g^-}-E_{g^+})t/\hbar} \cdot e^{-i(E_{\sigma^-}-E_{\sigma^+})t/\hbar)}\right). \tag{7.31}$$

Clearly, the time dependence cancels out for $(E_{g^-} - E_{g^+}) = -(E_{\sigma^-} - E_{\sigma^+})$.

In every case, a projective state measurement of the photon in $\hat{\sigma}_z$ basis to the eigenstates $|\sigma^\pm\rangle$ projects the atom to the corresponding state $\left|g^+\right\rangle$ or $|g^-\rangle$. Independent from the detection time of the atom (and the photon), we subsequently find the atom in one of these two states regardless of any global phase evolution of the $|g^\pm\rangle$ states. Therefore, when measuring the atom-photon state correlations in the $\sigma_z \otimes \sigma_z$ basis, we do not have to take into account the timing of the state detections.

7.3.2 Imperfections reducing the correlation contrast in $\hat{\sigma}_z \otimes \hat{\sigma}_z$ basis

In this subsection we summarise the effects that can lead to errors in the detection of the entangled state in the $\hat{\sigma}_z \otimes \hat{\sigma}_z$ basis.

Atomic state mapping via microwave pulses

The transfer fidelity of the microwave π-pulse for the presented measurement was 95.7(7) % (measured according to subsection 6.4.4). The effect of a non-perfect π-pulse manifest itself as an increased probability of measuring a bright ion, which can be described by the inequality

$$P(g^+|H_z) \cdot P(g^+|V_z) > P(0|V_z) \cdot P(0|H_z) \tag{7.32}$$

using the conditional probabilities introduced in this section.

Fluorescence state detection

The fluorescence state detection of the hyperfine qubit $|g^+\rangle / |0\rangle$ results in a correlation contrast reduction of 3.5(12) %. The value was simulated according to subsection 6.2.2.

Entangled state generation through deterministic excitation of the ion

To obtain the state initialisation fidelity of the pulsed laser, we perform a calculation of the probability amplitudes of the ion states after spontaneous decay for a polarisation misalignment of the excitation pulse (Figure 7.6). We do this according to the consideration of subsection 6.3.7. We also take the following imperfections into account: microwave π-pulse fidelity (95.7(7) %), fluorescence state detection (3.5(12) %) and $P(H_z) \neq P(V_z)$ (see Table 7). We achieve consistent values with the conditional probabilities shown in Figure 7.5 b) at an excited state preparation fidelity of

$$F_{\text{gen}} = (92 \pm 5)\,\%. \tag{7.33}$$

We infer this value from Figure 7.6 b)+c). This imperfect preparation of the excited state reduces the contrast of the correlation measurements by 4.2(28) % if no additional imperfections of the correlation measurement are considered (yellow curve in Figure 7.6 a)).

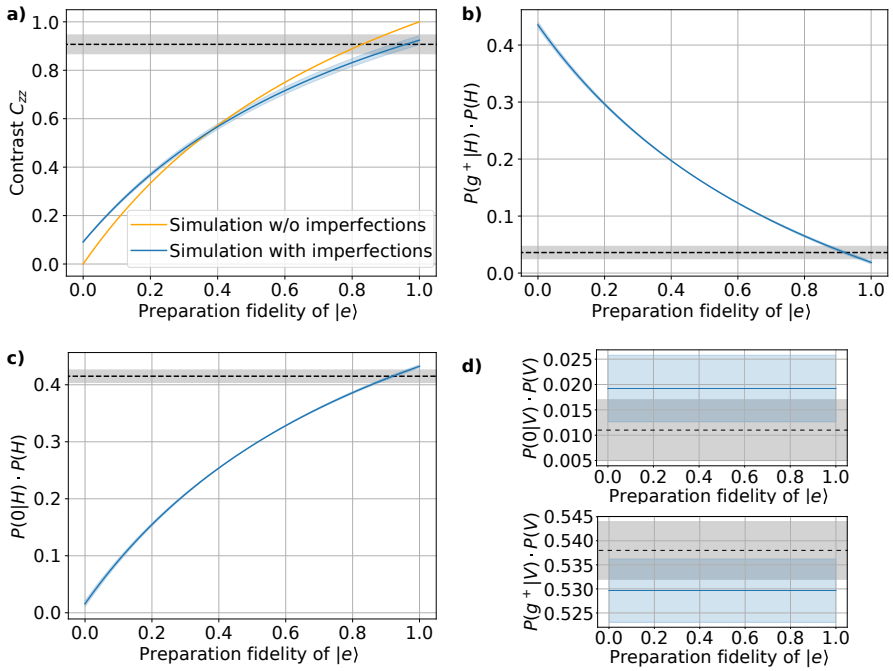

Figure 7.6: Calculation of the probability amplitudes of the ion states after spontaneous decay for a polarisation misalignment of the excitation pulse. We thereby assume equal excitation probabilities of the outer $|^2\mathrm{P}_{1/2}, F' = 1, m_F = \pm 1\rangle$ levels. We consider the probability amplitudes after state mapping. The values measured in the experiment are indicated in each case as black dashed lines. The shaded areas indicate the standard error. The results of a simulation including microwave π-pulse fidelity (95.7(7) %), fluorescence state detection (3.5(12) %) and $P(H_z) \neq P(V_z)$ are given as blue lines. **a)** Correlation contrast according to equation (7.29). **b), c), d)** Conditional probabilities. To be consistently with the experiment, we interpret a 'bright' ion to be in the $|g^+\rangle$ state in the simulation, whereas it could also be in a mixture of the $|g^+\rangle$, $|g^-\rangle$ and $|g^0\rangle = |^2\mathrm{S}_{1/2}, F = 1, m_F = 0\rangle$ states, which is indistinguishable by fluorescence state detection (see section 6.2).

Cavity SPC dark counts

Dark counts of the photon detectors reduce the measured correlation contrast, since for each of these false-positive photonic qubit detection events, a readout of the atomic qubit is also performed. We lower the contribution of false-positive events to the correlation statistics by applying a 10 ns time window to each detector in the post-analysis (Figure 5.19 a)), for which the measured photonic and atomic states contribute to the correlation statistics. Otherwise, we discard this shot of the experiment in the analysis.

We extract the remaining probability for the detection of a dark count within the 10 ns acceptance window from the offset of the photon statistic in Figure 5.19 a) and obtain

$$P_{\mathrm{d,dark}} = \{1.7(3)\,|\,3.1(6)\} \times 10^{-6} \text{ for the } \{H\,|\,V\}\text{-detector } (\hat{\sigma}_z \text{ basis}). \tag{7.34}$$

From the number of total detected photons $N_{\mathrm{total},i}$ on detector i we derive the ratio of dark counts $N_{\mathrm{dark},i}$ to the number of total detected events as

$$\xi_{z,i} = \frac{N_{\mathrm{dark},i}}{N_{\mathrm{total},i}} = \{1.4(3)|2.5(5)\}\,\% \text{ for } \{i = H\,|\,i = V\}\text{-detector.} \tag{7.35}$$

We estimate the reduction of the correlation contrast caused by dark counts by computing

$$\xi_{z,H+V} = \frac{N_{\mathrm{dark},H+V}}{N_{\mathrm{total},H+V}} = 2.0(3)\,\%, \tag{7.36}$$

since we assume an equal probability for measuring a dark or bright ion for each false-positive detection event[87]. We can make this assumption, since an entangled state was likely generated for the investigated sequence but the corresponding single photon was not detected. The generation of an entangled state happens with the excitation probability of the laser pulse of $> 90\,\%$ (see subsection 6.3.5).

In addition to a suppression of the false-positive events, we can correct for these events in the post-analysis by subtracting half of the expected false-positives on the bright and dark correlation side of the atom, since we expect an equal probability for a dark or bright ion.

Other sources of errors

We sum up the errors that contribute to a reduction of the measurable correlation contrast and compare this calculated value with the measured value (see Table 12). We conclude that the influence of the remaining error sources on the correlation contrast is in total $\lessapprox 1\,\%$.

7.4 Correlation measurements in the rotated bases $\hat{\sigma}_{x/y}$

So far, the measured correlations could also be explained by considering a statistical mixture of states. In contrast, for an entangled atom-photon state, the correlations between atom and photon states are visible in every two-qubit basis $\hat{\sigma}_i \otimes \hat{\sigma}_i$. In order to verify entanglement in different bases orthogonal to $\hat{\sigma}_z$, we first need to understand how the two-qubit state behaves in these bases. Starting from equation (7.19), we can rewrite the

[87] It is to be understood that for $\xi_{z,H+V} = 1$ the correlation contrast disappears completely.

photonic part of the entangled state in terms of general superposition states $|\beta\rangle$ similar to a rotation around $\pi/2$ on the Bloch-sphere. To this end, we define the states

$$\begin{aligned} |\beta\rangle &= \frac{1}{\sqrt{2}}\left(\left|\sigma^+\right\rangle + e^{i\beta}\cdot|\sigma^-\rangle\right) \\ \text{and } |\beta+\pi\rangle &= \frac{1}{\sqrt{2}}\left(\left|\sigma^+\right\rangle - e^{i\beta}\cdot|\sigma^-\rangle\right), \end{aligned} \tag{7.37}$$

which together form a rotated basis in the equatorial plane of the Bloch-sphere (see Figure 7.7).

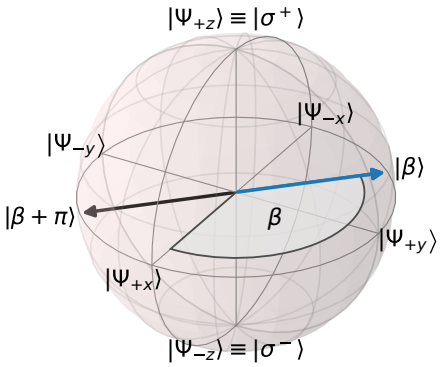

Figure 7.7: Visualisation of the photon states $|\beta\rangle$ (blue arrow) and $|\beta+\pi\rangle$ (black arrow) on the Bloch-sphere with a definition of the angle β. The eigenstates $\left|\Psi_{\pm x/\pm y/\pm z}\right\rangle$ of the bases $\hat{\sigma}_{x/y/z}$ are labelled according to equations (2.3) and (5.82).

By rewriting the eigenstates of the $\hat{\sigma}_z$ basis $|\sigma^{\pm}\rangle$ in terms of the rotated basis states $|\beta\rangle$ and $|\beta+\pi\rangle$ and inserting these expressions into equation (7.19), we get following equation:

$$\begin{aligned} |\Psi\rangle_{\text{atom-photon}} = \quad & \frac{1}{2}\left[\left(\left|g^+\right\rangle - |g^-\rangle\, e^{-i\beta}\right)|\beta\rangle + \left(\left|g^+\right\rangle + |g^-\rangle\, e^{-i\beta}\right)|\beta+\pi\rangle\right] \\ = \quad & \frac{1}{2}\left(\left|g^+\right\rangle - |g^-\rangle\, e^{-i\beta}\right)\cdot\frac{1}{\sqrt{2}}\left(\left|\sigma^+\right\rangle + e^{i\beta}\cdot|\sigma^-\rangle\right) \\ & + \frac{1}{2}\left(\left|g^+\right\rangle + |g^-\rangle\, e^{-i\beta}\right)\cdot\frac{1}{\sqrt{2}}\left(\left|\sigma^+\right\rangle - e^{i\beta}\cdot|\sigma^-\rangle\right). \end{aligned} \tag{7.38}$$

The angle β is determined by the rotation of the photon polarisation along its optical path. It is controllable by a set of wave plates according to subsection 5.5.4.

Since we detect the photon first, a mapping of the polarisation state according to

$$\begin{aligned} \frac{1}{\sqrt{2}}\left(\left|\sigma^+\right\rangle + e^{i\beta}\cdot|\sigma^-\rangle\right) &\to |V\rangle \\ \text{and } \frac{1}{\sqrt{2}}\left(\left|\sigma^+\right\rangle - e^{i\beta}\cdot|\sigma^-\rangle\right) &\to |H\rangle \end{aligned} \tag{7.39}$$

projects the ion to the corresponding state. For selected values of β, these states are listed in Table 8. For the sake of simplicity, time evolvement of the states is not included in this description, but is considered in subsection 7.4.1.

β	Atom/$\frac{1}{\sqrt{2}}$	Photon/$\frac{1}{\sqrt{2}}$	Corresponding photon basis
0	$\|g^+\rangle - \|g^-\rangle$ $\|g^+\rangle + \|g^-\rangle$	$\|\sigma^+\rangle + \|\sigma^-\rangle$ $\|\sigma^+\rangle - \|\sigma^-\rangle$	$\hat{\sigma}_x$
$\pi/2$	$\|g^+\rangle + i\,\|g^-\rangle$ $\|g^+\rangle - i\,\|g^-\rangle$	$\|\sigma^+\rangle + i\,\|\sigma^-\rangle$ $\|\sigma^+\rangle - i\,\|\sigma^-\rangle$	$\hat{\sigma}_y$
π	$\|g^+\rangle + \|g^-\rangle$ $\|g^+\rangle - \|g^-\rangle$	$\|\sigma^+\rangle - \|\sigma^-\rangle$ $\|\sigma^+\rangle + \|\sigma^-\rangle$	$-\hat{\sigma}_x$
$3\pi/2$	$\|g^+\rangle - i\,\|g^-\rangle$ $\|g^+\rangle + i\,\|g^-\rangle$	$\|\sigma^+\rangle - i\,\|\sigma^-\rangle$ $\|\sigma^+\rangle + i\,\|\sigma^-\rangle$	$-\hat{\sigma}_y$

Table 8: Atom-photon state correlations in rotated bases before state mapping.

The results in Table 8 show that correlations between photonic and atomic states are observable for projective measurements in the rotated bases. They also show, that measuring the photon in one of the eigenstates $|\Psi_{\pm x}\rangle_{\text{photon}}$ (eq. (2.3)) projects the atom to the corresponding basis but with a flipped sign of x, i.e. $|\Psi_{\mp x}\rangle_{\text{atom}}$. This results from the minus sign in the expression of the entangled state.

In advance to the detection of the atomic state, we have to map the eigenstates of the rotated bases to the eigenstates of the projective readout (see subsection 6.4.2). To this end, we rotate the hyperfine qubit using a $\pi/2$-pulse subsequent to the mapping π pulse, which we also applied for the $\sigma_z \otimes \sigma_z$ basis. The $\pi/2$-pulse has a phase of ϕ_2 and a phase difference of $\Delta\phi = \phi_2 - \phi_1$ with respect to the first π-pulse (ϕ_1) which allows to select a specific basis in the equatorial plane of the Bloch sphere (see equation (6.74)).

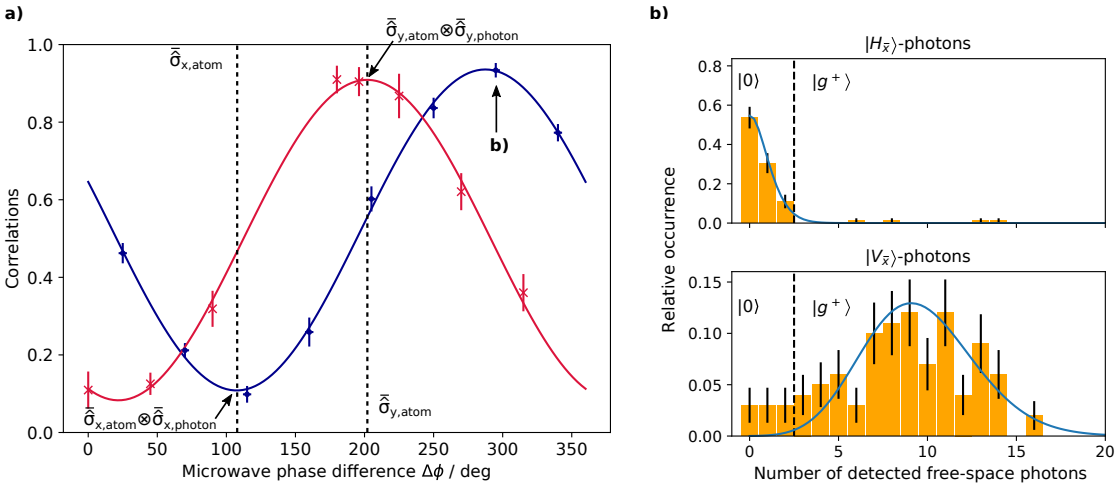

Figure 7.8: Spin-photon correlations in the rotated bases. **a)** Parity oscillations for a photon readout in $\bar{\hat{\sigma}}_x$ and $\bar{\hat{\sigma}}_y$ bases. The relative phase difference $\Delta\phi = \phi_2 - \phi_1$ of the microwave pulses sets the readout basis of the atomic qubit in the equatorial plane of the Bloch sphere. Red crosses: $P(0|H_{\bar{y}}) \cdot P(H_{\bar{y}}) + P(g^+|V_{\bar{y}}) \cdot P(V_{\bar{y}})$ correlations. Blue dots: $P(0|H_{\bar{x}}) \cdot P(H_{\bar{x}}) + P(g^+|V_{\bar{x}}) \cdot P(V_{\bar{x}})$ correlations. The conditional probabilities are dark-count corrected. The data in a) have also been published in [92]. **b)** Histogram of free-space photons detected within a time window of 800 μs in the single shot atomic readouts of 182 entanglement events measured in $-\bar{\hat{\sigma}}_{x,\text{atom}} \otimes \bar{\hat{\sigma}}_{x,\text{photon}}$ basis. The solid lines constitute fits to the Poisson distribution. The corresponding conditional probabilities are given in Table 9. Error bars show the standard error.

Figure 7.8 shows the oscillation of correlations between a photon readout in the basis $\bar{\hat{\sigma}}_x/\bar{\hat{\sigma}}_y$ and a varying atomic readout basis determined by $\Delta\phi$, also referred to as parity oscillations ($\bar{\hat{\sigma}}_k$ from equation (5.87)). We observe correlations with $C_{xx} = (81.3 \pm 15.8)\,\%$ contrast for $\bar{\hat{\sigma}}_x \otimes \bar{\hat{\sigma}}_x$ and $C_{yy} = (87.0 \pm 2.6)\,\%$ for $\bar{\hat{\sigma}}_y \otimes \bar{\hat{\sigma}}_y$.

The measured conditional probabilities for the $-\bar{\hat{\sigma}}_x \otimes \bar{\hat{\sigma}}_x$ ($\bar{\hat{\sigma}}_y \otimes \bar{\hat{\sigma}}_y$) correlations are listed in Table 9 (10).

	$H_{\bar{x}}$	$V_{\bar{x}}$
g^+	0.022(10)	0.500(15)
0	0.429(10)	0.049(15)
$P(\lvert\lambda\rangle)$	0.451	0.549

Table 9: Conditional probabilities for the fluorescence-based state readout in $-\bar{\hat{\sigma}}_{x,\text{atom}} \otimes \bar{\hat{\sigma}}_{x,\text{photon}}$ basis after atomic state mapping, corrected for detector dark counts (see Figure 7.8 b)). The photon states are $\lambda = \{H_{\bar{x}}, V_{\bar{x}}\}$.

	$H_{\bar{y}}$	$V_{\bar{y}}$
g^+	0.060(28)	0.433(22)
0	0.463(28)	0.045(22)
$P(\lvert\lambda\rangle)$	0.522	0.478

Table 10: Conditional probabilities for the fluorescence state readout in $\bar{\hat{\sigma}}_{y,\text{atom}} \otimes \bar{\hat{\sigma}}_{y,\text{photon}}$ basis after atomic state mapping, corrected for detector dark counts. The photon states are $\lambda = \{H_{\bar{y}}, V_{\bar{y}}\}$.

7.4.1 Time dependence of the rotated bases

For the $\hat{\sigma}_z \otimes \hat{\sigma}_z$ basis, the time evolvement of the eigenstates cancel out as global phases (subsection 7.3.1), but in the rotated basis they become important due to the superposition states. Inserting the time evolution of the basis states from equations (7.30) into equation (7.38) and defining the time of photon emission as $t = 0$ results in

$$\begin{aligned} |\Psi\rangle_{\text{atom-photon}}(t) = \quad & \frac{1}{2}\left(\left|g^+\right\rangle - \left|g^-\right\rangle e^{-i\beta} e^{-i\omega_L t}\right) \cdot \frac{1}{\sqrt{2}}\left(\left|\sigma^+\right\rangle + \left|\sigma^-\right\rangle \cdot e^{i\beta} e^{i\omega_L t}\right) \\ & + \frac{1}{2}\left(\left|g^+\right\rangle + \left|g^-\right\rangle e^{-i\beta} e^{-i\omega_L t}\right) \cdot \frac{1}{\sqrt{2}}\left(\left|\sigma^+\right\rangle - \left|\sigma^-\right\rangle \cdot e^{i\beta} e^{i\omega_L t}\right). \end{aligned} \tag{7.40}$$

The static magnetic field lifts the degeneracy between the $|g^-\rangle$ and $|g^+\rangle$ states, which results in a precession of the atomic and photonic superposition states in the laboratory frame with the frequency

$$\omega_L = \left(E_{g^-} - E_{g^+}\right)/\hbar = \left(E_{\sigma^+} - E_{\sigma^-}\right)/\hbar. \tag{7.41}$$

Upon detection of the photon after the time $t_{d,p}$, the ion is projected to the state corresponding to the detected photon state with an impressed phase of

$$\alpha = \beta + \omega_L \cdot t_{d,p}. \tag{7.42}$$

The combined atom-photon state collapses at the time $t_{d,p}$ to the atomic state

$$|\Psi\rangle_{\text{atom}}(t_{d,p}) = \frac{1}{\sqrt{2}}\left(\left|g^{+}\right\rangle \pm |g^{-}\rangle\, e^{-i\alpha}\right) \tag{7.43}$$

according to equation (7.40). In contrast to the photonic phase, which is fixed in the laboratory frame through detection, the atomic superposition spin state evolves further for $t \geq t_{d,p}$ in the laboratory frame with

$$|\Psi\rangle_{\text{atom}}(t) = \frac{1}{\sqrt{2}}\left(\left|g^{+}\right\rangle \pm |g^{-}\rangle\, e^{-i\alpha} \cdot e^{-i\omega_L(t-t_{d,p})}\right). \tag{7.44}$$

The phase of the atomic state depends on the time t elapsed since photon emission and the rotation of polarisation of the photon along its path β with the corresponding projective measurement. Equation (7.44) holds for detection of the photon in any basis orthogonal to $\hat{\sigma}_z$. We find that the phase of the atomic state at its detection on time $t_{d,a}$ reduces to

$$\alpha + \omega_L(t_{d,a} - t_{d,p}) = \beta + \omega_L \cdot t_{d,a} \equiv \gamma. \tag{7.45}$$

The correlation between atomic and photonic state changes according to the phase of the atomic state γ and of course still depends on the choice of the atomic readout basis with $\Delta\phi$. In order to perform the projective readout of the ion in a given basis and with a stable phase γ, we must achieve stability of three parameters during all the repetitions of the experiment performed for this purpose: i) The mapping microwave pulses have to have a fixed timing $t_{d,a}$ in the laboratory frame with respect to the photon emission time. ii) The energy splitting $\hbar\omega_L$ of the states $\left|g^{+}\right\rangle$ and $|g^{-}\rangle$ has to be constant for all repetitions of the experiment, which requires a stable magnetic field. iii) The concrete basis in which we perform the projective readout of the ion is set by the relative phase of the microwave pulses $\Delta\phi$. In order to avoid sampling over different bases, $\Delta\phi$ has to be fixed for all repetitions of the experiment.

The time scale of the phase evolution is given by the external magnetic field of 603.6(7) mG, which is applied along the cavity axis to define the quantisation axis. This results in a precession of the atomic and photonic superposition states in the laboratory frame with frequency $\omega_L = 2.8\,\frac{\text{MHz}}{\text{G}} \cdot (603.6 \pm 0.7)\,\text{mG} = 1.690(2)\,\text{MHz}$. Since the time profile of the collected cavity photons is much shorter than the period of phase precession of the superposition states ($\sim 10\,\text{ns} \ll 2\pi/\omega_L \approx 590\,\text{ns}$), we do not account for the photon arrival times in the post-analysis in terms of phase stability (see subsection 7.4.2 for the corresponding error estimation).

In contrast, there have been also experimental realisations of atom-photon entanglement with longer time profiles of the emitted photons, which require post-selection of the photon detection times to infer to which basis the atomic state was projected [25]. In general, the need for precise timing of the correlation measurements in the rotated bases is common to several experimental realisations of light-matter entanglement [167, 23, 180, 24]. However, it can also be completely eliminated by using tailored methods to generate the entangled atom-photon state [164], where the relevant phases evolve synchronously in time[88].

[88] Transferring this approach to the presented experiment, $\Delta\phi$ would have to evolve synchronously with γ for the atomic readout bases to be independent from $t_{d,a}$.

7.4.2 Imperfections reducing the correlation contrast in the rotated bases

The sources of erroneous state detection discussed in subsection 7.3.2 for the $\hat{\sigma}_z \otimes \hat{\sigma}_z$ basis are applicable to the rotated bases as well and are briefly adapted to the rotated bases in this subsection. Furthermore, we discuss effects arising only for correlation measurements in the rotated bases.

Dark counts
We correct for false-positive photon detection events on the cavity SPCs in a similar manner as for the $\hat{\sigma}_z \otimes \hat{\sigma}_z$ basis. Since we changed the photon readout setup in advance to the presented measurements, we have to repeat the analysis of subsection 7.3.2 for the rotated basis ($\bar{\hat{\sigma}}_{x,y}$). We observed slightly different values for the dark count analysis of the SPCs (see Table 11).

	H-detector	V-detector
$\bar{\hat{\sigma}}_y$-basis		
$P_{\mathrm{d,dark}}/10^{-6}$	2.1 ± 0.3	8.5 ± 1.0
$\xi_y/\%$	1.8(3)	7.6(9)
$\bar{\hat{\sigma}}_x$-basis		
$P_{\mathrm{d,dark}}/10^{-6}$	1.7 ± 0.5	5.1 ± 1.2
$\xi_x/\%$	0.5(2)	1.6(4)

Table 11: Dark count characteristic of the cavity-photon detectors.

Fluorescence state detection
We noticed an increased error in the atomic state detection due to formation of coherent dark states, as discussed in subsection 6.2.2. The photon number distribution for a dark ion shifted noticeable to higher expected photon numbers $\overline{N}_{\mathrm{dark},\bar{\hat{\sigma}}_{x/y}}$, due to the additional laser used to destroy the dark states. Furthermore, the expectation value of detected photons for a bright state was reduced to $\overline{N}_{\mathrm{bright},\bar{\hat{\sigma}}_{x/y}}$, due the limited ability of the second laser to destroy the dark states. The achieved values for a 800 μs readout time window are

$$\overline{N}_{\mathrm{dark},\bar{\hat{\sigma}}_{x/y}} = 0.61(2) \quad \text{and} \quad \overline{N}_{\mathrm{bright},\bar{\hat{\sigma}}_{x/y}} = 9.6(4). \tag{7.46}$$

The readout contrast of the fluorescence atomic state detection is extracted from Figure 6.7 as $(89.5 \pm 1.2)\,\%$.

Atomic state mapping
For the hyperfine qubit manipulation, an error estimation of the atomic state manipulation requires a more sophisticated analysis than for the $\hat{\sigma}_z \otimes \hat{\sigma}_z$ correlation measurement. Here, the qubit mapping microwave π-pulse and an additional $\pi/2$-pulse are applied, which have to be calibrated accurately. Assuming a perfect calibrated $\pi/2$-pulse, the fidelity of the π-rotation affects the measurable correlation contrast as described for the

$\hat{\sigma}_z \otimes \hat{\sigma}_z$ correlation. For a non-perfect $\pi/2$-pulse, however, we find from a full simulation of the atomic state manipulation according to subsection 6.4.1, how the measurable correlation contrast can be estimated from the pulse parameter calibration (detuning, length). Detuning of the pulses with respect to the atomic resonance tilts the rotation axes $\vec{r}$ of $\hat{R}^{\pi/2}_{\vec{r}}$ and $\hat{R}^{\pi}_{\vec{r}}$ according to equation (6.64). The tilted rotation axes result in an additional phase acquired during the pulse sequence, which changes the basis to which the atomic state is projected. However, by re-calibrating the pulse phase difference $\Delta\phi$, this effect can be mitigated. For an error estimation, we therefore focus on the pulse length error of both pulses. For $\hat{R}^{\pi}_{\vec{r}}$, we can infer the error directly from the rotation fidelity 98.9(6) % [100.0(4) %] for the $\bar{\hat{\sigma}}_x \otimes \bar{\hat{\sigma}}_x$ [$\bar{\hat{\sigma}}_y \otimes \bar{\hat{\sigma}}_y$] basis setting. For $\hat{R}^{\pi/2}_{\vec{r}}$, we consider a calibration uncertainty of 1 μs at a pulse lengths of $\sim$ 25 μs. Using these values, we obtain a maximal reduction in the measurable correlation contrast of 1.9 % [0.6 %] from the simulation.

Time dependence of superposition states

The time dependence of superposition states in the rotated bases (subsection 7.4.1) introduces the time dimension as a factor to the measurement, which has to be controlled to a high precision ($\sim$ 1 ns). In this subsection, the timing factor is discussed in detail as a source of error for the correlation measurements. To this end, we investigate the acquired phase of the atomic superposition state at its detection.

The phase γ introduced in subsection 7.4.1 determines the atomic state at time $t_{d,a}$. By adding the noise amplitude δa to a variable a in form of $a \to a + \delta a$ we obtain from equation (7.45)

$$\gamma + \delta\gamma = (\beta + \delta\beta) + (\omega_L + \delta\omega_L) \cdot (t_{d,a} + \delta t_{d,a}), \tag{7.47}$$

where the expression $\delta t_{d,a}$ might seems unintuitive, but represents a timing uncertainty for the phase determination, e.g., measuring the phase with a timing jitter. We assume that the change of the photon polarisation originating from varying optical path conditions ($\delta\beta$) is negligible for the considered time range of a measurement (a few hours). However, we observed a drift of the polarisation properties of the single-mode fibre with a time constant of a few days. Since we assume the noise to be small in amplitude, we can neglect the term $\delta\omega_L(t) \cdot \delta t_{d,a}$ as well. The remaining noise contribution to the atomic qubit phase at the detection time $t_{d,a}$ can be written as

$$\delta\gamma \approx \underbrace{\omega_L \cdot \delta t_{d,a}}_{\text{Timing: } \delta_T} + \underbrace{\delta\omega_L \cdot t_{d,a}}_{\text{B-field stability: } \delta_B} . \tag{7.48}$$

The expression $\omega_L \cdot \delta t_{d,a}$ describes everything related to a time uncertainty from the emission of the single photon to the detection of the atomic qubit state, which includes in particular the Purcell-enhanced decay of the excited state $|e\rangle$ with a lifetime of $\tau = 7.4(2)$ ns. We fix the start of the atomic state detection sequence with respect to the arrival time of the excitation pulse at the ion with a maximum jitter of 370 ps[89] according to section 7.2 and Figure 7.4. We neglect the excitation pulse length of $t_{\text{pulse}} \approx 140$ ps (subsection 6.3.4). According to equation (7.48), we end up with a phase uncertainty originating from timing

[89] 320 ps from trigger jitter of KEYSIGHT 33600A Waveform Generator. 50 ps from pulsed laser APE pulse-switch.

issues of

$$\delta_T = \omega_L \cdot \delta t_{d,a} \leq (370\,\mathrm{ps} + 7.4(2)\,\mathrm{ns}) \cdot 2\pi \cdot 1.690(2)\,\mathrm{MHz} = 0.026(7)\pi \tag{7.49}$$

with the frequency $\omega_L = 2\pi \cdot 1.690(2)\,\mathrm{MHz}$. The corresponding reduction in the measurable correlation contrast[90] is $\leq 0.7(1)\,\%$.

The second contribution to the phase uncertainty of the atomic qubit is represented by the expression $\delta\omega_L \cdot t_{d,a}$, which is determined by the magnetic field noise along the quantisation axis resulting in a varying Zeeman qubit transition frequency $\delta\omega_L$ of 2.8 MHz/G. The stability of the magnetic field is discussed in detail in section 6.6. From the results of the Ramsey-like pulse sequences shown in Figure 6.26, we estimate the reduction of the measurable correlation contrast due to magnetic field noise for a hold time of $t_{d,a} = 3.7\,\mu\mathrm{s}$ (time between emission of the photon and readout of the ion) to be smaller than

$$1 - \exp\left(\frac{-3.7\,\mu\mathrm{s}}{(496 \pm 42)\,\mu\mathrm{s}}\right) = 0.7(1)\,\%. \tag{7.50}$$

From this value we obtain for the phase noise

$$\delta_B = \delta\omega_L \cdot t_{d,a} \leq 0.026(7)\pi. \tag{7.51}$$

Decoherence during the microwave pulses is included in δ_B, since we use the same microwave sequence (π-pulse and $\pi/2$-pulse) for the atomic state mapping during the correlation measurements as for the readout of the superposition states during the coherence time measurements (see Figure 6.26). In the worst case, decoherence is even overestimated here. The fact that the values for δ_B and δ_T match is a coincidence by chance.

7.5 Full quantum state tomography

The reconstruction of a full quantum state requires repeated measurements on multiple realisations of the same quantum state, since a measurement generally changes the state. We can express the quantum state of a single qubit in terms of the eigenstates of the basis operators $\hat{\sigma}_i$ (Pauli matrices). Measuring the expectation values of these operators, in principle allows for a reconstruction of the state.

In order to map a single qubit state, projective measurements to the bases $\hat{\sigma}_{1,2,3} \equiv \hat{\sigma}_{x,y,z}$ are required[91]. For a two-qubit state, there are 9 combinations of $\hat{\sigma}_i \otimes \hat{\sigma}_j$ with $i, j \in \{1, 2, 3\}$. To calculate the expectation value of a specific projector, several measurements must be made for the respective state projection. However, the experimental implementations of the projectors may contain noise and imperfections and are not necessarily in compliance with the corresponding $\hat{\sigma}_i$ operator. This can lead to a limited ability of measuring the quantum state. Maximum likelihood estimation (MLE) mitigates parts of the problem by ensuring the measured state to be physical. From MLE we obtain the most likely physical state which is able to describe the outcome of our projective measurements. In addition, we need to ensure that the preparation of the quantum state does not change for all sets of measurements.

[90] Assuming the contrast reduction to be $\cos^2(\delta_T)$ for $|\delta_T| \leq \pi/2$

[91] One can also use an equivalent set of bases that is able map the Hilbert state space

7.5.1 Density formalism

The density operator of a quantum mechanical state is defined as [9]

$$\hat{\rho} = \sum_i a_i \left|\phi_i\right\rangle \left\langle\phi_i\right| , \tag{7.52}$$

with normalisation $\sum_i a_i = 1$ and ϕ_i being pure states. For the density matrix to be physical (e.g., not to produce expectation values greater than 1), additional requirements on $\hat{\rho}$ are:

$$\hat{\rho}^\dagger = \hat{\rho} \quad \text{and} \quad \mathrm{Tr}(\hat{\rho}) = 1. \tag{7.53}$$

We can express the density matrix of a single qubit through the Pauli operators $\hat{\sigma}_i$ and Stokes-parameters s_i as [75]

$$\hat{\rho} = \frac{1}{2} \sum_{i=0}^{3} s_i \hat{\sigma}_i. \tag{7.54}$$

The Stokes-parameters can be given in terms of the projections $E_{\lambda\cdot i} = \langle\Psi_{\lambda\cdot i}| \hat{\rho} |\Psi_{\lambda\cdot i}\rangle$ to the eigenstates of the qubit bases $\hat{\sigma}_i$ (see equation (2.3)), which reduces to $E_{\lambda\cdot i} = |\langle\Psi_{\lambda\cdot i}|\phi\rangle|^2$ in case of a pure state $|\phi\rangle$. The Stokes-parameters read [75]:

$$\begin{aligned} s_0 &= E_z + E_{-z}, \quad s_1 = E_x - E_{-x}, \\ s_2 &= E_y - E_{-y}, \quad s_3 = E_z - E_{-z}, \end{aligned} \tag{7.55}$$

where $s_0 = E_z + E_{-z} = E_x + E_{-x} = E_y + E_{-y}$.

We can extend this formalism to a two-qubit state by combining the Hilbert spaces of the two qubits $(\mathcal{H}_1, \mathcal{H}_2)$ to a single Hilbert $\mathcal{H}_{\mathrm{tot}}$ space via the tensor product $\mathcal{H}_{\mathrm{tot}} = \mathcal{H}_1 \otimes \mathcal{H}_2$. This results in the following equation for the density matrix of the two-qubit state [75, 25]:

$$\hat{\rho} = \frac{1}{4} \sum_{i,j=0}^{3} S_{i,j} \hat{\sigma}_i \otimes \hat{\sigma}_j, \tag{7.56}$$

where the joint probabilities $S_{i,j}$ for a two-qubit system are given by the combination $s_i \otimes s_j$ analogous to the Stokes-parameters in the expression of the one-qubit density matrix in equation (7.54).

In a matrix representation, we obtain a 4×4 density matrix with 15 independent real entries for a two-qubit system (see equations (7.53)). Diagonal elements indicate the probabilities for observing the system in the corresponding basis state. We define the basis states of the atom-photon system (before mapping) in a vector representation as:

$$\left|\sigma^+, g^+\right\rangle = \begin{pmatrix} 1 \\ 0 \\ 0 \\ 0 \end{pmatrix}, \left|\sigma^+, g^-\right\rangle = \begin{pmatrix} 0 \\ 1 \\ 0 \\ 0 \end{pmatrix}, \left|\sigma^-, g^+\right\rangle = \begin{pmatrix} 0 \\ 0 \\ 1 \\ 0 \end{pmatrix} \text{ and } \left|\sigma^-, g^-\right\rangle = \begin{pmatrix} 0 \\ 0 \\ 0 \\ 1 \end{pmatrix}, \tag{7.57}$$

where we use the notation $|\sigma^\pm, g^\pm\rangle \equiv |\sigma^\pm\rangle |g^\pm\rangle$.

The advantage of the density matrix formalism is the ability to represent mixed and pure quantum states. To clarify the difference between a mixed and an entangled state,

we first construct an atom-photon mixed state as an example

$$\hat{\rho}_{\text{mixed}} = \frac{1}{2}\left(\left|\sigma^+, g^+\right\rangle\left\langle\sigma^+, g^+\right| + \left|\sigma^-, g^-\right\rangle\left\langle\sigma^-, g^-\right|\right) = \begin{pmatrix} 0.5 & 0 & 0 & 0 \\ 0 & 0 & 0 & 0 \\ 0 & 0 & 0 & 0 \\ 0 & 0 & 0 & 0.5 \end{pmatrix}. \tag{7.58}$$

With this state, we would be able to observe correlations between the atomic and photonic states in the $\hat{\sigma}_z$ basis, since the atom-photon system in this example is prepared with equal probabilities in $|\sigma^+, g^+\rangle$ or $|\sigma^-, g^-\rangle$. If we would change to a rotated basis (e.g. $\hat{\sigma}_x$) for detection, the measurement results on the photonic and the atomic side would be uncorrelated, since the state on both sides would be in a superposition of the respective measurement basis states which, however, are projected independently on both sides.

In contrast, an entangled two-qubit state shows non-zero off-diagonal elements in $\hat{\rho}$ which represent the phase coherence. As derived in equation (7.19), the spontaneous decay of the $|e\rangle$ state prepares the atom-photon system in a maximally entangled state (rather than in a statistical mixture), which reads

$$|\Psi_{\text{atom-photon}}\rangle = \frac{1}{\sqrt{2}}\left(\left|\sigma^+, g^+\right\rangle - \left|\sigma^-, g^-\right\rangle\right). \tag{7.59}$$

We compute the density matrix representation of the entangled atom-photon state using equation (7.52) as

$$\begin{aligned} \hat{\rho}_{\text{target}} &= \frac{1}{2}\cdot\left(\left|\sigma^+, g^+\right\rangle - \left|\sigma^-, g^-\right\rangle\right)\cdot\left(\left\langle\sigma^+, g^+\right| - \left\langle\sigma^-, g^-\right|\right) \\ &= \begin{pmatrix} 0.5 & 0 & 0 & -0.5 \\ 0 & 0 & 0 & 0 \\ 0 & 0 & 0 & 0 \\ -0.5 & 0 & 0 & 0.5 \end{pmatrix}. \end{aligned} \tag{7.60}$$

The atom-photon state of the equation (7.60) shows a maximum correlation between the ion state and the photon state for measurements where both qubits are projected onto the same basis ($\hat{\sigma}_k \otimes \hat{\sigma}_k$).

7.5.2 Quantum state reconstruction

Using equation (7.56), we reconstruct the density matrix from the joint expectation values $S_{i,j}$ for 16 different combinations of Pauli basis and tensor products $\hat{\sigma}_i \otimes \hat{\sigma}_j$ with $\hat{\sigma}_{i/j} \in \{\mathbb{I}, \hat{\sigma}_x, \hat{\sigma}_y, \hat{\sigma}_z\}$ and $\mathbb{I}$ being the 2×2 identity matrix. We calculate the joint probabilities $S_{i,j}$ for the combined atom-photon state as

$$S_{i,j} = s_{i,\text{atom}} \otimes s_{j,\text{photon}} \tag{7.61}$$

analogous to the Stokes-parameter of a one-qubit system (equations (7.55)). Since our mapping of the eigenstates of all qubit bases $\hat{\sigma}_{x/y/z}$ to the eigenstates of the measurement operators preserves the corresponding eigenvalue $\lambda = \pm 1$ (see equations (5.86) and (6.73)), we can map the expectation values in the expression of the Stokes-parameters to the measured probabilities in the experiment for each detection basis $\hat{\sigma}_i$. For the photonic

qubit system this reads $E_i \to P(V_i)$ and $E_{-i} \to P(H_i)$. For the atom, we do it in a similar manner according to the mapping described in equations (6.73). As an example, we derive

$$S_{3,3} = \underbrace{P(0|H_z) \cdot P(H_z)}_{E_{-z,-z}} + \underbrace{P(g^+|V_z) \cdot P(V_z)}_{E_{+z,+z}} - \underbrace{P(0|V_z) \cdot P(V_z)}_{E_{-z,+z}} - \underbrace{P(g^+|H_z) \cdot P(H_z)}_{E_{+z,-z}} \quad (7.62)$$

as an expression based on the conditional probabilities measured in the experiment according to section 7.3.

We make use of the symmetry of the off-diagonal elements for the x-, y- and z-bases $S_{m,n} = S_{n,m}$ for $m/n \in \{x, y, z\}$ and $m \neq n$ and set $S_{00} = 1$ due to normalisation. We extract the values from the measurements shown in Figure 7.5 and Figure 7.8 and post-hoc transform the matrix as described in subsections 7.5.3 and 7.5.4. Finally, we obtain the most likely physical state described by our measured data. The corresponding density matrix is shown in Figure 7.9 and reads

$$\begin{aligned}\hat{\rho}' = &\begin{pmatrix} 0.54 \pm 0.02 & -0.01 \pm 0.00 & -0.00 \pm 0.00 & -0.43 \pm 0.01 \\ -0.01 \pm 0.00 & 0.01 \pm 0.02 & 0.01 \pm 0.01 & 0.02 \pm 0.00 \\ -0.00 \pm 0.00 & 0.01 \pm 0.01 & 0.04 \pm 0.02 & -0.01 \pm 0.00 \\ -0.43 \pm 0.01 & 0.02 \pm 0.00 & -0.01 \pm 0.00 & 0.42 \pm 0.02 \end{pmatrix} \\ &+i \begin{pmatrix} 0.00 \pm 0.00 & -0.01 \pm 0.01 & 0.00 \pm 0.01 & -0.00 \pm 0.00 \\ 0.01 \pm 0.01 & 0.00 \pm 0.00 & 0.01 \pm 0.00 & -0.02 \pm 0.01 \\ -0.00 \pm 0.01 & -0.01 \pm 0.00 & 0.00 \pm 0.00 & -0.02 \pm 0.01 \\ 0.00 \pm 0.00 & 0.02 \pm 0.01 & 0.02 \pm 0.01 & 0.00 \pm 0.00 \end{pmatrix}. \end{aligned} \quad (7.63)$$

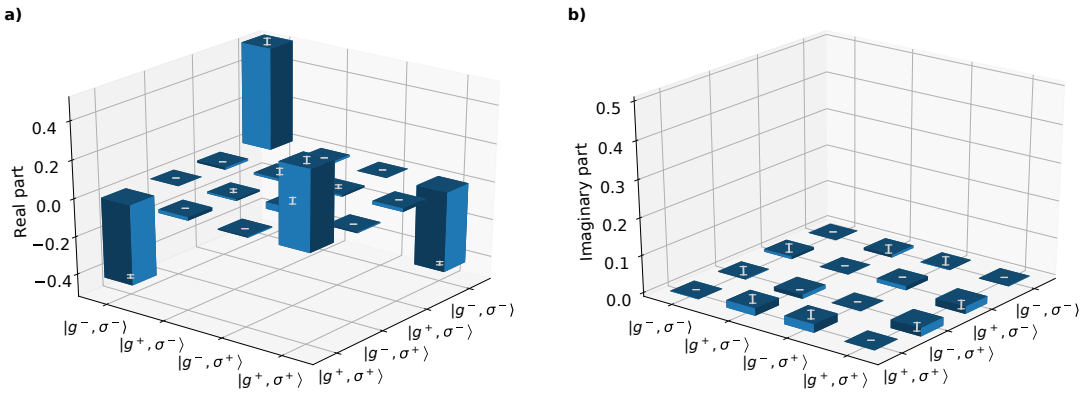

Figure 7.9: Real **a)** and imaginary **b)** part of the measured density matrix $\hat{\rho}'$ obtained from a full quantum state tomography (see equation (7.63)). The matrix is post-hoc transformed as described in subsection 7.5.3 and represents the most likely physical state obtained from MLE (subsection 7.5.5). Standard errors are indicated as white bars. The data have also been published in [92].

7.5.3 Unitary transformations

Unintended unitary transformations of the experimentally generated entangled state can lead to a reduction of the overlap with the expected maximally entangled state (equation (7.60)). These rotations of the state can be caused, for example, by misaligned wave

plates in the photonic readout part of the setup. Also for the atomic part, an inaccurate microwave $\pi/2$ pulse or phase difference $\Delta\phi$ could potentially rotate the state.

A general representation of an unitary transformation acting on a local qubit is given by [71]

$$U_T(\theta,\phi,\beta) = \begin{pmatrix} \cos(\theta/2) & -e^{i\beta}\sin(\theta/2) \\ e^{i\phi}\sin(\theta/2) & e^{i\beta+i\phi}\cos(\theta/2) \end{pmatrix}. \tag{7.64}$$

We apply this transformation to the bases $\hat{\sigma}_i$ and $\hat{\sigma}_j$ of each qubit in order to post-hoc maximise the overlap of the measured density matrix from equation (7.56) with the target state $\hat{\rho}_{\text{target}}$ from equation (7.60). To this end, we iteratively search for the maximal overlap[92] of the measured density matrix with the target matrix. The result strongly depends on the starting point of optimisation. It is not guaranteed that the solution is global. Instead it could also be a local maximum.

Using the post-hoc rotated state matrix, we determine the contribution of unwanted unitary rotations on the state fidelity to be less than 1 %. This upper bound indicates a high degree of experimental control over atom and photon basis.

7.5.4 Ensure physical consistency using maximum likelihood estimation

Following James et al. [75], we perform a maximum likelihood estimation (MLE) to ensure the measured density matrix to describe a valid physical state[93]. We use the matrix obtained in subsection 7.5.3 as starting point for the MLE optimisation. Again, as in subsection 7.5.3, it is not guaranteed that the solution found for the multivariate optimisation of the likelihood function is global. We obtain the final density matrix $\hat{\rho}'$ given in equation (7.63) from the MLE.

7.5.5 Entangled state fidelity

In this subsection, we investigate the detection fidelity of the atom-photon state using the density matrix $\hat{\rho}'$ after rotation optimisation (subsection 7.5.3) and MLE (subsection 7.5.4) as presented in equation (7.63).

With the purity $P = \text{Tr}\left(\hat{\rho}'^2\right) = (83.0 \pm 3.0)\,\%$ of the state, we can use the noise model presented in [31] to calculate an upper bound for the entanglement fidelity $F_{\max}$. To do so, we need to adapt the original calculations performed for a 2×2 density matrix to our 4×4 density matrix.

The contribution of experimental noise to the state fidelity can be calculated using the state purity P, which is expressed through the length of the Bloch vector $\vec{r}$ as

$$P = \frac{1}{2}\left(1 + |\vec{r}|^2\right). \tag{7.65}$$

The purity becomes 1 for a noise free pure entangled state, whereas for increasing noise it approaches 1/2. A pure state $|\psi\rangle$ mixed to a probability V with white noise can be written as

$$\hat{\rho}_n = V\,|\psi\rangle\langle\psi| + (1-V)\frac{\mathbb{I}}{4}, \tag{7.66}$$

[92] The FINDMINIMUM function in MATHEMATICA 11.3 was used to minimize the difference between the matrices.

[93] In other words: we search for the most likely physical state described by the measured matrix

where $\mathbb{I}$ is the 4×4 identity matrix. With $F = (1 + V)/2$, we obtain for the purity

$$P(F) = \mathrm{Tr}\left(\hat{\rho}_n^2\right) = 1 - 3F + 3F^2 \tag{7.67}$$

and subsequently for the fidelity $F_{\max}$ limited solely by white noise

$$F_{\max} = \frac{1}{2}\left(1 + \sqrt{\frac{4P-1}{3}}\right) = (94.0 \pm 1.0)\ \%. \tag{7.68}$$

If the measured value of the state fidelity F is close to this upper bound, it is mostly white noise-limited [31, 24]. We compute the fidelity as

$$F = \langle \Psi_{\text{atom-photon}} | \, \hat{\rho}' \, | \Psi_{\text{atom-photon}} \rangle = (90.1 \pm 1.7)\,\%, \tag{7.69}$$

using the the target state of equation (7.59). This result shows that apart from a contribution of $(6 \pm 1)\,\%$ that can be interpreted as white noise (e.g. state preparation), there is also $(4 \pm 2)\,\%$ reduction in the detection fidelity that comes from other sources. The fidelity of the detected state is a measure for the quality of the whole setup, as it includes nearly all experimental noise and errors like polarisation mixing effects, qubit manipulations, the atomic readout and the dephasing of the atomic qubit due to magnetic field noise. Summing the contributions of the individual error sources to the measurable correlation contrast gives a consistent result with the measured correlation contrast for each measurement basis. For a complete summary of the experimental imperfections and their influences on the measurable correlation contrast obtained in subsections 7.3.2 and 7.4.2, see Table 12.

Source	$\bar{\hat{\sigma}}_y \otimes \bar{\hat{\sigma}}_y$	$\bar{\hat{\sigma}}_x \otimes \bar{\hat{\sigma}}_x$	$\hat{\sigma}_z \otimes \hat{\sigma}_z$	(sub)section
Atomic qubit manipulation	≤ 1.9	≤ 0.6	4.3 ± 0.7	7.4.2 & 7.3.2
Atomic state discrimination	10.5 ± 1.2	10.5 ± 1.2	3.5 ± 1.2	6.2.2
Timing of atomic readout	$\leq 0.7 \pm 0.1$	$\leq 0.7 \pm 0.1$	-	7.4.2
Magnetic field noise	0.7 ± 0.1	0.7 ± 0.1	-	7.4.2
Atomic excitation	4.2 ± 2.8	4.2 ± 2.8	4.2 ± 2.8	7.3.2
Photonic basis selection	$\ll 1.0$	$\ll 1.0$	$\ll 1.0$	7.5.3
False detection events (dark counts)	4.7 ± 0.5	1.1 ± 0.2	2.0 ± 0.3	5.5.2
Summed contrast reduction (excluding dark counts)	$\leq 18.0 \pm 3.0$	$\leq 16.7 \pm 3.0$	12.0 ± 3.1	
Achieved contrast (corrected by dark counts)	81.3 ± 15.8	87.0 ± 2.6	90.7 ± 3.9	7.3 & 7.4

Table 12: Sources of error of the entangled state measurements with associated values of the correlation contrast reduction in % broken down by the measurement bases.

7.6 Summary

We presented the deterministic generation of entanglement between the internal spin state of the trapped Yb ion and the polarisation degree of freedom of a photon emitted into the mode of the fibre resonator. By performing a full quantum state tomography, we were able to identify the detected two-qubit state as the maximally entangled state according to our theoretical considerations with a fidelity of $F = (90.1 \pm 1.7)\,\%$. We obtained the full density matrix of the state from correlation analysis between the photonic polarisation state and the atomic spin state in different combinations of readout bases, where we also observed parity oscillations. We achieved an effective entanglement detection rate of 58 Hz by performing real-time sequence branching to realise a conditional readout of the ion. With the presented network node, we can currently achieve a maximum ratio of entanglement generation rate to decoherence rate of

$$\frac{R_{\text{entanglement,gen}}}{R_{\text{decoherence}}} = 76 \pm 29, \tag{7.70}$$

which states that we can use the system as an efficient quantum communication node where the distribution of phase coherence dominates its losses. This is particularly interesting for scaling a quantum network in terms of distance [172], but also in terms of nodes, e.g. for distributed quantum computing [68].

As the state detection fidelity is a measure for the quality of the whole setup, we investigated the contribution of each error source to the measured state fidelity and are able to describe the observed correlation contrast consistently with the sum of the errors for the studied bases. This shows that we have gained full insight into the relevant parts of the experimental system, which is particularly beneficial to make practical use of the presented two-qubit state in quantum communication. In chapter 8 we demonstrate that the advanced properties of the system enables the secure distribution of a certified random quantum key between two remote parties. This is made possible because we have achieved the required properties for quantum communication in a single experiment for the presented atom-photon entanglement: i) a high generation and distribution rate of entanglement, ii) the possibility to read out the two-qubit state on both sides in a controlled basis, especially without further communication between the participants and iii) to do this with a high detection fidelity of the state also without further communication and without the possibility of post-processing the results.

8 Quantum key distribution using an entangled memory qubit

Contents

8.1 Working principle of QKD 169
8.2 Technical implementation and key distribution protocol 170
8.3 Key rates, key reconciliation and privacy amplification 172
8.4 Randomness certification using the violation of Bell's inequalities 176
8.5 Security measures against side channel attacks 180
8.6 Summary 181

Securing communication is becoming an increasingly important task for all aspects of today's information technology. The need for data security is ranging from smart and mobile devices to global companies keeping their business secrets safe. In particular, the distribution of a secret key between two communication participants via a public channel, which they can subsequently use to encrypt and decrypt information, is essential for remote communication. This so-called key distribution problem is usually solved in classical information theory with methods of asymmetric cryptography, where security is based on computationally hard problems. With the rise of quantum computers, at least some assumptions about computational hardness need to be reconsidered. As an example, the implementation of Shor's factorisation algorithm on a sufficiently large quantum computer could reduce the computational effort of the RSA problem to a polynomial time [154, 144], which would have large impact on the current established cryptographic infrastructure.

At the same time, quantum key distribution (QKD) offers a paradigm-changing solution to the key distribution problem [110], enabling a new way of provably secure communication [155, 89]. Due to its simple prepare-and-measure architecture, the one-qubit BB84 protocol [14] was the first QKD protocol realised in an experimental setup. Here, the transmitted quantum bit is prepared in a certain state and basis by the sender and since the protocol does not require entangled quantum states, it was first used with weak coherent light pulses [108, 62]. However, the presence of pulses containing two or more photons potentially leakages information towards an eavesdropper [105]. This can be avoided by using true single-photon sources allowing for secure implementations of QKD [176, 89].

Without a trusted node in between, optical communication via a direct link encounters a fundamental limit when the loss of the communication channel over distance is considered [166, 137]. Entanglement-based QKD, as first proposed by A. K. Ekert in [47], offers a solution to this problem. It utilises an entangled two-qubit state distributed between the communication parties to derive a quantum key, rather than preparing a particular state in a particular basis and sending it over the wire. Especially by using stationary memory qubits entangled with communication qubits, the fundamental point-to-point limit of optical quantum communication can be surpassed [21]. This enables the realisation of so-called quantum repeaters, in which the quantum information is temporarily stored before further distribution [172]. The concept of using memory-based quantum repeaters for the derivation of keys requires the setup of memory-based key distribution frameworks. However, the implementation of QKD between two remote parties that includes an entangled memory qubit has not yet been reported.

In this chapter, we demonstrate the memory-based distribution of a quantum key between two distant communication parties using the entangled ion-photon state presented in chapter 7. We show that the setup presented in this thesis offers a number of advanced properties in the context of QKD. The trapped ion as a memory qubit serves two purposes: i) It is a true single-photon source as the backbone for secure QKD with a second-order correlation function of $g^2(0) = 0.00(5)$ (see subsection 6.3.6). ii) It generates and stores entanglement between the spin state of the ion and the polarisation state of a single emitted photon, which in principle allows key distribution over long distances.

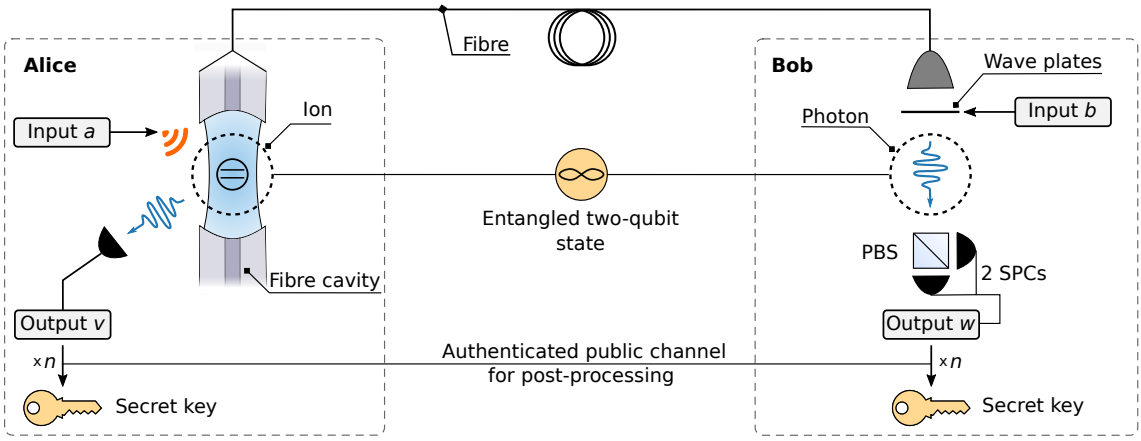

Figure 8.1: Sketch of the setup used for a quantum key distribution between two remote parties, Alice and Bob. The sender side (Alice) comprises of the single trapped ion inside the fibre cavity. The ion emits a photon whose polarisation state is entangled with the spin state of the ion. The receiver side (Bob) comprises of photon detectors and adjustable polarisation optics to detect the photon polarisation state in different bases.

When it comes to the generation of keys, cryptographically secure random number generators are an essential building block of secure systems. The use of pseudo-random processes to generate secret quantities can result in pseudo-security [44]. However, true random numbers are hard to generate and even harder to verify. This even applies to prepare-and-measure architectures of QKD, where the bit information of the key is prepared on the sender side and transmitted to the receiver side.

The presented entanglement-based measurement protocol, however, allows the communication partners to exploit fundamental quantum mechanical properties of the distributed two-qubit state to derive a secret key with excellent cryptographic properties. We demonstrate that we can certify the randomness of the distributed key using the non-locality of our entangled state, which in this strong form is not possible classically. In Figure 8.2, we show how the building blocks of our protocol work as a whole to ensure the crucial properties of a secret key, namely randomness, confidentiality and integrity.

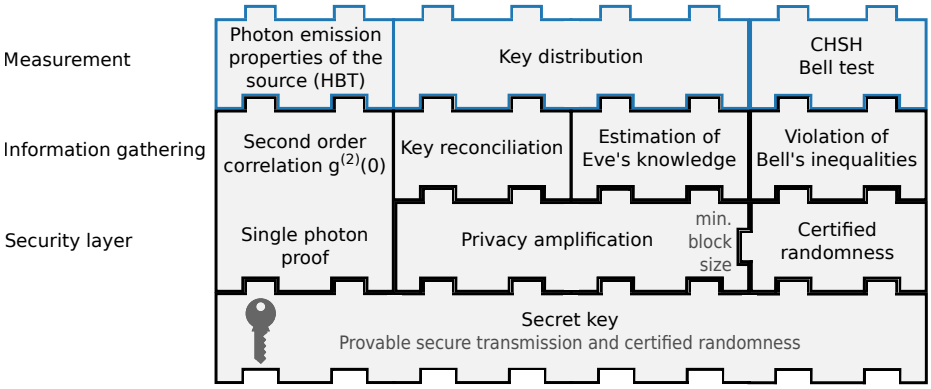

Figure 8.2: We base the security of our key derivation on various components. Measurement blocks exhibit a blue border whereas blocks of classical data processing are sketched with black borders. The certification of the ion as a single photon source using a Hanbury Brown and Twiss (HBT) setup is presented in subsection 6.3.6.

8.1 Working principle of QKD

Quantum key distribution takes advantage of the basic properties of a quantum communication channel, which can be used in various ways to achieve the security of a particular protocol. Consequently, several protocols and architectures have been proposed for QKD. A basic assumption is that one cannot duplicate an unknown quantum state [182]. This is used in various protocols to detect whether an eavesdropper has made a measurement on the quantum channel (and consequently disturbed the transmitted state) or not. This detection can only take place after the information has been transmitted, so a distributed key is declared secure or not secure in post-processing.

Within QKD, one can distinguish between prepare-and-measure schemes such as BB84 [14] and Bennett-1992 [12] and entanglement-based protocols such as the Ekert protocol [47] and the BBM92 protocol [15]. In entanglement-based protocols, the 'prepare' part as such is no longer necessary in the sense of encoding key information into the state. Instead, an entangled two-qubit state is distributed between the communication partners, where the result of a projective measurement on the entangled state is not predetermined in the ideal case and can be in fact inherently random (see section 8.4). Nevertheless, if the two-qubit state on both sides gets projected to the same basis, the measurement results on both sides are strongly correlated (see chapter 7), which can be used for key derivation. However, performing measurements always in the same basis does not exploit the possibilities of quantum communication and does not produce any security. In contrast, the random switching of measurement bases can be used to expose an eavesdropper making measurements on the quantum state.

For the presented protocol, security is achieved by performing the measurements on both sides of the distributed two-qubit state in a basis randomly chosen from two preselected bases such that any pair of eigenstates, one from each basis, has overlap 1/2, for example $\hat{\sigma_y}$ and $\hat{\sigma_z}$ (see section 8.2). When using different bases for state projection on both sides, the measurement results are completely uncorrelated. In particular, without further communication between the sides, it is not possible to distinguish whether a respective measurement has now delivered correlated results (same bases) or uncorrelated

results (different bases).

The same applies to a potential eavesdropper. Without any a priori knowledge of the choice of bases, the interception and re-transmission of the quantum states is only successful in a subset of all cases. The remaining fraction leads to uncorrelated measurement results and can be detected by the communication partners in post-processing by comparing a subset of the transmitted bits, where they would expect correlations. If this quantum bit error rate (QBER) is below an acceptance threshold, the transmission is considered to be secure, as it is assumed that no measurement of the state has taken place between the communication parties.

This is, of course, a simplified explanation intended to introduce the concept of QKD. The security proof of a protocol is more elaborate. In particular, it is possible to infer from the error rate a quantitative expression of the maximum knowledge of a potential eavesdropper by attributing all errors to potential measurements and thus to an increase in the eavesdropper's knowledge of the key (see section 8.3). By shortening the key accordingly, this knowledge can be taken into account and minimised to almost zero. In this context, quantum key distribution in its ideal implementation offers unconditional security, which means that even an attacker with unlimited time and computational resources is unable to break the system. Unconditional security of the key distribution was also theoretically proven for the protocol used in this chapter (BBM92) under the prerequisite of single photon transmission and no a priori knowledge about the choice of measurement bases [89, 184]. However, one must be aware that, for example, side-channel attacks, imperfect devices and imperfect implementation can undermine security in practice (see section 8.5).

8.2 Technical implementation and key distribution protocol

We utilise the entangled two-qubit state between the single trapped ion and a single photon, as presented in chapter 7, for the distribution of a quantum key between two remote parties A and B. The entangled atom-photon state is generated from deterministic excitation and subsequent decay of the ion under emission of the photon according to section 7.1. Before executing the key distribution protocol, Alice has to verify the generation of single photons from the source, for example by using a Hanbury Brown and Twiss (HBT) setup as presented in subsection 6.3.6. After that, the source remains under her control. The transmission of single photons is crucial for the security of the applied protocol and an advanced attacker (Eve) could imitate a single photon source. Therefore, a similar measurement on Bob's side during the key distribution does not provide relevant information for the security of the key.

For the distribution of entanglement between the two communication parties, the ion remains at side A (Alice) and the photon is transmitted to side B (Bob) (see Figure 8.1). The maximally entangled ion-photon state shared between both sides is given according to equation (7.19) as

$$|\Psi\rangle = \frac{1}{\sqrt{2}}\left(\left|\sigma^+\right\rangle\left|g^+\right\rangle - |\sigma^-\rangle\,|g^-\rangle\right) \equiv \frac{1}{\sqrt{2}}\left(|0\rangle_{\text{photon}}\,|0\rangle_{\text{atom}} - |1\rangle_{\text{photon}}\,|1\rangle_{\text{atom}}\right). \quad (8.1)$$

However, knowledge of the entangled two-qubit state is not required for the communication partners within the presented protocol and the state is given here for the sake of clarity.

If Bob receives the photon, Alice performs a projective measurement of the atomic spin state to a basis $\hat{\sigma}_i$, while Bob has detected the polarisation state of the photon in a basis $\hat{\sigma}_j$ (i.e., a total atom-photon state detection in $\hat{\sigma}_i \otimes \hat{\sigma}_j$ basis). In principle this conditional readout on Alice's side is not necessary for the protocol but greatly increases the repetition rate of the sequence since a readout on Alice's side lasts at least 400 μs. Of course, Bob has to ensure that the signal indicating a successful photon detection does not contain any information about the basis used and the measurement outcome.

For the practical key distribution, we adapt the entanglement-based BBM92 protocol [15] to the two-qubit quantum state of equation (8.1). Alice and Bob are using random inputs $a, b \in \{0, 1\}$ to set the basis of the projective state measurement on their respective side of the two-qubit system. Alice obtains a value $v \in \{0, 1\}$ from the measurement while Bob obtains $w \in \{0, 1\}$. We choose the $\hat{\sigma}_z$ basis for projective state measurement when $a, b = 0$ and the orthogonal $\hat{\sigma}_y$ basis[94] when $a, b = 1$. If Alice and Bob happen to measure in the same bases $a = b$, the measurement results v and w each contribute as one bit to the so-called sifted key on both sides. Since this corresponds to a measurement of the entangled state in a basis $\hat{\sigma}_i \otimes \hat{\sigma}_i$, a maximum correlation between the measurement results is expected (see sections 7.3 and 7.4).

For the detection of the photonic qubit on Bob's side, we extend the setup presented in subsection 5.5.1 by a wave plate with variable retardation[95], which is able to rotate the measurement basis of the polarisation qubit between the measurements. We adjust the fast axis of the variable retarder to be rotated by 22.5° with respect to the H/V-coordinate system. We set the detection path of the photon to project to the $\hat{\sigma}_z$-basis while setting the variable retardation to $0 \cdot \lambda$ retardation (see subsection 5.5.4). From this setting an orthogonal basis to $\hat{\sigma}_z$ can be selected by adjusting the variable retarder to $1/2 \cdot \lambda$ (see Figure 5.20 b)). To switch the properties of the wave plate accordingly takes 40 ms. The measurement bases on Bob's side are randomly selected by an external microcontroller in response to a control signal.

For the atomic side, we set the bases according to subsection 6.4.2 using microwave pulses. We create a separate experimental sequence branch for each measurement basis, which we execute in response to an external, randomly generated signal, similar to the conditional readout presented in section 7.2 (see Figure 8.3). This setup allows us to switch the bases of the photonic and atomic state detection independently and randomly.

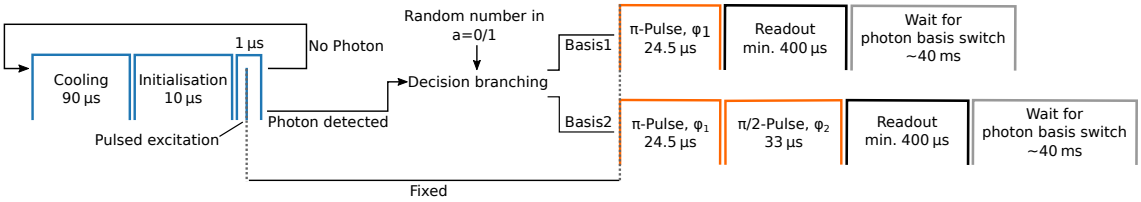

Figure 8.3: Experimental sequence on Alice's side for the measurement of one sifted key bit including the random switching of bases and photon generation. Bob generates the photon detection trigger and subsequently randomly changes his detection basis.

[94] In equation (5.87), we introduced the notation $\bar{\hat{\sigma}}_{x/y}$ to clarify the use of a different bases definition for the rotated bases. In this chapter, we drop this notation for the sake of simplicity and write $\hat{\sigma}_{x/y}$. However, we still refer to this definition of the bases.

[95] Liquid crystal wave plate (LCWP) LCC1411-A from Thorlabs

When Alice and Bob happen to measure in the same basis $a = b$, their outputs are ideally equal ($v = w$) as a consequence of the two qubits sharing the entangled state $|\Psi\rangle$ (see Figure 8.4). However, imperfections of the setup and Eve performing measurements on $|\Psi\rangle$ can also result in different outputs on both sides for $a = b$. After a measure-and-estimate phase of this quantum bit error rate (QBER) both parties agree on continuing with key distribution in case of an acceptable QBER (usually $\lesssim 15\,\%$ [59, 21]). For this purpose, we presuppose the existence of a public but authenticated classical communication channel between Alice and Bob. Up to now, the sequence is quite similar to an implementation of the BB84 protocol with the exception of not preparing a certain quantum state with value v in basis a at the senders side and sending it to the receiver measuring w. Instead, entanglement is distributed between the parties to make the qubits on sender and receiver side sharing a common wavefunction, which upon a state measurement gets projected to a certain basis. In this context, we show in section 8.4 that, in contrast to implementations of the BB84 protocol, the values of the outputs v, w are certifiable random.

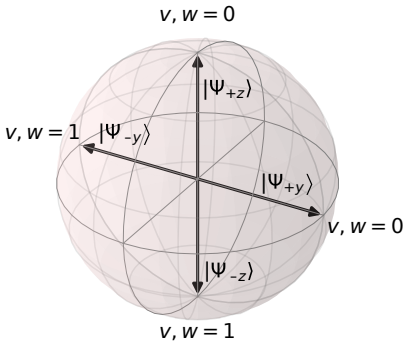

Figure 8.4: Eigenstate representation of $\hat{\sigma}_{y/z}$ on the Bloch sphere showing the assignment of a binary value v/w to the outcome of the projective state measurement on side A/B. Definition of $\left|\Psi_{\pm y/\pm z}\right\rangle$ according to equation (2.3).

8.3 Key rates, key reconciliation and privacy amplification

Alice and Bob compare their lists of measurement bases over an authenticated channel. From each projective state measurement for which they used the same basis ($\hat{\sigma}_i \otimes \hat{\sigma}_i$), they obtain one bit of their sifted keys $\mathbf{V} = \{v_1, .., v_n\}$ and $\mathbf{W} = \{w_1, .., w_n\}$, each with a total length n. At the beginning of this section we discuss the properties of sifted key generation and towards the end of the section we present the derivation of a secret key from the sifted key.

8.3.1 Key rates

In the experiment, the rate at which Alice and Bob obtain the bits of their sifted keys (sifted key rate) is limited by the switching time of the photon readout basis (40 ms), stationary qubit initialisation ($\sim 100\,\mu$s) and the channel loss (see Figure 8.3). For the presented experimental realisation, we achieved a maximum sifted key rate of 6 Hz.

Figure 8.5 shows the estimated sifted key rates as a function of the transmission channel loss for the current setup and two proposed improvements. We calculate the rates according to subsection 7.2.1 where the channel loss is given by the detection efficiency P_d of a

photon on Bob's side. Using a setup with passive basis switching could improve the sifted key rate by one order of magnitude by eliminating the active 40 ms switching of the variable wave plate. We achieved this rate in the context of the entanglement characterisation in chapter 7, where we also performed the measurements without an active switching of bases. A well known passive scheme can be realised with 4 single-photon counters for state detection, with each pair of detectors separated by a 50/50 beam splitter. Furthermore, another order of magnitude in the sifted key rate can be gained by exploiting the minimum state initialisation time of $\sim 4\,\mu$s of the memory qubit in advance to the deterministic photon generation (see subsection 7.2.1). However, each of the presented alternatives is limited at least by the state detection of the ion which lasts at least $\sim 400\,\mu$s.

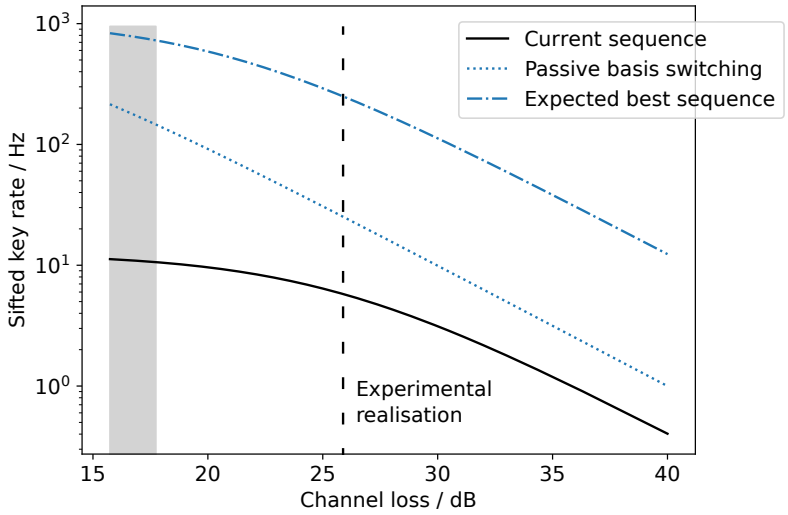

Figure 8.5: The performance of the current experimental sequence including the active switching of the photon basis is shown as solid black line. The channel loss of the setup (26 dB) is shown as vertical dashed line. The performance of an alternative setup in which active switching of the photon basis is avoided is shown as a blue dotted line. We reached this efficiency in chapter 7. An estimate of a sequence where also the generation rate of entangled photons is optimised by minimising the stationary qubit initialisation time to $4\,\mu$s is shown as blue dash-dotted line. The theoretical reachable minimal loss of the setup of 16.7(10) dB is shown as grey shaded area (assuming the same detection setup).

We currently perform our experiment at a channel loss of ~ 26 dB including path loss (η_{path}: 2.3(8) dB) and detector efficiencies (η_{Detector}: 6.7 dB loss). The channel loss is mainly limited by the photon extraction probability from the fibre-cavity (~ 7.8 dB loss), the mechanical stability of the fibre cavity and the localisation of the ion in the cavity (together ~ 17 dB loss), see subsections 5.5.3 and 5.5.3.

8.3.2 Quantum bit error rate (QBER)

In general, the sifted keys of Alice and Bob differ in m bits due to measurement or state preparation imperfections, or due to an attacker Eve performing measurements on the quantum state. In this subsection, we focus on the experimental imperfections contributing to the error rate of the measured sifted key bits. A detailed overview of the correlations

obtained between the atomic state and the photonic state, both measured in the same basis, is given in Table 12. However, for the measurements presented in this chapter, we have made some changes to the setup considered in Table 12 that are required by the QKD protocol: first, we keep the magnetic field constant at about 2 G (~ 5.5 MHz splitting of $|g^{\pm}\rangle$), which is important to consider for fluorescence state detection of the ion (subsection 6.2.2) and timing-precision of the atomic qubit manipulation (subsection 7.4.2). Second, the correction of false-positive readout events triggered by dark counts of the SPCs on Bob's side is not possible without further communication between Alice and Bob. However, on Bob's side, we can suppress dark counts on the detectors by applying a temporal gating on the arrival time of the photons at the cost of some detection efficiency, which we show in Figure 8.6 a) and b). By gating the photon arrival times with a $\Delta t_{\text{gate}} = 15$ ns time window, we can reduce the quantum bit error rate (QBER) to $e = m/n = 8.3\,\%$ (Figure 8.6 c)) while keeping a sufficient detection fraction of ~ 0.9.

Due to a beam splitter inserted on Bob's side into the detection arm of horizontally polarised photons (H-arm) for the purpose of fibre cavity locking (section 5.3), the V-arm detecting vertically polarised photons has a slightly higher detection efficiency compared to the H-arm. We have to account for the different efficiencies by randomly discarding a fraction of events on the V-detector in order to reach equal balanced detection efficiencies, which we achieved with a relative accuracy of $\geq 98\,\%$. Equal balanced detection efficiencies are crucial for the security of the key, as they directly influence the key statistics. We have also taken further security measures against side channel attacks, which we present in section 8.5.

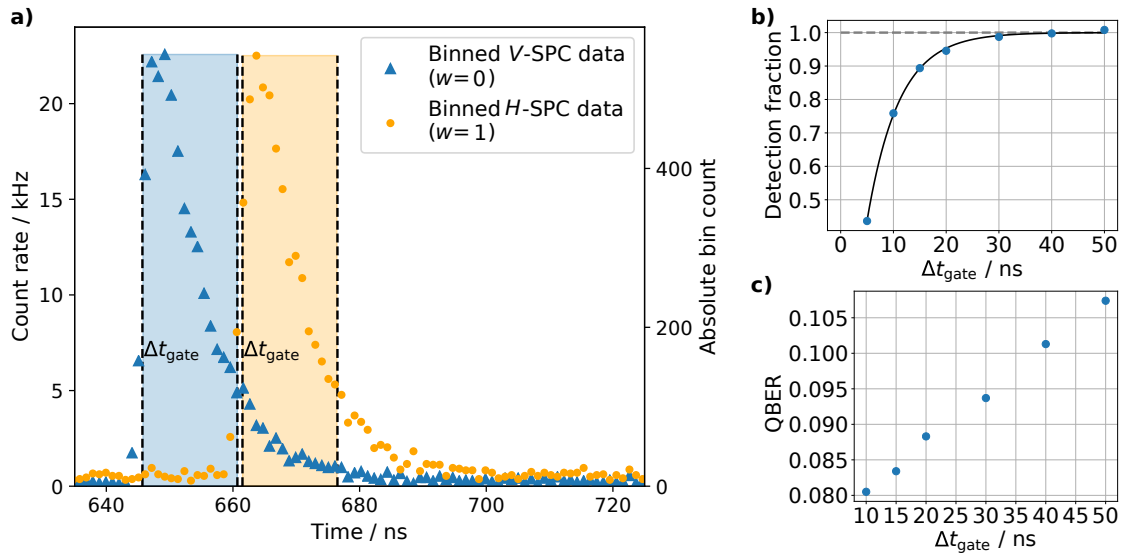

Figure 8.6: a) Binned single photon arrival times on Bob's side (bin width ≈ 1 ns). In order to suppress dark counts, a measured bit only contributes to the sifted key for the detection to happen in the time window $\Delta t_{\text{gate}} = 15$ ns which is shown as coloured areas for H/V respectively. We randomly discard fractions of V events to ensure the same detection efficiencies for H and V photons and thus obtain an unbiased key. **b)** The relative fraction of travelling qubits contributing to the sifted key is shown for different acceptance windows (blue points). The solid line constitutes an exponential saturation fit. **c)** Quantum bit error rate on the whole sifted key for different acceptance windows.

8.3.3 Key reconciliation and privacy amplification

In order to correct for the m errors in the sifted keys and to end up with the same key string on both sides, Alice and Bob perform a key reconciliation via an authenticated classical channel, where they may leak information about the reconciled key to the public. Using privacy amplification [16], the reconciled key with length n_r is shortened by a universal hash function to a final secret key length of $n_{\text{sec}} = n_r - d$ by each communication party, which reduces the information available to Eve. An adequate hash function for this purpose can be obtained by computing n_{sec} publicly chosen independent random subset parities of the reconciled key and keeping their values secret [13].

The number of bits d by which the key has to be shortened has to be determined concerning the knowledge Eve may have about the reconciled key. For this purpose, we have to consider that the presented QKD involves an entangled source on Alice's side. We follow the security proof of an arbitrary uncharacterised source by Koashi and Preskill [89] to determine the maximal knowledge Eve may have about the reconciled key. The proof is originally based on the BB84 protocol, but due to a similar measure-and-estimate scheme of BB84 and BBM92, the security proof is valid for the presented system as well [15, 184]. We are able to give an upper bound on Eve's knowledge without applying any restriction on the attack itself, however, requiring the transmission of true single photons, no a-priori information about the measurement bases, and fully characterised detectors on Bob's side [89] (for related side channel attacks, see section 8.5).

Assuming all errors of the sifted key to be caused by Eve, the length n_{sec} to which the secret key has to be shortened in order to account for the potential knowledge of the eavesdropper is given by [184]

$$n_{\text{sec}} = \sum_{i \in \{z,y\}} n_{\text{sec},i} \tag{8.2}$$

where

$$n_{\text{sec},z/y} = n_{z/y} \cdot \Big[1 - f_r \cdot H(e_{z/y}) - H(e_{y/z})\Big] \tag{8.3}$$

is the analytic lower bound on the secret key length for the number of sifted key bits $n_{z/y}$ measured in the $\hat{\sigma}_z \otimes \hat{\sigma}_z / \hat{\sigma}_y \otimes \hat{\sigma}_y$ basis respectively with $H(q) = -q \log_2(q) - (1-q) \log_2(1-q)$ being the binary entropy function. The QBER we obtain for the sifted key bits in the $\hat{\sigma}_{z/y} \otimes \hat{\sigma}_{z/y}$ basis is $e_z = 7.86\,\%$ and $e_y = 9.12\,\%$. Due to timing issues in the rotated basis originating from the Larmor precession of the atomic state, e_y is larger than e_z (see subsection 7.4.2). The quantity $f_r \geq 1$ states the inefficiency of the information reconciliation protocol that Alice and Bob apply to correct for the m errors in the sifted key [48]. An ideal reconciliation protocol would reveal a fraction $H(e)$ of the sifted key, while real protocols reveal a fraction $f_r \cdot H(e)$. Accounting for the inefficiency of information reconciliation allows to form a secure key in practice. It is convenient to introduce here the secret key rate

$$r_{\text{sec}} = \frac{n_{\text{sec}}}{n}, \tag{8.4}$$

which is normalised to the number of transmitted sifted key bits n.

For error correction, we apply the symmetric blind information reconciliation protocol [83][96], which is based on low density parity checks (LDPC), on the sifted key obtained on

[96] The authors have provided us with the source code and LDPC codes. I would like to thank E. Kiktenko in this context.

the sides A and B. We reach a reconciliation inefficiency of $f_r = 1.16$ and subsequently $r_{\text{sec}} = 0.096\,\text{bits}$ according to equation (8.4) [97]. However, r_{sec} states the asymptotic secret key rate for large n. For a finite key length, we obtain a non-vanishing finite secret key rate for a failure probability of $\epsilon \approx 2\,\%$ (see next paragraph).

Finally, privacy amplification has to take all information leakage into account by reducing the reconciled key to a length of n_{key} with $n_{\text{key}} \leq n_{\text{sec}}$. In total, we achieved for n_{sec} a bit rate of 0.6 Hz.

Finite key length

Due to statistical fluctuations, the measured error rate $e_{z/y}$ may differ from the underlying error rate $e'_{z/y}$ obtained in the asymptotic case of large n. An upper bound $e^{\max}_{z/y}$ of the underlying error rate $e'_{z/y}$ can be given using the Serfling inequality [153] according to [184, 38] as

$$e'_{z/y} \leq e^{\max}_{z/y} = e_{z/y} + \sqrt{\frac{\left(n_{z/y}+1\right)\log\left(1/\epsilon_{\text{sec}}\right)}{2n_{z/y}\left(n_{z/y}+n_{y/z}\right)}}, \tag{8.5}$$

where again $n_{z/y}$ is the number of measured sifted key bits in $\hat{\sigma}_{z/y} \otimes \hat{\sigma}_{z/y}$ basis. The total failure probability $\epsilon = \epsilon_{\text{sec}} + \epsilon_{\text{ec}}$ with the probabilities ϵ_{sec} of failure of secure transmission of the key and ϵ_{ec} of failure of error correction can be used according to [184] to derive a finite secret key length for which the security proof still applies. Using the upper bound $e^{\max}$ of the bit error rate e from equation (8.5), we can compute the finite secret key size according to [168, 184] as

$$n^{\text{finite}}_{\text{sec}} = \sum_{i\in\{z,y\}} n^{\text{finite}}_{\text{sec},i} \tag{8.6}$$

with

$$n^{\text{finite}}_{\text{sec},z/y} = n_{z/y}\cdot\left[1 - f_r\cdot H(e_{z/y}) - H(e^{\max}_{y/z})\right] - \log\left(\frac{2}{\epsilon_{\text{ec}}\epsilon^2_{\text{sec}}}\right) \tag{8.7}$$

assuming balanced detection paths. We define $r^{\text{finite}}_{\text{sec}} = n^{\text{finite}}_{\text{sec}}/n$ as the finite secret key rate. If we assume the error correction to fail in a very few cases, e.g. $\epsilon_{\text{ec}} = 0.1\,\%$, we obtain a non-vanishing finite secret key rate for a failure probability of the secure transmission of $\epsilon_{\text{sec}} \approx 2\,\%$.

8.4 Randomness certification using the violation of Bell's inequalities

The inability to describe the properties of a remote distributed entangled two-qubit state with the methods of local realism led to the terminology of non-locality to reflect this conflict (see section 2.3). The Bell inequalities are fulfilled by any system exhibiting local causality and hence, can be described deterministically [51] (see section 2.4). In contrast, systems violating the Bell inequalities exhibit a non-local, non-deterministic description and it has been proposed in [35] that the non-local correlations of quantum states can be used to exclude any deterministic (causal) connections.

In this section, we introduce how the exclusion of deterministic connections can be used to generate certified private randomness of the distributed secret key using the fundamental

[97] For comparison, we have also adopted the CASCADE error correction algorithm from [5], where we have achieved an inefficiency of $f = 1.21$

non-local properties of our entangled state, which in this strong form is not possible in classical information theory. Even when using quantum systems for the distribution of keys, certifiable randomness of those quantum keys is only achieved for systems that exhibit a violation of the Bell inequalities [11, 138].

To quantify the concept of randomness, we consider the uncertainty of an attacker with side information E about the system S, which can be expressed through the probability of guessing a measurement outcome x of measurement s on S [95]. In the extreme case of S being fully correlated to parts of E, the guessing probability becomes $P_{\text{guess}}(x) = 1$. In other cases, the state of S is (partly) independent of the attackers information E and the guessing probability can be described as [110]

$$P_{\text{guess}}(x) = \max_x P(x|s) \tag{8.8}$$

where $P(x|s)$ is the probability of measuring output value x for a measurement s and the maximum is taken over all possible output values x. True randomness is achieved, for example, for a sifted key string $\mathbf{V} = v_1, ..., v_n$ when $P(v_i|s) = \text{const}\, \forall v_i \in \{0, 1\}$ and for all measurements s. In this case, all possible combinations of $\mathbf{V}$ are equal probable as an outcome.

In classical information theory, the generation and even more the verification of random numbers (random bits) is hard to realise because one has to exclude any causal connections between the numbers, in particular the specification of an upper bound for $P_{\text{guess}}(x)$ is a problem. In contrast, in quantum theory the unpredictability of a measurement outcome is closely linked to the violation of the Bell inequalities. Using violation of the Bell inequalities one can quantify the closeness to a situation where a quantum system S is fully determined by the side information E [95] and when it is perfectly non-local and non-deterministic on the opposite without knowing the system's internal behaviour. Any system maximally violating the Bell inequalities exhibits a non-local, non-deterministic description, which excludes any deterministic (causal) connections and generates certified private randomness [35, 138].

Testing Bell's inequalities

We consider to test the violation of Bell's inequalities in the experiment in the form proposed by Clauser, Horne, Shimony and Holt (CHSH) [33] (see equation (2.14)), where a system that can be described local and deterministic satisfy

$$g^{\text{CHSH}} = \sum_{a,b} (-1)^{ab} \left[P_{v=w}(a, b) - P_{v \neq w}(a, b) \right] \leq 2, \tag{8.9}$$

where $P_{v=w}(a, b)$ is the probability of measuring the same output on both sides when using the measurement bases a and b. The quantum theory predicts a maximal violation of $2\sqrt{2}$ (see section 2.4).

We measure a violation of the CHSH inequality of

$$g_{\text{meas}} = 2.33(6) \tag{8.10}$$

by using the measurement basis $\hat{\sigma}_y$ for $b = 0$ and $\hat{\sigma}_x$ for $b = 1$ on Bobs side. On Alice's side we measure at $(\hat{\sigma}_y - \hat{\sigma}_x)/\sqrt{2}$ for $a = 0$ and at $(\hat{\sigma}_y + \hat{\sigma}_x)/\sqrt{2}$ for $a = 1$. The observed

outcomes of the measurements are shown in Table 13. The bases used for the Bell test are shown Figure 2.3 with a consistent nomenclature, i.e. the set $(\vec{a}, \vec{a}')$ corresponds to the atomic bases and $(\vec{b}, \vec{b}')$ to the photonic bases.

(a, b)	$(1, 0)$	$(0, 0)$	$(1, 1)$	$(0, 1)$
Basis $\hat{\sigma}_{\text{atom}} \otimes \hat{\sigma}_{\text{photon}}$	$\frac{\hat{\sigma}_y+\hat{\sigma}_x}{\sqrt{2}} \otimes \hat{\sigma}_y$	$\frac{\hat{\sigma}_y-\hat{\sigma}_x}{\sqrt{2}} \otimes \hat{\sigma}_y$	$\frac{\hat{\sigma}_y+\hat{\sigma}_x}{\sqrt{2}} \otimes \hat{\sigma}_x$	$\frac{\hat{\sigma}_y-\hat{\sigma}_x}{\sqrt{2}} \otimes \hat{\sigma}_x$
$P_{v=w}$	0.835 ± 0.020	0.791 ± 0.027	0.229 ± 0.013	0.770 ± 0.027

Table 13: Measurement of the Bell-violation. Observed outcome of the measurement outputs (v, w) for the binary choices of measurement bases (a, b).

Consistency of the measured Bell-violation with the state fidelity

We cross check the measured violation of the CHSH inequality g_{meas} with the Bell-violation g_{exp} we would expect from the measured state fidelity $F = (90.1 \pm 1.7)\,\%$. For this purpose, we assume the two-qubit state to be a pure state $|\psi\rangle$ mixed to a probability $(1 - V)$ with white noise as described in subsection 7.5.5. With the visibility $V = 2F - 1 = 0.80(3)$ of the state, we obtain $g_{\text{exp}} = 2\sqrt{2} \cdot V = 2.27 \pm 0.10$ according to [110], which is consistent with the measured Bell-violation $g_{\text{meas}} = 2.33(6)$.

Fair sampling

It is important to note that due to the entanglement generation and detection scheme of the presented setup, we measure a random subset of all generated two-qubit states, which opens a detection loophole for the measured violation of equation (8.9) as explained in subsection 2.4.1. However, we have no reason to doubt the assumption of fair sampling of the measured subset from the total set of generated entangled states. Furthermore, we implemented spatial, temporal and spectral filtering of photons on the detection side as a security measure against side channel attacks that could potentially violate the fair sampling assumption (see section 8.5).

Generation of random key bits

From the violation of the CHSH inequality g from equation (8.9), the upper bound on the guessing probability of each measurement outcome x by an attacker in the asymptotic limit (equation (8.8)) can be derived as [138]

$$P_{\text{guess}}(x) \leq 0.5 + 0.5\sqrt{2 - \frac{g^2}{4}}. \tag{8.11}$$

We assume that any reduction in non-locality of the state results in an increasing causality which may be fully accessible to an attacker. This is an important result because it allows us to put a number on 'how random' an outcome of a measurement is. For finite measurement rounds, the measured violation g_{meas} is an estimator of the CHSH inequality violation g and the guessing probability may be higher. It was shown in [138, 139] that a lower bound on g can computed from the estimator g_{meas} as

$$g \geq g_{\text{meas}} - \epsilon(k, \delta) \tag{8.12}$$

when the device was used k-times in succession. Here $\epsilon(k, \delta) = \sqrt{-\frac{\ln(\delta) \cdot 2(1/q + g_{\text{meas}})^2}{k}}$ with

an uncertainty parameter δ and $q = 0.25 = \min_{a,b}[P(a,b)]$ being the minimum of the probability distribution over the input states a and b.

For a single measurement s on the system S, the min-entropy $H_{\min}$ quantifies the amount of randomness generated in this measurement. It was shown, that the min-entropy per transmitted bit can be computed as [95]

$$H_{\min}(s|E) = -\log_2[P_{\text{guess}}(x)] \tag{8.13}$$

where $P_{\text{guess}}(x)$ is the probability of guessing the correct output x of measurement s by the attacker measuring the side information E [110].

Using equation (8.11) in combination with equation (8.13), we compute a lower bound on the min-entropy generated per measurement on the quantum system state $|\Psi\rangle$ as

$$H_{\min}(g) \geq -\log_2\left[0.5 + 0.5\sqrt{2 - \frac{g^2}{4}}\right] \equiv H_{\min}^{\geq} \tag{8.14}$$

in the asymptotic limit. Finite measurement rounds for the determination of g_{meas} can be considered using [138]

$$H_{\min}\left(g_{\text{meas}} - \epsilon(k,\delta)\right) \equiv H_{\min,\delta,k}^{\geq} \tag{8.15}$$

with δ being the confidence level of randomness generation. Equation (8.14) quantifies the asymptotic lower bound on the generated randomness per measurement, which is in our case $H_{\min}^{\geq} = 0.15(4)$ bits. In Figure 8.7 a) the lower bound on the min-entropy $H_{\min}^{\geq}$ is shown as a function of the Bell violation g. Figure 8.7 b) shows the subsequent lower bound on the min-entropy $H_{\min,\delta,k}^{\geq}$ as a function of the number k of measurements made for the estimation g_{meas} of the Bell violation and the confidence level δ according to equation (8.15). Further, we can calculate the minimum block size $l_B = \text{ceil}(1/H_{\min}^{\geq}) = (7 \pm 2)$ bits of the sifted key for which Alice and Bob have generated at least one random bit in the asymptotic limit. The key length n_{rand} for a final key to be entire random is bounded by $n_{\text{rand}} \leq \text{floor}(n_r/l_B)$ with $n_r \leq n$.

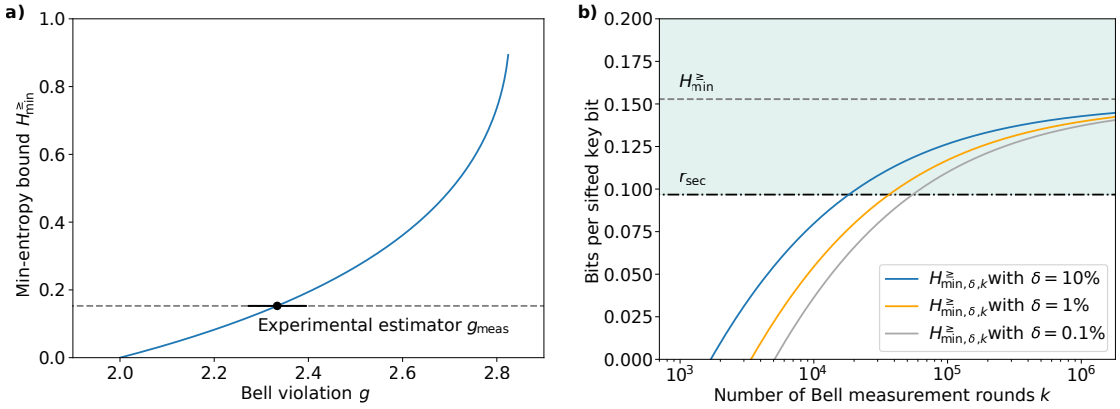

Figure 8.7: a) The lower bound on the min-entropy $H^{\geq}_{\min}$ generated per measurement on the two-qubit state $|\Psi\rangle$ is shown versus violation of the CHSH version of the Bell inequality g (see equation (8.14)). The error on the measured estimator g_{meas} is the standard error. **b)** Lower bound on the min-entropy $H^{\geq}_{\min,\delta,k}$ as a function of the number k of measurements made for the estimation of the Bell violation g_{meas} with the confidence level δ according to equation (8.15) (solid lines). The grey dashed line depicts the asymptotic limit of the min-entropy bound as shown in a). The coloured area depicts the region where the communication parties can be sure with a confidence level δ that the generated randomness per sifted key bit is larger than the secret key derived from the sifted key even in the asymptotic limit of a large sifted key length n (for the definition of r_{sec}, see equation (8.4)).

In total, we have to shorten the secret key to the length

$$n_{\text{key}} \leq \min\{n^{(\text{finite})}_{\text{sec}}, n_{\text{rand}}\}, \tag{8.16}$$

which is the smaller of the two maximal allowed key lengths to obtain: i) a certified random generated key with length $n_{\text{rand}} = n \cdot H^{\geq}_{\min,\delta,k}$ and ii) a provably secure transmitted key with length $n^{(\text{finite})}_{\text{sec}} = n \cdot r^{(\text{finite})}_{\text{sec}}$ (see section 8.3).

8.5 Security measures against side channel attacks

For the presented entanglement-based QKD, we use the security proof given in [89] for an uncharacterised source, which requires characterised detection setups. Therefore, the presented protocol is device-dependent, i.e., we prove security for this specific setup under ideal detection conditions. However, a real setup is vulnerable to attacks via side channels as well. We mitigate the known detection side-channel attacks according to [184] by taking into account the measurement methods.

Beam-splitting [103]
The attack describes gaining control over the measurement basis on Bob's side by forcing a click on a specific detector (pair). This can be achieved by sending photons of different wavelength exploiting the spectral response of the setup. This attack can be mitigated by spectral filtering of the incoming photons, which we do with a 10 nm spectral bandpass filter (see subsection 5.5.1).

Efficiency-mismatch [107]
Due to differing detection or path efficiencies of the photon detection setup on Bob's side, Eve can gain partial control over which detector clicks and bias the outcome of the measurement. As a countermeasure, we implemented a series of filters on Bob's side: i) Due to the photon guiding fibre being single mode, we restrict the spatial mode degree of freedom. ii) Using 10 nm spectral filters in front of each detector narrows the frequency degree of freedom. iii) We restrict the time degree of freedom by applying a 15 ns wide filter to the photon arrival time on Bob's side where we monitor the detection efficiencies and correct for a slightly higher efficiency of the V-arm by randomly discarding a fraction of detected events on this arm (see section 8.3). In total, we achieve equal detection efficiencies with an accuracy of more than 98 %.

Detector dead-time [106]
Subsequent to the detection of a photon, detectors usually exhibit a dead time in which they are blind for further photons. If there is a click followed by another click within the dead time of the detectors, it is clear to an attacker that two different detectors were involved which may reveals additional information. For example an attacker could force a detector to click in advance to a real photon detection event. We can counteract this attack by discarding runs where we noticed two clicks on Bob's side. We do this without loosing QKD rate, since the probability of detecting the single photon coming from Alice in normal operation of the experiment is $P_{\mathrm{det}} \approx 2.6 \times 10^{-3}$ per shot while the probability of a noise count is smaller than 10^{-5} within the dead time of the detectors which is < 20 ns. Assuming the transmission of true single photons, the probability of a noise click alongside with a photon detection is in the order of magnitude of $\sim 10^{-8}$. In the presence of an attacker attempting to blind the detectors, the fraction of discarded runs would naturally be higher and the protocol would decrease in rate.

Availability
Quantum key distribution is generally vulnerable to denial-of-service attacks and also for the presented system there is no countermeasure for e.g. simply blocking the transmitted photons. This type of attack is mentioned here for the sake of completeness and it does not affect the security or randomness of the derived key (if it was transferred in the end).

8.6 Summary

We have demonstrated the realisation of QKD between two remote parties including an entangled memory qubit on one side, which favours key exchange over large distances within the scope of memory-enhanced quantum communication, especially with respect to quantum repeaters. The trapped ion enables a secure distribution of the quantum key according to the laws of quantum mechanics by generating true single photons with $g^2(0) = 0.00(5)$. Considering the fundamental non-locality of the distributed two-qubit state for the generation of the final secret key, we have shown that certifiable randomness of the derived key can be ensured with a high confidence level $\delta < 0.01$ by performing a finite set of Bell test measurements $O(10^4)$. As a lower bound on the generated randomness we calculated $H_{\mathrm{min}}^{\geq} = 0.15(4)$ bits per sifted key bit in the asymptotic limit. This kind of

provable randomness is an outstanding property of entangled quantum systems violating the Bell inequalities and is impossible to obtain in classical information theory. We measure a Bell-violation of $g_{\mathrm{meas}} = 2.33(6)$, which is consistent with the measured entangled state fidelity of 90.1(17) %.

For a sifted key with a length of $n = 3080$, we have achieved a quantum bit error rate (QBER) of 8.3 %, which is expectable from the experimental imperfections and mainly limited by the state detection of the atomic qubit. The experimental repetition rate of $\sim 20\,\mathrm{kHz}$ and the channel loss determine the achieved sifted key rate of 6 Hz, which is more than three orders of magnitude higher than the sifted key rate reported for a non-distant quantum communication including an entangled memory qubit with a QBER of $\sim 11\,\%$ [21]. On the one hand, the use of memory qubits allows arbitrarily long communication distances within the framework of an ideal quantum repeater [172], but on the other hand requires comparatively long readout and preparation times, which in our case lead to a sifted key rate about two orders of magnitude lower compared to QKD implementations with entangled photon pairs [49, 109, 187]. There, the best achieved error rates are about a factor of 2 lower ($\gtrsim 4.5\,\%$) [184, 171, 134, 49] than the QBER presented here.

The security of the presented system in terms of key randomness, confidentiality and integrity is based on the violation of Bell's inequalities, photon correlation measurement and error rate estimation (see Figure 8.1). It is also possible to combine Bell inequality test and key distribution into a single sequence, which requires a small modification to the measurement bases of the presented distribution protocol so that they maximally violate the CHSH version of the Bell inequalities. Alice and Bob can then perform permanent Bell tests on the quantum system to ensure random generation and secure distribution of the key based on the violation of Bell's inequalities, as proposed in [173, 110].

In principle, the presented methods can be extended to any entangled two-qubit state and are especially applicable within the framework of entanglement-based quantum repeaters, which in particular enables the realisation of key distribution beyond the point-to-point limit of quantum communication (see Outlook).

9 Summary and outlook

The summary provides an overview of the results of the thesis. The discussion of the achievements in the context of current research can be found in the respective chapters and the corresponding summaries. We conclude the thesis with an outlook to possible improvements and put the presented setup in the context of a long-term perspective in quantum communication. We point out the role of memory-based network nodes for long-distant communication, especially with regard to the realisation of a quantum repeater.

9.1 Summary

In this thesis, we have laid the groundwork for entanglement-based quantum communication with fibre Fabry-Pérot cavities as efficient light-matter interfaces in combination with trapped ions as long-lived memory qubits.

We built an advanced fibre cavity setup resonant to the principal UV transition of Yb^+ at 370 nm and combined it with a miniature Paul trap. With this setup, we were able to overcome some of the limiting shortcomings of previous fibre cavity setups, such as degradation of the mirrors, incompatibility with microwave pulses and destabilisation of the ion trap. Using the fibre cavity as light-matter interface, we realised an efficient collection of photons emitted from the single trapped ion, where the photons have a controlled temporal profile, polarisation state and spatial mode, which are important properties for quantum information processing and quantum communication. We measured an effective light-matter coupling of $g_{\text{eff}} = (7.2 \pm 1.2)\,\text{MHz}$ and a photon collection efficiency of $P_{c,\text{eff}} = (8.4 \pm 2.2)\,\%$. At the same time, the cavity provides a fast extraction of collected photons of 1.4(1) ns with intrinsic fibre coupling, allowing for an easy distribution of quantum information to other elements of a network at a high rate.

The small size of the fibre cavity enables excellent optical access to the trapped ion allowing for precise control and manipulation of this long-lived stationary qubit. We demonstrated high-fidelity initialisation ($> 99\,\%$) and readout ($98.2(6)\,\%$) of the atomic qubit state and coherent storage of quantum information for up to 12 ms. Employing phase-coherent microwave pulses, we demonstrated the ability to perform arbitrary rotation operations on the qubit state with high fidelity and even complex state mappings between different qubit transitions.

In the context of setup optimisation, we presented a novel approach to create an empirical model of an experimental apparatus employing machine learning in the form of supervised or unsupervised learning. We applied this methodology to optimise the position of the ion in the Paul trap with a greatly reduced amount of required data. The resulting improvement in trapping stability supports general data acquisition on the setup and the availability of the ion as a communication node. Since the presented methods are based on general assumptions and are flexible in terms of implementation and deployment, they are applicable to a wide range of different optimisation tasks covering several fields of experimental physics.

Combining all these achievements, we demonstrated the deterministic generation of entanglement between the spin state of the ion and the polarisation degree of freedom of an emitted photon by utilising the spontaneous decay of the ion. To this end, we excited the ion with a probability of $(99 \pm 1)\,\%$ using picosecond long laser pulses and achieved a

success rate of detecting atom-photon entanglement per trial of $2.58(6)\times10^{-3}$. At the same time, to the best of our knowledge, we achieved the yet shortest temporal profile of photons extracted through the cavity of 9.3(9) ns by more than an order of magnitude compared to previous cavity-based realisations of entangled atom-photon states [143, 99, 164]. This is advantageous for impedance matching to further elements of a network [117] and high-fidelity state detection. By implementing real-time branching of experimental sequences, we achieved an entanglement detection rate of 58 Hz by performing a conditional readout of the atomic state only upon detection of the photonic qubit.

We performed a full tomography of the atom-photon state followed by a maximum likelihood estimation to ensure the obtained density matrix of the state to be physical. From the tomography, we obtained a state detection fidelity of $F = (90.1 \pm 1.7)\,\%$. We demonstrated full control over the state mapping of each qubit and performed a detailed investigation of the errors that contributed to the measured state fidelity.

Since we achieved in this thesis all requirements for memory-based quantum communication in a single experiment, we were able to demonstrate the first quantum key distribution between two remote parties involving an entangled memory qubit on one side. This achievement favours long-distance key exchange especially with respect to quantum repeaters. For the key distribution we achieved a quantum bit error rate of 8.3 % and a sifted key rate of 6 Hz. The trapped ion enables a secure distribution of the quantum key according to the laws of quantum mechanics by generating true single photons with a temporal second-order correlation of $g^2(0) = 0.00(5)$.

Considering the fundamental non-locality of our entangled two-qubit state for the generation of the final secret key, we have shown that certifiable randomness of the derived key can be ensured with a high confidence level $\delta < 0.01$ by performing a finite set of Bell test measurements. This kind of provable randomness is an outstanding property of entangled quantum systems violating the Bell inequalities and is impossible to obtain in classical information theory. We measured a Bell-violation of $g_{\mathrm{meas}} = 2.33(6)$ for the atom-photon state, which is consistent with the measured entangled state fidelity.

9.2 Outlook

As a short-term improvement to the experimental setup, optimising the experimental sequence used for generation and detection of the entangled atom-photon state could increase the rates of both by up to an order of magnitude ($\sim$ 600 Hz detection rate). However, this should be done while ensuring sufficient cooling of the ion, e.g. by separating entanglement generation sequences and cooling cycles. About the same gain over the current rate can be expected by exploiting the full potential of the fibre cavity. This requires improved mechanical stabilisation of the cavity structure for optimised coupling of the resonator mode to the atomic transition as well as precise longitudinal positioning of the ion in the resonator.

Although we achieved a remarkable improvement in trapping stability compared to previous experiments with UV fibre cavities, recent progress in printing metal layers on dielectric surfaces are promising for electrically shielding the unused areas of the fibre mirrors. Since the mode of the resonator on the mirrors is typically smaller than the diameter of the fibres, this stray electric field shielding could be realised without clipping the mode of the resonator (see Figure 9.1). This could support trapping stability and optimal localisation of the ion within the cavity mode due to a reduced exposure of the ion to stray electric fields originating from the charged dielectric mirror surfaces. Taking this further, one can even think about integrated ion traps at the tip of optical fibres.

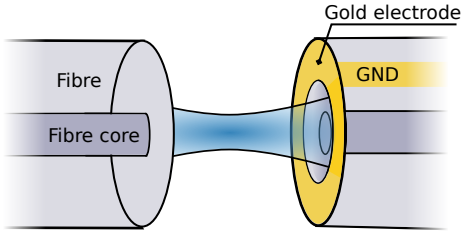

Figure 9.1: Two mirrors, each on a fibre tip, form an optical resonator. The area of each mirror is reduced by a ring-shaped gold electrode without clipping the resonator mode. GND: electrically grounded.

Where possible, applying these methods to the current or a future fibre resonator assembly could help to achieve a stable nominal light-matter coupling of $g \approx 2\pi \cdot 40\,\mathrm{MHz}$ for the existing design parameters of the resonator. In this case, the nominal collection efficiency would be about $P_c \sim 70\,\%$, while the cavity maintains a fast extraction of photons ($\kappa \approx 2\pi \cdot 60\,\mathrm{MHz}$).

Long distant quantum networks

Due to the high absorption of ultraviolet light in optical fibres, the presented applications of quantum communication are limited in their range in practice. A logical next step in the realisation of a quantum network node would be the inclusion of a frequency conversion to telecom wavelength, which has been demonstrated recently for Ca^+ ions [24, 99] and single Rubidium atoms [72]. The principle of a conversion between 370 nm and 1314 nm with 10.5 % efficiency [148] or 1580.3 nm with 9 % efficiency [79] has been demonstrated already for weak laser fields. Conversion pathways for matching the

trapped ion qubit to semiconductor quantum dots [117] or other emitters can also be explored, where the short temporal profile of the collected photons could be advantageous.

The ion-cavity system as a module for a quantum repeater

To exploit the capabilities of the trapped ion as a long-lived memory qubit, memory-enhanced quantum communication offers the ability to surpass the fundamental limit of quantum communication via point-to-point links (PLLs). These kind of links naturally encounter a physical limit when the loss of the communication channel over distance is considered [166, 137]. Due to the absorption of photons in optical fibres or in another medium, the path efficiency

$$\eta_{\text{path}}(d) = \exp\left[d \cdot \ln\left(\rho\right)\right] \tag{9.1}$$

scales exponentially with the distance of the path d, where ρ is the transmittance of the medium in units of d. However, with memory-based quantum repeaters, it is possible to overcome the point-to-point limit for quantum communication [172, 21] while maintaining the advantageous properties of quantum communication.

To understand the advantage of memory-based quantum communication, we investigate two different kinds of application schemes for the building block of atom-photon entanglement presented in this thesis. As mentioned before, the point-to-point link efficiency $R_{\text{ppl}}(d) \propto \eta_{\text{path}}(d)$ drops exponentially with the link distance d (equation (9.1)). A partial projective Bell-state measurement (BM) positioned centrally between the two communication participants allows to entangle both endpoints, with each photon travelling half the distance $d/2$ through the medium, as shown in Figure 9.2 a). However, this scheme is not able to increase the efficiency of the link. Here, the probability for a photon to be detected on a single photon detectors (SPC) is

$$P_{\text{d,eff}} = P_{\text{source}} \cdot \underbrace{\eta_{\text{detector+optics}}}_{\equiv\eta_{\text{detection}}} \cdot \underbrace{\eta_{\text{path}}(d/2)}_{=\exp[d/2\cdot\ln(\rho)]} , \tag{9.2}$$

where we summarised in P_{source} the efficiency of generating an entangled atom-photon state and coupling the photon into the optical fibre.

Using this efficiency, we can compute the expected link efficiency R_{bm} for the BM scheme. For a successful entanglement of both endpoint nodes, the photons emitted by the two nodes must both be detected at the SPCs in a single attempt, for which the probability is

$$R_{\text{bm}} = 0.5 \cdot P_{\text{source}}^2 \cdot \eta_{\text{detection}}^2 \cdot \eta_{\text{path}}^2(d/2) \propto \exp\left[2 \cdot d/2 \cdot \ln\left(\rho\right)\right], \tag{9.3}$$

where the factor of 0.5 considers the detection of 2 out of 4 Bell states according to [161]. We find that R_{bm} scales in the distance of the quantum link d equivalent to a PPL with $R_{\text{ppl}}(d) \propto \eta_{\text{path}}(d)$.

The requirement for simultaneous detection of both photons for the central Bell state measurement eliminates the gain from halving the travel distance of each photon. However, if we could entangle each half of the link by itself and then, after success on both halves, project the entanglement onto the two endpoint nodes, the scaling of the path efficiencies would be $\eta_{\text{path}}(d/2)$. This is exactly how the single node quantum repeater works. This

requires the caching of entanglement for which memory qubits are excellent candidates. Therefore, the usage of two ions to form repeater node as shown in Figure 9.2 b) could be explored using the network node presented in this thesis as a building block. The link efficiency for a single node quantum repeater (QR) in the so-called node-sends-photon configuration (NSP) scales as

$$R_{\mathrm{qr,nsp}} = 0.5 \cdot \eta_{\mathrm{node}} \cdot P_{\mathrm{source}}^2 \cdot \eta_{\mathrm{detection}}^2 \cdot \eta_{\mathrm{path}}^2(d/4) \propto \exp\left[d/2 \cdot \ln\left(\rho\right)\right], \tag{9.4}$$

where η_{node} takes into account the efficiency of the entanglement mapping at the repeater node, but is assumed to be $\eta_{\mathrm{node}} \approx 1$ for the following estimations. In this scheme of a memory-based quantum repeater, a distance d can be bridged, with each photon travelling the PPL-equivalent distance $d/2$ in an optical fibre.

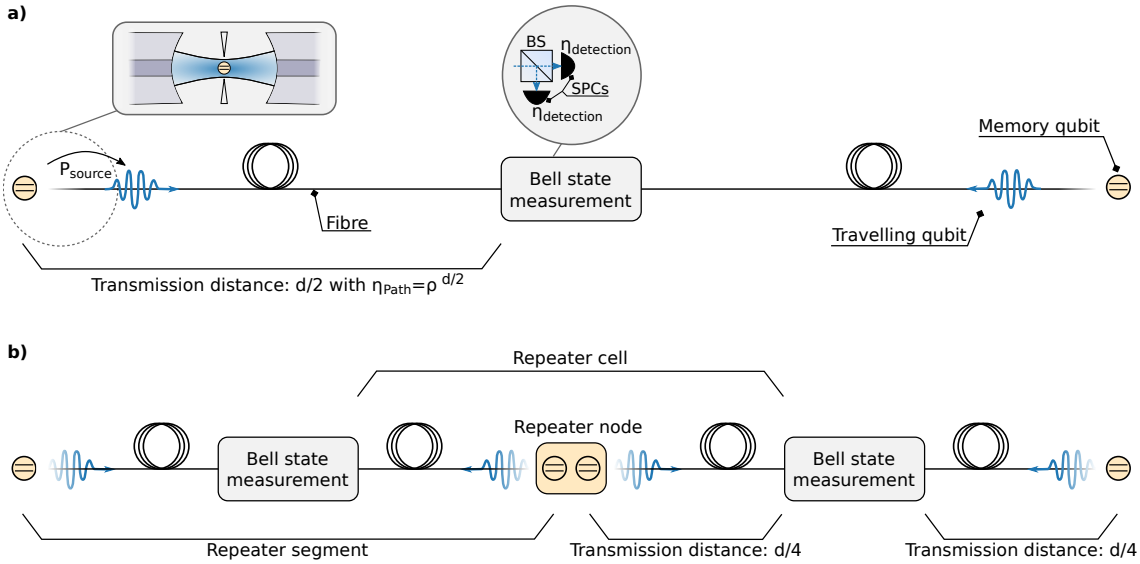

Figure 9.2: Quantum communication over distance d. Matter qubits acting as quantum memory are shown in yellow. Photons as travelling qubits are shown in blue. The building block of atom-photon entanglement was realised within this thesis (dashed circle). The inset at the Bell state measurement element shows the simplest implementation of a bell state measurement using a 50:50 beam splitter (BS) and two single photon counters (SPC). For calculations, a setup comprising of one BS, two polarising BSs and four SPCs is considered [161] **a)** Spin-spin entanglement using a Bell state measurement (BM) centrally between the communication endpoints. **b)** Quantum repeater in node-sends-photon (NSP) configuration. Nomenclature taken from [172].

For the communication schemes presented in Figure 9.2 a)+b), the expected link efficiencies according to equations (9.3) and (9.4) are shown in Figure 9.3 a) for the parameters currently achieved in the experiment[98]: $\rho = 0.83(10)\,\mathrm{m}^{-1}$, $P_{\mathrm{source}} = (1.9 \pm 0.6)\,\%$ and $\eta_{\mathrm{detection}} = (16.9 \pm 1.0)\,\%$. In Figure 9.3 b) the calculations are shown for the achievable parameters resulting in $P_{\mathrm{source}} = (16.4 \pm 2.4)\,\%$, which we inferred from the design of the system according to subsection 5.5.3. In both cases the repeater scheme is superior to the centrally Bell state measurement scheme. Using the repeater, it could be even possible to

[98] We take the numbers from equation (5.67) with $P_{\mathrm{d,eff}} = \underbrace{\eta_{\mathrm{exc}} \cdot P_{\mathrm{c,eff}} \cdot \eta_{\mathrm{ext}} \cdot \epsilon_m}_{P_{\mathrm{source}}} \cdot \eta_{\mathrm{detector}} \cdot \eta_{\mathrm{path+optics}}$. We defined $\eta_{\mathrm{detection}}$ to contain the detector quantum efficiency η_{detector} and the optics in front, such that we have the net effect of the photon path encoded in the quantity η_{path}.

beat the absolute theoretical upper limit of any equivalent point-to-point communication in a high channel loss approximation of $\sim 1.44 \cdot \eta_{\mathrm{path}}(d)$ [137]. For this purpose, a PPL equivalent channel loss of $\sim 110\,\mathrm{dB}$ would be required with the current parameters and a channel loss of $\sim 75\,\mathrm{dB}$ at minimum. For the latter, we expect $R_{\mathrm{qr,nsp}} \approx 10^{-7}$, which at a repetition rate of $1/(3.1\,\mu\mathrm{s})$ would correspond to about 2 entanglement events between the endpoint nodes per minute, which is definitely a detectable rate.

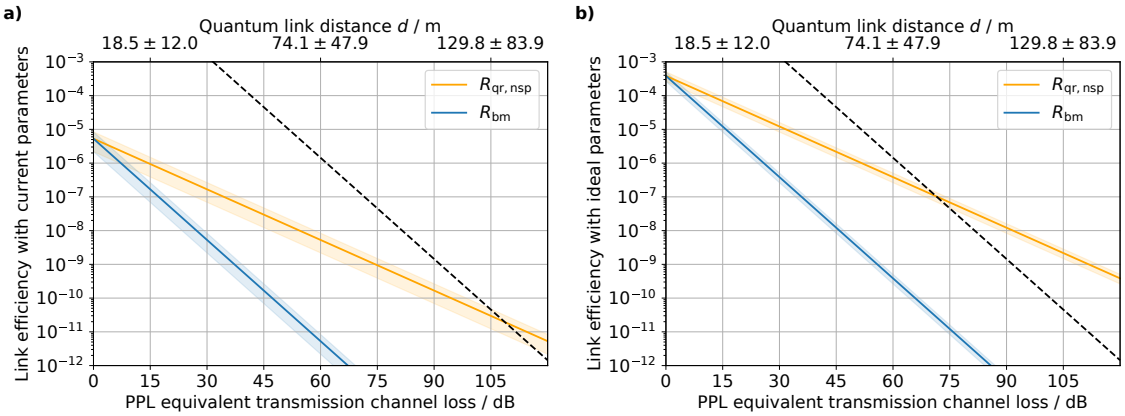

Figure 9.3: Link efficiency vs. PPL-equivalent channel loss $\eta_{\mathrm{path,ppl}}$ and the corresponding link distance d with $\eta_{\mathrm{path,ppl}} \equiv \eta_{\mathrm{path}}(d)$ according to equations (9.1), (9.3) and (9.4) with $\rho = 0.83(10)\,\mathrm{m}^{-1}$ (UV-fibre). **a)** Parameters currently achieved in the experiment. **b)** Achievable parameters inferred from the design of the system according to subsection 5.5.3. The shaded areas depicts the uncertainty of the calculations based on the errors of the included parameters. The dashed black line depicts the upper bound of $-\log_2(1-\eta_{\mathrm{path,ppl}}) \approx 1.44 \cdot \eta_{\mathrm{path,ppl}}$ of 'repeaterless' communication for high losses $\eta_{\mathrm{path,ppl}}$ [137].

10 Appendix

A Standard error on binned photon statistic

The standard error Δp on the relative occurrence $p = k/n$ of a bin containing k out of n events is calculated as $\Delta p = \sqrt{p \cdot (1.0 - p)/n}$ according to the binomial distribution.

B Clebsch-Gordan coefficients of $^{171}Yb^{+}$

As derived in subsection 5.4.1, the coupling strength between to states $|e\rangle$ and $|g\rangle$ is determined by the dipole matrix element $\langle g|\,\hat{\mathbf{d}}\,|e\rangle$. We omitted the explicit calculation of these matrix elements so far, but their relative strengths becomes particular interesting when dealing with a multi level system where the transitions in general differ in coupling strengths. Using the Wigner-Eckart theorem, it is possible to separate the calculation of the dipole matrix element into an angular dependent part and a pure radial term called 'reduced matrix element'[99]. The latter can be measured experimentally from the excited state lifetime, whereas the angular parts gives the relative coupling strength.

We are particularly interested in the $^2S_{1/2} \leftrightarrow {}^2P_{1/2}$ hyperfine transitions of $^{171}Yb^{+}$ since we use this transitions for cooling, atomic state detection and entanglement generation in the experiment (see subsection 6.2.2 and section 7.2). Therefore, we define: $|e\rangle = |F', J', m'_F\rangle$ and $|g\rangle = |F, J, m_F\rangle$.

For calculation of the dipole matrix element, it is useful to write the dipole operator in the spherical basis as [85]

$$\hat{\mathbf{d}} = e\hat{\mathbf{r}} = e\hat{r}\sum_q \sqrt{\frac{4\pi}{2l+1}} Y_q^1 \cdot \hat{e}_q, \tag{10.1}$$

where q labels the component of the spherical basis and Y_m^l are the spherical harmonics. Using the Wigner-Eckart theorem, we derive for a specific component q of the dipole matrix element $\langle g|\,\hat{\mathbf{d}}\,|e\rangle_q$ the expression

$$\begin{aligned}\langle F, J, m_F|\, er_q\,|F', J', m'_F\rangle &= \langle J|\,|e\hat{r}|\,|J'\rangle\,(-1)^{F'+J+1+I}\sqrt{(2F'+1)\,(2J+1)} \\ &\quad\cdot(-1)^{F'-1+m_F}\sqrt{2F+1}\begin{Bmatrix} J & J' & 1 \\ F' & F & I\end{Bmatrix}\begin{pmatrix} F' & 1 & F \\ m'_F & q & -m_F\end{pmatrix} \\ &\equiv \langle J|\,|e\hat{r}|\,|J'\rangle \cdot c_g(F, J, m_F, F'J', m'_F, I, q)\end{aligned} \tag{10.2}$$

according to [156], where the reduced matrix element is denoted with double bars. The Wigner 3-j symbol (round brackets) ensures that $m_F = m'_F + q$ holds. The curly brackets denotes the Wigner- 6-j symbol. The expression c_g represents the so-called Clebsch-Gordan coefficient of the transition. Considering the coupling of a dipole moment to a radiation field with polarisation components $\sigma^{\pm}$ and π, we fully couple to the σ^+ polarisation component in the case of $m'_F = m_F + 1$, for $m'_F = m_F$ we couple to π and for $m'_F = m_F - 1$ we couple to σ^-.

Using equation (10.2), the relative transition strength and phase of $|g\rangle \leftrightarrow |e\rangle$ can be computed for a certain polarisation component of the field. If we consider the coupling of

[99] There exists another convention including a factor of $\sqrt{2J+1}$ into the reduced matrix element. Here, we follow the convention of [156]

an excited state to several decay channels, the phase of the respective channel becomes particularly interesting for the generation of an entangled atom-photon state by spontaneous emission into a superposition of ground states.

The Clebsch-Gordan coefficients c_g of the allowed $^2S_{1/2} \leftrightarrow {}^2P_{1/2}$ hyperfine transitions are shown in Figure 10.1.

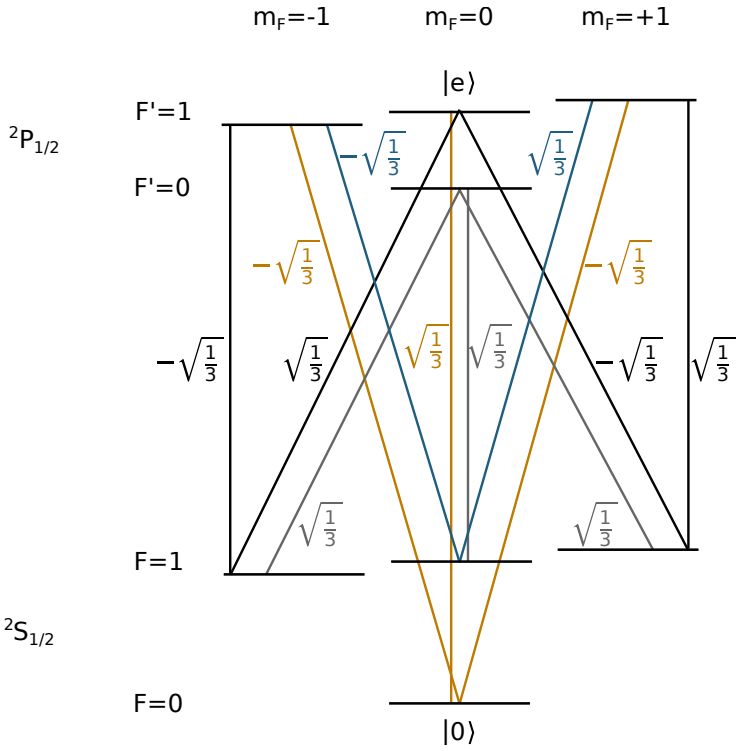

Figure 10.1: Clebsch-Gordan coefficients of the allowed $^2S_{1/2} \leftrightarrow {}^2P_{1/2}$ hyperfine transitions of $^{171}Yb^+$. The coefficients were calculated using equation (10.2) and a nuclear spin of $I = 1/2$.

As an example, the decay of the $|e\rangle = |F' = 1, J' = 1/2, m'_F = 0\rangle$ state into a superposition $|F = 1, J = 1/2, m_F = -1\rangle$ and $|F = 1, J = 1/2, m_F = +1\rangle$ is used for the generation of spin-photon entanglement in this thesis. The decay channels exhibit equal Clebsch-Gordan coefficients but with opposite sign.

C Spatial emission characteristics of a classical dipole

The ability of an atom to emit photons into different polarisation modes is a key element of information encoding in these travelling qubits. We can tailor the resulting entangled state between atom and photon by collecting emitted photons only along a certain axis in space. This is the case, due to the atom exhibiting an angular dependence on its photon emission properties. In the following, we derive the angular dependence of the polarisation modes by describing the atom as a classical electric dipole antenna with dipole moment $\mathbf{d}$.

The time-averaged power radiated per unit solid angle can be computed as [74][100]

$$\frac{dP_\pi}{d\Omega} = \frac{c}{8\pi} k^4 \cdot |\mathbf{n} \times (\mathbf{n} \times \mathbf{d})|^2. \tag{10.3}$$

For a localised charge oscillating along the z-axis, the dipole moment becomes $\mathbf{d} = d_0 \cos(\omega t)\hat{e}_z$. If we assume the electric field of the radiation to be linearly polarised along the oscillation axis, which is also known as π-polarisation, we obtain

$$\frac{dP_\pi}{d\Omega} = \frac{c}{8\pi} k^4 d_0^2 \cdot \sin^2(\theta), \tag{10.4}$$

where $k = \omega/c$ is the wave number of the electromagnetic radiation and θ the angle between the z-axis and the unit vector $\mathbf{n}$ pointing along the observation direction. This result is consistent with the result obtained from a quantum mechanical consideration of spontaneous photon emission in a linear polarisation basis and its detection in equation (7.9). The total average radiated power can be computed as

$$P_\pi = \int \frac{dP_\pi}{d\Omega} d\Omega = \frac{ck^4}{3} \cdot d_0^2. \tag{10.5}$$

We can describe circularly polarised radiation ($\sigma^\pm$) by assuming an electrical dipole moment rotating in the x, y-plane with $d = d_0 (\cos(\omega t)\hat{e}_x + \sin(\omega t)\hat{e}_y)$. The angular distribution of the time-averaged radiated power with a circularly polarised electric field can be computed analogously using equation (10.3) as

$$\frac{dP_\sigma}{d\Omega} = \frac{c}{8\pi} k^4 d_0^2 \cdot \left(1 + \cos^2(\theta)\right). \tag{10.6}$$

The total average power radiation for circular polarisation is

$$P_\sigma = \int \frac{dP_\sigma}{d\Omega} d\Omega = 2 \cdot \frac{ck^4}{3} \cdot d_0^2. \tag{10.7}$$

The factor of 2 in the total radiated power with respect to a linear oscillating dipole results from the phase of $\pi/2$ between the oscillations which makes it equivalent to a description using a superposition of two oscillating dipoles [63].

For further calculations we normalise the average power radiation per unit solid angle to the total average radiated power and transfer the findings to the emission of photons from an atomic decay. Two special cases are particular interesting:

- Perpendicular to the quantization axis ($\theta = 90°$) the emitted field from a π-decay has twice the intensity as for a σ^+ or σ^- decay [161].
- Along the quantisation axis ($\theta = 0°$) the emission of π-polarised light is fully suppressed.

[100] Note that in reference [74] the author makes use of electro statical units. For SI units a factor $1/(4\pi\epsilon_0)$ is missing

D Magnetic field generation

Here, we introduce the generation of a custom magnetic field at the ion's position on a technical level. We present a detailed calibration of the magnetic field in subsection 6.6.1 employing the ion as a sensor. With three pairs of coils we are able to generate a magnetic field at the position of the trapped ion that can point in any spatial direction. The coils have a diameter of about 17 cm and are arranged in pairs with about the same distance of 17 cm. Each pair of coils generates a magnetic field vector at its centre position, which points along the x-, y- or z- direction of the spatial coordinate system. Figure 10.2 shows a 3D CAD model[101] of the setup including the magnetic field generating coils and a definition of the spatial axes.

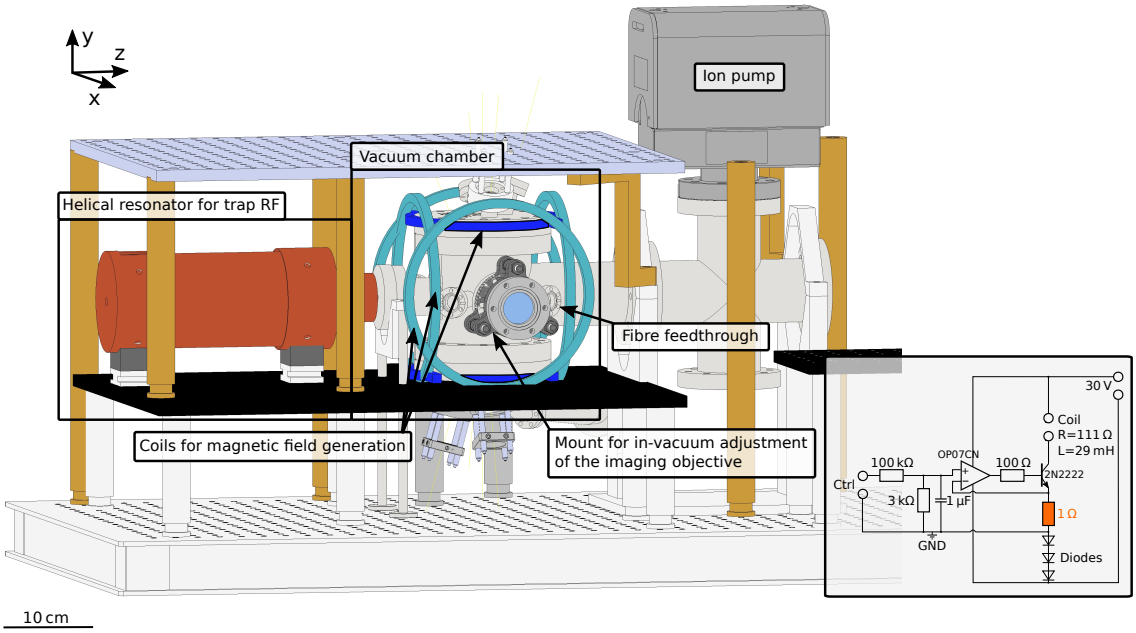

Figure 10.2: 3D CAD model of the vacuum chamber setup showing the magnetic field generation. Not shown are optics, shielding and electronics. Where available, 3D models of the manufacturers were used. The remaining parts were modelled in [115, 157]. Inset: Electric circuit diagram of the current regulator of the z-axis (cavity axis), which is insensitive to load resistance fluctuations and therefore allows to vary the absolute B-field within the experiment. The output current ($\lesssim 250$ mA) is set via a control voltage (Ctrl, 0-10 V).

Since we want to be able to change the magnetic field along the z-axis (cavity and quantisation axis) in the experiment, we have to control the current flow through this pair of coils. This allows to compensate for possible impedance fluctuations when the temperature of the coils changes as the electrical power supply changes. Figure 10.2 shows the control circuit taking a reference voltage as an input, which sets the current flowing through a nominal 1 Ω reference resistance. Instead of the resistance of the coils, this 1 Ω resistor sets the current flowing through the coils. The noise of the current flow is mainly given by the ripple of the applied control voltage. We measure the ripple to be smaller than 0.1 mA in total, which results in $< 10^{-3}$ relative B-field stability.

[101] Generated in Inventor from Autodesk

For the magnetic field generation along the two remaining spatial axes (x, y), we use commercial power supplies[102] with a nominal peak-to-peak ripple of 10 mV in a constant voltage (CV) regulation mode. This transforms to a 0.1 mA current ripple on the magnetic field coils as well ($R \sim 111\,\Omega$). Since the performance of the power supplies in constant current mode is at least by a factor of 5 worse, we use CV mode on this coils. In this mode, the commercial supplies do not react on impedance changes of the coils and a steady state of the coil temperature and consequently the current flow is reached after a few hours, which is fine for a static application of a magnetic field.

Furthermore, we observed a weak magnetisation of the setup on the order of ~ 100 mG for changing magnetic fields. Reliable and repeatable magnetic field values for a given value of coil current can be achieved by slowly ramping the magnetic field to zero before applying the desired current value.

E Experimental setup

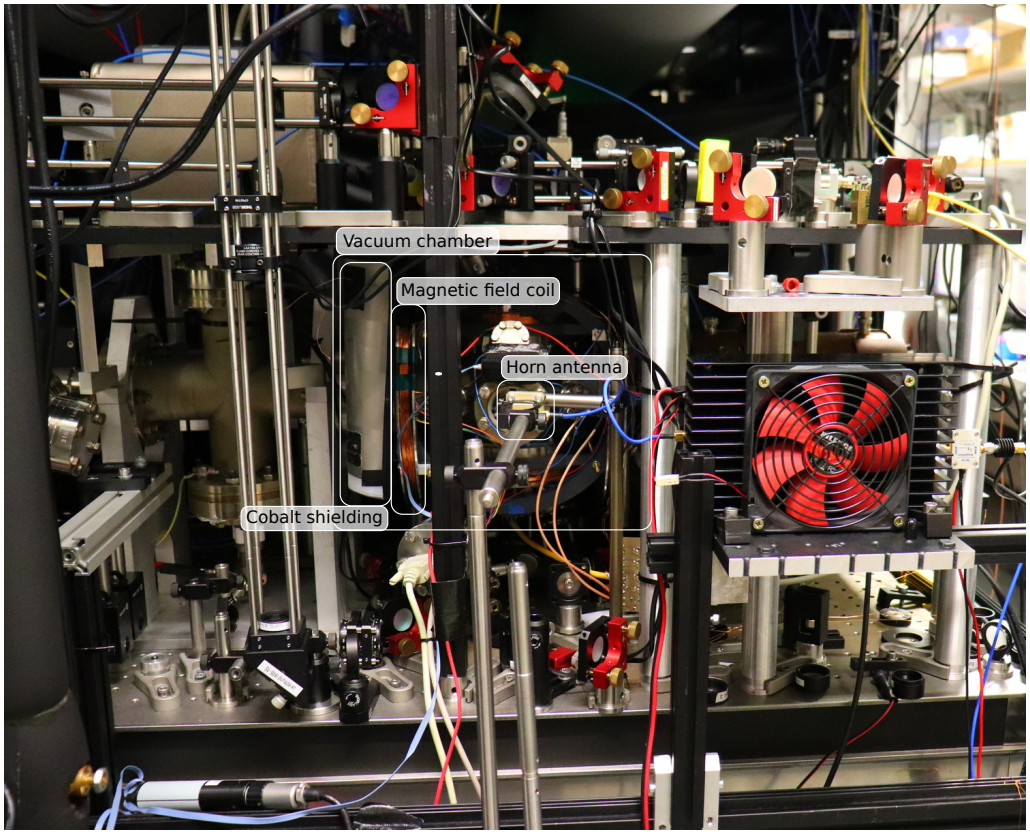

Figure 10.3: Picture of the vacuum chamber setup including optics and parts of the microwave setup.

[102] ES 030-5 and ES 075-2 from Delta Elektronika

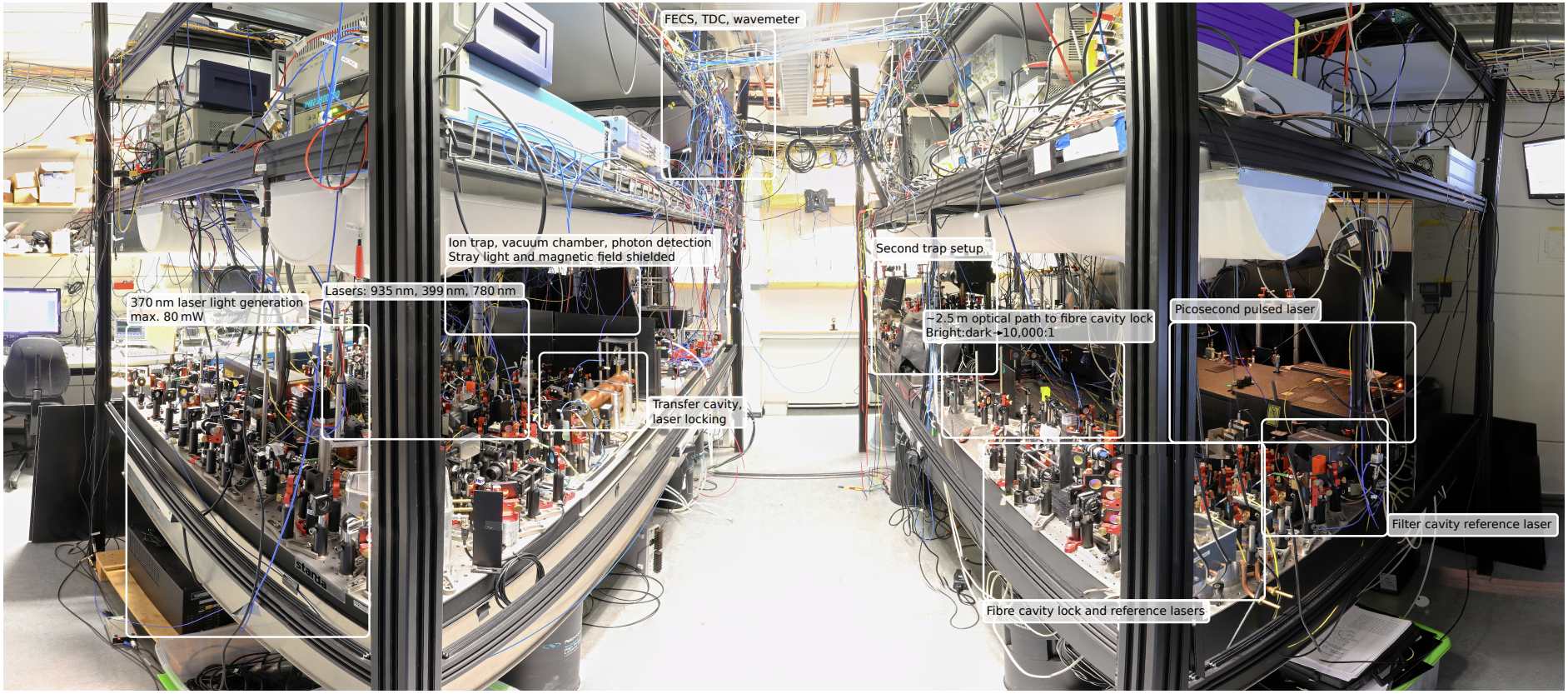

Figure 10.4: Overview of the experimental setup. The panorama is composed of 28 individual photos. There may be errors in the assembly and the complete image should be used as an overview rather than for a detailed study. Created with Hugin.

List of Figures

1.1 Light-matter interface . . . 2
1.2 Quantum network node . . . 3
1.3 Key distribution . . . 4
2.1 Definition and representation of an example qubit state . . . 7
2.2 Rotation of a state $|\Psi\rangle$ to a state $|\Psi'\rangle$ . . . 8
2.3 Choice of bases for a maximum violation of the CHSH inequality . . . 11
3.1 Realisation of a Paul trap with two needle-shaped electrodes . . . 12
3.2 Paul trap configurations . . . 13
3.3 Ion trajectories with and without stray field . . . 15
3.4 Resonances of the $^1S_0 \leftrightarrow {}^1P_1$ transition for neutral Ytterbium . . . 17
3.5 Energy levels of Yb^+ . . . 18
3.6 Sketch of the laser setup . . . 21
3.7 Charging effect of the 399 nm laser . . . 23
3.8 Laser beam paths . . . 24
3.9 Polarisation alignment of the laser beams . . . 25
3.10 Free space imaging of the ion fluorescence . . . 27
3.11 Measurement of the collection efficiency of the imaging system . . . 28
3.12 Block diagram of the experimental control . . . 30
3.13 Post-processing of recorded TDC data . . . 31
4.1 Machine learning for compensation tasks . . . 32
4.2 Micromotion detection . . . 35
4.3 Micromotion compensation . . . 37
4.4 Trace of a single gradient descent optimisation . . . 38
4.5 Hyperplane model introduction . . . 39
4.6 Hyperplane model schematic . . . 40
4.7 Hyperplane model performance . . . 41
4.8 PCA performance . . . 43
4.9 Eigenspace to real space transformation . . . 44
4.10 Sketch of a neural network architecture . . . 46
4.11 Comparison of the performance of the different compensation methods . . . 47
5.1 Sketch and picture of the light-matter interface. . . . 50
5.2 Transverse mode of a resonator . . . 52
5.3 Overview of the cavity-trap setup . . . 53
5.4 Surface profile of the fibre tips . . . 55
5.5 Cavity resonance . . . 55
5.6 Longterm finesse measurement . . . 56
5.7 Alignment of the cavity within the experiment . . . 57
5.8 Cavity length stabilisation setup . . . 59
5.9 Calibration of the atomic reference laser . . . 60
5.10 Calibration of the cavity reference laser . . . 61
5.11 Electrical connection of the fibre cavity . . . 63
5.12 Mechanical resonances of the fibre cavity measured with a lock-in amplifier 64
5.13 Mechanical resonances of the fibre cavity obtained from a FFT . . . 65

5.14 Atom-field interaction . . . 66
5.15 Two-level system coupled to a resonator . . . 70
5.16 Adjustment of the transversal cavity mode to the ion's position . . . 74
5.17 Setup used for the detection of photons leaving the cavity mode . . . 76
5.18 Electronic circuit of photon detection . . . 76
5.19 Temporal profile and time gating of the photons . . . 78
5.20 Characterisation of the polarisation rotation of the photon detection setup . 83
5.21 Basis definition of a polarisation state . . . 85
5.22 Estimated frequency splitting of the cavity polarisation modes . . . 86
6.1 Qubit transition definitions . . . 89
6.2 State initialisation of the atomic qubit . . . 90
6.3 Conceptional sketch of fluorescence state detection . . . 92
6.4 Experimental sequence for a measurement of the excited state population . 93
6.5 Experimental implementation of the single-shot atomic state readout . . . 94
6.6 Steady state approach of the state readout . . . 97
6.7 Measured and simulated contrast of the atomic fluorescence state detection 99
6.8 Numerical calculation the excited state population for a pulsed excitation . 104
6.9 Setup used for synchronisation of the photon detection time stamps . . . 106
6.10 Pulsed laser setup . . . 107
6.11 Linewidth measurement of the pulse filter cavity . . . 109
6.12 Experimental sequence for measuring the excitation probability of a pulse . 110
6.13 Calibration of pulse parameters . . . 111
6.14 Experimental setup for single photon generation and verification . . . 113
6.15 Effects of non-perfect polarisation of the pulsed laser . . . 114
6.16 A driven three-level system . . . 116
6.17 Application of a resonant microwave pulse . . . 119
6.18 Simultaneous driving of two atomic qubit transitions . . . 120
6.19 Coherent state mapping . . . 122
6.20 Mapping of eigenstates of an example basis . . . 123
6.21 Pulse sequence of a coherent state mapping . . . 125
6.22 Generation and application of microwave pulses . . . 127
6.23 Calibration of the microwave pulse parameters . . . 128
6.24 Ramsey-like pulse sequence . . . 129
6.25 Effect of magnetic field noise on the microwave detuning . . . 130
6.26 Coherence time . . . 131
6.27 Calibration of the magnetic field . . . 133
6.28 Active cancellation of magnetic field noise . . . 135
6.29 Reconstruction of the time dependence of the magnetic field noise . . . 137
7.1 Multilevel decay . . . 143
7.2 Emission characteristics of a radiating dipole . . . 144
7.3 Spin-photon entanglement generation . . . 145
7.4 Experimental sequence for the generation of an entangled atom-photon state 147
7.5 Spin-photon correlations in $\hat{\sigma}_z \otimes \hat{\sigma}_z$ basis . . . 150
7.6 Fidelity of state generation . . . 152
7.7 Visualisation of the photon states in a rotated bases . . . 154

7.8 Spin-photon correlations in the rotated bases . . . 155
7.9 Measured density matrix of the entangled state . . . 163
8.1 Experimental sketch QKD protocol . . . 168
8.2 Experimental building blocks of the QKD protocol . . . 169
8.3 Experimental sequence of the QKD protocol . . . 171
8.4 Deriving key bits from the state measurement . . . 172
8.5 Calculated maximum sifted key rate vs. channel loss . . . 173
8.6 Measurement of the transmitted qubits on Bob's side . . . 174
8.7 Generated randomness vs. Bell-violation. . . . 180
9.1 Metal layers on fibre tips . . . 185
9.2 Distant quantum communication . . . 187
9.3 Link efficiencies vs. channel loss . . . 188
10.1 Clebsch-Gordan coefficients of $^2S_{1/2} \leftrightarrow {}^2P_{1/2}$ . . . 190
10.2 Vacuum chamber with magnetic field generation . . . 192
10.3 Picture of the vacuum chamber . . . 193
10.4 Overview of the experimental setup . . . 194

List of Tables

1 Effective experimental parameters calculated from the measurement of the Purcell-enhanced linewidth and the theoretical values calculated from cavity parameters . . . 80
2 Characteristic cavity parameters achieved with previous cavity-based atom-photon entanglements . . . 81
3 Measured conditional probabilities for a single shot bright/dark hyperfine state discrimination at 4.6 G, $I/I_0 \approx 0.25$ and 400 μs readout . . . 95
4 Applied coil current for a compensation of the magnetic offset field . . . 134
5 Comparison of magnetic field noise cancellation methods . . . 139
6 Maximal achievable rates of experimental repetition R_{exp} and entanglement detection $R_{\mathrm{detection}}$ . . . 149
7 Conditional probabilities for a readout in $\hat{\sigma}_z \otimes \hat{\sigma}_z$ basis, corrected for detector dark counts . . . 151
8 Atom-photon state correlations in rotated bases before state mapping . . . 155
9 Conditional probabilities for the fluorescence-based state readout in $-\bar{\hat{\sigma}}_{x,\mathrm{atom}} \otimes \bar{\hat{\sigma}}_{x,\mathrm{photon}}$ basis . . . 156
10 Conditional probabilities for the fluorescence state readout in $\bar{\hat{\sigma}}_{y,\mathrm{atom}} \otimes \bar{\hat{\sigma}}_{y,\mathrm{photon}}$ basis . . . 156
11 Dark count characteristic of the cavity-photon detectors . . . 158
12 Sources of error of the entangled state measurements with associated values of the correlation contrast reduction in % broken down by the measurement bases . . . 165
13 Measurement of the Bell-violation . . . 178

Bibliography

[1] R. Albrecht, A. Bommer, C. Deutsch, J. Reichel, and C. Becher. Coupling of a Single Nitrogen-Vacancy Center in Diamond to a Fiber-Based Microcavity. *Phys. Rev. Lett.*, 110:243602, Jun 2013.

[2] M. Almendros, J. Huwer, N. Piro, F. Rohde, C. Schuck, M. Hennrich, F. Dubin, and J. Eschner. Bandwidth-Tunable Single-Photon Source in an Ion-Trap Quantum Network. *Phys. Rev. Lett.*, 103:213601, Nov 2009.

[3] F. Arute, K. Arya, R. Babbush, D. Bacon, J. C. Bardin, R. Barends, R. Biswas, S. Boixo, F. G. S. L. Brandao, D. A. Buell, B. Burkett, Y. Chen, Z. Chen, B. Chiaro, R. Collins, W. Courtney, A. Dunsworth, E. Farhi, B. Foxen, A. Fowler, C. Gidney, M. Giustina, R. Graff, K. Guerin, S. Habegger, M. P. Harrigan, M. J. Hartmann, A. Ho, M. Hoffmann, T. Huang, T. S. Humble, S. V. Isakov, E. Jeffrey, Z. Jiang, D. Kafri, K. Kechedzhi, J. Kelly, P. V. Klimov, S. Knysh, A. Korotkov, F. Kostritsa, D. Landhuis, M. Lindmark, E. Lucero, D. Lyakh, S. Mandrà, J. R. McClean, M. McEwen, A. Megrant, X. Mi, K. Michielsen, M. Mohseni, J. Mutus, O. Naaman, M. Neeley, C. Neill, M. Y. Niu, E. Ostby, A. Petukhov, J. C. Platt, C. Quintana, E. G. Rieffel, P. Roushan, N. C. Rubin, D. Sank, K. J. Satzinger, V. Smelyanskiy, K. J. Sung, M. D. Trevithick, A. Vainsencher, B. Villalonga, T. White, Z. J. Yao, P. Yeh, A. Zalcman, H. Neven, and J. M. Martinis. Quantum supremacy using a programmable superconducting processor. *Nature*, 574(7779):505–510, Oct 2019.

[4] A. Aspect, P. Grangier, and G. Roger. Experimental tests of realistic local theories via Bell's theorem. *Phys. Rev. Lett.*, 47(7):460, 1981.

[5] B. Rijsman. Cascade-Python. https://cascade-python.readthedocs.io/. Accessed: 14 Feb 2021.

[6] T. G. Ballance. *A fibre-cavity based ion interface for ultraviolet photons*. PhD thesis, Magdalene College, University of Cambridge, 2016.

[7] T. G. Ballance, H. M. Meyer, P. Kobel, K. Ott, J. Reichel, and M. Köhl. Cavity-induced backaction in Purcell-enhanced photon emission of a single ion in an ultraviolet fiber cavity. *Phys. Rev. A*, 95:033812, Mar 2017.

[8] C. Balzer, A. Braun, T. Hannemann, C. Paape, M. Ettler, W. Neuhauser, and C. Wunderlich. Electrodynamically trapped Yb^+ ions for quantum information processing. *Phys. Rev. A*, 73:041407, Apr 2006.

[9] S. M. Barnett. *Quantum information*. Oxford University Press, 2009.

[10] H. G. Barros, A. Stute, T. E. Northup, C. Russo, P. O. Schmidt, and R. Blatt. Deterministic single-photon source from a single ion. *New Journal of Physics*, 11(10):103004, Oct 2009.

[11] J. S. Bell. *Speakable and Unspeakable in Quantum Mechanics: Collected Papers on Quantum Philosophy*. Cambridge University Press, 2004.

[12] C. H. Bennett. Quantum cryptography using any two nonorthogonal states. *Phys. Rev. Lett.*, 68:3121–3124, May 1992.

[13] C. H. Bennett, F. Bessette, G. Brassard, L. Salvail, and J. Smolin. Experimental quantum cryptography. *Journal of cryptology*, 5(1):3–28, 1992.

[14] C. H. Bennett and G. Brassard. In Proc. IEEE International Conference on Computers, Systems and Signal Processing, Bangalore, India . *IEEE Press, New York*, pages 175–179, 1984.

[15] C. H. Bennett, G. Brassard, and N. D. Mermin. Quantum cryptography without Bell's theorem. *Phys. Rev. Lett.*, 68:557–559, Feb 1992.

[16] C. H. Bennett, G. Brassard, and J.-M. Robert. Privacy amplification by public discussion. *SIAM Journal on Computing*, 17(2):210–229, 1988.

[17] R. W. Berends, E. H. Pinnington, B. Guo, and Q. Ji. Beam-laser lifetime measurements for four resonance levels of Yb II. *Journal of Physics B: Atomic, Molecular and Optical Physics*, 26(20):L701–L704, Oct 1993.

[18] D. J. Berkeland and M. G. Boshier. Destabilization of dark states and optical spectroscopy in Zeeman-degenerate atomic systems. *Phys. Rev. A*, 65:033413, Feb 2002.

[19] D. J. Berkeland, J. D. Miller, J. C. Bergquist, W. M. Itano, and D. J. Wineland. Minimization of ion micromotion in a Paul trap. *Journal of Applied Physics*, 83(10):5025–5033, 1998.

[20] R. A. Berner. Automatisierte dopplerfreie Ytterbium-Spektroskopie und Bau einer doppelresonanten 12,6 GHz Filtercavity für ein bestehendes Ramanlaser-Setup. Bachelor's thesis. University of Bonn, 2018.

[21] M. K. Bhaskar, R. Riedinger, B. Machielse, D. S. Levonian, C. T. Nguyen, E. N. Knall, H. Park, D. Englund, M. Lončar, D. D. Sukachev, and M. D. Lukin. Experimental demonstration of memory-enhanced quantum communication. *Nature*, 580(7801):60–64, Apr 2020.

[22] R. Blatt and D. Wineland. Entangled states of trapped atomic ions. *Nature*, 453(7198):1008–1015, Jun 2008.

[23] B. B. Blinov, D. L. Moehring, L.-M. Duan, and C. Monroe. Observation of entanglement between a single trapped atom and a single photon. *Nature*, 428(6979):153–157, 2004.

[24] M. Bock, P. Eich, S. Kucera, M. Kreis, A. Lenhard, C. Becher, and J. Eschner. High-fidelity entanglement between a trapped ion and a telecom photon via quantum frequency conversion. *Nature Communications*, 9(1):1998, 2018.

[25] M. Bock, P. Eich, S. Kucera, M. Kreis, A. Lenhard, C. Becher, and J. Eschner. High-fidelity entanglement between a trapped ion and a telecom photon via quantum frequency conversion, Supplementary information. *Nature Communications*, 9(1):1998, 2018.

[26] X. Bonnetain, M. Naya-Plasencia, and A. Schrottenloher. Quantum Security Analysis of AES. *IACR Transactions on Symmetric Cryptology*, 2019(2):55–93, Jun 2019.

[27] A. D. Boozer, A. Boca, R. Miller, T. E. Northup, and H. J. Kimble. Reversible State Transfer between Light and a Single Trapped Atom. *Phys. Rev. Lett.*, 98:193601, May 2007.

[28] B. Brandstätter, A. McClung, K. Schüppert, B. Casabone, K. Friebe, A. Stute, P. O. Schmidt, C. Deutsch, J. Reichel, R. Blatt, and T. E. Northup. Integrated fiber-mirror ion trap for strong ion-cavity coupling. *Review of Scientific Instruments*, 84(12):123104, 2013.

[29] M. Breyer. A UV fibre cavity for quantum information applications with trapped single ions. Master's thesis, Rheinische Friedrich-Wilhelms-Universität Bonn, Nov 2017.

[30] R. H. Brown and R. Q. Twiss. Correlation between Photons in two Coherent Beams of Light. *Nature*, 177(4497):27–29, Jan 1956.

[31] F. Bussières, C. Clausen, A. Tiranov, B. Korzh, V. B. Verma, S. W. Nam, F. Marsili, A. Ferrier, P. Goldner, H. Herrmann, C. Silberhorn, W. Sohler, M. Afzelius, and N. Gisin. Quantum teleportation from a telecom-wavelength photon to a solid-state quantum memory. *Nature Photonics*, 8(10):775–778, 2014.

[32] G. Carleo, I. Cirac, K. Cranmer, L. Daudet, M. Schuld, N. Tishby, L. Vogt-Maranto, and L. Zdeborová. Machine learning and the physical sciences. *Rev. Mod. Phys.*, 91:045002, Dec 2019.

[33] J. F. Clauser, M. A. Horne, A. Shimony, and R. A. Holt. Proposed Experiment to Test Local Hidden-Variable Theories. *Phys. Rev. Lett.*, 23:880–884, Oct 1969.

[34] Coherent. *The Coherent Mira Optima 900-P Laser, Operator's Manual.*

[35] R. Colbeck. *Quantum and Relativistic Protocols for Secure Multi-Party Computation.* PhD thesis, University of Cambridge, 2007.

[36] Y. Colombe, T. Steinmetz, G. Dubois, F. Linke, D. Hunger, and J. Reichel. Strong atom-field coupling for Bose-Einstein condensates in an optical cavity on a chip. *Nature*, 450(7167):272–276, 2007.

[37] C. Crocker, M. Lichtman, K. Sosnova, A. Carter, S. Scarano, and C. Monroe. High purity single photons entangled with an atomic qubit. *Opt. Express*, 27(20):28143–28149, Sep 2019.

[38] M. Curty, F. Xu, W. Cui, C. C. W. Lim, K. Tamaki, and H.-K. Lo. Finite-key analysis for measurement-device-independent quantum key distribution. *Nature Communications*, 5(1):1–7, 2014.

[39] S. Daiss, S. Langenfeld, S. Welte, E. Distante, P. Thomas, L. Hartung, O. Morin, and G. Rempe. A quantum-logic gate between distant quantum-network modules. *Science*, 371(6529):614–617, 2021.

[40] K. De Greve, L. Yu, P. L. McMahon, J. S. Pelc, C. M. Natarajan, N. Y. Kim, E. Abe, S. Maier, C. Schneider, M. Kamp, S. Höfling, R. H. Hadfield, A. Forchel, M. M. Fejer, and Y. Yamamoto. Quantum-dot spin-photon entanglement via frequency downconversion to telecom wavelength. *Nature*, 491(7424):421–425, 2012.

[41] A. de Touzalin (European Commission), C. Marcus (University of Copenhagen), F. Heijman (NL ministry for economic affairs), I. Cirac (Max-Planck Institute for Quantum Optics), R. Murray (Innovate UK), and T. Calarco (IQST Centre, Ulm). Quantum Manifesto. May 2016.

[42] C. L. Degen, F. Reinhard, and P. Cappellaro. Quantum sensing. *Rev. Mod. Phys.*, 89:035002, Jul 2017.

[43] R. W. P. Drever, J. L. Hall, F. V. Kowalski, J. Hough, G. M. Ford, A. J. Munley, and H. Ward. Laser phase and frequency stabilization using an optical resonator. *Applied Physics B*, 31(2):97–105, Jun 1983.

[44] D. Eastlake, J. Schiller, and S. Crocker. Randomness requirements for security. *RFC4086*, 2005.

[45] A. Einstein, B. Podolsky, and N. Rosen. Can Quantum-Mechanical Description of Physical Reality Be Considered Complete? *Phys. Rev.*, 47:777–780, May 1935.

[46] S. Ejtemaee, R. Thomas, and P. C. Haljan. Optimization of Yb^+ fluorescence and hyperfine-qubit detection. *Phys. Rev. A*, 82:063419, Dec 2010.

[47] A. K. Ekert. Quantum cryptography based on Bell's theorem. *Phys. Rev. Lett.*, 67:661–663, Aug 1991.

[48] D. Elkouss, A. Leverrier, R. Alleaume, and J. J. Boutros. Efficient reconciliation protocol for discrete-variable quantum key distribution. In *2009 IEEE International Symposium on Information Theory*, pages 1879–1883, 2009.

[49] C. Erven, C. Couteau, R. Laflamme, and G. Weihs. Entangled quantum key distribution over two free-space optical links. *Opt. Express*, 16(21):16840–16853, Oct 2008.

[50] P. Farrera, G. Heinze, and H. de Riedmatten. Entanglement between a Photonic Time-Bin Qubit and a Collective Atomic Spin Excitation. *Phys. Rev. Lett.*, 120:100501, Mar 2018.

[51] A. Fine. Hidden Variables, Joint Probability, and the Bell Inequalities. *Phys. Rev. Lett.*, 48:291–295, Feb 1982.

[52] C. J. Foot. *Atomic Physics*. Oxford University Press, 2005.

[53] M. Fox. *Quantum optics: an introduction*, volume 15. OUP Oxford, 2006.

[54] J. Gallego, W. Alt, T. Macha, M. Martinez-Dorantes, D. Pandey, and D. Meschede. Strong Purcell Effect on a Neutral Atom Trapped in an Open Fiber Cavity. *Phys. Rev. Lett.*, 121:173603, Oct 2018.

[55] D. Gangloff, M. Shi, T. Wu, A. Bylinskii, B. Braverman, M. Gutierrez, R. Nichols, J. Li, K. Aichholz, M. Cetina, L. Karpa, B. Jelenković, I. Chuang, and V. Vuletić. Preventing and reversing vacuum-induced optical losses in high-finesse tantalum (V) oxide mirror coatings. *Opt. Express*, 23(14):18014–18028, Jul 2015.

[56] W. B. Gao, P. Fallahi, E. Togan, J. Miguel-Sanchez, and A. Imamoglu. Observation of entanglement between a quantum dot spin and a single photon. *Nature*, 491(7424):426–430, 2012.

[57] S. Garcia, F. Ferri, K. Ott, J. Reichel, and R. Long. Dual-wavelength fiber Fabry-Perot cavities with engineered birefringence. *Opt. Express*, 26(17):22249–22263, Aug 2018.

[58] S. Gerber, D. Rotter, M. Hennrich, R. Blatt, F. Rohde, C. Schuck, M. Almendros, R. Gehr, F. Dubin, and J. Eschner. Quantum interference from remotely trapped ions. *New Journal of Physics*, 11(1):013032, Jan 2009.

[59] N. Gisin, G. Ribordy, W. Tittel, and H. Zbinden. Quantum cryptography. *Rev. Mod. Phys.*, 74:145–195, Mar 2002.

[60] T. F. Gloger, P. Kaufmann, D. Kaufmann, M. T. Baig, T. Collath, M. Johanning, and C. Wunderlich. Ion-trajectory analysis for micromotion minimization and the measurement of small forces. *Phys. Rev. A*, 92:043421, Oct 2015.

[61] X. Glorot, A. Bordes, and Y. Bengio. Deep Sparse Rectifier Neural Networks. In G. Gordon, D. Dunson, and M. Dudík, editors, *Proceedings of the Fourteenth International Conference on Artificial Intelligence and Statistics*, volume 15 of *Proceedings of Machine Learning Research*, pages 315–323, Fort Lauderdale, FL, USA, Apr 2011. PMLR.

[62] C. Gobby, Z. L. Yuan, and A. J. Shields. Quantum key distribution over 122 km of standard telecom fiber. *Applied Physics Letters*, 84(19):3762–3764, 2004.

[63] D. J. Griffiths. *Introduction to Electrodynamics*. Cambridge University Press, 4 edition, 2017.

[64] G. R. Guthöhrlein, M. Keller, K. Hayasaka, W. Lange, and H. Walther. A single ion as a nanoscopic probe of an optical field. *Nature*, 414(6859):49–51, Nov 2001.

[65] M. Harlander, M. Brownnutt, W. Hänsel, and R. Blatt. Trapped-ion probing of light-induced charging effects on dielectrics. *New Journal of Physics*, 12(9):093035, Sep 2010.

[66] B. Hensen, H. Bernien, A. E. Dréau, A. Reiserer, N. Kalb, M. S. Blok, J. Ruitenberg, R. F. L. Vermeulen, R. N. Schouten, C. Abellán, W. Amaya, V. Pruneri, M. W. Mitchell, M. Markham, D. J. Twitchen, D. Elkouss, S. Wehner, T. H. Taminiau, and R. Hanson. Loophole-free Bell inequality violation using electron spins separated by 1.3 kilometres. *Nature*, 526(7575):682–686, Oct 2015.

[67] H. Hotelling. Relations Between Two Sets of Variates. *Biometrika*, 28(3/4):321–377, 1936.

[68] P. C. Humphreys, N. Kalb, J. P. J. Morits, R. N. Schouten, R. F. L. Vermeulen, D. J. Twitchen, M. Markham, and R. Hanson. Deterministic delivery of remote entanglement on a quantum network. *Nature*, 558(7709):268–273, Jun 2018.

[69] D. Hunger, T. Steinmetz, Y. Colombe, C. Deutsch, T. W. Hänsch, and J. Reichel. A fiber Fabry–Pérot cavity with high finesse. *New Journal of Physics*, 12(6):065038, Jun 2010.

[70] Y. Ibaraki, U. Tanaka, and S. Urabe. Detection of parametric resonance of trapped ions for micromotion compensation. *Appl. Phys. B*, 105:219–233, 2011.

[71] IBM and qiskit community. Single Qubit Gates. https://qiskit.org/textbook/ch-states/single-qubit-gates.html. Accessed: 01 Mar 2020.

[72] R. Ikuta, T. Kobayashi, T. Kawakami, S. Miki, M. Yabuno, T. Yamashita, H. Terai, M. Koashi, T. Mukai, T. Yamamoto, and N. Imoto. Polarization insensitive frequency conversion for an atom-photon entanglement distribution via a telecom network. *Nature Communications*, 9(1):1997, 2018.

[73] R. Islam, E. E. Edwards, K. Kim, S. Korenblit, C. Noh, H. Carmichael, G.-D. Lin, L.-M. Duan, C.-C. Joseph Wang, J. K. Freericks, and C. Monroe. Onset of a quantum phase transition with a trapped ion quantum simulator. *Nature Communications*, 2(1):377, Jul 2011.

[74] J. D. Jackson. *Classical Electrodynamics*. John Wiley and Sons, Inc., 1962.

[75] D. F. V. James, P. G. Kwiat, W. J. Munro, and A. G. White. Measurement of qubits. *Phys. Rev. A*, 64:052312, Oct 2001.

[76] Y.-Y. Jau, H. Partner, P. D. D. Schwindt, J. D. Prestage, J. R. Kellogg, and N. Yu. Low-power, miniature ^{171}Yb ion clock using an ultra-small vacuum package. *Applied Physics Letters*, 101(25):253518, 2012.

[77] R. Jozsa and N. Linden. On the role of entanglement in quantum-computational speed-up. *Proceedings of the Royal Society of London. Series A: Mathematical, Physical and Engineering Sciences*, 459(2036):2011–2032, 2003.

[78] E. Kassa, H. Takahashi, C. Christoforou, and M. Keller. Precise positioning of an ion in an integrated Paul trap-cavity system using radiofrequency signals. *Journal of Modern Optics*, 65(5-6):520–528, 2018.

[79] S. Kasture, F. Lenzini, B. Haylock, A. Boes, A. Mitchell, E. W. Streed, and M. Lobino. Frequency conversion between UV and telecom wavelengths in a lithium niobate waveguide for quantum communication with Yb^+ trapped ions. *Journal of Optics*, 18(10):104007, Sep 2016.

[80] A. Kell. Frequenzverdopplung eines gepulsten Lasers. Bachelor's thesis. University of Bonn, 2014.

[81] J. Keller, H. L. Partner, T. Burgermeister, and T. E. Mehlstäubler. Precise determination of micromotion for trapped-ion optical clocks. *Journal of Applied Physics*, 118(10):104501, 2015.

[82] M. Keller, B. Lange, K. Hayasaka, W. Lange, and H. Walther. Continuous generation of single photons with controlled waveform in an ion-trap cavity system. *Nature*, 431(7012):1075–1078, Oct 2004.

[83] E. O. Kiktenko, A. S. Trushechkin, C. C. W. Lim, Y. V. Kurochkin, and A. K. Fedorov. Symmetric Blind Information Reconciliation for Quantum Key Distribution. *Phys. Rev. Applied*, 8:044017, Oct 2017.

[84] H. J. Kimble. The quantum internet. *Nature*, 453:1023–1030, 2008.

[85] B. E. King. Angular Momentum Coupling and Rabi Frequencies for Simple Atomic Transitions, 2008. arXiv:0804.4528.

[86] D. P. Kingma and J. Ba. Adam: A Method for Stochastic Optimization, 2014. arXiv:1412.6980.

[87] N. Kjaergaard, L. Hornekaer, A. M. Thommesen, Z. Videsen, and M. Drewsen. Isotope selective loading of an ion trap using resonance-enhanced two-photon ionization. *Applied Physics B*, 71(2):207–210, Aug 2000.

[88] E. Knill, R. Laflamme, and G. J. Milburn. A scheme for efficient quantum computation with linear optics. *Nature*, 409(6816):46–52, Jan 2001.

[89] M. Koashi and J. Preskill. Secure Quantum Key Distribution with an Uncharacterized Source. *Phys. Rev. Lett.*, 90:057902, Feb 2003.

[90] P. Kobel. A UV Fiber-Cavity as an Interface for trapped Ytterbium-Ions. Master's thesis, Rheinische Friedrich-Wilhelms-Universität Bonn, Dec 2016.

[91] P. Kobel, R. A. Berner, and M. Köhl. Secure distribution of a certified random quantum key using an entangled memory qubit, 2021. arXiv:2111.14523.

[92] P. Kobel, M. Breyer, and M. Köhl. Deterministic spin-photon entanglement from a trapped ion in a fiber Fabry–Perot cavity. *npj Quantum Information*, 7(1):6, Jan 2021.

[93] P. Kobel, M. Link, and M. Köhl. Exponentially improved detection and correction of errors in experimental systems using neural networks, 2020. arXiv:2005.09119.

[94] H. Kogelnik and T. Li. Laser Beams and Resonators. *Appl. Opt.*, 5(10):1550–1567, Oct 1966.

[95] R. König, R. Renner, and C. Schaffner. The Operational Meaning of Min- and Max-Entropy. *IEEE Transactions on Information Theory*, 55(9):4337–4347, 2009.

[96] A. Kramida, Yu. Ralchenko, and J. R. and NIST ASD Team. NIST Atomic Spectra Database (ver. 5.8). Available: `https://physics.nist.gov/asd`. Accessed: 9 Jan 2021. National Institute of Standards and Technology, Gaithersburg, MD., 2020.

[97] F. Krausz, M. E. Fermann, T. Brabec, P. F. Curley, M. Hofer, M. H. Ober, C. Spielmann, E. Wintner, and A. J. Schmidt. Femtosecond solid-state lasers. *IEEE Journal of Quantum Electronics*, 28(10):2097–2122, 1992.

[98] P. T. Kristensen, C. V. Vlack, and S. Hughes. Generalized effective mode volume for leaky optical cavities. *Opt. Lett.*, 37(10):1649–1651, May 2012.

[99] V. Krutyanskiy, M. Meraner, J. Schupp, V. Krcmarsky, H. Hainzer, and B. P. Lanyon. Light-matter entanglement over 50 km of optical fibre. *npj Quantum Information*, 5(1):72, 2019.

[100] P. G. Kwiat, K. Mattle, H. Weinfurter, A. Zeilinger, A. V. Sergienko, and Y. Shih. New High-Intensity Source of Polarization-Entangled Photon Pairs. *Phys. Rev. Lett.*, 75:4337–4341, Dec 1995.

[101] C. Langer, R. Ozeri, J. D. Jost, J. Chiaverini, B. DeMarco, A. Ben-Kish, R. B. Blakestad, J. Britton, D. B. Hume, W. M. Itano, D. Leibfried, R. Reichle, T. Rosenband, T. Schaetz, P. O. Schmidt, and D. J. Wineland. Long-Lived Qubit Memory Using Atomic Ions. *Phys. Rev. Lett.*, 95:060502, Aug 2005.

[102] D. Leibfried, R. Blatt, C. Monroe, and D. Wineland. Quantum dynamics of single trapped ions. *Rev. Mod. Phys.*, 75:281–324, Mar 2003.

[103] H.-W. Li, S. Wang, J.-Z. Huang, W. Chen, Z.-Q. Yin, F.-Y. Li, Z. Zhou, D. Liu, Y. Zhang, G.-C. Guo, W.-S. Bao, and Z.-F. Han. Attacking a practical quantum-key-distribution system with wavelength-dependent beam-splitter and multiwavelength sources. *Phys. Rev. A*, 84:062308, Dec 2011.

[104] M. Link. A simplified laser system for trapping and cooling Ytterbium (+) ions. Master's thesis, Rheinische Friedrich-Wilhelms-Universität Bonn, Aug 2015.

[105] H.-K. Lo, X. Ma, and K. Chen. Decoy State Quantum Key Distribution. *Phys. Rev. Lett.*, 94:230504, Jun 2005.

[106] L. Lydersen, C. Wiechers, C. Wittmann, D. Elser, J. Skaar, and V. Makarov. Hacking commercial quantum cryptography systems by tailored bright illumination. *Nature Photonics*, 4(10):686–689, Oct 2010.

[107] V. Makarov, A. Anisimov, and J. Skaar. Effects of detector efficiency mismatch on security of quantum cryptosystems. *Phys. Rev. A*, 74:022313, Aug 2006.

[108] C. Marand and P. D. Townsend. Quantum key distribution over distances as long as 30 km. *Opt. Lett.*, 20(16):1695–1697, Aug 1995.

[109] I. Marcikic, A. Lamas-Linares, and C. Kurtsiefer. Free-space quantum key distribution with entangled photons. *Applied Physics Letters*, 89(10):101122, 2006.

[110] L. Masanes, S. Pironio, and A. Acín. Secure device-independent quantum key distribution with causally independent measurement devices. *Nature Communications*, 2(1):238, Mar 2011.

[111] C. Maurer, C. Becher, C. Russo, J. Eschner, and R. Blatt. A single-photon source based on a single Ca^+ ion. *New Journal of Physics*, 6:94–94, Jul 2004.

[112] S. Mavadia, V. Frey, J. Sastrawan, S. Dona, and M. J. Biercuk. Prediction and real-time compensation of qubit decoherence via machine learning. *Nature Communications*, 8(1):14106, 2017.

[113] W. S. McCulloch and W. Pitts. A logical calculus of the ideas immanent in nervous activity. *The bulletin of mathematical biophysics*, 5(4):115–133, Dec 1943.

[114] J. J. McLoughlin, A. H. Nizamani, J. D. Siverns, R. C. Sterling, M. D. Hughes, B. Lekitsch, B. Stein, S. Weidt, and W. K. Hensinger. Versatile ytterbium ion trap experiment for operation of scalable ion-trap chips with motional heating and transition-frequency measurements. *Phys. Rev. A*, 83:013406, Jan 2011.

[115] H.-M. Meyer. *A fibre-cavity based photonic interface for a single ion.* PhD thesis, University of Cambridge, Mar 2014.

[116] H. M. Meyer, M. Breyer, and M. Köhl. Monolayer graphene as dissipative membrane in an optical resonator. *Applied Physics B*, 122(12):290, Nov 2016.

[117] H. M. Meyer, R. Stockill, M. Steiner, C. Le Gall, C. Matthiesen, E. Clarke, A. Ludwig, J. Reichel, M. Atatüre, and M. Köhl. Direct Photonic Coupling of a Semiconductor Quantum Dot and a Trapped Ion. *Phys. Rev. Lett.*, 114:123001, Mar 2015.

[118] A. Migdall, S. V. Polyakov, J. Fan, and J. C. Bienfang. *Experimental Methods in the Physical Sciences, Volume 45, Single-photon generation and detection: physics and applications.* Academic Press, 2013.

[119] V. Milner and Y. Prior. Multilevel Dark States: Coherent Population Trapping with Elliptically Polarized Incoherent Light. *Phys. Rev. Lett.*, 80:940–943, Feb 1998.

[120] D. L. Moehring, M. J. Madsen, B. B. Blinov, and C. Monroe. Experimental Bell inequality violation with an atom and a photon. *Phys. Rev. Lett.*, 93(9):090410, 2004.

[121] D. L. Moehring, P. Maunz, S. Olmschenk, K. C. Younge, D. N. Matsukevich, L.-M. Duan, and C. Monroe. Entanglement of single-atom quantum bits at a distance. *Nature*, 449(7158):68–71, Sep 2007.

[122] A. Muller, E. B. Flagg, M. Metcalfe, J. Lawall, and G. S. Solomon. Coupling an epitaxial quantum dot to a fiber-based external-mirror microcavity. *Applied Physics Letters*, 95(17):173101, 2009.

[123] W. Neuhauser, M. Hohenstatt, P. E. Toschek, and H. Dehmelt. Localized visible Ba^+ mono-ion oscillator. *Phys. Rev. A*, 22:1137–1140, Sep 1980.

[124] C. T. Nguyen, D. D. Sukachev, M. K. Bhaskar, B. Machielse, D. S. Levonian, E. N. Knall, P. Stroganov, R. Riedinger, H. Park, M. Lončar, and M. D. Lukin. Quantum

Network Nodes Based on Diamond Qubits with an Efficient Nanophotonic Interface. *Phys. Rev. Lett.*, 123:183602, Oct 2019.

[125] NobelPrize.org. Nobel Media AB 2021. Wolfgang Paul – Facts. https://www.nobelprize.org/prizes/physics/1989/paul/facts/. Accessed: 27 Jan 2021.

[126] J. Nocedal and S. Wright. *Numerical Optimization*. Second Edition. Springer Science & Business Media, 2006.

[127] T. E. Northup and R. Blatt. Quantum information transfer using photons. *Nature Photonics*, 8(5):356–363, 2014.

[128] S. Olmschenk, D. Hayes, D. N. Matsukevich, P. Maunz, D. L. Moehring, K. C. Younge, and C. Monroe. Measurement of the lifetime of the $6p\ ^2P^o_{1/2}$ level of Yb^+. *Phys. Rev. A*, 80:022502, Aug 2009.

[129] S. Olmschenk, K. C. Younge, D. L. Moehring, D. N. Matsukevich, P. Maunz, and C. Monroe. Manipulation and detection of a trapped Yb^+ hyperfine qubit. *Phys. Rev. A*, 76:052314, Nov 2007.

[130] Y. Onoda, K. Sugiyama, M. Ikeda, and M. Kitano. Loading rate of Yb^+ loaded through photoionization in radiofrequency ion trap. *Applied Physics B*, 105(4):729–740, Dec 2011.

[131] K. Ott, S. Garcia, R. Kohlhaas, K. Schüppert, and P. Rosenbusch. Millimeter-long fiber Fabry-Perot cavities. *Optics Express, Optical Society of America*, 24 (9):pp.9839–9853, 2016.

[132] W. Paul. Electromagnetic traps for charged and neutral particles. *Rev. Mod. Phys.*, 62:531–540, Jul 1990.

[133] K. Pearson. LIII. On lines and planes of closest fit to systems of points in space. *The London, Edinburgh, and Dublin Philosophical Magazine and Journal of Science*, 2(11):559–572, 1901.

[134] M. P. Peloso, I. Gerhardt, C. Ho, A. Lamas-Linares, and C. Kurtsiefer. Daylight operation of a free space, entanglement-based quantum key distribution system. *New Journal of Physics*, 11(4):045007, Apr 2009.

[135] Z. Peng-Yi, X. Zhuan-Xian, L. Jie, H. Ling-Xiang, and B. Lu. Magneto-Optical Trapping of Ytterbium Atoms with a 398.9 nm Laser. *Chinese Physics Letters*, 25:3631, Oct 2008.

[136] S. Pirandola, B. R. Bardhan, T. Gehring, C. Weedbrook, and S. Lloyd. Advances in photonic quantum sensing. *Nature Photonics*, 12(12):724–733, Dec 2018.

[137] S. Pirandola, R. Laurenza, C. Ottaviani, and L. Banchi. Fundamental limits of repeaterless quantum communications. *Nature Communications*, 8(1):15043, Apr 2017.

[138] S. Pironio, A. Acín, S. Massar, A. B. de la Giroday, D. N. Matsukevich, P. Maunz, S. Olmschenk, D. Hayes, L. Luo, T. A. Manning, and C. Monroe. Random numbers certified by Bell's theorem. *Nature*, 464(7291):1021–1024, Apr 2010.

[139] S. Pironio and S. Massar. Security of practical private randomness generation. *Phys. Rev. A*, 87:012336, Jan 2013.

[140] A. Poppe, A. Fedrizzi, R. Ursin, H. R. Böhm, T. Lorünser, O. Maurhardt, M. Peev, M. Suda, C. Kurtsiefer, H. Weinfurter, T. Jennewein, and A. Zeilinger. Practical quantum key distribution with polarization entangled photons. *Opt. Express*, 12(16):3865–3871, Aug 2004.

[141] A. Reiserer, N. Kalb, G. Rempe, and S. Ritter. A quantum gate between a flying optical photon and a single trapped atom. *Nature*, 508(7495):237–240, Apr 2014.

[142] K. F. Renk. *Basics of Laser Physics*. Second Edition. Springer Verlag, 2017.

[143] S. Ritter, C. Nölleke, C. Hahn, A. Reiserer, A. Neuzner, M. Uphoff, M. Mücke, E. Figueroa, J. Bochmann, and G. Rempe. An elementary quantum network of single atoms in optical cavities. *Nature*, 484(7393):195–200, 2012.

[144] R. L. Rivest, A. Shamir, and L. Adleman. A method for obtaining digital signatures and public-key cryptosystems. *Communications of the ACM*, 21(2):120–126, 1978.

[145] C. Robens, S. Brakhane, W. Alt, F. Kleißler, D. Meschede, G. Moon, G. Ramola, and A. Alberti. High numerical aperture (NA=0.92) objective lens for imaging and addressing of cold atoms. *Opt. Lett.*, 42(6):1043–1046, Mar 2017.

[146] K. Rossmann. Point spread-function, line spread-function, and modulation transfer function: tools for the study of imaging systems. *Radiology*, 93(2):257–272, 1969.

[147] D. E. Rumelhart, G. E. Hinton, and R. J. Williams. Learning representations by back-propagating errors. *Nature*, 323(6088):533–536, Oct 1986.

[148] H. Rütz, K.-H. Luo, H. Suche, and C. Silberhorn. Quantum Frequency Conversion between Infrared and Ultraviolet. *Phys. Rev. Applied*, 7:024021, Feb 2017.

[149] B. Saleh and M.C.Teich. *Fundamentals of Photonics*. Second Edition. John Wiley & Sons, Inc., 2007.

[150] J. Schmitz, H. M. Meyer, and M. Köhl. Ultraviolet Fabry-Perot cavity with stable finesse under ultrahigh vacuum conditions. *Review of Scientific Instruments*, 90(6):063102, 2019.

[151] M. Schubert, I. Siemers, R. Blatt, W. Neuhauser, and P. E. Toschek. Transient internal dynamics of a multilevel ion. *Phys. Rev. A*, 52:2994–3006, Oct 1995.

[152] M. O. Scully and M. Suhail Zubairy. *Quantum optics*. Cambridge University Press, 1997.

[153] R. J. Serfling. Probability inequalities for the sum in sampling without replacement. *The Annals of Statistics*, pages 39–48, 1974.

[154] P. W. Shor. Algorithms for quantum computation: Discrete logarithms and factoring. *IEEE*, page 124ff, 1994.

[155] P. W. Shor and J. Preskill. Simple Proof of Security of the BB84 Quantum Key Distribution Protocol. *Phys. Rev. Lett.*, 85:441–444, Jul 2000.

[156] D. A. Steck. Rubidium 85 D Line Data, available online at http://steck.us/alkalidata (revision 2.1.6, 20 Sep 2013).

[157] M. Steiner. *A Single Ion Inside a Miniature Cavity*. PhD thesis, Robinson College, University of Cambridge, 2014.

[158] M. Steiner, H. M. Meyer, C. Deutsch, J. Reichel, and M. Köhl. Single Ion Coupled to an Optical Fiber Cavity. *Phys. Rev. Lett.*, 110:043003, Jan 2013.

[159] M. Steiner, H. M. Meyer, J. Reichel, and M. Köhl. Photon Emission and Absorption of a Single Ion Coupled to an Optical-Fiber Cavity. *Phys. Rev. Lett.*, 113:263003, Dec 2014.

[160] T. Steinmetz, Y. Colombe, D. Hunger, T. W. Hänsch, A. Balocchi, R. J. Warburton, and J. Reichel. Stable fiber-based Fabry-Pérot cavity. *Applied Physics Letters*, 89(11):111110, 2006.

[161] L. J. Stephenson, D. P. Nadlinger, B. C. Nichol, S. An, P. Drmota, T. G. Ballance, K. Thirumalai, J. F. Goodwin, D. M. Lucas, and C. J. Ballance. High-Rate, High-Fidelity Entanglement of Qubits Across an Elementary Quantum Network. *Phys. Rev. Lett.*, 124:110501, Mar 2020.

[162] A. Stute. *A light-matter quantum interface: ion-photon entanglement and state mapping*. PhD thesis, Leopold-Franzens-Universität Innsbruck, 2012.

[163] A. Stute, B. Casabone, B. Brandstätter, K. Friebe, T. E. Northup, and R. Blatt. Quantum-state transfer from an ion to a photon. *Nature Photonics*, 7(3):219–222, 2013.

[164] A. Stute, B. Casabone, P. Schindler, T. Monz, P. O. Schmidt, B. Brandstätter, T. E. Northup, and R. Blatt. Tunable ion–photon entanglement in an optical cavity. *Nature*, 485(7399):482–485, May 2012.

[165] H. Takahashi, E. Kassa, C. Christoforou, and M. Keller. Cavity-induced anticorrelated photon-emission rates of a single ion. *Phys. Rev. A*, 96:023824, Aug 2017.

[166] M. Takeoka, S. Guha, and M. M. Wilde. Fundamental rate-loss tradeoff for optical quantum key distribution. *Nature Communications*, 5(1):5235, Oct 2014.

[167] E. Togan, Y. Chu, A. Trifonov, L. Jiang, J. Maze, L. Childress, G. Dutt, A. Sørensen, P. Hemmer, A. Zibrov, and M. Lukin. Quantum Entanglement Between an Optical Photon and a Solid-State Spin Qubit. *Nature*, 466:730–4, Aug 2010.

[168] M. Tomamichel, C. C. W. Lim, N. Gisin, and R. Renner. Tight finite-key analysis for quantum cryptography. *Nature Communications*, 3(1):1–6, 2012.

[169] A. D. Tranter, H. J. Slatyer, M. R. Hush, A. C. Leung, J. L. Everett, K. V. Paul, P. Vernaz-Gris, P. K. Lam, B. C. Buchler, and G. T. Campbell. Multiparameter optimisation of a magneto-optical trap using deep learning. *Nature Communications*, 9(1):4360, 2018.

[170] Q. A. Turchette, C. S. Wood, B. E. King, C. J. Myatt, D. Leibfried, W. M. Itano, C. Monroe, and D. J. Wineland. Deterministic Entanglement of Two Trapped Ions. *Phys. Rev. Lett.*, 81:3631–3634, Oct 1998.

[171] R. Ursin, F. Tiefenbacher, T. Schmitt-Manderbach, H. Weier, T. Scheidl, M. Lindenthal, B. Blauensteiner, T. Jennewein, J. Perdigues, P. Trojek, B. Ömer, M. Fürst, M. Meyenburg, J. Rarity, Z. Sodnik, C. Barbieri, H. Weinfurter, and A. Zeilinger. Entanglement-based quantum communication over 144 km. *Nature Physics*, 3(7):481–486, Jul 2007.

[172] P. van Loock, W. Alt, C. Becher, O. Benson, H. Boche, C. Deppe, J. Eschner, S. Höfling, D. Meschede, P. Michler, F. Schmidt, and H. Weinfurter. Extending Quantum Links: Modules for Fiber- and Memory-Based Quantum Repeaters. *Advanced Quantum Technologies*, 3(11):1900141, 2020.

[173] U. Vazirani and T. Vidick. Fully Device-Independent Quantum Key Distribution. *Phys. Rev. Lett.*, 113:140501, Sep 2014.

[174] J. Volz. *Atom-Photon Entanglement*. PhD thesis, Ludwig-Maximilians-Universität München, 2006.

[175] J. Volz, M. Weber, D. Schlenk, W. Rosenfeld, J. Vrana, K. Saucke, C. Kurtsiefer, and H. Weinfurter. Observation of Entanglement of a Single Photon with a Trapped Atom. *Phys. Rev. Lett.*, 96:030404, Jan 2006.

[176] E. Waks, K. Inoue, C. Santori, D. Fattal, J. Vuckovic, G. S. Solomon, and Y. Yamamoto. Quantum cryptography with a photon turnstile. *Nature*, 420(6917):762–762, Dec 2002.

[177] T. Walker, K. Miyanishi, R. Ikuta, H. Takahashi, S. Vartabi Kashanian, Y. Tsujimoto, K. Hayasaka, T. Yamamoto, N. Imoto, and M. Keller. Long-Distance Single Photon Transmission from a Trapped Ion via Quantum Frequency Conversion. *Phys. Rev. Lett.*, 120:203601, May 2018.

[178] Y. Wang, M. Um, J. Zhang, S. An, M. Lyu, J.-N. Zhang, L.-M. Duan, D. Yum, and K. Kim. Single-qubit quantum memory exceeding ten-minute coherence time. *Nature Photonics*, 11(10):646–650, Oct 2017.

[179] G. Weihs, T. Jennewein, C. Simon, H. Weinfurter, and A. Zeilinger. Violation of Bell's inequality under strict Einstein locality conditions. *Phys. Rev. Lett.*, 81(23):5039, 1998.

[180] T. Wilk, S. C. Webster, A. Kuhn, and G. Rempe. Single-Atom Single-Photon Quantum Interface. *Science*, 317(5837):488–490, 2007.

[181] D. J. Wineland and W. M. Itano. Laser cooling of atoms. *Phys. Rev. A*, 20:1521–1540, Oct 1979.

[182] W. K. Wootters and W. H. Zurek. A single quantum cannot be cloned. *Nature*, 299:802–803, Oct 1982.

[183] K. Wright, K. M. Beck, S. Debnath, J. M. Amini, Y. Nam, N. Grzesiak, J.-S. Chen, N. C. Pisenti, M. Chmielewski, C. Collins, K. M. Hudek, J. Mizrahi, J. D. Wong-Campos, S. Allen, J. Apisdorf, P. Solomon, M. Williams, A. M. Ducore, A. Blinov, S. M. Kreikemeier, V. Chaplin, M. Keesan, C. Monroe, and J. Kim. Benchmarking an 11-qubit quantum computer. *Nature Communications*, 10(1):5464, Nov 2019.

[184] J. Yin, Y.-H. Li, S.-K. Liao, M. Yang, Y. Cao, L. Zhang, J.-G. Ren, W.-Q. Cai, W.-Y. Liu, S.-L. Li, R. Shu, Y.-M. Huang, L. Deng, L. Li, Q. Zhang, N.-L. Liu, Y.-A. Chen, C.-Y. Lu, X.-B. Wang, F. Xu, J.-Y. Wang, C.-Z. Peng, A. K. Ekert, and J.-W. Pan. Entanglement-based secure quantum cryptography over 1,120 kilometres. *Nature*, 582(7813):501–505, Jun 2020.

[185] N. Yu and L. Maleki. Lifetime measurements of the $4f^{14}5d$ metastable states in single ytterbium ions. *Phys. Rev. A*, 61:022507, Jan 2000.

[186] M. J. Zawierucha. Coherent Qubit Control in a $^{171}Yb^{+}$ ion using Microwave and Raman Transitions. Master's thesis, Rheinische Friedrich-Wilhelms-Universität Bonn, Sep 2017.

[187] T. Zhong, H. Zhou, R. D. Horansky, C. Lee, V. B. Verma, A. E. Lita, A. Restelli, J. C. Bienfang, R. P. Mirin, T. Gerrits, S. W. Nam, F. Marsili, M. D. Shaw, Z. Zhang, L. Wang, D. Englund, G. W. Wornell, J. H. Shapiro, and F. N. C. Wong. Photon-efficient quantum key distribution using time–energy entanglement with high-dimensional encoding. *New Journal of Physics*, 17(2):022002, Feb 2015.

[188] R. W. Ziolkowski, J. M. Arnold, and D. M. Gogny. Ultrafast pulse interactions with two-level atoms. *Phys. Rev. A*, 52:3082–3094, Oct 1995.

[189] C. Zipkes. *A Trapped Single Ion Inside a Bose–Einstein Condensate*. PhD thesis, Robinson College, University of Cambridge, 2011.

Acknowledgement

First of all, I would like to thank Prof. Dr. Michael Köhl, who was, among other roles, supervisor, source of ideas and crisis manager for the project of this thesis. Thank you for the hours of time it sometimes took to find a solution when everyone else was at their wits' end. At the same time, I would like to thank you for the freedom and trust in the development process of this project, in which I was able to fulfil myself and my research interests. The fact that everything worked out in the end was an incredible joy.

Another person who has strongly influenced my way and that of the experiment is Dr. Hendrik-Marten Meyer. You were always an example and brought good humour to the lab. With your help, it was always possible to 'to sort out the mess again' if necessary. Thank you for your time, advice, overview and for setting up this great experiment.

A big thank you also goes to Dr. Tim Ballance who entrusted me with the experiment he set up during the course of his PhD and taught me how to make the right decisions so as not to spend several days doing damage control.

I would also like to thank in particular the people who contributed significantly to the research results of this thesis, such as Martin Link, who not only contributed to the experiment with his Master's thesis, but also worked on the machine-learning part of this thesis and set the decisive impulses there, as well as proofread parts of this thesis. Thanks to Moritz Breyer for the manifold support at the experiment and the construction of the great fibre cavity, which can be really hard work in some parts and requires a lot of patience and a steady hand. Thank you for the partial proofreading of this thesis. Many thanks also go to Ralf Berner for the upgrades of the experiment as part of his Bachelor's and Master's thesis and for the support during the final phase of data collection. You asked important questions which helped to solve some major problems. Thank you for proofreading this thesis.

A very special thank you goes to Thorsten Langerfeld, who was involved in this work on several fronts. Firstly, on a professional level by discussing problems, partially proofreading this thesis and supporting me in the lab when some things were literally and figuratively burning. And secondly, of course, on a social level as a friend and fellow student from the first day of my physics studies, which has significantly influenced my way to this point. It is great that we have been able to use our excellent teamwork to this point.

I would also like to thank several people who worked on the experiment during my research phase, such as Kilian Kluge, who was a major contributor to technical innovations. In addition, Maximilian Zawierucha, Ashwin Boddeti, Vidhya Sair and Moritz Scharfstädt also contributed to the success of the experiment.

I would especially like to thank all further members of my examination board: Prof. Dr. Sebastian Hofferberth for writing the second review of this thesis, Prof. Dr. Dagmar Bruß for her support and impulses on the theory side of quantum key distribution, and Prof. Dr. Michael Meier for contributing his perspective from the field of IT security. Thank you all for the very interesting discussions.

Furthermore, I would like to thank Pia Fürtjes, Leon Reiffert and Santhosh Surendra, who have taken the production of the fibre surfaces to a new level.

Special thanks go to the members of the "Start-up corner" where agile working and creative problem solving was the order of the day, especially to Jonas Schmitz, Steffen

Gohlke and Felix Rönchen.

Excellent competence was provided at all times by the neighbouring experiments with Nicola Wurz, Nick Klemmer, Dr. Alexandra Behrle, Dr. Kuiyi Gao, Andreas Kell, Janek Fleper, Dr. Jeffrey Chan, Andreas von Haaren and Marcell Gall. I would like to address a very special thank you to Marcell for proofreading large parts of this thesis, sharing experiences during the writing of this thesis and the ability to solve very specific problems, for example in the high frequency domain.

Thanks also to Dr. Akos Hoffmann for his professional expertise in the field of electronics, which could be consulted at any time. I would also like to thank the head of the workshop, Mr. Christen, for his support.

On a very personal level, several people have accompanied, supported and influenced me along my way. In particular, I would like to say a huge thank you to the physicists from day one who walked the path of studying physics with me, such as Max Werninghaus, Sebastian Hölzl and Nils Wittenburg. Without you, studying would have been much harder and certainly much more boring.

I would like to thank Stefanie Müller for her enormous support, especially during the difficult and stressful phases of this project. Without you, I would not have been able to manage it in this way. Thank you for proofreading large parts of this work and listening to lectures on ion trapping, quantum networks and fibre resonators.

I would like to thank my family that they now all know what a 'cavity lock' is. But of course especially for the support, the encouragement and all the joy I get from you. Moreover, I would like to thank my parents for providing me every opportunity and for always being able to count on their support.